

SMALL ENGINE FLASH VAPOR JP-8 FUEL INJECTOR TESTING,  
SIMULATION AND DEVELOPMENT

A Dissertation

by

XIAOHUA ZHANG

Submitted to the Office of Graduate and Professional Studies of  
Texas A&M University  
in partial fulfillment of the requirements for the degree of

DOCTOR OF PHILOSOPHY

Chair of Committee,	Alan Palazzolo
Committee Members,	Won-jong Kim
	Eric Petersen
	Hamid Toliyat
Head of Department,	Andreas Polycarpou

December 2014

Major Subject: Mechanical Engineering

Copyright 2014 Xiaohua Zhang

## ABSTRACT

Following U.S. Army's single fuel initiative, Wankel rotary engines used in U.S. Army's shadow unmanned aerial vehicles (UAVs) need to be retrofitted from running on aviation gasoline (AVGAS) to JP-8. The feasibility of retrofitting the engine with a flash vapor direct fuel injector was investigated. A commercial off-the-shelf direct fuel injector was used in the study. A photo detector measurement tool was developed to measure high frequency ( $>100$  Hz) injection event. A coupled electrical-electromagnetics-fluid-mechanical system was simulated to understand the pintle dynamics during an injection event. Optimal injector power drive was revealed to be a multi-stage current profile. A flash heater was designed and tested to be capable of heating up JP-8 from room temperature to its vaporization temperature ( $>310$ F) under one tenth of a second at the required flow rate. An ignition test rig was built to compare ignition behavior between AVGAS and heated JP-8. Test result showed that the 550F pre-heated JP-8 had equal or superior ignition pressure rise / ignition delay time than AVGAS.

## DEDICATION

This work is dedicated to my mother, Lichun Liu, for her love and support.

## ACKNOWLEDGMENTS

This work has been made possible by the help of many people. In particular, I would like to express my deepest gratitude to my committee chair, Dr. Palazzolo. During the past six years (both my Master's and PhD), I have been indebted to him who has given me guidance, ideas, encouragement and support even in my most difficult times. I would surely remember the long testing days and nights we worked together on the fuel injector. It was a lot of work, but also a lot of fun when I look back! I would also like to thank my committee members, Dr. Kim, Dr. Petersen, and Dr. Toliyat, for contributing their time and knowledge throughout the course of my study.

I have been fortunate to have worked with some of the greatest colleagues. I want to thank them not just for their work, but also for who they are as a person. Randall Tucker and Willie Simpson are two of those I would like to thank most. Randy has taught me a lot of hands-on knowledge and how to use common-sense to make sound judgment on engineering problems. Both of them gave me a big hand when I needed it most.

I am also in great debt to my advisors from U.S. Army Research Lab. Mr. Albert Kascak (now retired) and Dr. Chol-Bum Kweon have patiently guided and supported me over the years. Their vision and technical guidance always ensure the project to be on the right track. Mr. Kascak is the first person who proposed the JP-8 flash heating method.

I would also like to thank many students and colleagues who have worked with me on designing and building stuff. I especially want to thank Layne Wylie, back then



the machinist of Department of Mechanical Engineering machine shop. Countless components of the test rigs have his magic touches.

Acknowledgment also goes to the Texas A&M Supercomputing Facility (<http://sc.tamu.edu/>) for providing computing resources in conducting the research. I would also like to thank Dr. James T. Edwards (Air Force Research Laboratory) for providing the JP-8 test fuel.

Deep thanks also go to my friends and lab colleagues who have kindly lent their hands throughout the years. I always see myself as a lucky one who receives countless help from other people in my life. I was taught, when somebody ever lent you a drop of water, you should pay them back with a full tank of water. Among those water lenders, I would like to especially thank Kent Marshall, Judy Marshall, Wan Zhong, Xu Han, Junho Suh, Zhengyu Lu, and Tiberio Garza.

I would also like to thank my wonderful girlfriend Brittany Dorazio for her lovingly support during the long-hour studies and works.

Finally, thanks to my mother who always sees me as an apple in her eyes. Her unconditional love has always been one of the motivations to keep me going higher and stronger.

## NOMENCLATURE

AC	Alternating Current
AVGAS	Aviation Gasoline
BSFC	Brake Specific Fuel Consumption
CDI	Capacitive Discharge Ignition
CFD	Computational Fluid Dynamics
CI	Compression Ignition
COTS	Commercial Off-The-Shelf
CR	Compression Ratio
DAQ	Data Acquisition
DI	Direct Injection
EDM	Electrical Discharge Machining
FEA	Finite Element Analysis
FEM	Finite Element Method
FPS	Frame Per Second
GDI	Gasoline Direct Injection
HP	Horse Power
IC	Internal Combustion
IGBT	Insulated-Gate Bipolar Transistor
NPT	National Pipe Thread
PFI	Port Fuel Injection

PID	Proportional-Integral-Derivative
PPM	Parts Per Million
RCM	Rapid Compression Machine
RPM	Rotations Per Minute
SI	Spark Ignition
STD	Standard Deviation
TDC	Top Dead Center
TTL	Transistor-transistor Logic
UAV	Unmanned Aerial Vehicle
WOT	Wide Open Throttle

## TABLE OF CONTENTS

	Page
ABSTRACT .....	ii
DEDICATION .....	iii
ACKNOWLEDGMENTS.....	iv
NOMENCLATURE.....	vi
TABLE OF CONTENTS .....	viii
LIST OF FIGURES.....	x
LIST OF TABLES .....	xx
CHAPTER I INTRODUCTION .....	1
About JP-8.....	1
About Wankel Rotary Engines.....	3
Challenges .....	4
Proposed Solutions.....	6
Organization .....	9
CHAPTER II LITERATURE REVIEW AND PRELIMINARY STUDY .....	11
Literature Review .....	11
Early Experimentation.....	15
Objective .....	28
Novelty of Contributions.....	30
Importance.....	33
CHAPTER III DIRECT FUEL INJECTOR STUDY .....	35
Overview .....	35
Injector Temporal Measurement Tool.....	36
Power Drive Requirement for Optimized Performance.....	50
Room Temperature Test Results.....	89
CHAPTER IV FLASH HEATER DEVELOPMENT .....	99
Overview .....	99
JP-8 Flash Heater Design .....	99
Fabrication.....	148

	Page
High Temperature Test Results.....	150
Conclusion.....	171
<b>CHAPTER V IGNITION TEST .....</b>	<b>174</b>
Overview .....	174
Ignition of JP-8.....	175
Ignition Test Rig Design .....	178
Test Results .....	206
Advantages of the Heated JP-8 .....	227
<b>CHAPTER VI CONCLUSION.....</b>	<b>229</b>
<b>REFERENCES .....</b>	<b>231</b>

## LIST OF FIGURES

FIGURE	Page
1 Vapor percentage vs. temperature for gasoline, diesel and JP-8.....	2
2 Rotary engine working principle.....	4
3 Small piston engine used in the preliminary study .....	16
4 Modified piston head to include direct fuel injector .....	17
5 Modified injector with 1/8 inch NPT thread .....	17
6 Injector configuration on the piston head.....	18
7 Engine test bench setup.....	19
8 Pre-heater and insulation of fuel feed-in line .....	20
9 Small piston engine JP-8 fuel system schematic.....	21
10 Injector timing schematic in the preliminary engine test .....	22
11 Bentley sensor position in the preliminary engine test .....	22
12 Small piston engine pre-heating JP-8 test rig.....	25
13 Screenshot from engine running at 2692 rpm with pre-heated JP-8 injection .....	25
14 Cylinder head after a few runs with JP-8 .....	27
15 Thermowell is surrounded by carbonized JP-8 fuel.....	27
16 BOSCH direct fuel injector used in this study .....	35
17 Photo detector for measuring an injector spray event.....	37
18 Photo detector drive circuit .....	37
19 Support ring for mounting the fuel injector and photo detector.....	38
20 Section view of the mounting structure with nitrogen path .....	38
21 Hydraulic system illustration of the injector test bench .....	39

FIGURE	Page
22	Injector drive system with PWM servo amplifier .....41
23	Control voltage, current and photo detector signals for a two-stage PWM amplifier powered direct fuel injector spray event.....43
24	Zoomed-in view of Figure 23 showing signals for a single injection event .....43
25	The spray temporal definitions.....44
26	Injection events with different control signal on-times.....45
27	High speed camera spray chamber .....47
28	High speed camera test setup .....47
29	Frame-to-frame photos during one injection event using high-speed camera. ....49
30	Time to reach 8.5 A with different time constants .....52
31	Electrical circuit in Maxwell circuit editor .....53
32	Inductance at different air gaps from Maxwell .....54
33	Flux path in the magnetic circuit analysis .....55
34	Current level vs. elapsed times at the calculated inductances .....57
35	Maxwell calculated and measured current shapes .....57
36	Magnetic flux density vector plot at $t = 0.4$ ms from 2D Maxwell transient with the two-stage current shown in Figure 35 .....58
37	Calculated magnetic forces at different air gaps and current levels with Equation (9) and Maxwell.....60
38	Magnetic force profile with and without pintle movement using Maxwell .....61
39	Saturation study for different materials and air gaps .....62
40	Magnetic force vs. current at 0.1 mm air gap with steel 1008 (2T saturation) ....63
41	Mechanical system of the pintle with force illustration .....64
42	Magnetic force profile .....65

FIGURE	Page
43	Calculated static pressure forces at pintle closed position under different inlet pressures .....66
44	Grid independence study .....68
45	Meshed fluid region from ICEMCFD .....68
46	Small gap between ball and valve seat at the “closed” position .....69
47	Pintle displacement profiles at different inlet pressures with power strategy (a) .....71
48	1/6th of pressure forces on the pintle at different inlet pressures with power strategy (a).....71
49	1/6th of mass flow rates at different inlet pressures with power strategy (a).....72
50	Current profile comparison between power strategy (a) and (b) .....75
51	Pinlte displacement profiles with power strategy (b) and (a) at 200 atm supply pressure .....75
52	1/6th of pressure forces on the pintle with power strategy (b) and (a) at 200 atm supply pressure .....76
53	1/6th of mass flow rates with power strategy (b) and (a) at 200 atm supply pressure.....76
54	Current profile comparison among power strategy (a), (b) and (c) .....78
55	Pintle displacement profiles with power strategy (c) and (a) at 200 atm supply pressure .....78
56	1/6th of pressure forces on the pintle with power strategy (c) and (a) at 200 atm supply pressure .....79
57	1/6th of mass flow rates with power strategy (c) and (a) at 200 atm supply pressure.....79
58	Current requirement illustration during one injection event .....81
59	Current profile illustration for implementation .....82



FIGURE	Page
60 Average mass flow rate comparison during one injection event with power strategy (a) at different supply pressures.....	83
61 Photo detector output with 1st stage current of 8 A, 1st stage on-time 0.2 ms, 2nd stage current of 3.5 A, 2nd stage on-time 0.8 ms; at 200 atm supply pressure.....	86
62 Photo detector output with 1st stage current of 8 A, 1st stage on-time 0.16 ms, 2nd stage current of 3.5 A, 2nd stage on-time 0.84 ms; at 200 atm supply pressure.....	87
63 Photo detector output with 1st stage current of 8 A, 1st stage on-time 0.2 ms, 2nd stage current of 2.5 A, 2nd stage on-time 0.8 ms; at 200 atm supply pressure.....	87
64 Weighing system concept.....	90
65 Actual weighing system .....	90
66 Injector test fixture .....	91
67 Injector test cabinet .....	91
68 Electronics module for injector testing .....	93
69 Electrical and electronics system .....	93
70 Injector program Labview user interface .....	94
71 Opening delay and spray duration times measured with photo detector.....	96
72 Average mass flow vs. injection pulse width 140 and 200 atm fuel supply pressures .....	96
73 Average mass flow rate per shot vs. injection pulse width .....	97
74 Carbon deposit vs. different alloys.....	100
75 500 C (932 F) JP-8 carbon deposit under 34 atm (500 psi) with 1 mL/min flow rate.....	101
76 Thermal conductivity comparison between water and JP-8.....	103
77 The dissection of direct fuel injector shows possible heater location .....	103

FIGURE	Page
78 2D section view of pressure vessel using direct heating method .....	104
79 Direct heating method FEA model.....	105
80 Temperature transient profile at three different locations .....	105
81 FEA model for thin circular fuel passage.....	106
82 Transient response of a thin circular fuel passage heating model.....	107
83 Insulated inner boundary, thin circular fuel passage.....	108
84 Transient response of insulated inner boundary, thin circular fuel passage heater .....	109
85 Bundle tube heater concept .....	110
86 FEM model of one tiny tube in a bundled tube heater .....	111
87 Central fuel temperature transient with 26 mil tube and 400 F wall.....	112
88 Small-hole tube heater concept .....	113
90 Small-hole tube heater's inner metal temperature transient response.....	114
89 Small-hole tube heater FEA model .....	114
91 Small-hole tube heater's fuel temperature transient response.....	115
92 Evolution of heater ideas.....	116
93 Rectangular shape fuel heating vessel.....	116
94 Middle fuel temperature from a rectangular shape heater.....	117
95 Flat channel preheater .....	118
96 Integrated slot heater with fuel injector concept .....	120
97 Integrated slot heater with thin rectangular fuel passage .....	121
98 Heated injector assembly .....	121
99 Analytical solution: fuel temp. vs. time at different locations .....	123

FIGURE	Page
100 ANSYS heat transfer model for rectangular heater .....	124
101 Numerical solution with ANSYS: fuel temp. vs. time at different locations .....	125
102 Steady-state outlet fuel temperature vs. volumetric flow rate at different power levels.....	127
103 Cross section view of the heat transfer model.....	128
104 Model with periodic boundaries.....	129
105 Further simplified model for heat transfer analysis .....	130
106 Meshed domain in ICEMCFD .....	133
107 Grid independence study.....	134
108 Mesh quality: angle and determinant .....	134
109 Boundary conditions in the CFX-Pre .....	136
110 Transient static heating: avg. outlet fuel temperature .....	137
111 Mid-plane temperature distribution at the end of 10 sec heating with fuel flow rate of 0.8721 g/s.....	138
112 Avg. fuel outlet temp. with 245 watts * 50% (efficiency) heat flux, 0.8721 g/s mass flow rate .....	139
113 Study of temperature dependent property effect .....	139
114 Heater design variables .....	140
115 Stress under 3000 psi with 0.03'' distance between the tip of the slot and outer wall.....	142
116 Zoomed-in view of the stress under 3000 psi with 0.03'' wall thickness.....	142
117 Stress distribution of the .01'' wall thickness case under 3000 psi pressure .....	143
118 Transient heating results of different No. of slots with 0.35'' radius .....	146
119 Transient heating results of different radius with 40 slots .....	146

FIGURE	Page
120	Transient heating results of different radius with 50 slots ..... 147
121	Direct fuel injector before (left) and after (right) modified..... 149
122	Heated fuel injector assembly ..... 150
123	Injector test cabinet ..... 151
124	Top plate of injector test fixture with o’ring seal ..... 152
125	Labview user interface for heating test ..... 154
126	Load cell calibration curve ..... 158
127	Load cell output during two injection tests ..... 159
128	Volume per shot vs. pulse width using weighing system ..... 160
129	Thermocouples to measure spray temperature..... 161
130	Flow rate data from May 17 test ..... 162
131	Temperature data from May 17 heating test ..... 163
132	Transient temperature response at the start of injection measured at the nozzle exit using 500 F pre-heating temperature without fuel ..... 166
133	Transient temperature response at the start of injection measured at the nozzle exit using 500 F pre-heating temperature with fuel ..... 166
134	Overlapping 0.1 second time constant curve with transient temperature profile in the case of preheating without fuel at 500 F..... 168
135	JP-8 distillation curve..... 169
136	Heater efficiency determination ..... 171
137	Piston assembly in the ignition test rig..... 180
138	Piston assembly ..... 180
139	Cylinder assembly ..... 181
140	Operating procedure of the piston assembly ..... 182

FIGURE	Page
141 Air valve position illustration.....	182
142 Pressure profiles using different operating modes .....	184
143 Pressure profiles using pre-charge modes .....	185
144 Test rig schematic.....	188
145 Ignition test rig concept.....	189
146 Top half of the ignition test rig.....	189
147 Bottom half of the ignition test rig .....	190
148 Components on the bottom plate of the ignition cylinder .....	191
149 Bottom view inside the ignition test rig .....	192
150 The whole ignition test rig .....	193
151 Labview user interface for ignition test.....	194
152 Ignition circuit diagram.....	196
153 Original injector-spark plug configuration on the bottom plate.....	198
154 Pilot injection configuration.....	199
155 Close view of pilot injection configuration.....	200
156 Scanned Wankel engine housing.....	201
157 Scanned Wankel engine rotor.....	201
158 Maximum volume without pocket .....	202
159 Minimum volume without pocket.....	202
160 Pocket volume .....	203
161 Timing diagram for ignition test .....	207
162 Actual signals during ignition test.....	208

FIGURE	Page
163 Injection timing: 0.5 ms, injection control on-time: 0.45 ms, fuel rail pressure: 3000 psi, 1 <sup>st</sup> shot ignition.....	210
164 Zoomed-in view of Figure 163.....	211
165 AVGAS ignition pressure rise under different rail pressures at 0.4 ms injection timing and 0.35 ms injection control on-time .....	212
166 AVGAS ignition delay time under different rail pressures at 0.4 ms injection timing and 0.35 ms injection control on-time .....	213
167 AVGAS ignition pressure rise at different injection control on-times with 1 ms injection timing and 3000 psi rail pressure .....	214
168 AVGAS ignition delay time at different injection control on-times with 1 ms injection timing and 3000 psi rail pressure.....	214
169 AVGAS 1 <sup>st</sup> shot ignition success rate at different injection timing under 1500 psi rail pressure.....	215
170 AVGAS 1 <sup>st</sup> shot ignition pressure rise at different injection timing under 1500 psi rail pressure.....	215
171 AVGAS 1 <sup>st</sup> shot ignition delay times at different injection timing under 1500 psi .....	216
172 Preheated JP-8, injection timing: 0.2 ms, injection control on-time: 0.35 ms, fuel rail pressure: 1500 psi, 1st shot ignition.....	218
173 Zoom-in view of Figure 172 .....	218
174 1 <sup>st</sup> shot ignition success rate vs. JP-8 pre-heating body temperature .....	219
175 1 <sup>st</sup> shot ignition pressure rise vs. JP-8 pre-heating body temperature .....	219
176 500 F preheated JP-8's 1 <sup>st</sup> shot ignition success rate at different injection control on-times.....	220
177 500 F preheated JP-8's 1 <sup>st</sup> shot ignition pressure rise at different injection control on-times.....	221
178 500 F preheated JP-8's 1 <sup>st</sup> shot ignition delay times at different injection control on-times.....	221

FIGURE	Page
179 500F preheated JP-8's pressure rise at different injection timings .....	222
180 500F preheated JP-8's ignition success rate at different injection timings .....	223
181 Preheated JP-8 at different injection timings .....	224
182 1st shot ignition success rate with different fuels .....	225
183 1 <sup>st</sup> shot ignition pressure rise with different fuels .....	225
184 1 <sup>st</sup> shot ignition delay time with different fuels.....	226

## LIST OF TABLES

TABLE	Page
1 Fuel vapor pressures (kPa) at various temperatures.....	2
2 Technical specifications of the piston engine in the preliminary study .....	16
3 Calculation of the JP-8 consumption rate for 6.5 HP test engine .....	24
4 Summary of the small piston engine successfully running on pre-heated JP-8 using direct fuel injection.....	26
5 Direct fuel injector specification .....	36
6 Photo detector's electronics properties .....	37
7 PWM servo amplifier specification.....	40
8 Power strategy used in this study .....	41
9 Test conditions .....	45
10 Spray temporal characteristics with different control signal on-times.....	46
11 High-speed camera used in this study .....	48
12 Fuel injection temporal characteristics comparison with high-speed camera (HS) and photo detector (PD) methods under the same test conditions.....	48
13 Electrical properties of the fuel injector coil and PWM power amplifier .....	52
14 Parameters for inductance calculation.....	56
15 Mesh information for fluid model.....	67
16 Key physical parameters for the fluid model .....	70
17 Boundary conditions .....	70
18 Initial opposing forces, required magnetic forces and threshold current levels under different pressures .....	73
19 Spray temporal characteristics comparison between calculated and measured data .....	84



TABLE	Page
20 Analytical solution comparison between 1D flat model and 1D axisymmetric model.....	119
21 Analytical solution to the slot heater.....	123
22 Temperature dependence of JP-8 density and specific heat.....	126
23 Slot heater geometric parameters .....	128
24 Initial and boundary conditions for heat transfer with mass flow problem.....	135
25 Stainless steel 304 properties vs. temperature.....	135
26 JP-8 (liquid form) properties vs. temperature .....	136
27 Design variables for heater optimization.....	144
28 Parametric models with different variables.....	145
29 Test matrix for heating test 1.....	154
30 Test matrix for heating test 2.....	155
31 Test matrix for heating test 3.....	156
32 JP-8 transient-heating test .....	164
33 Long duration heating test.....	168
34 Test condition with AVGAS .....	209
35 Test condition with JP-8.....	216
36 AVGAS and heated JP-8 test condition .....	224

# CHAPTER I

## INTRODUCTION

In 2004, Department of Defense (DoD) mandated all the engine systems to be transitioned to run on a single fuel – JP-8, known as U.S. Army’s single fuel initiative. The reason behind this single fuel initiative is for simplified logistics and improved safety in the battlefield. JP-8 is strategically chosen to be the single fuel to be operated in the future battlefield due to its wide availability across regions, as well as its lubrication properties.

### **About JP-8**

JP-8 is kerosene based heavy fuel which has more than one hundred additives. Its commercial version is Jet A, which is widely used in commercial airliners. JP-8 has auto-ignition temperature of 460 °F (238 °C) at 1 atm and its vapor pressure at 100 °F (38 °C) is .029 psia, which is very low compared with gasoline. JP-8 has boiling range: 313.3-504.3 °F (156.3-262.4 °C) and it will start decomposing at 325 °F.

As a heavy fuel, JP-8 has low vapor pressure which indicates poor vaporization characteristics. The low octane number means JP-8 has high tendency to pre-ignite or knock. Vapor pressure is a measure of fuel volatility. High vapor pressure fuel, i.e. gasoline, tends to evaporate at lower temperature, while low vapor pressure ones, i.e. diesel, jet fuel, need higher temperature to create the same amount of vapor. The measure of vapor pressure has direct relation with how easy (or how difficult) for it to form ignitable fuel-air mixture. Figure 1 shows the vapor percentage vs. temperature for

gasoline, diesel and JP-8. Table 1 lists vapor pressures for different fuels at different temperatures.

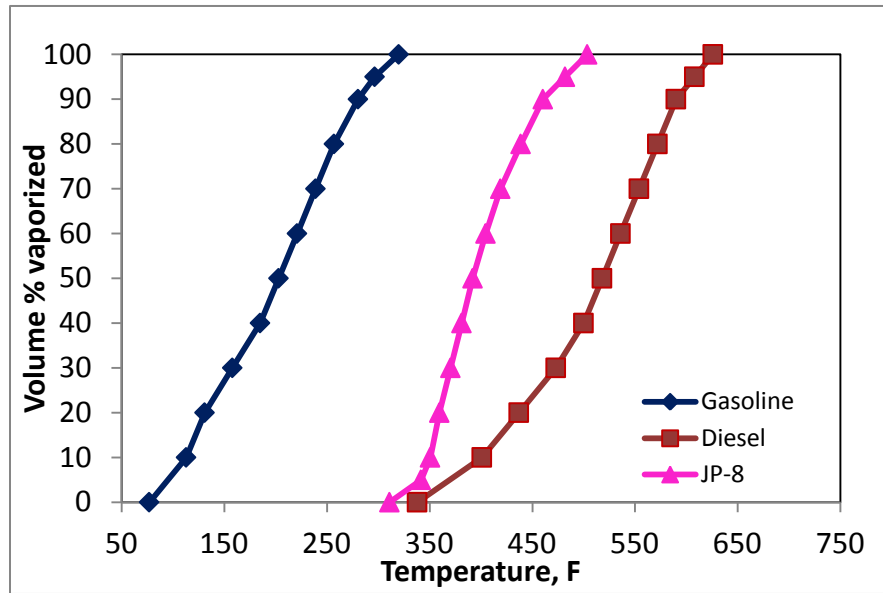


**Figure 1. Vapor percentage vs. temperature for gasoline, diesel and JP-8 (reproduced from [1] and [2])**

**Table 1. Fuel vapor pressures (kPa) at various temperatures [3]**

Temperature (F)	isooctane	n-heptane	aviation gasoline	JP-8
68	5.2	4.7	23	0.05
122	19.5	18.9	70	1.3
140	28.6	28	94	2
176	56.9	56.9	190	5
212	103.6	105.6	250 (est)	8.4

As can be seen, the JP-8 and diesel start vaporization process beyond 300 F, while gasoline has fully vaporized at this temperature.

In general, the smaller the droplet, the easier it can reach ignitable fuel-air equivalence ratio. Low vapor pressure fuel droplet is more difficult to be vaporized. Because of its poor evaporation characteristic, low vapor pressure fuel can cause long ignition delays. This long ignition delays can be problematic to run rotary engine, which is normally operated at 6,000 rpm range. Because of this high engine speed, there is very limited time for room temperature fuel droplet to be vaporized and ignited on each compression-combustion cycle.

### **About Wankel Rotary Engines**

Wankel rotary engines are used in U.S. Army's shadow unmanned aerial vehicles (UAVs). Developed by Felix Wankel in 1951, rotary engines have been under constant improvement since then. It is well-known for its simplicity, low vibration, smooth running at high speed and low weight to power ratio compared with piston engines. The low weight to power ratio is especially attractive to aviation industry. This is one of the reasons why UAVs are equipped with rotary type engines.

As shown in Figure 2, the engine uses its eccentricity to create three chambers that separate the whole housing. These three chambers are constantly moving in the same direction, which makes it perfect for the intake-compression-combustion-exhaust internal combustion cycle. Because of its one directional motion, it eliminates sudden acceleration and deceleration experienced in piston engines. This enables it to run at higher speed with lower mechanical stresses.

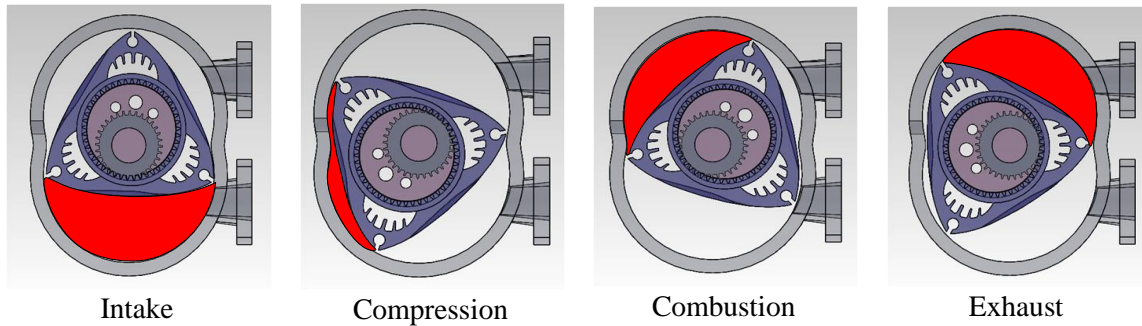


**Figure 2. Rotary engine working principle**

Despite its many merits, i.e. low vibration, high power to weight ratio, etc., rotary engines generally have low compression ratio. This low compression ratio creates low chamber temperature at its maximum compression, which becomes the main limiting factor of running it on heavy fuel, i.e. diesel and jet fuel.

The engine we are working with is a 38 hp rotary engine. It is designed to run on aviation gasoline (AVGAS) with carbureted fuel delivery system. Because of its low compression ratio (measured to be 8:1), it utilizes spark plugs to initiate ignition. The speed range of this engine is 4,500 – 9,000 rpm. The maximum power output is 38 hp at 6,000 rpm, at which the fuel consumption rate is 250 cc/min.

### **Challenges**

Inevitably, the single fuel initiative with JP-8 has the largest impact on power plants which are designed to run on high vapor pressure fuels such as gasoline. This type of engines has low compression ratio and uses spark ignition (SI). Unlike diesel compression ignition (CI) engine, which has high compression ratio, SI engine relies on

evaporation of high vapor pressure fuels and uses spark plug to ignite the fuel air mixture.

Evaporation rate has large impact on how the engine and ignition system works. Because of its high vapor pressure, gasoline tends to evaporate and mix with air really well. This fuel air charge is readily ignitable if minimum ignition (activation) energy is met.

In low compression ratio SI engines, spark plugs give fuel air mixture the minimum ignition energy to initiate the combustion. While in high compression ratio CI engines, the combustion chamber temperature reaches ignition temperature through compression, thus no ignition source is required to initiate the combustion.

SI engines are designed in such a way that the high vapor pressure fuel evaporates before spark takes place. To run the same low compression ratio gas engine with low vapor pressure JP-8, the fuel air ratio needs to be similar to the one runs on high vapor pressure gasoline.

JP-8 is a low vapor pressure fuel, which is similar to diesel. Its low evaporation rate may hinder it from running on low compression ratio engine even with the assist of spark plug. If no extra effort is put in to evaporate JP-8 in this low compression ratio rotary engine, the injected fuel will most likely form incombustible droplets that have too large of the volume-to-surface ratio to cause any ignition.

Thus, the key to successfully running SI engines with JP-8 is the evaporation of fuel. With low vapor pressure JP-8, it risks not having enough fuel vapor to form

ignitable mixture in a timely manner. The low vapor pressure of JP-8 becomes one of the main hindrances of running low compression ratio Wankel rotary engines on JP-8.

On the other hand, CI engines run on heavy fuels even though those fuels have low vapor pressures like JP-8. The way it works is that high compression ratio provides high enough temperature for the evaporation of fuel. Because of its low compression ratio, the rotary engine in this study would have difficulty in evaporating JP-8 and creating ignitable fuel air mixture. The low compression ratio becomes another main hindrance of running the engine on JP-8.

### **Proposed Solutions**

Now the key to run this engine on JP-8 becomes clear: improve the evaporation and form combustible fuel air mixture.

Compared with gasoline, JP-8 has evaporation property that is similar to diesel. As shown in Figure 1, the vaporized percentage of JP-8 starts off from 310 °F and reaches full vapor at 500 °F. In other words, JP-8 temperature needs to be at least 310 °F to achieve partial vaporization.

The best scenario of fuel air mixture is that the fuel is fully vaporized and mixed with air at stoichiometric ratio. This requires fuel air mixture to maintain at high temperature (above 500 °F) before ignition. High temperature fuel air mixture might risk pre-ignition since multiple auto-ignitions could happen if temperature exceeds its auto-ignition temperature. Note that JP-8 has 470 °F auto-ignition temperature at 1 atm. This means if fuel air ratio falls into the ignitable range, JP-8 would auto-ignite before it reaches full vaporization. The auto-ignition could cause destructive detonation which has

a sudden release of energy. Since all IC engines are designed to run on smooth release of energy, or deflagration combustion, lower than auto-ignition temperature of JP-8 is highly recommended.

### ***Design Considerations-Temperature Requirement***

Knowing that there is no need for fully vaporization of fuel lowers the higher temperature boundary (<500 °F) of fuel air mixture, while knowing there is a need for at least partial vaporization defines the lower temperature boundary (310 °F) of fuel air mixture. Now the question becomes how to realize this high temperature requirement of fuel air mixture.

Generally, there are two ways. One is heating the fuel, which is a direct way of realizing the temperature requirement of partial vaporization. The other one is heating the air, which is an indirect way and it relies on heat transfer from air to vaporize the fuel. Heating the air would lower the mass air intake due to the decrease of air density at higher temperature, which lowers the maximum fuel quantity that can be consumed in the combustion process. The decrease of air mass results in lowered energy release associated with the chemical reaction, which lowers the engine power output.

The elevated fuel temperature shortens the evaporation time which is normally required to transfer the heat from ambient air to fuel and then maintain the fuel air equilibrium. Previous research regarding heating fuel include heating diesel fuel in the diesel engines, which did not give advantage in terms of fuel consumption, heat release rate and output power. The high temperature improves atomization quality, but lowers the penetration depth which is believed to be the cause of decreased engine performance.



In a study by Kubota et al. [4], they found crank angles at ignition and maximum pressure are delayed and the maximum combustion pressure is decreased as the fuel temperature rises. The delay of the ignition and maximum pressure is due to the delay of injection as temperature increases. This delay of injection is due to the lowered local speed of sound, as well as increased compressibility (more back pressure on the pintle movement) [5]. In another study by She, he also claimed heated diesel fuel retarded fuel injection timing and found that fuel supply advance angle improved BSFC. He mentioned that the results of deteriorated BSFC in the normal fuel supply angle might be due to pump losses at increased temperature [6].

The method we propose to use is to introduce heated fuel into spark-ignition engine and the fuel temperature should not exceed its auto-ignition temperature. Ideally, heating the fuel makes heavy fuel readily vaporizable with air just like room temperature high vapor pressure fuels. Furthermore, heating the fuel will not involve lowering the mass air intake like the air heating method does.

However, heating the fuel has another issue one must tackle: fuel decomposition, or fuel coking. When fuel temperature stays high, fuel molecules go through decomposition and react with oxygen dissolved in the fuel. This creates larger particles which form deposit on the porous locations on the wall of heater. JP-8 coking deteriorates heat transfer of the heater wall and eventually clogs up heating passages.

JP-8 cokes in two different temperature ranges:

– Lower temperature: 325-550 F (162.8-287.8 °C or 435.9-560.9 K) due to dissolved oxygen in the fuel (about 50 ppm) –called autoxidative regime (< 482 F).

– Higher temperature: above 900 °F (482.2 °C or 755.4 K) due to fuel molecule breaking down – called pyrolytic regime (>752 °F).

Besides temperature, there are other factors that affect the speed and quantity of coking, i.e. wall coating, dissolved oxygen level, time staying at elevated temperature, etc.

In order to heat the fuel while keeping it from coking is tricky. The idea of flash heating is to heat the JP-8 quickly (in the magnitude of milli-seconds) as it passes through heater so that there is little time for heated JP-8 to react with dissolved oxygen. In the event of oxidized carbon particle already formed, it ensures that there is no time for it to deposit on metal surface. This incentive came from Mr. Albert Kascak, who was the director of this project before retiring from U.S. Army Research Lab in 2011.

## **Organization**

There are three major areas involved in the development of the flash vapor fuel injector: direct fuel injector study and test, flash heater development, and ignition comparison between AVGAS and heated JP-8. The dissertation is organized as follows:

Chapter II gives a literature review of running gasoline engines on JP-8. Following the literature review, a preliminary study is done to prove the concept of running small gasoline engines on heated JP-8.

Chapter III studies a commercial off-the-shelf (COTS) direct fuel injector. This includes a photo detector measurement tool development and a multi-physics modeling of a coupled electrical, electromagnetic, fluid dynamics, and rigid body dynamic system. Based on this multi-physics model, the fuel injector's power drive is optimized for the

shortest injection delays, injection consistency and least power consumption. Room temperature fuel injector test is done using the developed photo detector measurement tool to validate the simulation results.

Chapter IV focuses on the development of a flash heater. The conductive heater is designed to have the fastest fuel heating capability. Finite Element Analysis (FEA) code ANSYS is applied to study static heating cases, while Computational Fluid Dynamics (CFD) code ANSYS CFX is used to study transient heating cases and optimize the heater geometry. The final design contains ultra-thin fuel passages that allow fuel to be heated up super-fast as it passes through the heater. The designed heater is then manufactured and integrated with direct fuel injector. Finally, high temperature test results validate the designed heater.

Chapter V compares ignition characteristics of AVGAS, unheated JP-8 and heated JP-8 to show the advantage of the heated JP-8 using the developed flash vapor fuel injector.

Chapter VI concludes the study with summary and future work.

## CHAPTER II

### LITERATURE REVIEW AND PRELIMINARY STUDY

#### **Literature Review**

For an overview of the development of Wankel rotary engines, please refer to [7] which listed progress from 1958 to 1971. Given the task of retrofitting the existing carbureted gasoline Wankel rotary engines, the focus of previous related work is the method of running Wankel rotary engines on JP-8.

Mount and Greiner discussed the application of advanced and highly advanced technologies to the direct injected, liquid cooled, Jet-A fueled, Stratified Charge Rotary engine for high specific output, advanced and highly advanced general aviation engines [8]. This article presented the technologies involved to make rotary engine run on Jet-A fuel using direct fuel injection. One of the key technologies was the pilot injection. As explained in the U.S. Patent No. 3,894,518, stratified charge dual fuel injection systems for rotary internal combustion engines was a recognized approach to the solution of exhaust pollution and fuel consumption of rotary internal combustion engines [9].

Later, a few successes of rotary engine development also came from Curtiss-Wright. During 1973 and 1976, they developed direct injected, spark ignited, stratified charge rotary engines for automotive applications [10]. The engine takes advantage of pilot injection configuration and is capable of running multi-fuels. This study gives more details on the working principle of dual fuel injection system.

Another similar study came from U.S. Navy, where a 1000 – 1500 kW rotary engine was tested with a direct fuel injector. Test results were summarized in [11]. The

study showed the engine is capable of operating on a wide range of fuels without regards to octane or cetane rating.

The rotary engines in the above articles are large displacement, high power engines. The studies did not mention the speed or the engine parameters. It is believed that they are low speed, high compression ratio diesel type engines.

After John Deere purchased the license from Curtiss-Wright to make Wankel rotary engines in the mid 1980's, the development of the engine continued. One of the efforts is to focus on the multi-fuel capability and their respective performance [12]. In the multi-fuel testing, Jet A, 100 octane low lead AVGAS and No.2 diesel fuels were used. Cold start at -25 F (-32 °C) were successfully achieved on all three fuels. Again, the engine has 10 times displacement than the engine we targeted to retrofit. After referring to its multiple references [13], the engine (RCI-350 or SCRCI-40T) was found to be a 7.5:1 low compression ratio engine. The pilot injection was the key to make this engine run on heavy fuels. With pilot injection configuration, extensive retrofit would be required to modify the Wankel rotary engine to run on JP-8. The rotary engine in the study was only running at 5,800 rpm. To put this number in comparison, 9,000 rpm or above is common practice for our rotary engines. As one can imagine, if ignition delay is too great on heavy fuels, then the higher speed of rotary engines cannot be realized.

In a related work, the detail of pilot injection was revealed [14]. The developed stratified charge rotary engines had pilot injection of  $4.65 \text{ mm}^3/\text{stroke}$ , which counted as 5% of total flow. Back then, the challenge of the work was the shot-to-shot variation of pilot injection. This shows the importance of injection consistency.

Badgley et al. summarized all the enabling technologies in a stratified charge rotary aircraft engine in a report [15]. In this report, a high frequency multiple sparking system with controllable duration was another key besides the fuel injection technology.

For small rotary engines like the ones installed on UAVs, their compression ratio is lower than many of their larger counterparts developed from 1970's to 1990's. The challenge with lower compression ratio is the lower maximum temperature in the compression cycle. In addition, the small rotary engine has very limited space on the housing which creates difficulty to use pilot injection configuration. Typically, pilot injection requires two injectors and one spark plug. The only literature that was found successfully running heavy fuel on small rotary engine is a single-injector configuration [16], in which extensive experimental work has been done to run a small spark assisted rotary engine on diesel fuel. The experimental parameters include rotor recess geometry, fuel injector and spark plug positions, fuel injection pressure, as well as fuel injection and spark timing. The rotary engine underwent extensive modifications for these fine-tuned parameters to work with heavy fuels, i.e. diesel, JP-4 and JP-8. This study reveals one of the keys to run small SI rotary engines on heavy fuel is the ignition delay of combustible mixture. With heavy fuels, ignition delay tends to be longer due to the lower vaporization pressure, thus causing trouble for the heavy fuel combustion to keep up with high engine speed. Besides this work, there is no further literature on the success of running small rotary engines on heavy fuels using direct fuel injection.

Though there is only one reference that has successfully run small rotary engines on heavy fuel, there has been a lot of work done using small piston engines to run on

heavy fuels. Since rotary engines have better knock tolerance than their piston counterparts, the work done on small piston engines should also be applicable to rotary engines.

Wilson et al. and Groenewegen et al. modified a 33.5 cc, 2 hp, 4-stroke carbureted piston engine (originally designed to run AVGAS) to run on JP-8, diesel, and camelina (kerosene) using port fuel injection (PFI). The study found that, though there is more tendency of pre-ignition or knock, heavy fuels can be run when variable spark ignition is used. This variable spark ignition system allows a greatly retardation in timing. Preliminary results indicate heavy fuels could meet power requirements while lowering fuel consumption. Compared to AVGAS, the BSFC was decreased after the optimization of fuel injection and spark ignition [17] [18].

Suhy et al. studied the feasibility of a kerosene fueled spark ignited two-stroke engine (note that JP-8 is a kerosene based fuel). They developed a pre-mixing chamber to improve fuel atomization before entering the main combustion chamber. They found that, in order to prevent knock with kerosene (low octane number), rich fuel-air mixture or retarded spark timing is required, which could reversely affect the indicated mean fuel consumption rate. Another important study in this paper was the cold start capability of kerosene. They developed a cold-start procedure that, with the assist of heating up air, the engine could be cold-started. They speculated that partial vaporization near spark plug is necessary for cold start. Without fuel vaporization, even gasoline would have hard time to start the engine in the cold weather [19]. This study proved the difficulty of running spark ignition engines on heavy fuels.

In general, there are three major issues with conventional spark ignition engines on heavy fuel operation [20]:

1. Pre-ignition & knocking.
2. Spark plug fouling/carboning (If spray wets the plug, no arc would be possible).
3. Poor starting, especially at cold ambient conditions.

For our rotary engines, ignition delay times could also play an important role when it comes to high speed, i.e. above 9,000 rpm. Too much ignition delay would create problems to run the engine at high speed.

### **Early Experimentation**

As a proof-of-concept, a 6.5 hp, 196 cc, 4-stroke carbureted gasoline piston engine (shown in Figure 3) was modified to study the feasibility of running JP-8 using direct fuel injection at early stage of this project. Its specifications are listed in Table 2.

This study shows the promise of heating up heavy fuel to reach partial vaporization, while using direct fuel injection to solve pre-ignition and knocking problem.

### ***Background***

With the goal of retrofitting Wankel rotary engines used in UAVs to run on JP-8, a study of retrofitting a small piston engine to run on JP-8 was proposed. This study serves the purpose of proving the concept of running small gasoline engine (low compression ratio) with direct injection of heated JP-8.





**Figure 3. Small piston engine used in the preliminary study**

**Table 2. Technical specifications of the piston engine in the preliminary study**

<b>Engine type</b>	4 Stroke piston
<b>Bore x Stroke</b>	68 mm x 54 mm
<b>Compression ratio</b>	8.5:1
<b>Displacement</b>	196cc
<b>Fuel type</b>	91+ octane unleaded gasoline
<b>Speed</b>	3600 +/- 150 RPM
<b>Engine rating</b>	6.5 hp
<b>Fuel system</b>	carburetion

#### *Direct Fuel Injector*

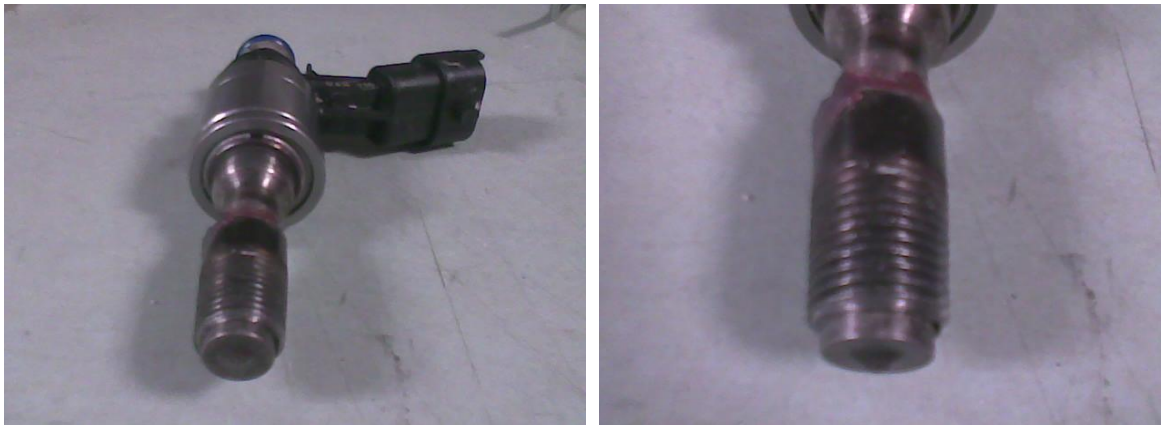
The original engine used carbureted gasoline. In order to run the engine with heated JP-8, the piston head was modified to include a BOSCH direct fuel injector. The direct fuel injection reduces heat loss of heated JP-8 and allows better timing control.

Figure 4 shows the modification of piston head to include direct fuel injector and its relative position to original spark plug.



**Figure 4. Modified piston head to include direct fuel injector**

An 1/8 inch NPT pipe thread fitting was silver soldered onto the injector body. The details of modified injector and cylinder head are shown in Figure 5 and Figure 6.



**Figure 5. Modified injector with 1/8 inch NPT thread**

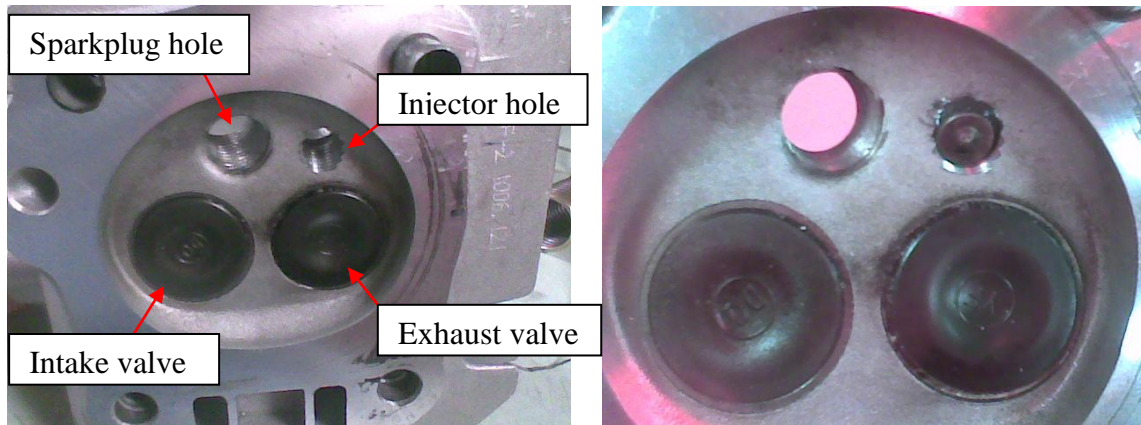


**Figure 6. Injector configuration on the piston head**

### *Engine Setup*

The engine was set up in a way that a 5 hp electric motor could drive the engine through a torquemeter as shown in Figure 7. The torquemeter transmits torque between the engine and the electric motor using timing belts.

There are two functionalities of the electric motor. One is to start the engine. Once the engine is started, the electric motor would be in free running mode, allowing the engine to run without load. On the other hand, a load is applied using a braking pad on the electric motor output shaft. This load can be read from the torquemeter output.

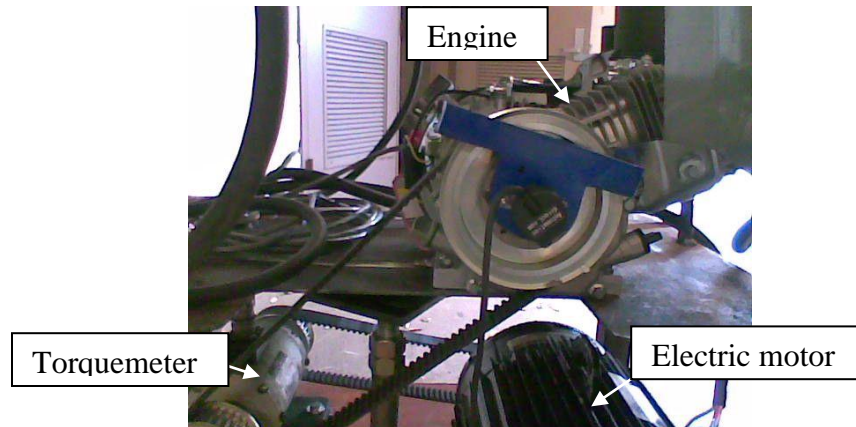


**Figure 7. Engine test bench setup**

### *Pre-heater*

A pre-heater was located in the upstream of the fuel line to pre-heat fuel. The pre-heater used in this study was a cartridge heater with a WATLOW PID controller. The thermo well around the cartridge formed a decent volume of heated JP-8 bank. The JP-8 temperature inside the heater was maintained by the set temperature. Fuel temperature at the exit of heater was recorded using a thermocouple. This temperature was the actual fuel temperature at the heater exit. Heavy insulation was wrapped around fuel lines to keep the cooling effect minimal. The pre-heater and its nearby fuel line is shown in Figure 8. A by-pass valve was located after the heater with a cooler to cool down the heated return fuel. Together with fuel injector, this by-pass valve controlled the flow rate of the fuel flowing through the pre-heater.

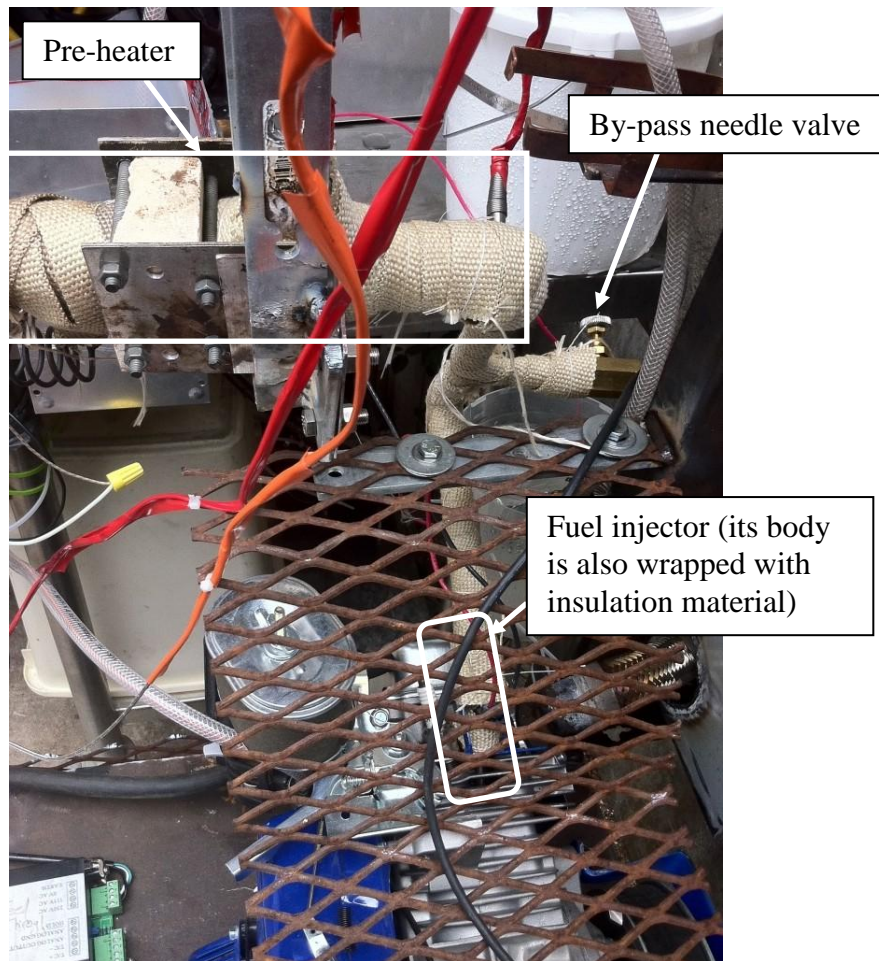


**Figure 8. Pre-heater and insulation of fuel feed-in line**

### *Fuel System*

A model GP-F10-13 high pressure hydraulic pump driven by an AC servo motor (model SVM-210) was used in this study. A 12V diesel micro electric fuel pump (#12D) was used to feed the high pressure pump.

The high pressure pump could be over-heated due to the low flow rate. The fuel flow rate through the pump was maintained with the help of by-pass needle valve 1 as shown in Figure 9. Because of JP-8's low viscosity, 720 psi pressure was achieved with



by-pass valve partially open to maintain the pump cool (about 90 °F). The servo motor, which drove the pump, worked at its rated speed of 2,000 rpm. Needle valves could be over-heated easily without the cooler due to the friction heating of the returning fuel. Cooler 1 and 2 were used to maintain the needle valves cool. Cooler 3 further reduced temperature of the fuel returning to the fuel tank. The whole fuel system schematic is shown in Figure 9.

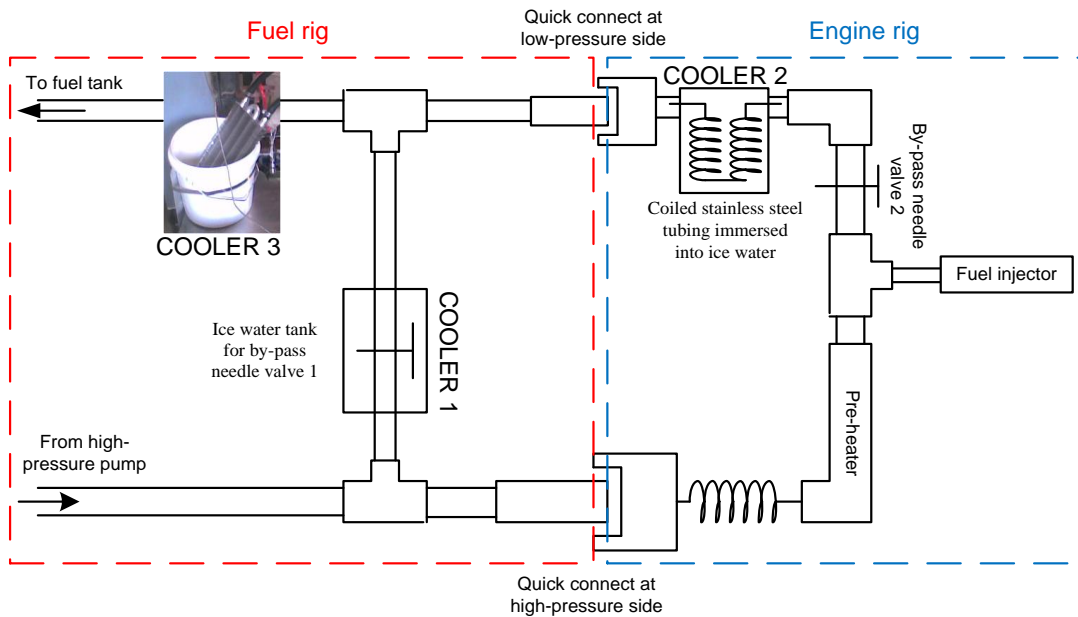


**Figure 9. Small piston engine JP-8 fuel system schematic**

### *Engine Control System*

A heavy duty (BEI model no. L25 series) encoder was used in the initial test. However, the encoder was trashed in a few runs due to the engine vibration. Bently proximity sensors were adopted after the encoder was found inadequate to handle engine

application. The injection timing was based on the engine output shaft position. NI PCI 6230 was used as the data acquisition card. It has two 32 bits 80 MHz counters to accept two timing signals from the engine output shaft: once per rev and 1000 pulses per rev (56 pulses per rev after switching to Bently proximity probe, as shown in Figure 11). The injection timing schematic is shown in Figure 10. A Labview program was written to monitor engine speed and allow users to adjust the injection signal based on the output shaft position. The injector fired every two revs. The output shaft position signal was reset every once per rev.

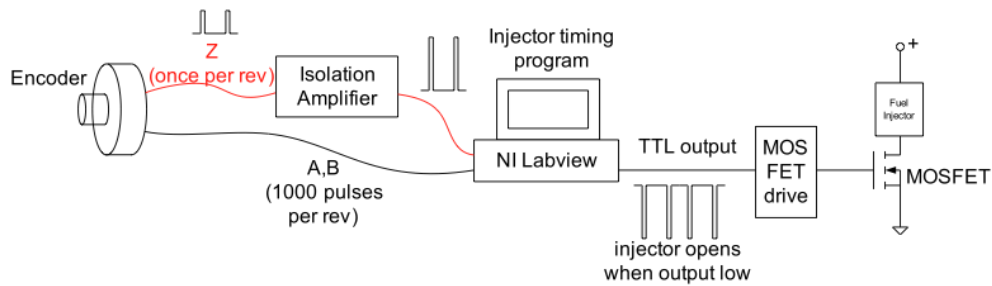


**Figure 10. Injector timing schematic in the preliminary engine test**

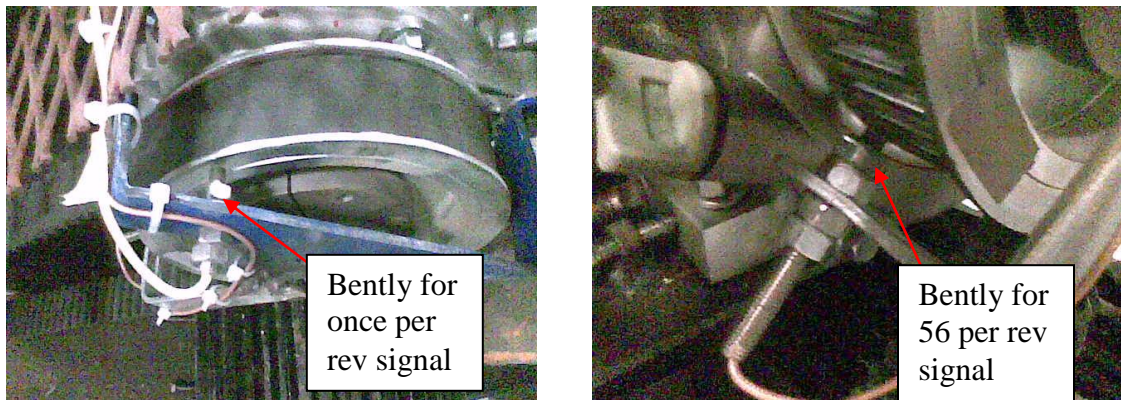


**Figure 11. Bently sensor position in the preliminary engine test**

The injector drive was not optimized by the time of this preliminary study. Labview DAQ card generated TTL signal based on engine shaft position (or crank angle) to control fuel injector power electronics. Please refer to chapter III for the correct injector drive information.

#### *Test Procedure*

The engine was first tested using gasoline only. The engine speed was 2,800 rpm where torquemeter and electric motor's friction was the only load. Then, the engine was running in a dual fuel mode, where gasoline was supplied by carburetor as the main fuel while JP-8 was injected into the cylinder every 2 minutes with each time running the injector for about 10 – 20 seconds. The injection duration only allowed less than 1 mm<sup>3</sup> JP-8 being injected at each shot. The engine was running at 2,600 rpm at this mode, which is slightly lower than the run with just gasoline. Lastly, the engine was operated only on direct fuel injection of JP-8 at wide open throttle (WOT).

#### *Test Results*

The results suggested the engine had very hard time to start with JP-8 unless the JP-8 was heated to certain temperature. We also tried to start the engine with carbureted gasoline and then switch to JP-8 direct injection. However, it would not run once the fuel was switched to JP-8. The only success was achieved when JP-8 was heated to above 200 F using a pre-heater located in the upstream of fuel injector. In this case, the engine could be started with rich pre-heated JP-8 (5 milli-second injection pulse, more than 40 mm<sup>3</sup>/shot) and ran continuously with reduced pre-heated JP-8 (4.5 milli-second injection



pulse, more than 30 mm<sup>3</sup>/shot), while the required volume per shot for JP-8 is calculated to be 23 mm<sup>3</sup>/shot. The parameters for this calculation are listed in Table 3.

**Table 3. Calculation of the JP-8 consumption rate for 6.5 HP test engine**

<b>Engine power:</b>	4.78 KW(6.5 HP)
<b>Speed:</b>	3000 rpm
<b>Injection frequency:</b>	1500 times per minute (once per 2 revs)
<b>Assumed engine efficiency:</b>	20%
<b>Density of fuel:</b>	800 kg/ m <sup>3</sup> at 77 °F (705 kg/m <sup>3</sup> at 325 °F)
<b>JP-8's enthalpy of combustion:</b>	42.8 MJ/kg

Engine power can be calculated by multiplying Efficiency and Energy provided by the fuel per second.

The calculated Fuel consumption rate is 792 mm<sup>3</sup>/second at 77 °F (or 698 mm<sup>3</sup>/second at 325 °F).

The piston engine with pre-heating JP-8 test rig is shown in Figure 12. Figure 13 shows the screenshot of the Labview engine test program during a run with direct injection of the pre-heated JP-8.



**Figure 12. Small piston engine pre-heating JP-8 test rig**

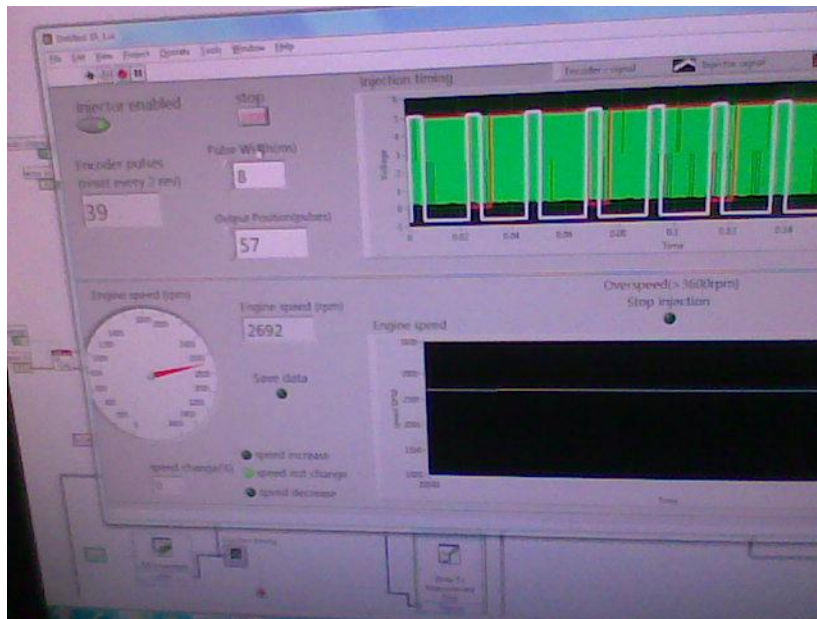


**Figure 13. Screenshot from engine running at 2692 rpm with pre-heated JP-8 injection**

**Table 4. Summary of the small piston engine successfully running on pre-heated JP-8 using direct fuel injection**

<b>Engine speed(RPM)</b>	2100
<b>Injection pulse width (ms)</b>	5 ms to start, 4.5 ms stable running
<b>Injection position(56 pulses per rev)</b>	33 or 90 depends on which cycle to fire
<b>Pre-heater temperature(F)</b>	390
<b>Exit temperature from pre-heater(F)</b>	220
<b>Injector body temperature(F)</b>	170

We found that the temperature has a large impact on the success of running the engine on JP-8. As indicated from Table 4, when injector body temperature dropped to 130 F, we were not able to start the engine or keep the engine running on JP-8.

We also noticed that even though the engine ran with pre-heated JP-8, the fuel consumption was huge and a great amount of soot and heavy smoke could be seen from exhaust. This is a certain sign of poor combustion due to the incomplete burn of JP-8. Further proof of the poor JP-8 combustion can be seen from Figure 14, which shows heavy black soot forming inside the combustion chamber.

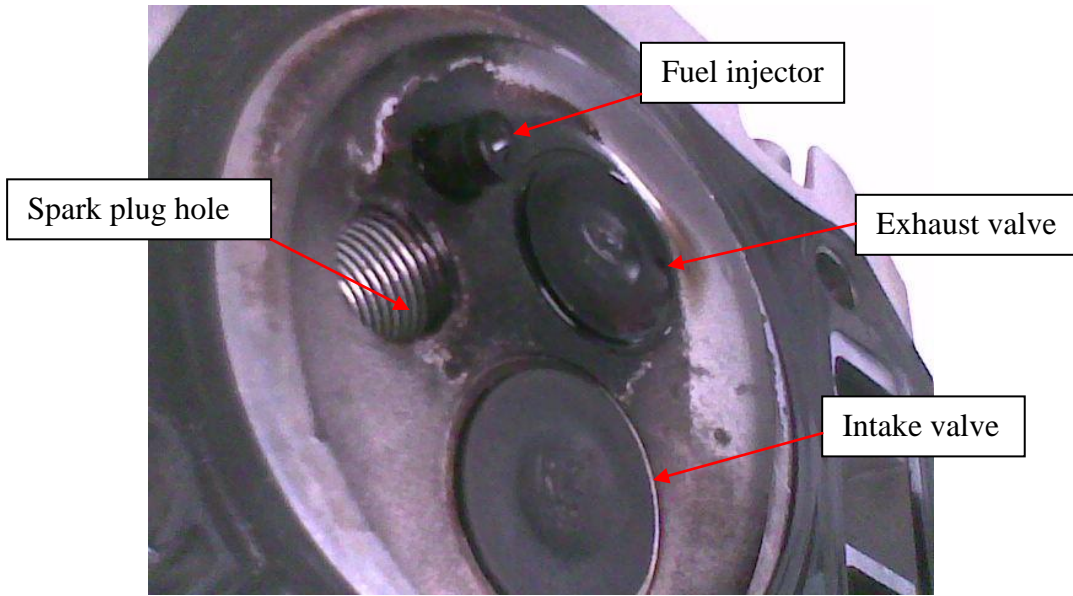


**Figure 14. Cylinder head after a few runs with JP-8**

As shown in Figure 15, coke (carbonized JP-8) was built up in the pre-heater after an hour heating test with heater temperature set at 400 F. The coking prevented the heat transfer from cartridge heater and eventually would clog up the fuel pipeline.



**Figure 15. Thermowell is surrounded by carbonized JP-8 fuel**

### ***Conclusion of the Study***

The modified small piston gasoline engine with direct fuel injector could not run on JP-8 unless the fuel was heated to certain temperature. This small piston engine has similar compression ratio (8.5:1) as the Wankel rotary engine we are going to retrofit. The preliminary test results from this small piston engine provide valuable lessons and guidance to retrofitting the Wankel rotary engine:

1. Direct fuel injection technology can be applied to replace the carbureted fuel delivery system. Direct fuel injection provides better control of fuel metering and timing. It also prevents pre-ignition or knock when fuel with low octane number is used.

2. Low compression ratio gasoline engines could be modified to run heavy fuel if the heavy fuel can be heated to certain temperature. The heated fuel improves the vaporization, thus improving its mixing ability with air. This makes timely combustion of heavy fuel in the low compression ratio engines possible.

3. Coking was observed in the pre-heater after JP-8 heating test. This is a major issue to tackle if fuel heating method will be used. The proposed flash heating might be the solution to this problem.

Overall, this early experimentation encourages us to explore the fuel heating method to make running Wankel rotary engines on JP-8 possible.

### **Objective**

Chapter I and chapter II discussed the background and the logic behind developing the flash vapor fuel injector. From the preliminary study, it was found that the fuel heating method did have potential to run SI engines with JP-8. This gives the

incentive of further developing such fuel injector that would meet the aforementioned requirements.

Therefore, the focus of this study is to develop a flash vapor fuel injector that solves heavy fuel running on low compression SI engines problem, as well as fuel coking problem when fuel is heated at high temperatures.

The objective of this study is to develop a flash vapor fuel injector that enables Wankel rotary engines on shadow UAVs to run on JP-8. Due to rotary engines' high speed requirement and JP-8's pre-ignition tendency, a COTS direct fuel injector is chosen and studied. Through multi-physics modeling, injector power drive system is optimized for the fastest operation, consistent injection and least power consumption. An optical spray measurement system is developed to validate the simulation results and calibrate the fuel injector. The temperature requirement of injected JP-8 guides the development of a flash heater that is capable of heating up JP-8 from room temperature to its vaporization temperature ( $>300$  °F) under one tenth of a second. The flash heating capability prevents coking issues that are found in high temperature JP-8 heaters, while the 300 °F mark ensures partial vaporization of JP-8 after injection. The prototype flash vapor fuel injector is manufactured, tested, and validated through high temperature heating tests. The advantage of the flash vapor fuel injector is shown through ignition tests, where ignition characteristics are compared among AVGAS, unheated JP-8, and heated JP-8.

## **Novelty of Contributions**

The following paragraphs give an overview of the uniqueness of this study to differentiate this work from previous studies.

Overall, the novelty of this work lies in the development of direct fuel injectors that meet key requirement of running Wankel rotary engine on JP-8. This involves extensive test and design effort to understand the physics inside direct fuel injector. The following are the design considerations of high performance fuel injectors that will enable Wankel rotary engines to run on JP-8:

- a) High frequency.
- b) Short pulse width.
- c) Minimal delay times.
- d) High flow rate.
- e) High pressure.
- f) High temperature.

In order to study injector characteristics, a commercial off-the-shelf (COTS) direct fuel injector was used to provide design baseline. The specific novelties this work contributes are as follows:

1. A photo detector system which is capable of continuously detecting injection frequency above 100 Hz was developed to measure the direct fuel injector's temporal characteristics, i.e. opening / closing delay and actual spray duration times [21]. Previous same detection system can only measure up to 2 Hz injection events. This measurement system is described in chapter III.

The injector test matrix is the first publicized work regarding direct fuel injector delay and actual spray times on JP-8 fuel.

2. A coupled electrical-electromagnetics-mechanical-fluid multiphysics system was modeled to understand electromagnetic circuitry, internal flow and pintle dynamics [22]. This multiphysics model, to the author's best knowledge, is the first attempt to couple electrical circuit, 2D electromagnetic analysis, 3D fluid system and pintle dynamics in a solenoid actuator design.

3. Direct fuel injector power drive system was optimized and validated based on the multiphysics model and photo detector measurement tool [22]. The study of injector driver requirement is, to the author's best knowledge, the first publicized work explaining the details of multi-stage current requirement to drive direct fuel injector.

4. A novel flash heater was designed, integrated, and tested to finalize the development of flash vapor fuel injector. Locally flash heat JP-8 to above 300 °F with 800 mm<sup>3</sup>/s flow rate within milli-seconds is the shortest heating time found in literature.

This is also the first work to integrate flash heater with direct fuel injector and be able to achieve vaporization temperature (> 310 °F outlet fuel temperature) without damaging the injector. The commercial heated injector is only capable of heating fuel to a little above room temperature for cold start.

In addition, what makes this heater unique is its flash heating ability. It is capable of heating JP-8 above 300 °F within milli-seconds. The possibility of heating the non-deoxygenated JP-8 at this temperature without coking will be a breakthrough.



5. Ignition test of heated JP-8 at different temperatures is the first publicized work of characterizing the ignition behavior with heated JP-8 in its low temperature range (<550 °F preheater temperature).

6. The developed flash vapor JP-8 fuel injector is a unique device that has not been developed before. This device is now in the process of being patented for U.S. provisional patent [23]. It is aimed at solving the aforementioned problems: running heavy fuels on SI engines and fuel coking issue by flashing heating.

The closest effort to the proposed flash heating of JP-8 is a work done by U.S. Air Force. It developed a flash vapor system for detonation engines [24]. Due to the requirement of detonation, the JP-8 was heated up to its full vaporization temperature (>500 °F). To prevent coking, the fuel was deoxygenated with nitrogen before the use.

There are three basic differences between our design and this flash vapor system:

a). Flash heating capability. The flash vapor system they developed for detonation engine uses the word “flash” not to describe the heating time. Instead, it was used to describe the state of the JP-8 after injection: it reaches critical temperature that no liquid-form fuel droplet could exist. The heater used to heat up the fuel was a furnace type heater. No effort was made to heat the fuel quickly.

b). How to cope with coking issue. The proposed flash heater resolves coking by quickly heating and releasing JP-8 so there is little time for the JP-8 reacts with dissolved oxygen or deposit on the heater wall, while their flash vapor system deoxygenated the fuel before it could be used. The deoxygenation process added complexity to the fuel system.

c). JP-8 temperature. Unlike heating up JP-8 to its full vaporization temperature (>500 °F) to achieve detonation in their system, our heater aims at heating up JP-8 to its partial vaporization temperature (>300 °F). The lower temperature prevents auto-ignition which could lead to detonation. Ironically, their system aims at detonation while we are trying to avoid it in our system.

### **Importance**

This work is the initiation of a new era for the development of internal combustion engines with flash vapor direct fuel injector. The ability of running on heavy fuel for low compression ratio engines has broadened the vision of running engines on flexible fuels, light or heavy, without re-designing the engine. This can be made possible by flash heating and direct injection of heated fuel. As a result, it vaporizes heavy fuel to create easy ignitable fuel-air mixture. This technology also holds the promise of reducing emission while increasing the engine efficiency because of more complete combustion thanks to the flash vapor direct fuel injector.

The key component to make JP-8 successfully run on rotary engine is the flash vapor direct fuel injector. It integrates a flash heater with direct fuel injector and is demonstrated to be able to run at high temperature without compromising its injection characteristics.

Besides the development of flash heater, direct fuel injector temporal characteristics were determined with a cost-effective photo detector measurement system. It determines actual spray event under different operating conditions. This makes more accurate tuning of engine possible.

In addition, direct fuel injector power drive (current shape) was optimized based on a coupled electrical-electromagnetics-mechanical-fluid multiphysics model. This gives insight on how to design high-performance direct fuel injector in future. Both room temperature and high temperature test results from direct fuel injector were obtained to validate theoretical models and predictions.

An ignition test rig was developed to test the heated JP-8's ignition behavior in comparison with AVGAS, which is the fuel designed to run the rotary engine. Test results show the superiority of heated JP-8 at elevated temperature in terms of ignition delay time and ignition pressure rise over AVGAS. This result makes the developed flash vapor fuel injector a contending technology for future clean and flexible-fuel engine development.

## CHAPTER III

### DIRECT FUEL INJECTOR STUDY\*

#### Overview

In order to study injector characteristics, a commercial-off-the-shelf (COTS) BOSCH direct fuel injector (shown in Figure 16) is used to provide design baseline. Its specifications are listed in Table 5. Direct fuel injector's temporal characteristics are determined with a cost-effective photo detector measurement system. It determines actual spray event under different operating conditions. This makes more accurate tuning of engine possible. In addition, direct fuel injector power drive (current shape) is optimized based on a coupled electrical-electromagnetics-mechanical-fluid multiphysics model. This analysis gives insight on how to design high-performance direct fuel injector in future. The optimized direct fuel injector power drive system is validated based on the photo detector measurement tool. Room temperature test results from direct fuel injector are obtained to validate theoretical predictions.



**Figure 16. BOSCH direct fuel injector used in this study**

---

\*Part of this chapter is reprinted with permission from SAE paper 2014-01-1444 and 2014-01-1442 Copyright 2014 SAE International. This paper may not be reprinted, copied, distributed, or saved on any retrieval system without prior permission from SAE.

**Table 5. Direct fuel injector specification[25]**

<b>Fuel injector</b>	BOSCH HDEV 5.2
<b>Fuel injector resistance</b>	1.5 ohm
<b>Measured inductance</b>	L = 1.9 mH @ 1 kHz L = 3.9 mH @ 0.12 kHz
<b>Operating pressure</b>	200 bar
<b>Number of holes</b>	6

### **Injector Temporal Measurement Tool [21]**

The objective of this study is to measure high-frequency, short-duration, actual liquid fuel spray events using a simple photo detector and validate the results with high-speed camera measurements.

The following paragraphs discuss a cost-effective photo detector method that improves the photo detector-based measurement system for injection frequencies up to 100 Hz. Its measurement accuracy is validated with the high-speed camera measurements under the same conditions. This technique does not include the measurement of the individual injections at the multi-hole injector nor its injection rate shape. In other words, only the bulk spray's temporal characteristics can be obtained using this method.

### ***Measurement System***

#### ***Photo Detector***

The photo detector employed for fuel injection temporal measurement is a model H21B1 as shown in Figure 17. The photo detector's electronics properties are listed in

Table 6. The injected fuel travels between the emitter and receiver and blocks the light signal, lowering the quantity of photons impinging on the receiver, thus changing the photo detector output voltage. The circuitry in the present system, as shown in Figure 18, is designed to amplify the output voltage when the photo detector senses a fuel spray.

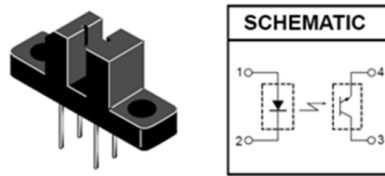


Figure 17. Photo detector for measuring an injector spray event[26]

Table 6. Photo detector's electronics properties

<b>Output configuration</b>	photodarlington
<b>Current – DC Forward</b>	60 mA
<b>Voltage – Collector Emitter Breakdown (Max)</b>	30 V
<b>Turn-on Time</b>	7 $\mu$ s
<b>Turn-off Time</b>	45 $\mu$ s

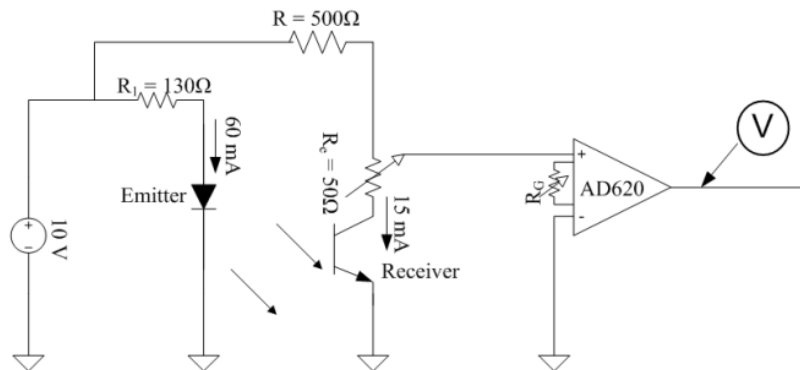
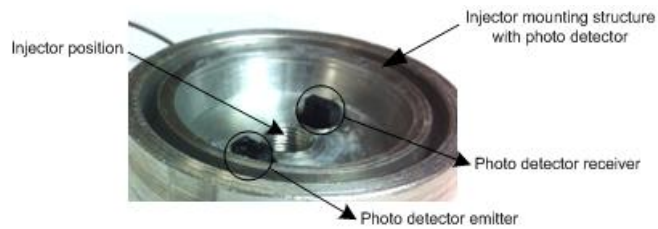


Figure 18. Photo detector drive circuit

### *Implementation*

Test fixtures are shown in Figure 19 and Figure 20. The purging nitrogen is the key in the experiment to repeatedly measure injection event at 100 Hz. Figure 21 shows the hydraulic system schematic for the fuel injector test bench.



**Figure 19. Support ring for mounting the fuel injector and photo detector**

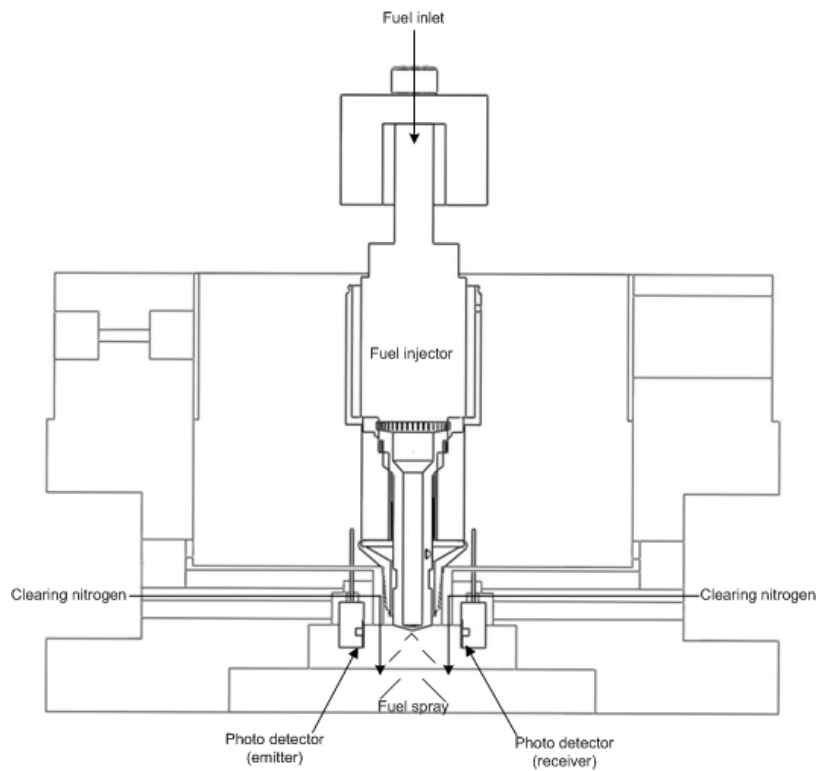


**Figure 20. Section view of the mounting structure with nitrogen path**

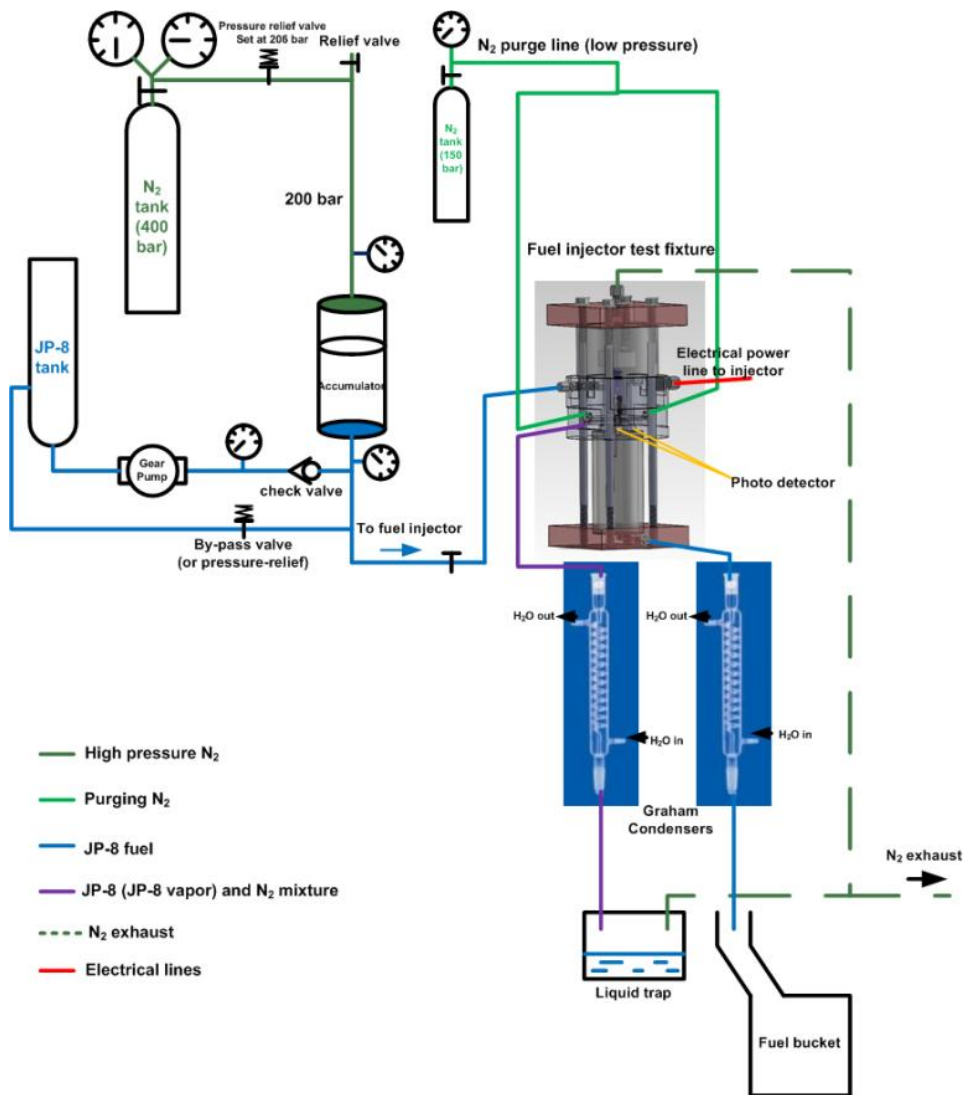


**Figure 21. Hydraulic system illustration of the injector test bench**

### *Injector Power Drive System*

A Pulse-Width-Modulation (PWM) servo amplifier is often used in modern direct fuel injectors. It not only saves power by switching on and off at high frequency, but also is capable of outputting current shapes that accurately follow the input control



voltage through feedback circuits built inside. The specification of the PWM servo amplifier used in this study is listed in Table 7.

**Table 7. PWM servo amplifier specification**

<b>Model</b>	50A20T by Advanced Motion Control
<b>Peak current</b>	50 A
<b>Continuous current</b>	25 A
<b>Supply voltage</b>	40 ~ 190 VDC
<b>PWM Switching frequency</b>	22 kHz

A two-stage power strategy is used to drive the fuel injector. The 1<sup>st</sup> stage current usually has large peak values and its total on-time is 300 ~ 500  $\mu$ s. The large peak value is to ensure a fast rising current even though the threshold current may be much lower than the peak value. Due to the rise time and supply voltage relationship  $t \propto \frac{1}{V}$ , a larger supply voltage can achieve a desired current level faster. An advantage of the PWM servo amplifier approach is to regulate the peak current values via the input control voltage, while maintaining the same rise time as the constant voltage source RL circuit case. A 120 VDC power supply was used together with a large capacitor as the power supply to the PWM servo amplifier. The purpose of the 1<sup>st</sup> stage current is to open the pintle, while the 2<sup>nd</sup> stage current is to maintain the pintle at the fully open position. The operating pressure force is the major force that the threshold current has to overcome for the 1<sup>st</sup> stage. This pressure force drops to nearly zero at the pintle fully open position,

and steady flow forms at the pintle valve seat. Thus, the 2<sup>nd</sup> stage current only needs to overcome the compressed spring force, which is much lower than the operating pressure force at the closed pintle position. This permits lower current to be utilized to keep the pintle at its open position for the 2<sup>nd</sup> stage.

The drive current specification is listed in Table 8. The current amplitude at each stage is chosen to be more than sufficient to operate the injector at 200 atm supply pressure.

**Table 8. Power strategy used in this study**

1 <sup>st</sup> stage peak current	1 <sup>st</sup> stage on-time	2 <sup>nd</sup> stage current	2 <sup>nd</sup> stage on-time
14 A	300 ~ 500 $\mu$ s	5 A	100 ~ 2600 $\mu$ s

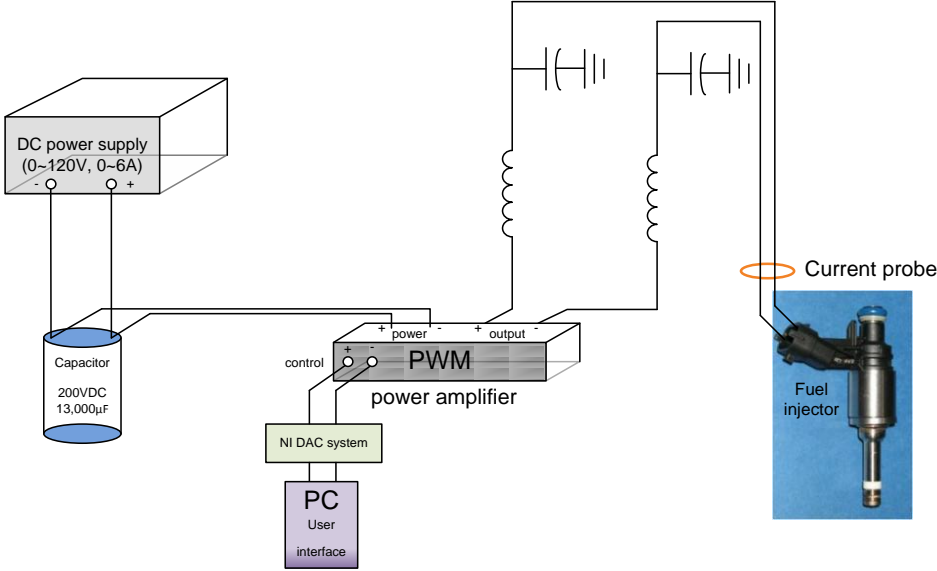


**Figure 22. Injector drive system with PWM servo amplifier**

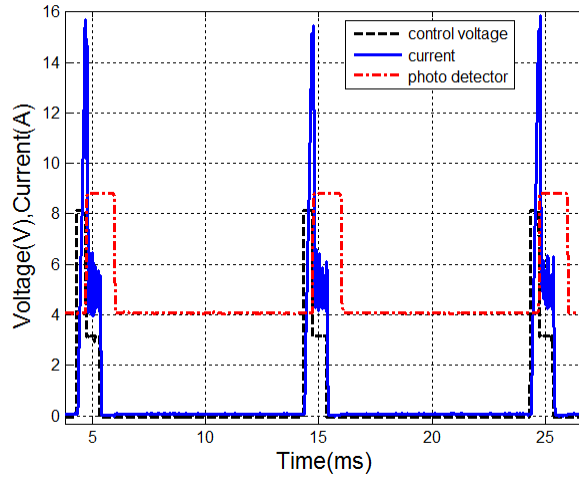
Figure 22 shows the injector drive system. Injector power drive strategy was selected by varying the 1<sup>st</sup> stage current and time duration, as well as the 2<sup>nd</sup> stage current in order to operate the injector consistently with the least power consumption. Since the focus of this section is on implementation of the photo detector to measure the temporal characteristics of fuel spray, the power strategy used in this section is only for illustrative purpose. The next section “Direct fuel injector power drive system optimization” gives details on how to choose the right power strategies.

## ***Results and Discussion***

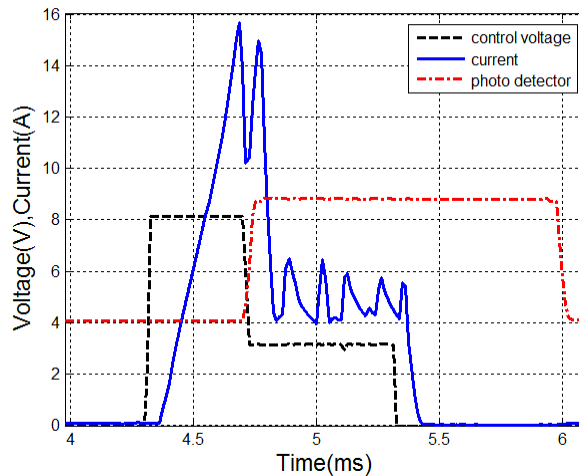
### *Injector Test Results with Photo Detector System*

Figure 23 shows the signals with JP-8 fuel, injector supply pressure of 200 atm and 1 ms total injection signal on-time (1<sup>st</sup> stage-0.4 ms at 14 A peak current and 2<sup>nd</sup> stage-0.6 ms at 5 A holding current) case. The sampling rate of the data acquisition system was 80 kHz for each of the 3 channels employed. The black dashed line shows the two-stage control voltage input to the PWM servo amplifier. The blue solid line is the current from the PWM servo amplifier to the fuel injector. The red dash-dotted line is the photo detector output signal (in volts). As previously mentioned, the high voltage (approximately 9 V) indicates a light barrier (fuel spray in this case) being detected, and the low voltage (4 V) indicates there is no barrier (no fuel spray in this case) being detected. The well defined profile of the photo detector output signal was maintained by purging with nitrogen gas to prevent the fuel spray mist from depositing on the emitter and detector. Removal of the purge gas would result in significant deterioration of the

photo detector signal. Figure 24 shows a zoomed-in plot of the first injection event of Figure 23.



**Figure 23. Control voltage, current and photo detector signals for a two-stage PWM amplifier powered direct fuel injector spray event at 100 Hz injection rate under 200 atm fuel pressure**



**Figure 24. Zoomed-in view of Figure 23 showing signals for a single injection event**

The time traces of the acquired signals provide a means to measure the injector valve opening time, injection duration time, and injector valve closing time. For example, Figure 25 shows the injector valve opening time ( $t_2-t_1$ ) which is the time delay between the control signal from the Labview system and the actual spray coming out from the nozzle sensed by the photo detector. The injector valve closing time ( $t_4-t_3$ ) is the time delay between the closing signal and actual closing of the pintle, plus the delay between actual closing of the pintle and the photo detector off signal. The injection duration time ( $t_4-t_2$ ) is the photo detector high time.

Figure 26 shows injection signals from four different control on-times. Table 10 lists the temporal characteristics for these four cases.

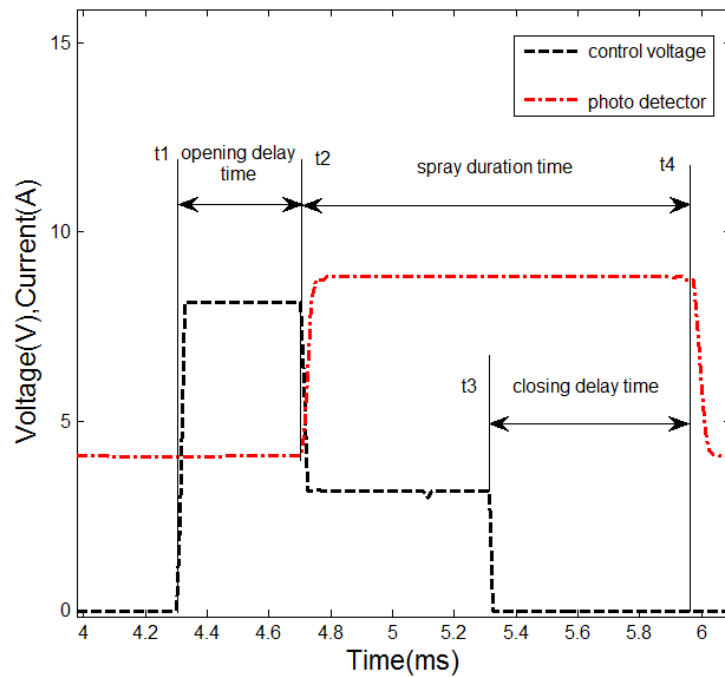
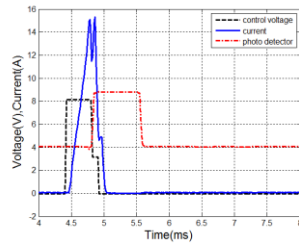


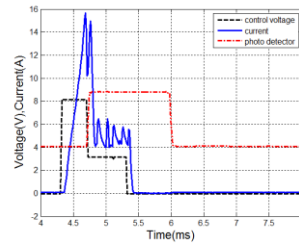
**Figure 25. The spray temporal definitions**

**Table 9. Test conditions**

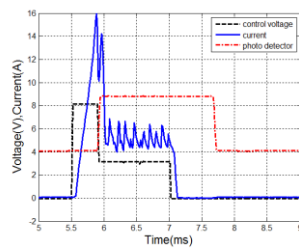
<b>Control signal on-time</b>	0.5~2 ms
<b>1<sup>st</sup> stage peak current</b>	14 A
<b>1<sup>st</sup> stage on-time</b>	0.4 ms
<b>2<sup>nd</sup> stage current</b>	5 A
<b>2<sup>nd</sup> stage on-time</b>	0.1~1.6 ms
<b>Injection rate</b>	100 Hz
<b>Supply pressure</b>	200 atm (gauge pressure)
<b>Ambient pressure</b>	1 atm (absolute pressure)



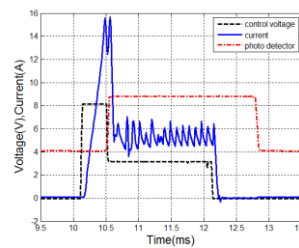
(a)



(b)



(c)



(d)

**Figure 26. Injection events with different control signal on-times at 100 Hz injection rate under 200 atm fuel supply pressure**

**Table 10. Spray temporal characteristics with different control signal on-times**

<b>Control signal on-time</b>	<b>Opening delay time (ms)</b>	<b>Duration time (ms)</b>	<b>Closing delay time (ms)</b>
0.5 ms	0.40	0.75	0.65
1 ms	0.40	1.28	0.68
1.5 ms	0.40	1.78	0.68
2 ms	0.40	2.28	0.68

*Injector Test results with High-Speed Camera System*

A high-speed camera was used to capture the injection events under the same conditions as listed in Table 9, in order to validate the results with the photo detector. Table 11 lists its specification.

A different spray chamber (shown in Figure 27) was specifically made for high-speed camera system. This chamber provided optical access to the spray. Other than that, all parameters including nitrogen purge and ambient pressure were the same as the previous set-up for photo detector system. The high-speed camera test setup is shown in Figure 28.

The camera was triggered using the same signal to trigger the fuel injector from Labview DAQ system. This gives us a time reference of the pictures taken by a high-speed camera with respect to the injector control signal. Figure 29 shows the frame-to-frame photos of the 1ms total control signal on-time case at 10,000 frame per second (fps).



**Figure 27. High speed camera spray chamber**



**Figure 28. High speed camera test setup**



**Table 11. High-speed camera used in this study**

<b>Model</b>	Photron FASTCAM SA3
<b>Max. frame rate</b>	60,000 fps
<b>Frame rate in the study</b>	10,000 ~ 30,000 fps
<b>Resolution in the study</b>	512 x 256 pixels at 10,000 fps 128 x 128 pixels at 30,000 fps
<b>Trigger-type in the study</b>	TTL triggered

*Validation*

The temporal characteristics of the fuel spray were measured with both the photo detector method and high-speed camera method. Table 12 compares the opening delay, duration and closing delay times under the test conditions listed in Table 9. Findings from both methods illustrate very close results on fuel spray temporal characteristics.

**Table 12. Fuel injection temporal characteristics comparison with high-speed camera (HS) and photo detector (PD) methods under the same test conditions**

<b>Control signal on-time</b>	<b>Opening delay time (ms)</b>		<b>Duration time (ms)</b>		<b>Closing delay time (ms)</b>	
	<b>HS</b>	<b>PD</b>	<b>HS</b>	<b>PD</b>	<b>HS</b>	<b>PD</b>
0.5 ms	0.4	0.40	0.7	0.75	0.6	0.65
1 ms	0.4	0.40	1.3	1.28	0.7	0.68
1.5 ms	0.5	0.40	1.7	1.78	0.7	0.68
2 ms	0.4	0.40	2.3	2.28	0.7	0.68

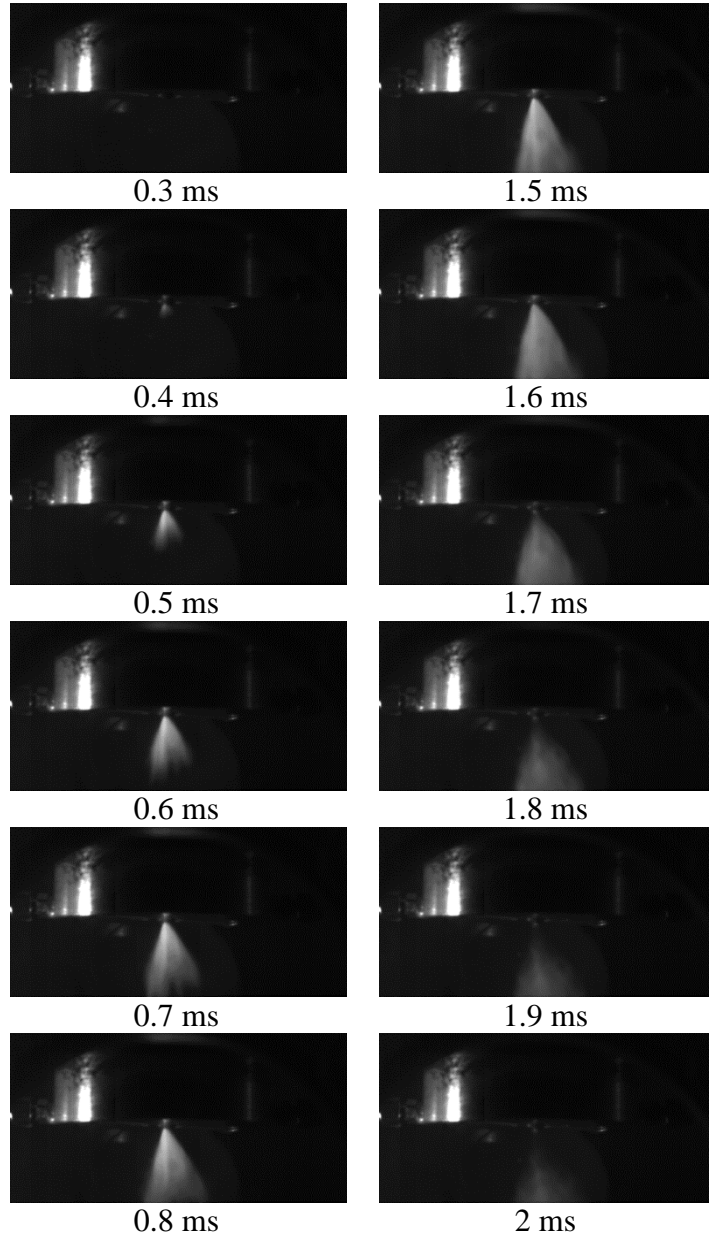


**Figure 29. Frame-to-frame photos during one injection event using high-speed camera. (test condition: 1 ms control signal on-time at 100 Hz injection rate under 200 atm supply pressure)**

## ***Conclusions***

The photo detector method is a cost-effective approach to obtain the spray temporal characteristics such as opening delay, duration and closing delay times at injection rates up to 100 Hz under 200 atm. The developed photo detector measurement tool is accurate when compared with high speed camera.

The opening delay time of this direct fuel injector is 0.4 ms, while the closing delay time is 0.7 ms. The next section will discuss the details of the power drive to this direct fuel injector, as well as a multi-physics model to give insights on delay times and injection consistency.

## **Power Drive Requirement for Optimized Performance [22]**

The objective of this section is to optimize the injector power drive system for improved fuel injection quantity and timing control. The power drive system was optimized for improved injection repeatability under different operating conditions such as fuel supply pressures. A coupled simulation of injector electromagnetic, pintle (needle) rigid body motion and computational fluid dynamics (CFD) model was employed to generate the optimal values of the 1<sup>st</sup> stage current, the 1<sup>st</sup> stage on-time and the 2<sup>nd</sup> stage current. The simulation results were validated against the experimental data measured with a photo detector measurement system developed from previous section.

## ***Subsystems***

### ***Injector Power Drive System Basics***

The governing equation for a simple resistor-inductor circuit (RL circuit) is

$$V = i \cdot R + L \cdot \frac{di}{dt} \quad (1)$$

Where V is the voltage across the coil; R is the resistance; and L is the inductance. The step voltage input response of the current is obtained by solving (1) to obtain:

$$i(t) = \frac{V}{R} \cdot (1 - e^{-\frac{R}{L}t}) = \frac{V}{R} \cdot (1 - e^{-\frac{1}{\tau}t}) \quad (2)$$

Where  $\frac{L}{R}$  is the electrical subsystem time constant  $\tau$ . The inductance was measured to be 1.9 milli-henry (mH) at 1 kHz and 3.9 mH at 0.12 kHz at the maximum air gap. In our case,

$$\tau = \frac{L}{R} = \frac{(1.9 \sim 3.9)mH}{1.5\Omega} = 1.26 \sim 2.6ms \quad (3)$$

This means it takes 1.26~2.6 ms to reach 63.2% of the steady-state current  $\frac{V}{R}$ ;

where R, L are measured values.

Figure 30 illustrates the times to reach 8.5 A for different voltage inputs. The reason for 8.5 A in the analysis will be discussed in the later section where the magnetic force requirement is specified.

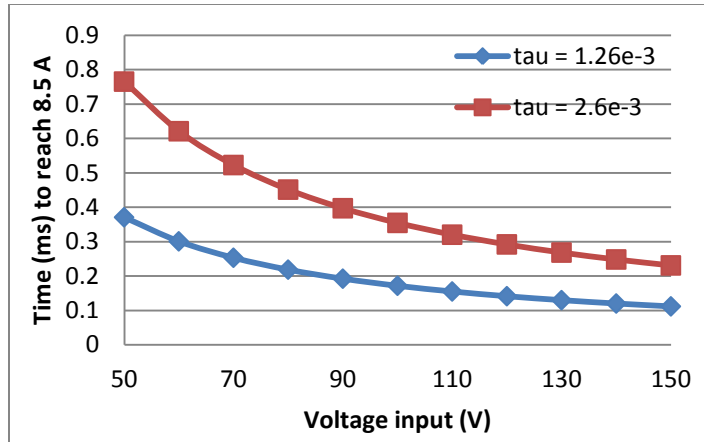


**Figure 30. Time to reach 8.5 A with different time constants**

A PWM servo-power amplifier was used to provide current to the fuel injectors. Nowadays, PWM amplifiers become the preferred way of driving fuel injectors. Compared with power MOSFETs, PWM power amplifiers are more power efficient and easier to use.

*Electromagnetic System*

The electrical properties of the fuel injector coil and PWM power amplifier are listed in Table 13.

**Table 13. Electrical properties of the fuel injector coil and PWM power amplifier**

<b>Resistance</b>		1.5 Ω
<b>Inductance</b>		1.9 mH at 1 kHz; 3.9 mH at 0.12 kHz
<b>Number of turns</b>		160
<b>PWM switching frequency</b>		22 kHz
<b>PWM power range</b>	<b>Peak current</b>	50 A
	<b>Continuous current</b>	25 A
	<b>Supply voltage</b>	40-190 VDC

The electrical circuit was modeled in Maxwell circuit editor, as shown in Figure 31. It included a voltage source with a switch controlling on and off time, a pulse current source for the peak current, and another pulse current source for the holding current. This circuit model was imported into a 2D axisymmetric finite element code Maxwell as external excitation source for the coil. The time constant  $\tau$  in the RL circuit (see equation 3) determines the maximum current increasing rate. The inductance, which is represented as winding1 in the circuit, changes as the geometry changes. It takes into account of the pintle motion in the magnetic circuit. Figure 32 shows the inductance profile with respect to the change of air gap. The inductance from Maxwell was calculated through the relationship  $L = \frac{d\lambda}{di}$  at each time step in the transient analysis. It is shown that the change of the inductance due to pintle motion counts for about 10% of coil's total inductance.

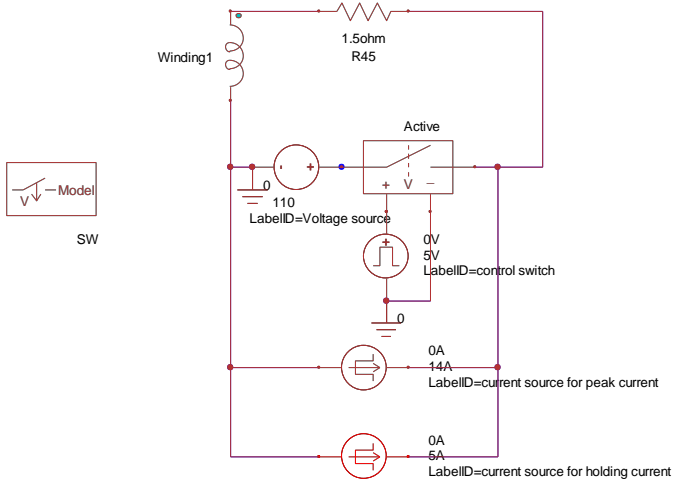


**Figure 31. Electrical circuit in Maxwell circuit editor**

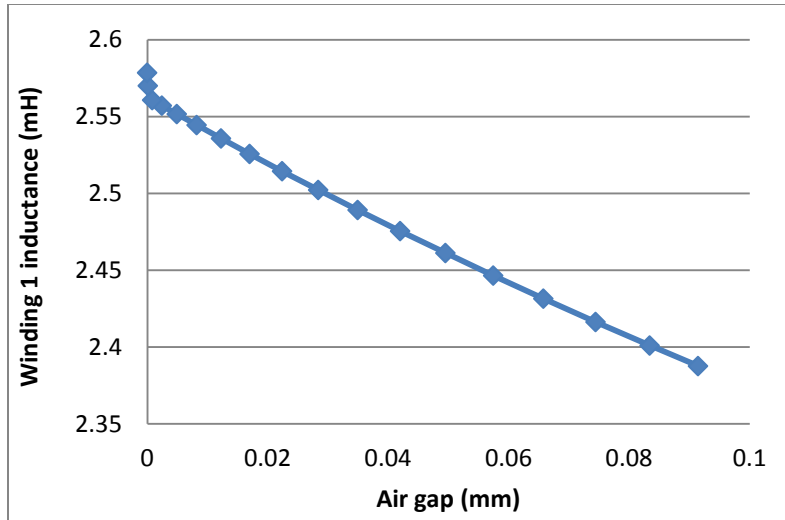


**Figure 32. Inductance at different air gaps from Maxwell**

This inductance plays an important role in determining the current rise time. A 1D magnetic analysis is provided below to compare with the inductance calculation from Maxwell.

From Ampere's law  $\oint_c \vec{H} \times d\vec{l} = I_{net}$

$$H_1 \cdot \Delta x + H_2 \cdot w + H_3 \cdot w = N \cdot I \quad (4)$$

Where, the parameters in Equation (4) are illustrated in Figure 33.

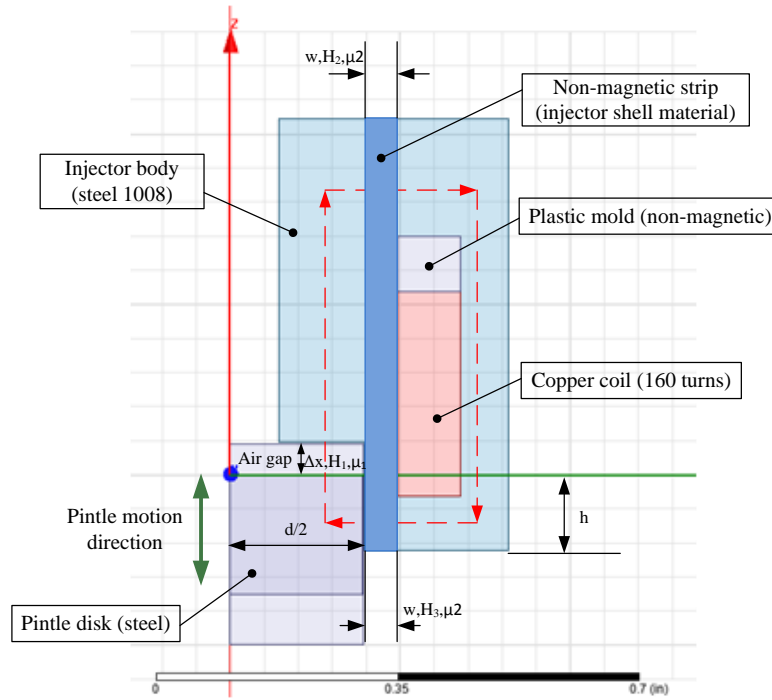


**Figure 33. Flux path in the magnetic circuit analysis**

Apply Gauss M around pintle disk,  $\oint_s \vec{B} \times d\vec{a} = 0$

Which yields

$$\mu_1 \cdot H_1 \cdot \frac{\pi}{4} d^2 - \mu_2 \cdot H_3 \cdot \pi d \cdot h = 0 \quad (5)$$

Assume no fringing and leakage,

$$H_2 \cong H_3 \quad (6)$$

Also, the permeability in the air  $\mu_1$  and the one in the non-magnetic strip  $\mu_2$  are

similar:  $\mu_1 \cong \mu_2$  ;

Apply flux linkage  $\lambda = N \cdot \int_s \vec{B} \times d\vec{a}$  on the top plane of the pintle disk,



$$\lambda = \left[ \frac{N^2 \cdot \mu_1 \cdot \frac{\pi}{4} \cdot d^2 \cdot h}{\frac{d \cdot w}{2} + \Delta x \cdot h} \right] \cdot i \quad (7)$$

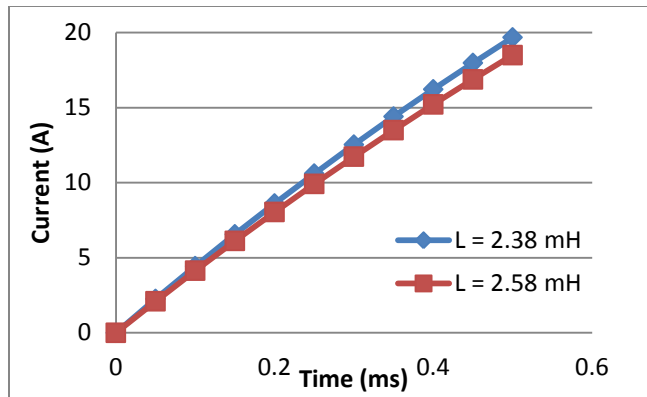
Where, inductance  $L = \frac{N^2 \cdot \mu_1 \cdot \frac{\pi}{4} \cdot d^2 \cdot h}{\frac{d \cdot w}{2} + \Delta x \cdot h}$ .

The geometric parameters were obtained by measuring the dimensions with a cut-open injector. Table 14 lists the parameters used in the calculation. The calculated inductance (2.4 ~ 2.6 mH) correlates well with the measured inductance, which ranges from 1.9 mH at 1 kHz to 3.9 mH at 0.12 kHz.

**Table 14. Parameters for inductance calculation**

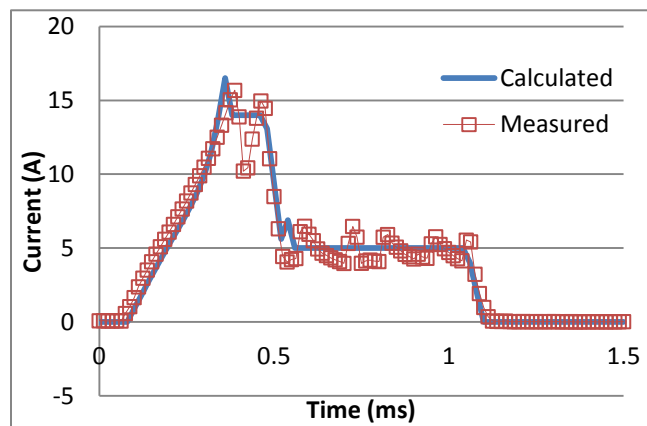
<b>Non-magnetic strip width w [mm]</b>	0.8
<b>Pintle disk diameter d [mm]</b>	10
<b>Pintle height h [mm]</b>	4
<b>Air gap <math>\Delta x</math> [mm]</b>	0 ~ 0.1
<b>Permeability <math>\mu_1</math> [H/m]</b>	1.256e-6
<b>Number of coil turns</b>	160
<b>Calculated inductance using eqn (7) [mH]</b>	2.4 ~ 2.6

Figure 34 shows elapsed times for different current targets at the calculated inductances with the same 110 V voltage source using Equation (2).



**Figure 34. Current level vs. elapsed times at the calculated inductances**

Figure 35 compares the calculated current shape from Maxwell and the measured one with the 1<sup>st</sup> stage on-time of 400  $\mu$ s and 2<sup>nd</sup> stage on-time of 600  $\mu$ s. The calculated current profile, especially the rise time (which is the key to the opening delay time), fits well with the measured current.



**Figure 35. Maxwell calculated and measured current shapes**

In the electrical circuit simulation, the current limit was set by the PWM power amplifier and the voltage source was turned off when the current reached the current limit. This was done to capture the characteristics of the rising curve and the current limit. Another pulse current source was used to provide the 2<sup>nd</sup> stage current. In practice, once a desired current shape is determined, it is relatively easy to adjust the current magnitude and duration by changing the DC power supply voltage, control signal amplitude, current limit and command signal's time durations.

In Figure 36, the 2D axisymmetric model in Maxwell shown in Figure 33 was simulated in transient. Magnetic density B vector plot was shown at time  $t = 0.4$  ms at which the 1<sup>st</sup> stage current reached its steady-state.

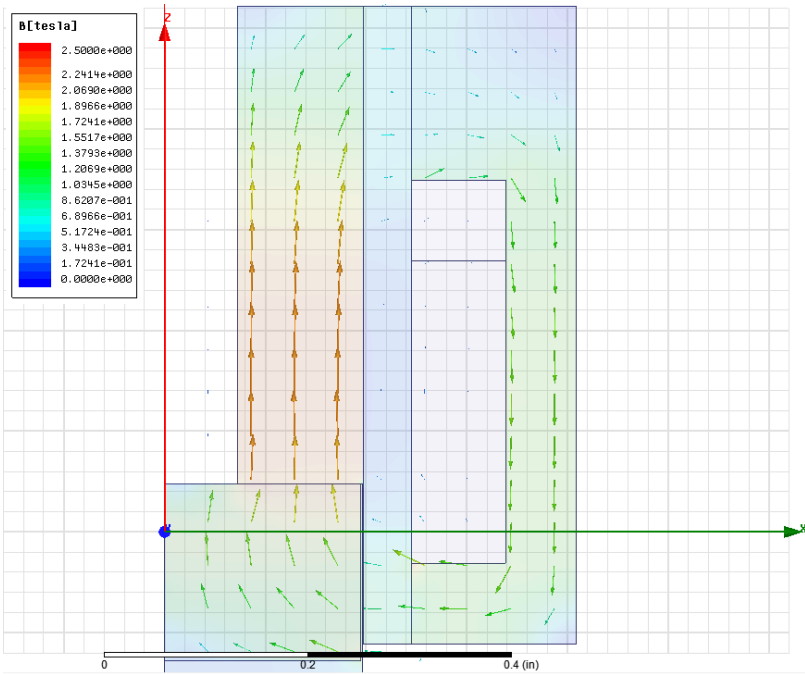


**Figure 36. Magnetic flux density vector plot at  $t = 0.4$  ms from 2D Maxwell transient with the two-stage current shown in Figure 35**

The magnetic field density was calculated using the ampere's law and the constitutive relationship between flux density  $B$  and magnetic field strength  $H$ :

$B = \mu \cdot H$ . Then, Maxwell force law was used to calculate the magnetic force, given the magnetic flux density, permeability and area.

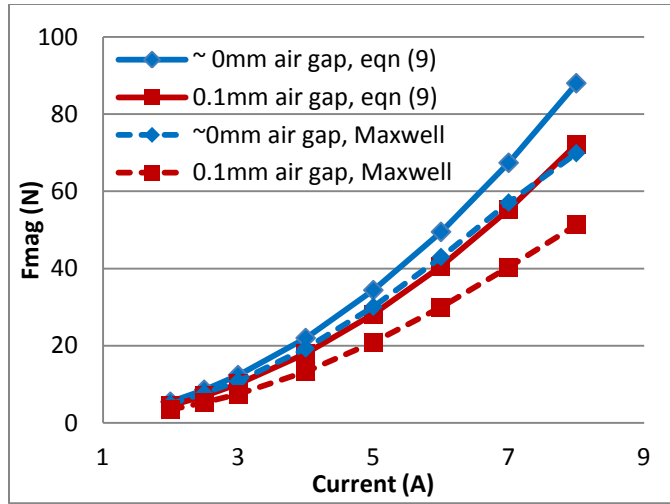
$$F_{mag} = \frac{B^2 A}{2\mu} = \frac{(\mu \cdot H_1)^2 A}{2\mu} \quad (8)$$

Where,  $B$  is the flux density at  $H_1$ ;  $A$  is the area on the upper surface of pintle disk;  $\mu$  is the permeability of air.

Solving Equations (4-6) for  $H_1$ , then substituting  $H_1$  into Equation (8), the magnetic force becomes

$$F_{mag} = \frac{\mu \cdot N^2 \cdot h^2 \cdot A}{2\left(\frac{d \cdot w}{2} + \Delta x \cdot h\right)^2} \cdot i^2 \quad (9)$$

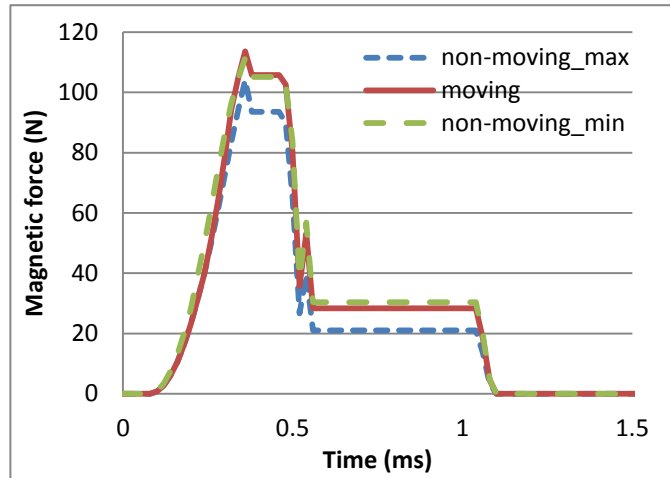
The magnetic force was also calculated using the finite element code Maxwell. Figure 37 compares the magnetic forces calculated with Equation (9) and Maxwell at different air gaps and current levels.



**Figure 37. Calculated magnetic forces at different air gaps and current levels with Equation (9) and Maxwell**

The 2D axisymmetric finite element code Maxwell considered the non-linearity of the B-H curve of the magnetic material and the fringing loss. Therefore, the magnetic force calculated using Maxwell was less than the theoretical force calculated from Equation (9) as excitation current increased. However, the two force curves are close enough to justify the results from Maxwell.

Figure 38 shows the magnetic forces calculated using finite element code Maxwell with the current shape shown in Figure 35 under three different conditions: with pintle motion and without pintle motion at extreme pintle positions.



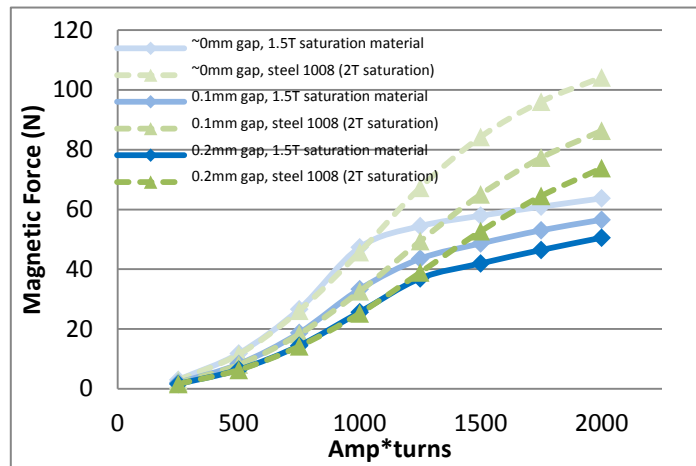
**Figure 38. Magnetic force profile with and without pintle movement using Maxwell**

Figure 38 shows that the magnetic force with moving pintle (solid) falls in-between the magnetic forces at extreme pintle positions without pintle motion (dotted and dashed). For simplicity, the magnetic force with non-moving pintle at its minimum air gap (~0mm) was used in the following coupled analysis assuming that the magnetic force is only a function of time given a certain current shape.

Besides current and air gap, another important factor that affects the magnetic force is the magnetic saturation. The magnetic saturation imposes the maximum resultant magnetic force due to the flux saturation in the magnetic circuit. Therefore, the magnetic force cannot increase infinitely with the increasing current. Figure 39 shows the magnetic forces at different currents, pintle positions, and saturation levels.

Amp\*turns is the multiplication of current (amp) and coil's number of turns. In our case, the total number of turns was 160.

The resultant magnetic forces of less than 1000 amp-turns were similar for different saturation materials. However, the difference of the resultant magnetic forces could be as much as 15 N at the same current (1500 amp\*turns) and air gap (0.1mm), only with the change of magnetic material from 1.5 Tesla (T) saturation to 2 T saturation. Therefore, in order to obtain the largest possible magnetic force, it is preferred to use high saturation material in the magnetic path.



**Figure 39. Saturation study for different materials and air gaps**

Figure 40 shows the magnetic force versus the current (Amp\*turns) using steel 1008 with 0.1 mm air gap. 1250 amp\*turns (7.8 A at 160 turns) created about 50 N magnetic force.

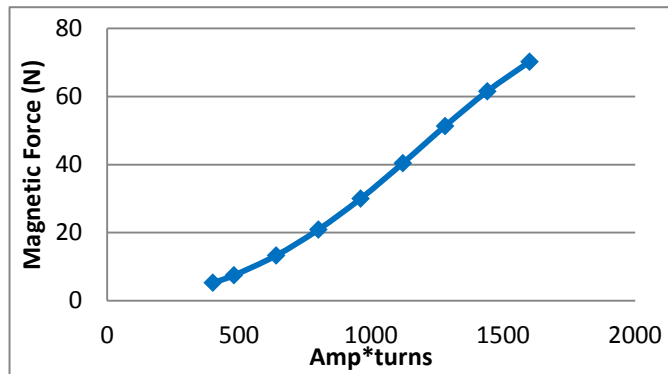


**Figure 40. Magnetic force vs. current at 0.1 mm air gap with steel 1008 (2T saturation)**

### *Mechanical System*

The mechanical system model predicts the rigid body motion of the pintle. The force illustration is shown in Figure 41. At the beginning, the pintle sits on the valve seat where there are five forces acting on it: pressure, gravity, spring, contact friction and supporting forces. The pressure force is due to the pressure on the pintle. Spring force is due to the return spring's compression. Contact friction force takes into account of the initial friction due to its contact with the valve seat. And the support force from valve seat, represented as spring and damper, is the equal and opposite force of all other forces when pintle rests on the pintle valve. The magnetic force increases as the current in the coil increases. In the event of pintle movement, magnetic force overcomes pressure, gravity, spring and contact friction forces. The pintle motion is limited by the stator, which is represented as another set of spring and damper at the distance of 0.09mm. This distance was measured with a miniature dial indicator in the event of pintle motion under the condition where there was no fluid inside the fuel injector.



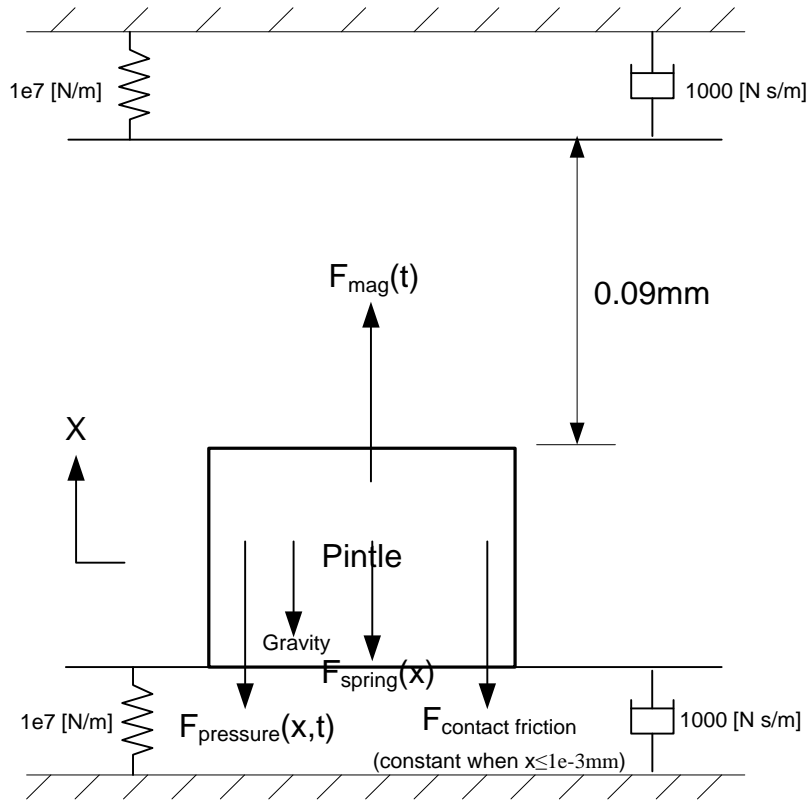


**Figure 41. Mechanical system of the pintle with force illustration**

The non-moving pintle at ~0mm air gap with steel 1008 and current shape shown in Figure 35 was used to create the magnetic force profile shown in Figure 42. The magnetic force  $F_{mag}(t)$  can be expressed by segmenting the force profile and curve-fitting at different segments:

$$F_{mag}(t) = \begin{cases} 0, & 0ms < t < 0.08ms \\ 110.6 \cdot e^{-\frac{(t-0.3823)^2}{0.1241}} + 20.68 \cdot e^{-\frac{(t-0.2471)^2}{0.08861}}, & 0.08ms < t < 0.37ms \\ 105, & 0.37ms < t < 0.47ms \\ -914.9 \cdot t + 536.9, & 0.47ms < t < 0.55ms \\ 30.35, & 0.55ms < t < 1.05ms \\ -528.5 \cdot t + 579.1, & 1.05ms < t < 1.09ms \\ 0, & t > 1.09ms \end{cases} \quad (10)$$

Where  $t$  in the expression is in [ms].

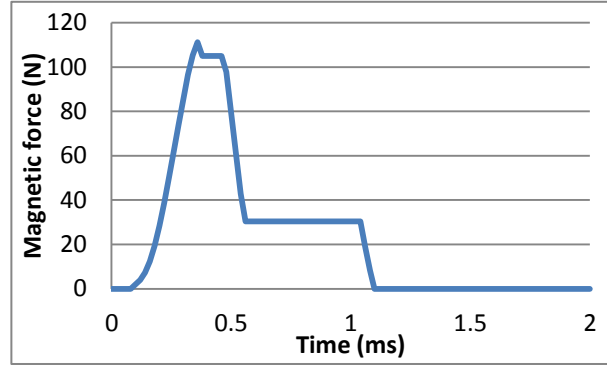


**Figure 42. Magnetic force profile**

The spring force  $F_{spring}$  can be expressed as,

$$F_{spring}(x) = F_0 + K_{spring} \cdot x \quad (11)$$

Where,  $F_0 = -6.5 \text{ N}$  is the initial compression force;  $K_{spring} = -12140 \text{ [N / m]}$  is the spring constant, which is obtained by performing the return spring test.

The initial contact friction force is,

$$F_{initial\ contact\ friction}(x) = \begin{cases} -13.8 \text{ N}, & x \leq 1e - 3 \text{ mm} \\ 0, & x > 1e - 3 \text{ mm} \end{cases} \quad (12)$$

The initial spring compression and initial contact friction forces were determined by performing the threshold current test which was conducted to investigate the minimum current to open the pintle valve under non-fluid condition.

When the pintle moves 0.09 mm distance upwardly, a barrier is enforced by applying a stiff spring and damper to simulate that the pintle hits the stator. The force acting on pintle from the upper wall can be expressed mathematically as follows,

$$F_{upper\ wall}(x) = \begin{cases} -K * (x - 0.09\text{mm}) - c * \dot{x}, & x > 0.09\text{mm} \\ 0, & x < 0.09\text{mm} \end{cases} \quad (13)$$

When the pintle moves back to the zero position (i.e. closed position), another barrier is enforced to simulate the supporting force from the bottom wall,

$$F_{bottom\ wall}(x) = \begin{cases} -K * x - c * \dot{x}, & x < 0 \\ 0, & x > 0 \end{cases} \quad (14)$$

Where K is the wall stiffness and  $K = 1e7$  [N/m] for the current case; c is the damping coefficient and  $c = 1000$  [N s/m] in this study.

The pressure force  $F_{pressure}(x, t)$  on the pintle in vertical direction (i.e. pintle moving direction) was calculated using a CFD program in its transient simulation. This pressure force was also calculated statically at  $x=0$  (i.e. pintle at its closed position) using the relation  $F_{pressure}(x = 0) = P \cdot A_x$ . Figure 43 shows the calculated static pressure forces at pintle closed position at different inlet pressures.

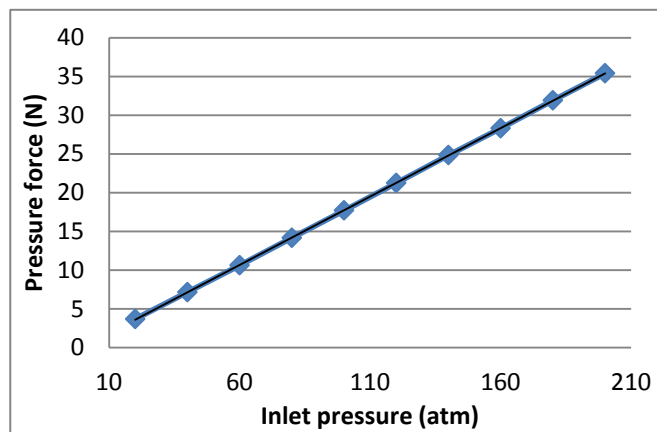


**Figure 43. Calculated static pressure forces at pintle closed position under different inlet pressures**

The pintle's equation of motion can be expressed as (ignoring gravity force and damping of the fluid),

$$m \cdot \ddot{x} = F_{mag}(t) + F_{spring}(x) + F_{contact\ friction}(x) + F_{upper\ wall}(x) + F_{bottom\ wall}(x) + F_{pressure}(x, t) \quad (15)$$

*Fluid System*

The CFD program used in this study was ANSYS CFX. The mesh preparation was done using the ICEM CFD mesh generation software. Only one sixth of the fluid region was modeled due to its periodicity. The pintle valve seat facets were simplified with smooth curvatures. A small inner radius was created instead of a singular point to make the mesh to be strictly hexahedral elements. Table 15 lists the mesh information. Figure 44 shows the convergent result of inlet and outlet mass flow rate as element numbers increase to above 16000.

The geometry of the modeled fluid region is shown in Figure 45.

**Table 15. Mesh information for fluid model**

<b>Total elements</b>	<b>Total nodes</b>	<b>Lowest angle and the percentage</b>	<b>Lowest determinant 2x2x2 and the percentage</b>
16097	12948	9~13.5 (0.703%)	0.25~0.3 (0.009%)

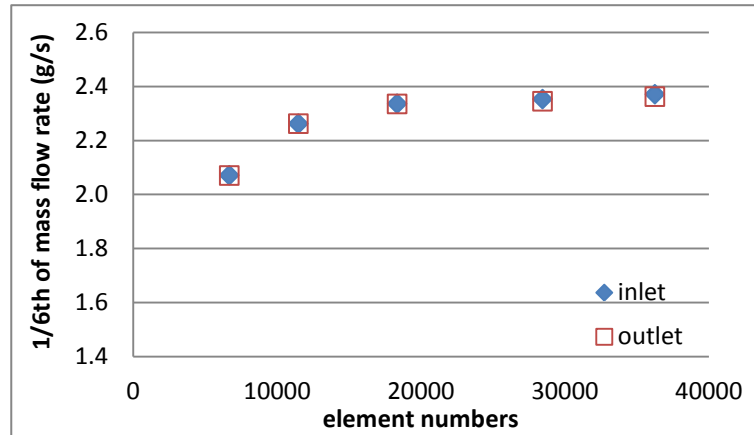


**Figure 44. Grid independence study**

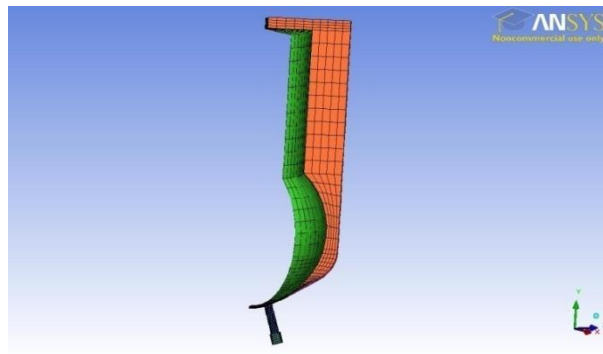


**Figure 45. Meshed fluid region from ICEMCFD**

Notice that this geometry only represents the initial fluid region. During the transient simulation in ANSYS CFX, the mesh will be deformed and the gap between the ball and valve seat will change. Since the software does not allow a zero or negative element, the complete separation of fluid region is not possible during the transient simulation. Therefore, a small gap ( $2.54 \times 10^{-3}$  mm) was used to create the valve “closed”

condition. The detail of this initial geometry at the ball valve location is shown in Figure 46.

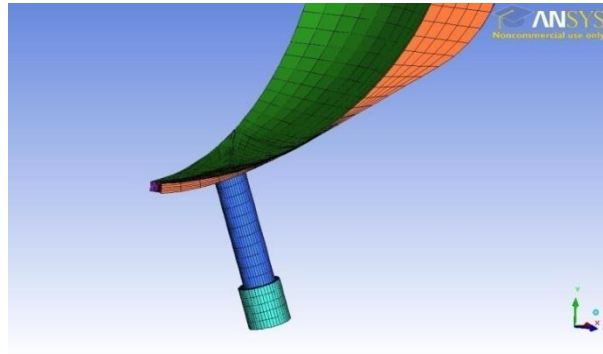


**Figure 46. Small gap between ball and valve seat at the “closed” position**

Transient cavitation flow simulation was performed in ANSYS CFX where a multiphase homogeneous model was used. In order to correlate with the experiments, Jet A fuel and air at 25 °C were used as fluid and vapor phases, respectively. Note that the saturation pressure of the Jet A fuel is 240 Pa. For room temperature simulation, the fluid temperature was set at 25 °C and the entire fluid region was assumed to be isothermal. The turbulence model was K-epsilon.

Mesh deformation strategy was used to incorporate rigid body motion in the transient simulation. The rigid body motion was applied to the pintle ball. The external forces on the ball were: spring force, electromagnetic force, initial contact friction force, and upper and bottom wall contact forces. The details of the force expressions were discussed in the previous section. Only a vertical (in the pintle moving direction) degree of freedom was allowed. Some key physical parameters are listed in Table 16.

**Table 16. Key physical parameters for the fluid model**

<b>1/6<sup>th</sup> of the pintle mass</b>	<b>Pintle ball radius</b>	<b>Nozzle diameter</b>	<b>Initial pintle displacement</b>
0.507 g	1.524mm	0.1524mm	2.54e-3mm

Boundary conditions, listed in Table 17, were specified as inlet, outlet and wall. Total and static pressures were used as inlet and outlet boundary conditions, respectively. The rest which includes the ball, valve seat, two periodic sides, and nozzle wall, were specified as no-slip wall boundary. The transient simulation's total run time was 2 ms and the time step was 0.25  $\mu$ s.

**Table 17. Boundary conditions**

<b>Inlet</b>	Total pressure: 20 ~ 200 atm
<b>Outlet</b>	Avg. static pressure: 0 atm (reference pressure is 1 atm)
<b>Others</b>	No-slip wall

## **Results and Discussion**

### **Power Strategy (a)**

The current profile in Figure 35 was named as the power strategy (a) which was used in the simulation to understand the dynamics of the pintle and the pressure force during the pintle opening event. The results gave insights into the optimal power strategy to drive the fuel injector under different operating pressures.

The resultant magnetic force from Maxwell was expressed in Equation (10) which used the power strategy (a) current profile.

After running cases for different inlet pressures, three major results were obtained from ANSYS CFX transient simulation: pintle displacement, pressure force, and mass flow rate.

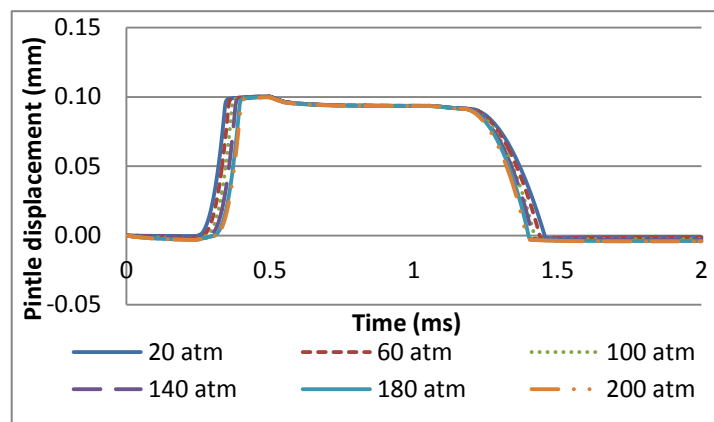


**Figure 47. Pintle displacement profiles at different inlet pressures with power strategy (a)**

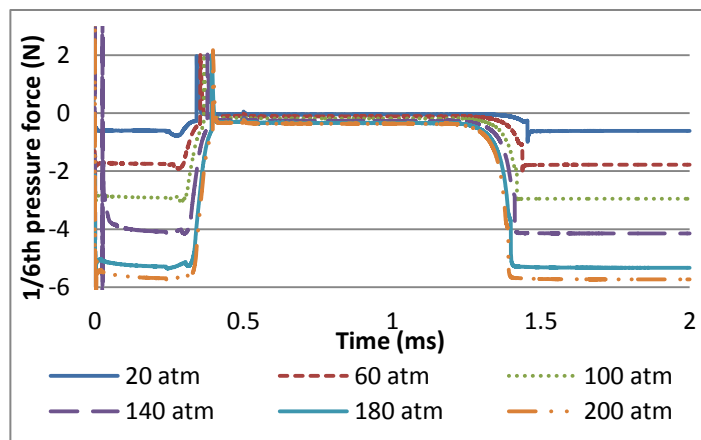


**Figure 48. 1/6th of pressure forces on the pintle at different inlet pressures with power strategy (a)**



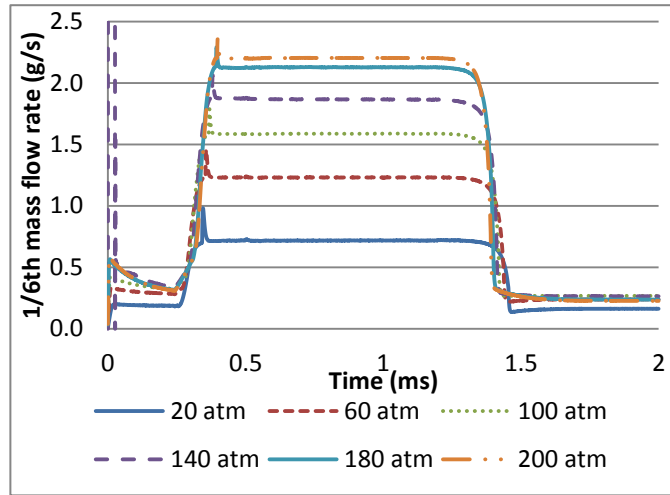


**Figure 49. 1/6th of mass flow rates at different inlet pressures with power strategy (a)**

In Figure 47, the pintle opening delay time started from 0.25 ms at 20 atm and increased to 0.31 ms at 200 atm. This increasing opening delay time was caused by the increasing initial pressure forces on the pintle ball as shown in Figure 48, from 3.6 N (total pressure force) at 20 atm to 35.4 N at 200 atm. Since the power strategy was the same, it took more time for the magnetic force to reach higher levels to overcome this increased initial pressure force. Therefore, in order to have minimum opening delay time, the 1<sup>st</sup> stage current increasing rate needed to be high so that it could reach the same current level with less time. Due to the limitation of the power supply's maximum voltage rating and the relation between the time to reach certain current level and supply voltage:  $t \propto \frac{1}{V}$ , the current increasing rate remained the same for all power strategies given the same voltage supply. Therefore, higher voltage rating power supplies are recommended for fast pintle opening.

After the current increase rate was determined, the next question was how much current was required for the 1<sup>st</sup> stage to initiate the pintle opening. As discussed earlier, the magnetic force is needed to overcome the initial pressure, spring and contact friction forces. Table 18 listed the required magnetic forces at different inlet pressures. The relationship between the magnetic force and current was given in Figure 39. Saturation study for different materials and air gaps. Using 0.1mm as the initial air gap and 160 as the number of coil turns in Maxwell, the corresponding threshold current levels were calculated using the force and current relationship in Figure 40. The resultant threshold current values were listed on the far right column of Table 18. For example, it required 8.4 A to open the pintle valve in the case of 200 atm inlet pressure.

***Table 18. Initial opposing forces, required magnetic forces and threshold current levels under different pressures***

<b>Inlet pressure (atm)</b>	<b>Initial pressure force (N)</b>	<b>Initial spring force (N)</b>	<b>Initial contact friction force (N)</b>	<b>Combined forces (required magnetic forces) (N)</b>	<b>Threshold current (A)</b>
0	0	6.5	13.8	20.3	4.9
20	3.7	6.5	13.8	24	5.4
40	7.1	6.5	13.8	27.4	5.8
60	10.6	6.5	13.8	30.9	6.2
80	14.2	6.5	13.8	34.5	6.5
100	17.7	6.5	13.8	38	6.8
120	21.2	6.5	13.8	41.5	7.2
140	24.8	6.5	13.8	45.1	7.5
160	28.3	6.5	13.8	48.6	7.7
180	31.8	6.5	13.8	52.1	8.0
200	35.4	6.5	13.8	55.7	8.4

After this threshold current was determined for different inlet pressures, the next question was about the on-time of the 1<sup>st</sup> stage current.

As shown in Figure 48, the pressure force was the maximum when the pintle was at its “closed” position. As soon as the magnetic force overcame the initial opposing forces, this pressure force dropped dramatically to nearly zero. Depending on the supply fuel pressure, the pintle opening time varied a small amount. The time also varied only a small amount between when the pintle opened and when it reached the fully open position. This time duration between when pintle opened and when it reached the fully open position was important because only when the pintle reached the fully open position, did the steady flow form (as shown in Figure 49) and the pressure force dropped to nearly zero. And only when the pressure force dropped to nearly zero could we possibly drop the current to the 2<sup>nd</sup> stage holding current, which was only required to overcome the spring force.

If the 1<sup>st</sup> stage current dropped sooner than it required to keep the pintle motion going until it reached the fully open position, the pintle might experience early fall back due to the inadequate magnetic force compared to the combined pressure and spring force during this opening process. This created inconsistent injection. This situation was modeled using 0.25 ms on-time of the 1<sup>st</sup> stage current. We called this power strategy (b), with a current profile shown in Figure 50. The pintle displacement, pressure force and mass flow rate plots under power strategy (b) are shown in Figure 51, Figure 52, and Figure 53, respectively.

*Power Strategy (b)*

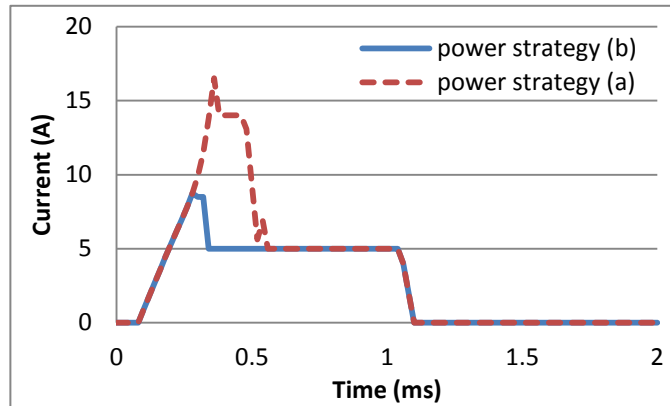


**Figure 50. Current profile comparison between power strategy (a) and (b)**

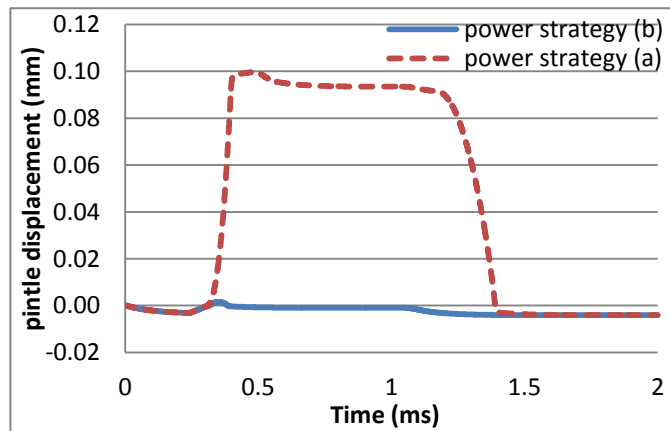


**Figure 51. Pintle displacement profiles with power strategy (b) and (a) at 200 atm supply pressure**

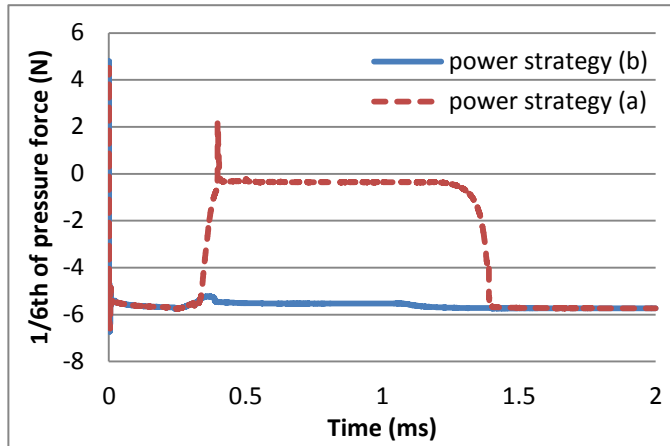


**Figure 52. 1/6th of pressure forces on the pintle with power strategy (b) and (a) at 200 atm supply pressure**

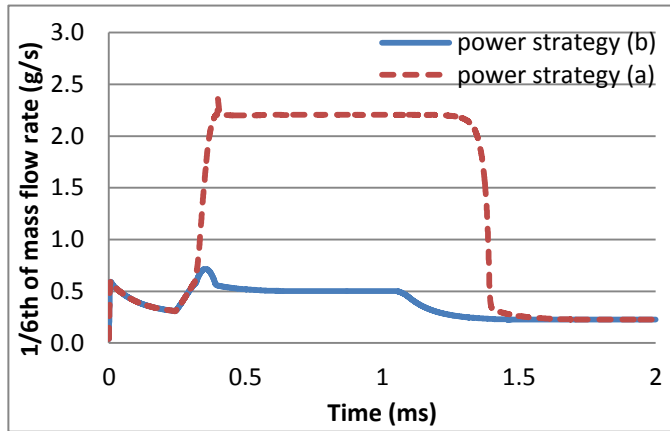


**Figure 53. 1/6th of mass flow rates with power strategy (b) and (a) at 200 atm supply pressure**

Power strategy (b) failed to completely open the pintle at 200 atm inlet pressure. The pintle was first initiated but it fell back before it reached the upper wall of the stator. Therefore, even though the 1<sup>st</sup> stage current level might be enough to overcome the

threshold opposing forces (i.e. pressure force, spring force and initial contact friction force), it might create early fall (or random position) of the pintle as shown in the 200 atm inlet pressure case, if the current dropped too soon (i.e. before the pintle reached the upper wall of the stator). This caused injection inconsistency. The ideal current of the 1<sup>st</sup> stage should remain at a certain level until the pintle reaches its maximum position to ensure consistency of fuel injection. The time that it took to fully open the pintle was estimated to be at most 0.4 ms based on the case with 200 atm supply pressure in Figure 48.

After the pintle was fully opened (i.e. the 1<sup>st</sup> stage), the magnetic force at the 2<sup>nd</sup> stage could be reduced significantly due to the drop of the pressure force at the pintle fully open position. Still, the magnetic force should be large enough to overcome the spring force at the pintle fully open position to hold the valve open. If the 2<sup>nd</sup> stage current level creates less magnetic force than the compressed spring force, the pintle might experience early fall as well. This is illustrated using current profile shown in Figure 54 which is named as power strategy (c). The pintle displacement, pressure force and mass flow rate plots with power strategy (c) under 200 atm supply pressure are shown in Figure 55, Figure 56, and Figure 57, respectively.

*Power Strategy (c)*

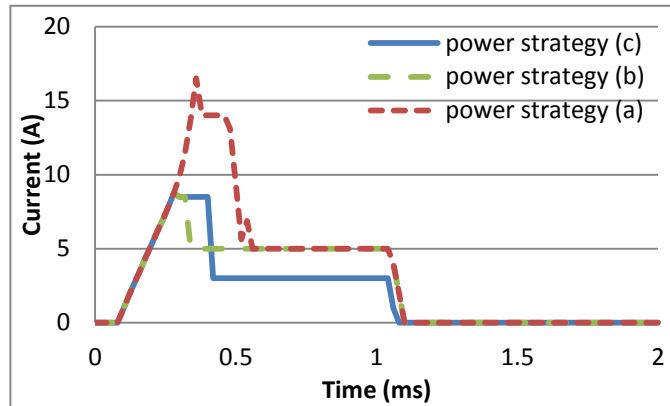


**Figure 54. Current profile comparison among power strategy (a), (b) and (c)**

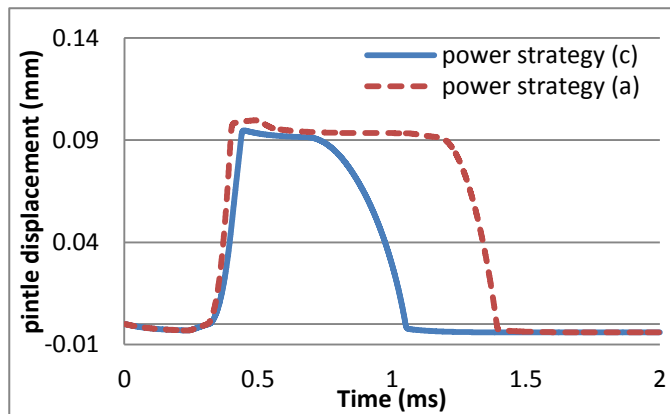


**Figure 55. Pintle displacement profiles with power strategy (c) and (a) at 200 atm supply pressure**

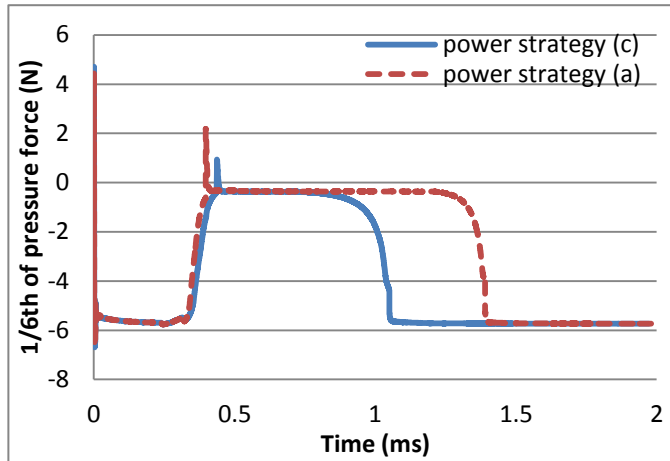


**Figure 56. 1/6th of pressure forces on the pintle with power strategy (c) and (a) at 200 atm supply pressure**

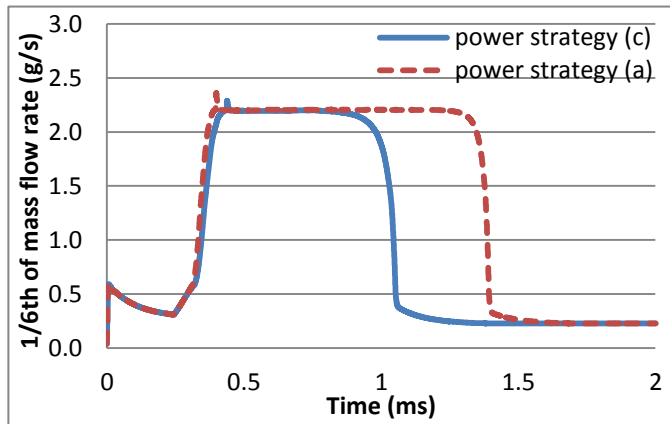


**Figure 57. 1/6th of mass flow rates with power strategy (c) and (a) at 200 atm supply pressure**

With power strategy (c), pintle fell back earlier due to the inadequate 2<sup>nd</sup> stage magnetic force (at 3 A) to hold the pintle at its fully open position. Therefore, even though the 2<sup>nd</sup> stage current could be dropped, it required a minimum value (>3A, which



created  $>7.5$  N magnetic force at the fully open position. The spring force at the fully open position was  $7.7$  N) so that the magnetic force could still overcome the spring and pressure forces at the pintle fully open position. As discussed earlier, steady flow was formed and the pressure force dropped to nearly zero when the pintle was at its fully open position.

### *Optimal Power Strategy*

After the trials of different power strategies, the magnetic force requirement that led to the current requirement gradually formed. From the previous discussion, there are three key parameters that determine whether or not the pintle could be successfully opened and held open: threshold current, the 1<sup>st</sup> stage on-time and the 2<sup>nd</sup> stage current. These key parameters are illustrated in Figure 58.  $I_{\text{threshold}}$  at different inlet pressures can be referred to Table 18. For example,  $I_{\text{threshold}} = 8.4$  A at 200 atm supply pressure.

$I_{\text{pick-up}}$  can be lowered based on the fact that once the pintle motion is initiated, the initial contact friction force drops to zero.  $I_{\text{pick-up}}$  can be determined using the corresponding current value of the combined force minus the initial contact friction force at different inlet pressures in Table 18. For example,  $I_{\text{pick-up}} \approx 7.5$  A at 200 atm supply pressure.

$I_{\text{hold}}$  is the holding current for almost all pressure cases after pintle reaches the fully open position. Based on the spring force calculation (i.e.  $F_{\text{spring}} = 7.7$  N at pintle fully open position), the magnetic force at the pintle fully open position requires  $I_{\text{hold}} > 3$  A. Refer to Figure 39 for  $\sim 0$  mm air gap and steel 1008 case.

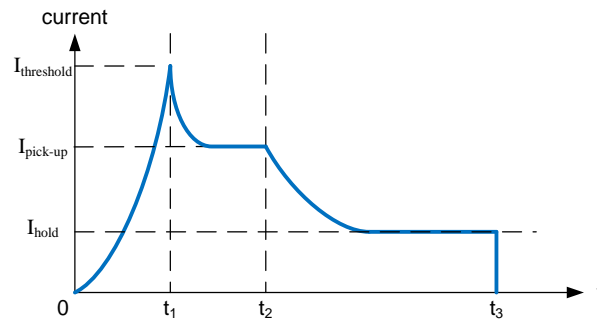


**Figure 58. Current requirement illustration during one injection event**

The three key current levels shown in Figure 58 are often mentioned as peak, pick-up and holding currents in the user’s manual of fuel injectors. The previous discussion explained the reason for having these three key parameters. Threshold current is the current to overcome the initial contact friction, pressure force and spring force. Pick-up current is the current to keep the pintle opening motion going until it reaches fully open position. Holding current is the current to keep the pintle at its fully open position.

In a real application, the pick-up stage lasts a very short amount of time, the threshold and pick-up stages are often combined to form the 1<sup>st</sup> stage. Holding stage is to be called as the 2<sup>nd</sup> stage. Figure 59 illustrates how the current shape looks like for implementation.

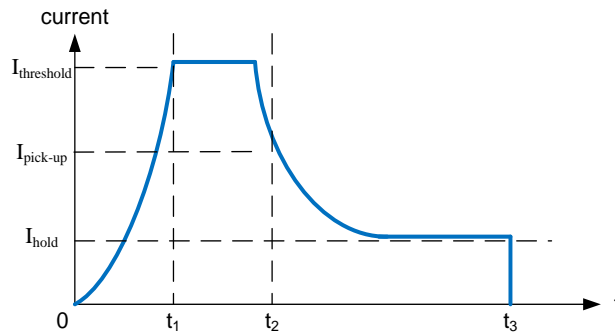


**Figure 59. Current profile illustration for implementation**

On the time axis,  $t_1$  is the time when the pintle motion is initiated;  $t_2$  is the time when the pintle reaches its fully open position;  $t_3$  is the time when the injection is to be stopped. Among these times,  $t_2$  is the time that ensures the pintle motion continues from when the motion gets initiated to the time when the pintle reaches its fully open position. This time is called the 1<sup>st</sup> stage on-time. It is around 0.4 ms based on the results from test and simulation.  $t_3$  simply defines the total spray duration time. Despite the fact that the closing delay time is also closely related to pressure and magnetic forces (i.e. higher inlet pressure has the tendency to push the pintle back quicker, thus creating less closing delay time), it was found in the previous injector temporal measurement section that, the closing delay time is almost constant regardless of  $t_3$ , given adequate  $t_2$  value and the spray duration time is proportional to total command signal on-time.

## Validation

### Validation under Power Strategy (a)

JP-8 fuel was used in the validation experiment. JP-8 fuel was selected because the injector power drive system was designed to control a heavy fuel direct fuel injector for military applications. However, any other liquid fuel should be a sound substitute in the study. The test and simulation results on average mass flow rate during an opening event (total injection quantity divided by injection duration time) were compared at different supply pressures in Figure 60. Power strategy (a) was used for all cases. The total injection quantity was measured by a scale after a specified number of injections.

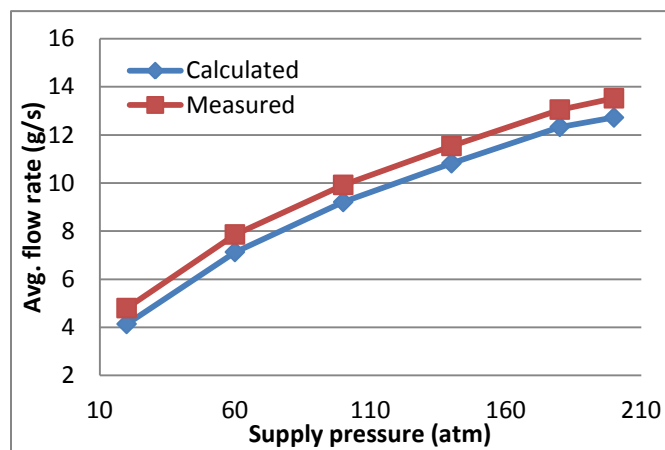


**Figure 60. Average mass flow rate comparison during one injection event with power strategy (a) at different supply pressures**

Accuracy of pintle displacement profiles was validated with the experimental data taken using a photo detector, which is an indicator of pintle motion. This approach

assumes little time delay between the pintle motion and the detected spray. The discrepancy between the photo detector measured data and computer simulated pintle movement data are mainly due to this assumption. Overall, because of the high velocity spray under high supply pressure, the results from measuring the spray should give insights to the pintle behavior, which is the main purpose of this validation work. The photo detector is an electronic device which emits an infrared beam to the receiver end. The change of the output of the receiver circuitry indicates whether or not there is an obstacle blocking the path. In our case, the fuel spray is the obstacle that causes the change of the photo detector output signal. The details of using the photo detector to measure the injection event can be found in the previous section. The spray temporal characteristics (i.e. opening delay and spray duration times) between calculated and measured data are compared in Table 19.

***Table 19. Spray temporal characteristics comparison between calculated and measured data***

Supply pressure (atm)	Opening delay time (ms)		Spray duration (ms)	
	Calculated	Measured	Calculated	Measured
20	0.25	0.43	1.21	1.25
60	0.27	0.41	1.17	1.31
100	0.28	0.39	1.14	1.31
140	0.29	0.39	1.12	1.30
180	0.31	0.39	1.09	1.28
200	0.31	0.40	1.08	1.28

As shown in Table 19, the measured delay times did not follow the monotonous increasing trend of the calculated values as the supply pressure was increased. The discrepancy between the calculated and measured delay times was mainly due to the delay time between the first drop of spray coming out from the nozzle and the time when the photo detector sensed it. As the supply pressure was increased, the velocity of the first drop of spray increased as well. This shortened the delay time at higher pressures. Therefore, even though the pintle was opened quicker at lower pressures, it took longer time for the photo detector to detect the spray. The end result was about the same delay time (~0.4 ms) from photo detector measurement for all pressures.

*Validation of Predicted Phenomena under Power Strategy (b) and (c)*

The purpose of the multi-physics model developed in this study was to optimize the power strategy to drive fuel injectors. This gave insights into the requirement of threshold current, the 1<sup>st</sup> stage on-time and the 2<sup>nd</sup> stage current. The multi-physics model predicted the failure of the power strategy (b) and (c). We then tested the injector using the similar power strategies and confirmed the inconsistency of the photo detector output, which was the indication of the early fall of pintle as we predicted in the simulation.

Figure 61 and Figure 62 compare two power strategies with the same 1<sup>st</sup> stage current, 2<sup>nd</sup> stage current, total control signal on-time, but different 1<sup>st</sup> stage on-times. Figure 61 shows the consistency (same spray duration time between pulses) of the case with 0.3 ms 1<sup>st</sup> stage on-time, while Figure 62 shows the inconsistency (different spray duration times between pulses) of the case with 0.16 ms 1<sup>st</sup> stage on-time. The latter case

is the demonstration of power strategy (b) in the simulation, which failed to open the pintle to its fully open position. The early fall back of the pintle was the cause of inconsistent spray duration times.

Figure 61 and Figure 63 compare two power strategies with the same 1<sup>st</sup> stage current, 1<sup>st</sup> stage on-time, 2<sup>nd</sup> stage on-time, but different 2<sup>nd</sup> stage current levels. Figure 61 shows the consistency (same spray duration time between pulses) of the case with 3.5 A 2<sup>nd</sup> stage current, while Figure 63 shows the inconsistency (different spray duration times between pulses) of the case with 2.5A 2<sup>nd</sup> stage current. The latter case is the demonstration of power strategy (c) in the simulation, which failed to hold the pintle at its fully open position. The early fall back of the pintle was the cause of inconsistent spray duration times.

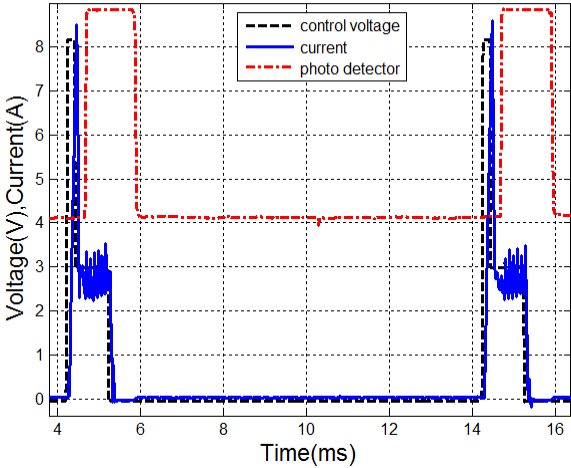


**Figure 61. Photo detector output with 1st stage current of 8 A, 1st stage on-time 0.2 ms, 2nd stage current of 3.5 A, 2nd stage on-time 0.8 ms; at 200 atm supply pressure**

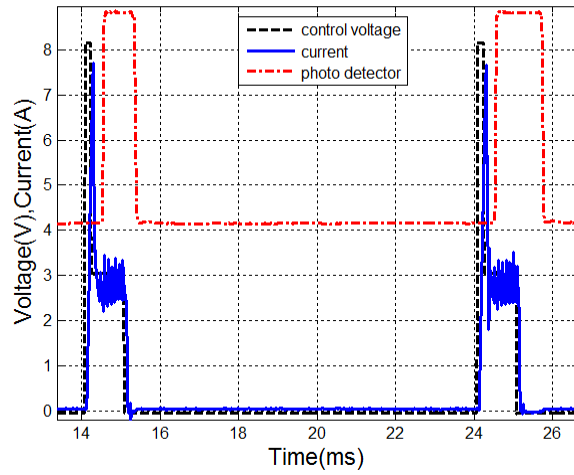


**Figure 62. Photo detector output with 1st stage current of 8 A, 1st stage on-time 0.16 ms, 2nd stage current of 3.5 A, 2nd stage on-time 0.84 ms; at 200 atm supply pressure**

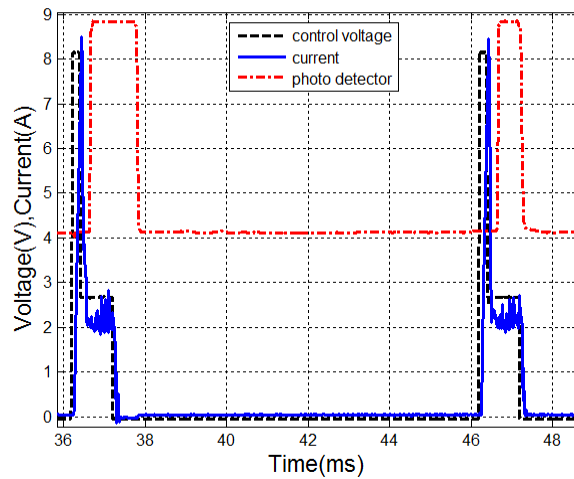


**Figure 63. Photo detector output with 1st stage current of 8 A, 1st stage on-time 0.2 ms, 2nd stage current of 2.5 A, 2nd stage on-time 0.8 ms; at 200 atm supply pressure**



## ***Conclusion***

The optimal power requirement for a two-stage PWM current controlled approach was obtained to improve the injection repeatability at minimum power consumption:

1. The 1<sup>st</sup> stage current needs to overcome initial opposing forces such as spring, pressure and contact friction force ( $I_{\text{threshold}} > 8 \text{ A}$  at 200 atm supply pressure). The threshold current can be lowered at lower operating pressures. It is always recommended to use higher voltage rating power supplies for fast pintle opening.

2. The 1<sup>st</sup> stage on-time needs to be long enough to keep the pintle movement going until it reaches its fully open position ( $t_2 \approx 0.4 \text{ ms}$ ). Otherwise the pressure force will push the pintle back to create early fall back, which is one cause of injection inconsistency;

3. The 2<sup>nd</sup> stage current can be lowered significantly due to the drop of pressure force at pintle fully open position, yet it needs to maintain at certain level to overcome the spring force and hold the pintle at its fully open position ( $I_{\text{hold}} > 3 \text{ A}$ ). Otherwise the pintle will experience an early fall as well due to the spring force, which is another cause of injection inconsistency. The 2<sup>nd</sup> stage current requirement does not increase as the supply pressure increases due to the fact that once the pintle is at its fully open position, the steady flow forms and the pressure force on the pintle drops to nearly zero.

4. The 2<sup>nd</sup> stage on-time has not been discussed due to the fact that the closing delay time does not vary with on-times and the total injection time is proportional to

control signal's total on-time. The injection time can be easily adjusted by changing the 2<sup>nd</sup> stage on-time.

The multiphysics model also has given insight on how to design a high-performance fuel injector:

1. High magnetic saturation material is preferred to build fuel injectors to create larger magnetic force to initiate the pintle motion.

2. The return force (spring force in this study) determines the closing delay time. Thus, large return force would create less closing delay time.

3. The fluid model can be used to better understand the physics during the fuel injection. For example, the relationship between nozzle diameter and mass flow rate; the effect of geometry changes on the cavitation zone at various operating pressures. The cavitation can thus be reduced or eliminated by carefully choosing the right geometries and pintle motions.

### **Room Temperature Test Results**

The importance of the previous two sections cannot be stressed more in this section. Because of the correct drive and measurement tool we have for spray event detection, we are confident of the results in this section.

#### ***Test Equipment***

1. High Pressure System. Please refer to Figure 21 for details.
2. Weighing System uses a load cell to measure the weight in a lever type mechanism. As illustrated in Figure 64, the accumulator sits on the left of the lever,

while the counter-weight sits on the right with a load cell attached to the right side measuring the tension force. Actual weighing system is shown in Figure 65.

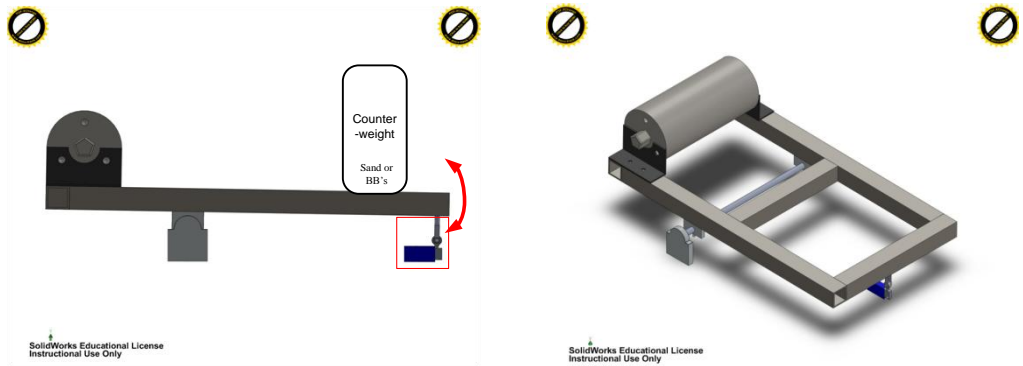


**Figure 64. Weighing system concept**

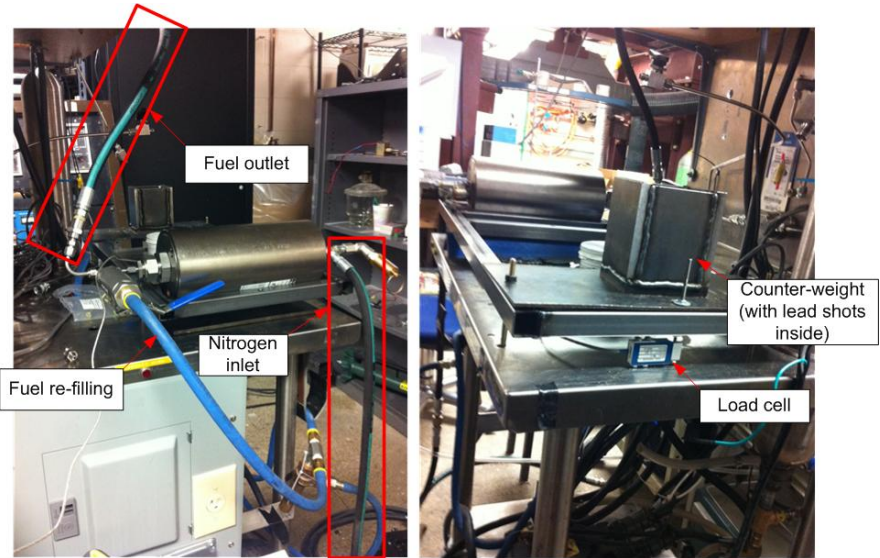


**Figure 65. Actual weighing system**

### 3. Injector Test Fixture (Figure 66 and Figure 67):

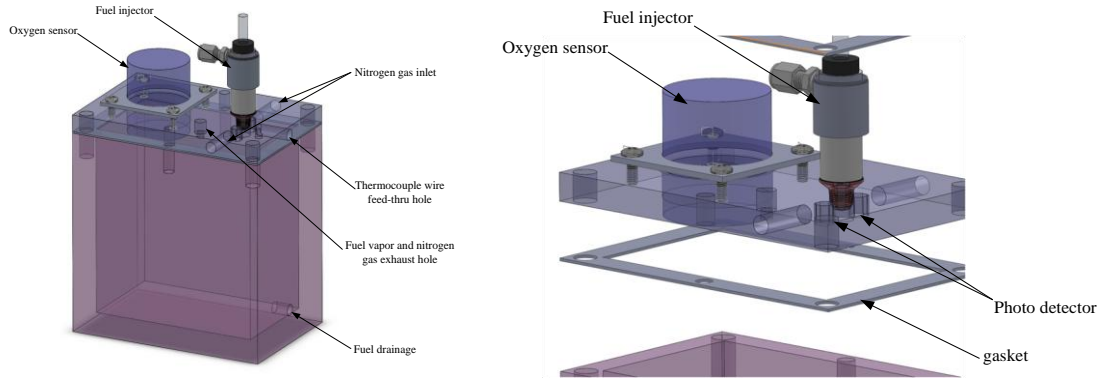


**Figure 66. Injector test fixture**

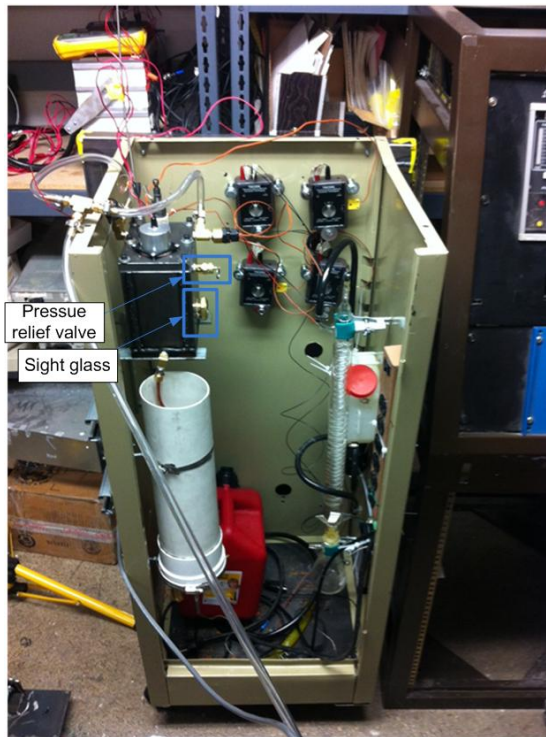


**Figure 67. Injector test cabinet**

#### 4. Electronic and Power System:

The electronics module and their power system are shown in Figure 68 and Figure 69, respectively. Seven analog input channels are used for data login. These are:

- a. Control voltage input to PWM power amplifier;
- b. Photo detector output;
- c. Current to the injector;
- d. Load cell (two channels are taken);
- e. Oxygen sensor 1 (inside the fuel spraying chamber);
- f. Oxygen sensor 2 (inside the fire cabinet);

Another 5 pairs of analog input channels (differential input) are reserved for thermocouple reader outputs (on another DAQ board).

The circuit board electronics module has the following functionalities:

- a) Two stage fuel injector control circuit;
- b) Photo detector driving circuit;
- c) Load cell filtering circuit;
- d) Relays for drain valve;
- e) Front panel: current probe BNC, 37 pin DAQ board quick connection;

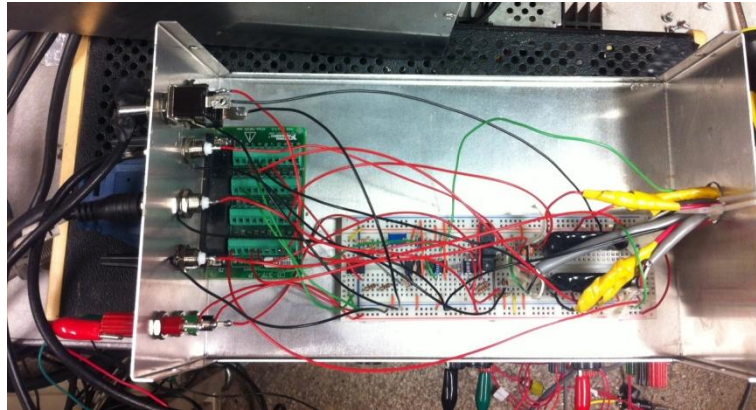


**Figure 68. Electronics module for injector testing**

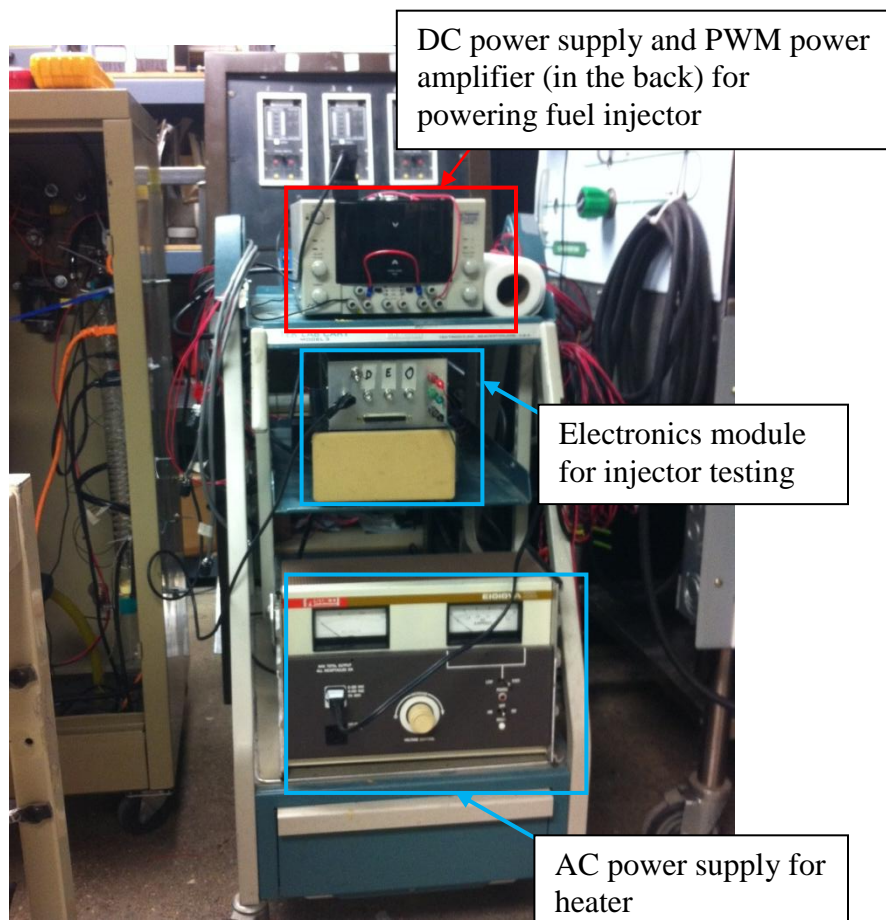


**Figure 69. Electrical and electronics system**

### ***Test Procedure***

Each injector test lasted at least 30 seconds. The volume being injected was read through a graduate cylinder where fuel was collected after the injection. The fuel injector fuel line was maintained at predefined pressure using compressed nitrogen.

The exact number of shot was specified through a Labview program. Volume per shot was averaged over the entire test period. In other words, the volume per shot was obtained through dividing the number of shot by total injected volume. Figure 70 shows the screen shot during an injection test. Within the signal window, the red is the injection control voltage, yellow is the current to injector (x0.1) and blue is the photo detector output.

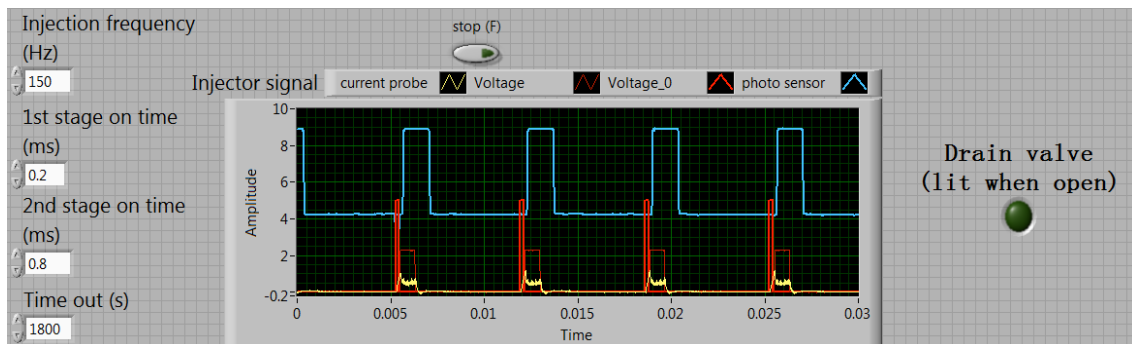


**Figure 70. Injector program Labview user interface**

The injector was pressurized through an accumulator using high pressure nitrogen. The supply pressure varied from 20 atm to 200 atm for the following test.

The injection timing measurement used photo detector system. Nitrogen gas was purged in the test process to make sure each injection recording was clear and free of mist interference.

The injector current was a two-stage shape discussed in the previous section. It had 14 A, 0.4 ms on-time for the first stage and 5 A, 0.1 ~ 2.6 ms on-time for the second stage. The total control signal pulse width varied from 0.5 ms to 3 ms. The injection frequency was 100 Hz.

The opening delay times were found to be independent of supply pressures when the time delay from pintle moved and the first droplet was detected by photo detector was considered. Thus, the detected opening delay with photo detector was longer in the lower supply pressure cases due to the velocity of injected jet was slower. This slower velocity led to longer time required to travel from nozzle to photo detector position. With that time difference between droplet traveling from nozzle to photo detector being excluded (thus higher supply pressure cases have higher fidelity), the opening delay time is about 0.4 ms regardless of the pulse width and the actual injection duration times vary almost linearly with pulse width.

The most frequent values were selected for each injection opening delay and duration time case. The measured opening delay and spray duration times are more accurate under 200 atm supply pressures due to the aforementioned detection delays using photo detector. Figure 71 shows the injection opening delay at actual spray times measured by photo detector under 200 atm supply pressures.



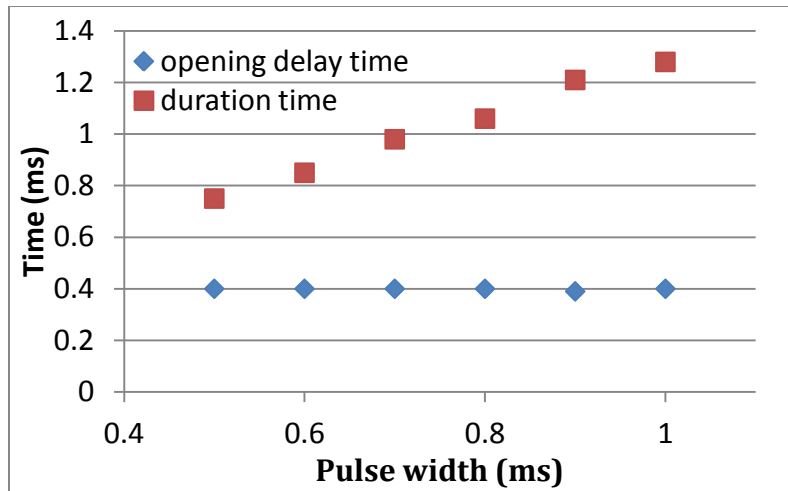


**Figure 71. Opening delay and spray duration times measured with photo detector**

All injected mass was measured from a weight scale. The scatter between testes was very small, typically within 1 g per 30 seconds. Figure 72 shows the average mass flow at different injection pulse width under 140 and 200 atm fuel supply pressures.

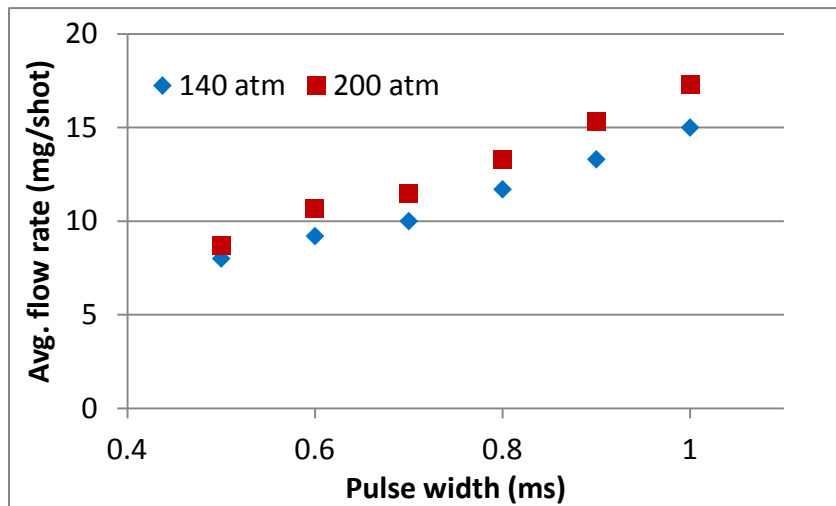


**Figure 72. Average mass flow vs. injection pulse width 140 and 200 atm fuel supply pressures**

Dividing mass per shot by the actual spray duration time, one can get average mass flow rate during one injection event.

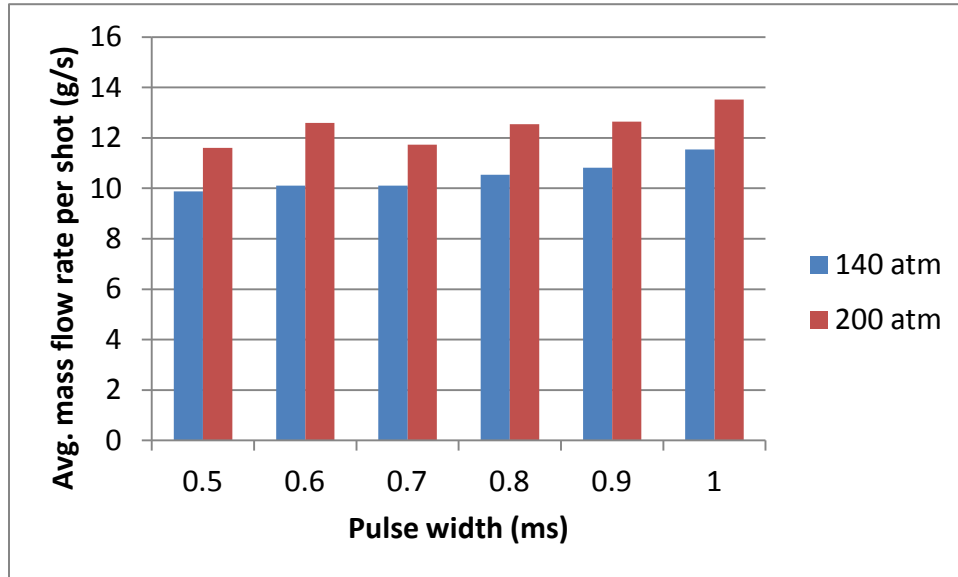


**Figure 73. Average mass flow rate per shot vs. injection pulse width**

As can be seen from Figure 73, the average mass flow rate per injection event is quite similar regardless of pulse width. It increases with the supply pressures, i.e. it has an average mass flow rate of 10.5 g/s per injection event at 140 atm, while at 200 atm supply pressure, this flow rate increases to 12.5 g/s per injection event. One can calculate how long of the actual spray time is required to achieve certain mass per shot under certain pressure.

### ***Conclusion***

The test revealed injection delay, duration and mass flow rate at different operating conditions, i.e. supply pressures, control signal on-times. These test data were

used as references for future engine test, as well as to provide baseline measurement for high temperature heating test.

## CHAPTER IV

### FLASH HEATER DEVELOPMENT

#### **Overview**

The objective of this chapter is to develop a heated fuel injector which integrates both a direct fuel injector and a flash heater that can flash heat JP-8 to its vaporization temperature ( $>310$  °F). The direct fuel injector is a commercial off-the-shelf (COTS) BOSCH gasoline direct fuel injector, as discussed in chapter III. It is retrofitted with a heater that has “flash” heating capability. Design evolution of this “flash” heater is presented with analytical and numerical (FEA, CFD) methods to justify its flash heating effectiveness. The outlet steady-state fuel temperature and its transient temperature profile are obtained at different heater power levels. The final heater design is integrated with direct fuel injector. The prototype flash vapor fuel injector is manufactured and tested to validate the design/simulation results. A heating test rig is constructed to measure the quick temperature response of outlet fuel. The test results show almost instantaneous fuel outlet temperature rise at required fuel flow rate.

#### **JP-8 Flash Heater Design**

##### ***Requirements of the JP-8 Heater***

1. Heat JP-8 from room temperature to its vaporization temperature (typically greater than 300 °F) at required fuel flow rate.
2. Flash heating capability to avoid coking.
3. Locate the heater near nozzle to avoid heat loss.

### ***Heater Material***

To start the heater design, a material that would suppress the reaction with JP-8 will be selected. The ideal heater material should have the following properties:

- High thermal conductivity;
- High temperature capability;
- High strength;
- Low specific heat capacity;
- Not reactive to JP-8;
- Prevent coking of JP-8 at high temperature;
- Easy for machining (wire Electrical Discharge Machining, or EDM);

From literature, we found research has been done using different metal alloys to measure the deposition of carbonaceous solids under thermal stressing (500 °C or 932 °F) of JP-8 fuel. Figure 74 shows carbon deposit vs. different metal alloys [27].

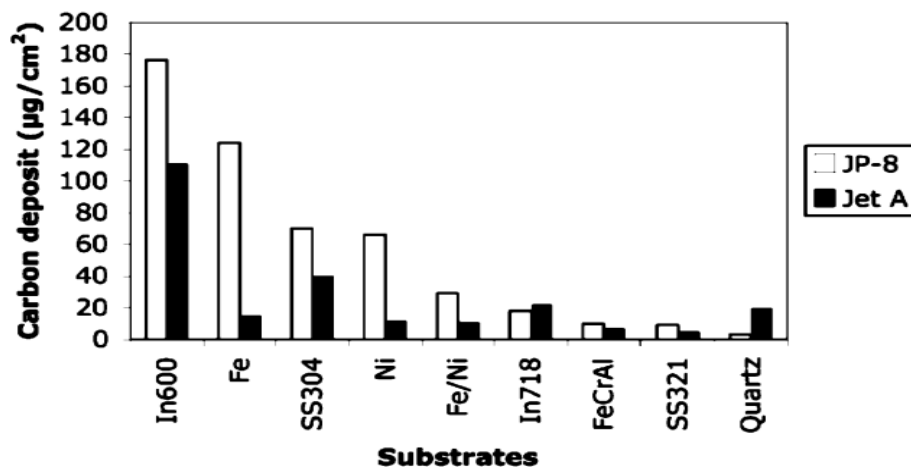


**Figure 74. Carbon deposit vs. different alloys [27]**

Stainless steel 321 was found to be the metal alloy that created least amount of carbon deposit under 500 °C (932 °F) thermal stress for 5 h at 34 atm (500 psi).

In another study, JP-8 was preheated and went thru a tube made of different materials. The authors found ss304 is better than ss316 and nickel in terms of carbon deposition on tubes. Figure 75 compares the carbon deposit with different materials under JP-8 thermal stressing. The authors also found that all metals react with JP-8 except glass lined from the observation that the only clear colored JP-8 comes from glass lined tubes [28].

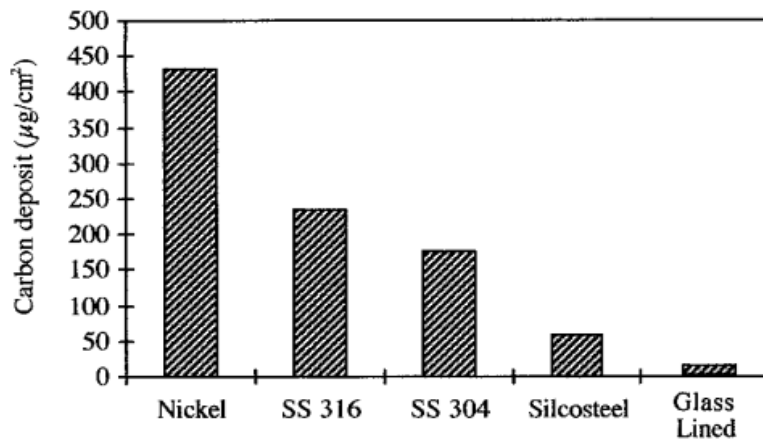


**Figure 75. 500 C (932 F) JP-8 carbon deposit under 34 atm (500 psi) with 1 mL/min flow rate [28]**

Considering these thermal deposition studies and the manufacturing (wire EDM) plausibility with different metals (wire EDM does not work on non-conductive materials such as glass or ceramics, or most plastics), we decided to use ss304 as the heater material.

### ***Heating Method***

Various heating methods can be applied to heat up the JP-8, i.e. dielectric heating (capacitive heating under radio frequency or microwave), inductive heating, conductive heating.

Dielectric heating makes use of JP-8's dielectric property (poor electrical conductor). By alternating the electrical field at high frequency, heat is generated inside JP-8 molecules. The ability of local heating makes this method a very efficient one. However, the equipment becomes very complex when high voltage source and wave generator, as well as the way of containing the wave are required [29].

Inductive heating makes use of the eddy current formed in the conducting media. This method takes advantage of JP-8's poor yet small electrical conductivity. By alternating the magnetic field created by the coil current, JP-8 molecules constantly change their direction in the magnetic field and get heated up. This method has not been demonstrated working for JP-8. The limitation of using this method is obvious when the whole fuel injector is considered. Because the surrounding body material is made of stainless steel, it is inevitable that the body may get to higher temperature as part of the inductive heating result.

Conductive heating makes use of the thermal conductivity of JP-8. Though the thermal conductivity is low for JP-8, conduction heating provides an easy and reliable way to implement. Figure 76 compares thermal conductivity between JP-8 and water. As can be seen, water can conduct heat five times better than JP-8.

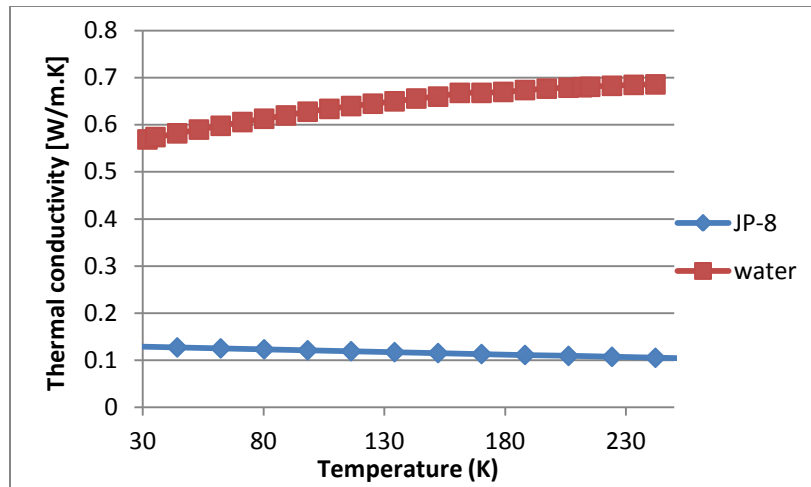


**Figure 76. Thermal conductivity comparison between water and JP-8**

***Static Heating Analysis – FEA (Proprietary Material)***

If the heater is located away from injector, the heat of the JP-8 along the fuel pipeline will be dissipated before it reaches nozzle. Therefore, the best way of preventing this loss is to locate heater as close to the nozzle as possible. This is how the idea of local heating of JP-8 at the nozzle came about. Figure 77 shows dissection view of the injector. The possible heater location will be around the neck area.

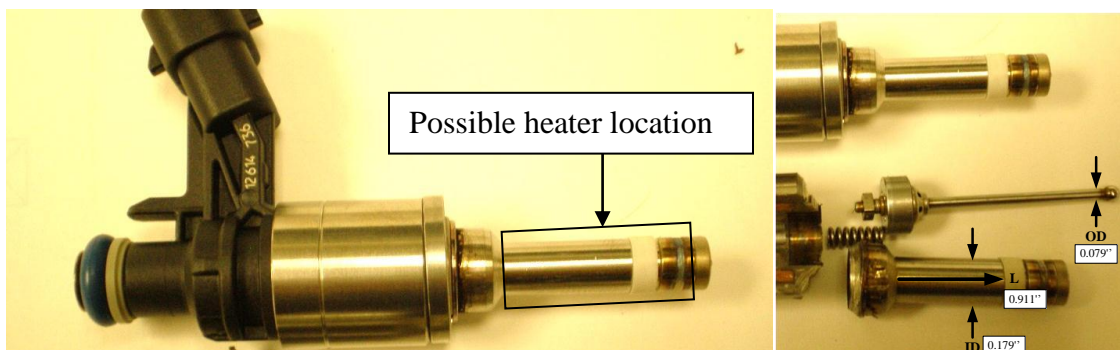


**Figure 77. The dissection of direct fuel injector shows possible heater location**

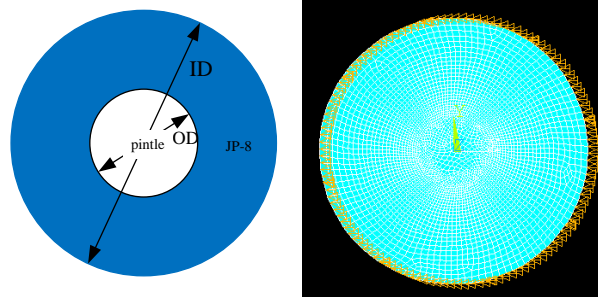


## *Different Heater Concepts*

The following shows the evolution of the heater design.

### 1. Direct Heater without any Modification

This heater applies heat directly on the outer wall of the injector fuel passage as illustrated in Figure 78. The steady-state heating without fuel flowing is assumed for static heating analysis. This case illustrates how fast the fuel inside the fuel passage can be heated up to certain temperature by static heating.



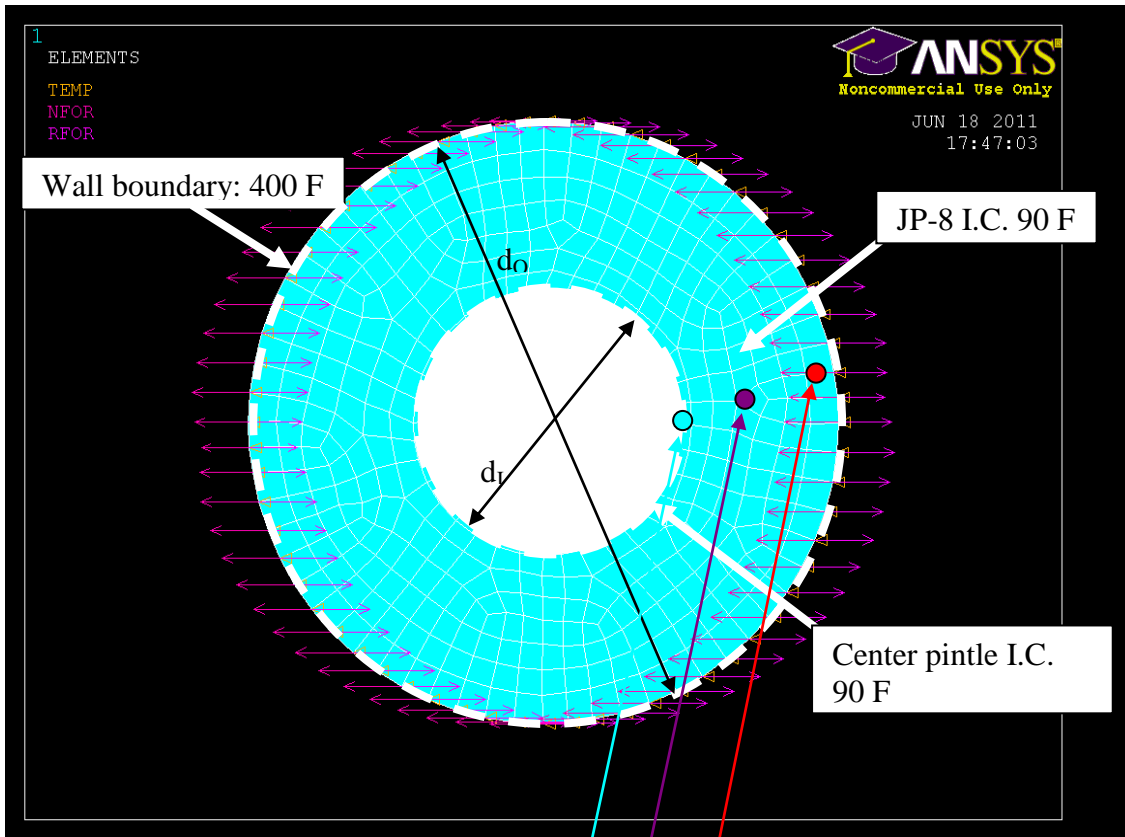
**Figure 78. 2D section view of pressure vessel using direct heating method**

Figure 79 shows a 2D heat transfer model includes JP-8 annulus and pintle in the central circle. The outside circle subjects to input heat flux and is maintained at 400 °F. Assuming 90 °F as the initial temperature for all nodes, the transient solution at different nodes is shown in Figure 80. The dimensions are as follows:

$$d_1 = .079''(0.002 \text{ m}), \text{ pintle diameter}$$

$$d_o = 0.179''(0.0045466 \text{ m}), \text{ fuel vessel diameter}$$

$$\text{Fuel vessel area} = \frac{\pi}{4}(d_o^2 - d_1^2) = 0.1308 \times 10^{-4} \text{ m}^2$$



**Figure 79. Direct heating method FEA model**

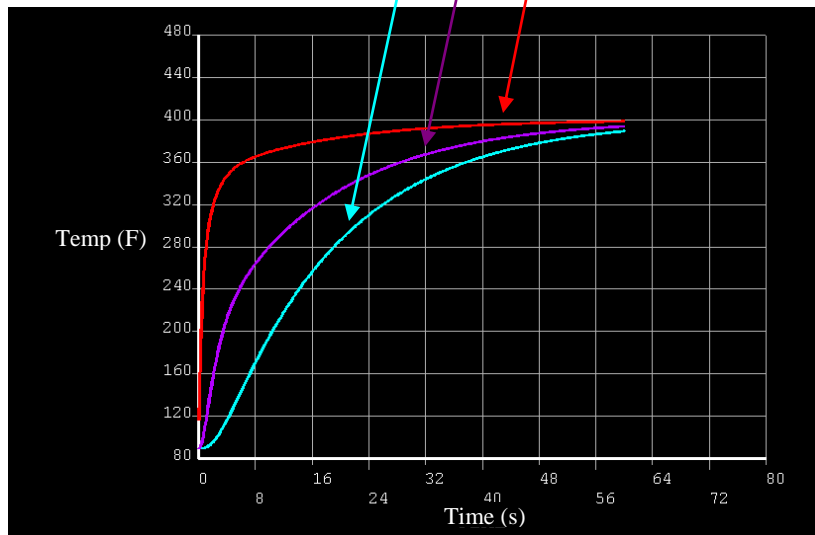


**Figure 80. Temperature transient profile at three different locations**

This heater configuration requires little modification of the existing fuel injector. However, as we can see, the results from three different nodes in the fuel vessel show very slow temperature rise due to JP-8's low thermal conductivity.

Learned from this first analysis, higher fuel temperature can be achieved with closer proximity to the heating wall. This gives the insight of achieving quick heating of JP-8: create thin fuel passages so that the heat does not have to go through long conduction path to heat the fuel that is far from the wall.

## 2. A Centralizer to Create Thin Circular Fuel Passage

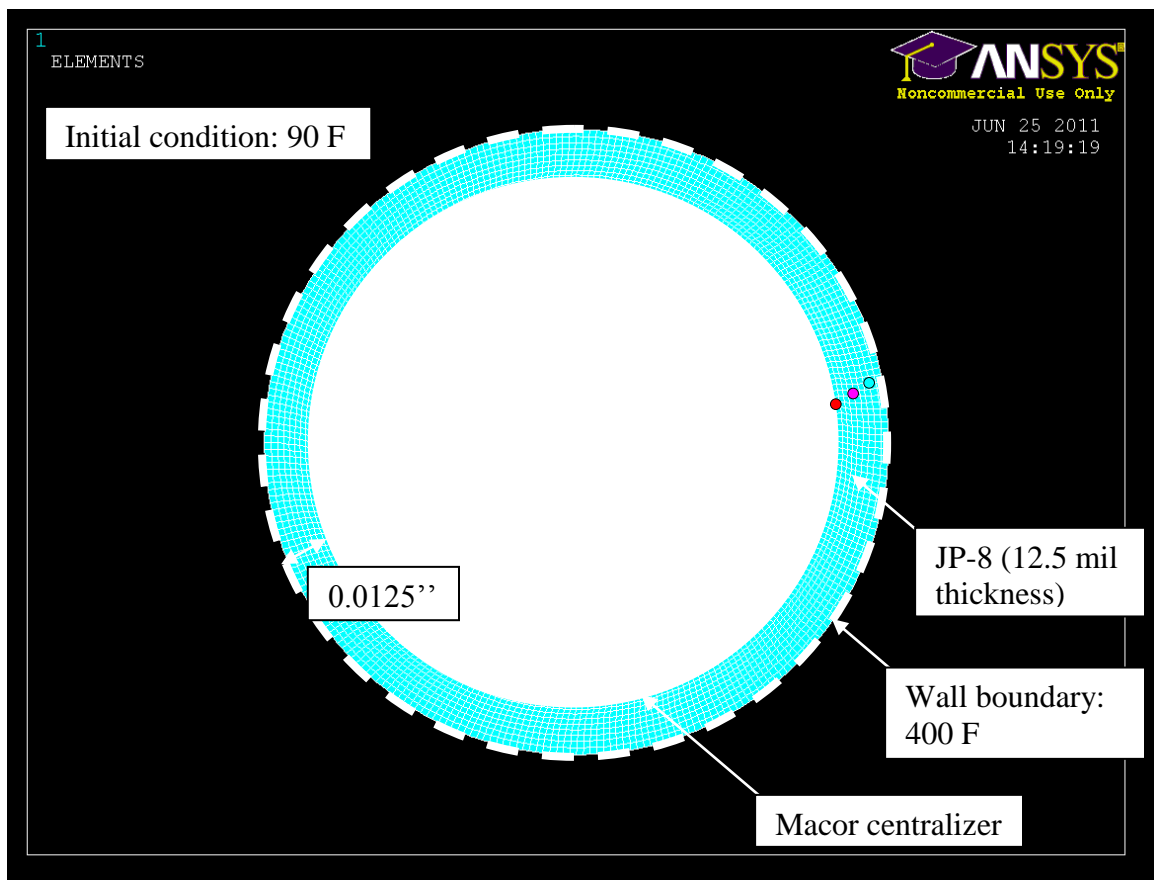


**Figure 81. FEA model for thin circular fuel passage**

Macor is a high-temp ceramic material. The ANSYS FEA model for this thin circular fuel passage is shown in Figure 81. The dimensions are listed in the following:

Fuel OD: .516''

Centralizer OD: .490''

Fuel thickness: 0.0128''

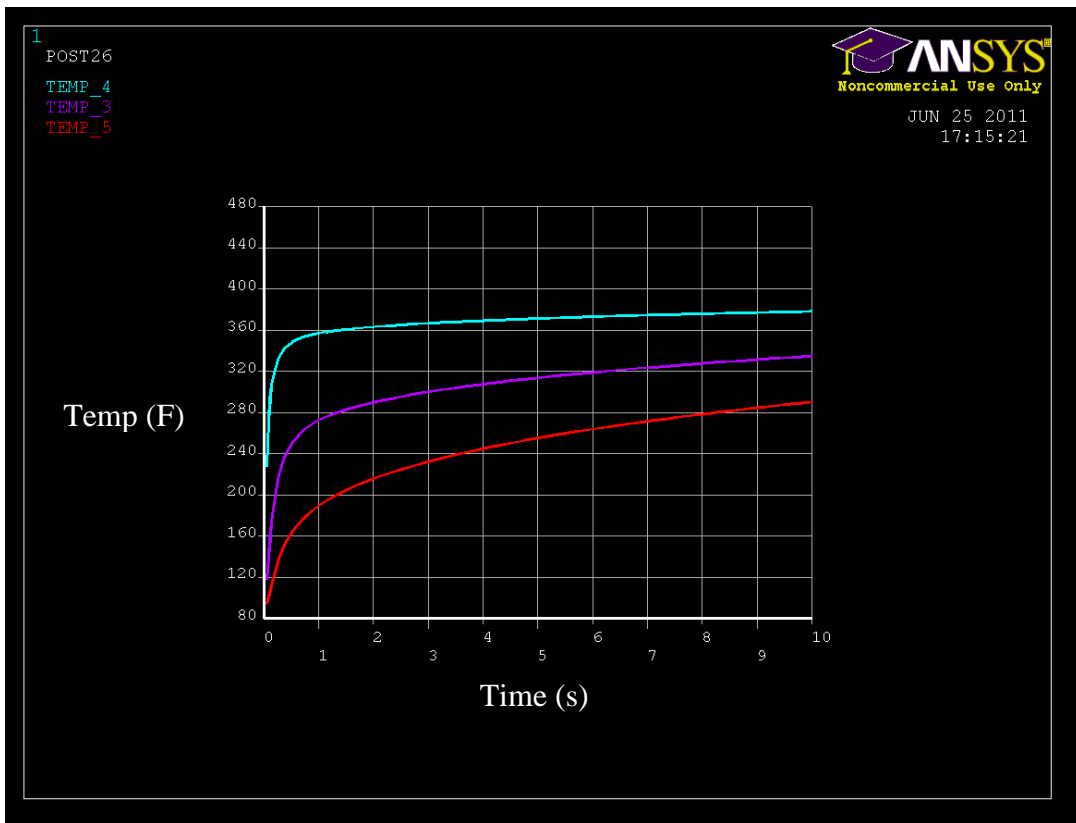


**Figure 82. Transient response of a thin circular fuel passage heating model**

The three colored curves in Figure 82 correspond to the three colored positions in Figure 81. The inner fuel temperature rise is still very slow due to the heat being conducted into the macor centralizer.

However, the temperature response at inner layers does improve quite a bit compared to the first case without centralizer, which means the thin fuel passage does help on bringing the response time down.

### 3. Use Insulated Inner Boundary

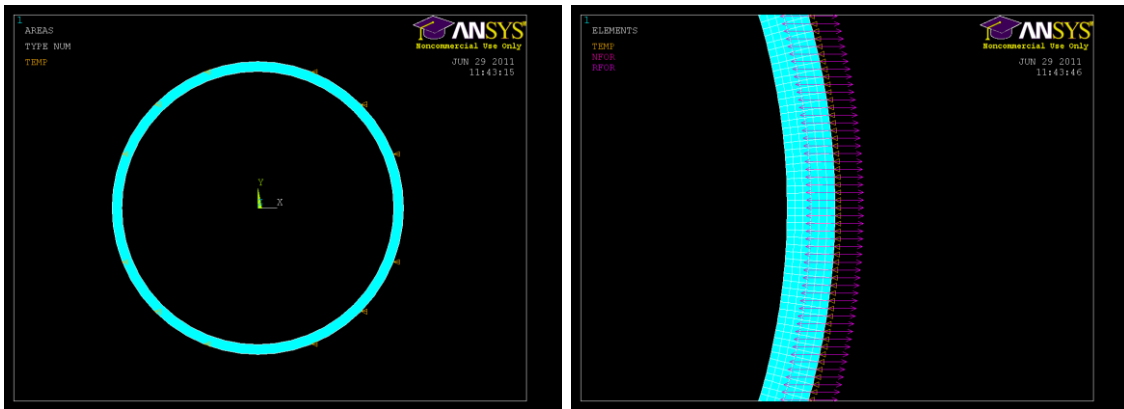


**Figure 83. Insulated inner boundary, thin circular fuel passage**

Figure 83 shows the insulated inner boundary, thin circular fuel passage model in ANSYS. Its transient heating result is shown in Figure 84, where the red line is the fuel temperature close to the outside wall, the blue line is the inner wall fuel temperature, and the purple line is the fuel temperature in the middle of the clearance.

As we can see, the response time gets much faster with insulated inner boundary. However, this thin circular fuel passage is much harder to create in reality. It not only needs to be perfectly centered (so the fuel passage would be even all around), but also requires high pressure capability. In addition, to place the centralizer inside the fuel injector without changing its designed dynamics is a challenging task if possible. This is

due to the pre-spring force being set with certain distance of compression, the opening and re-welding of the injector body would inevitably change this force. Therefore, in order to retain the dynamics of the original fuel injector, the fuel injector itself is not opened. Instead, an external fuel path is created to feed the heated fuel to the nozzle. This solution frees the physical dimension limitation of the heater somewhat. With this freedom, the next focus becomes designing a quick external heater of JP-8 and locating it as close to the nozzle as possible.

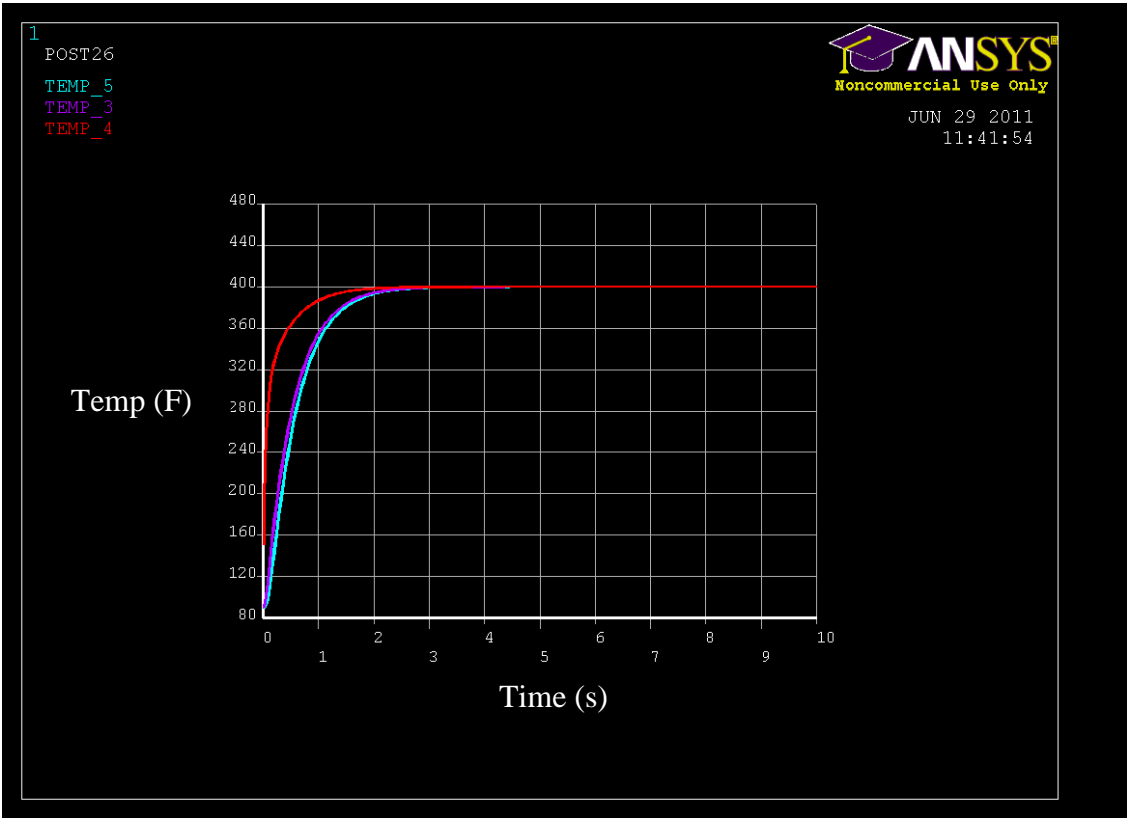


**Figure 84. Transient response of insulated inner boundary, thin circular fuel passage heater**

This thin circular passage requires the concentricity of two cylindrical parts, which would be a manufacturing challenge. Based on the thin fuel passage idea, there are several concepts which use tiny tubes to heat up JP-8.

#### 4. Bundle Tube Preheater

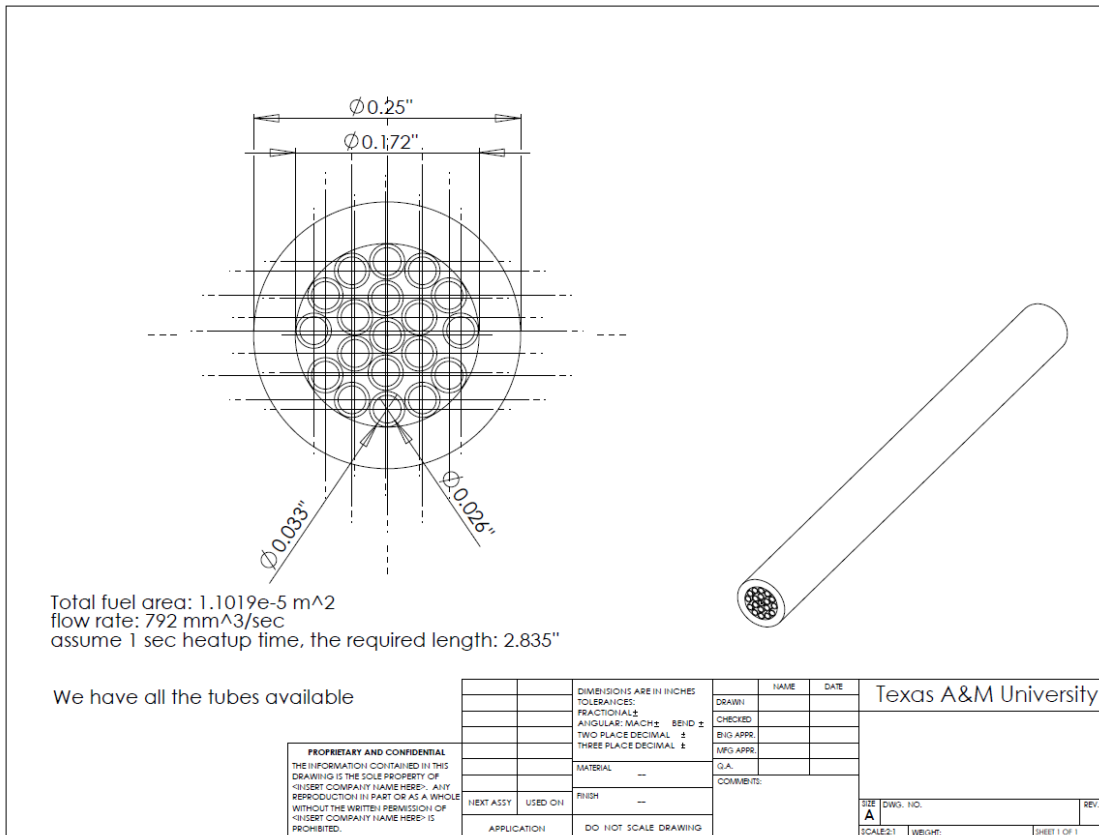


**Figure 85. Bundle tube heater concept**

While Figure 85 shows the grand view of the bundled tube, only one tube is modeled in the ANSYS. The model is shown in Figure 86 for the 26 mil ID tube.

Assume wall temperature for small tubes: 400 °F. The central fuel temperature transient response is shown in Figure 87.

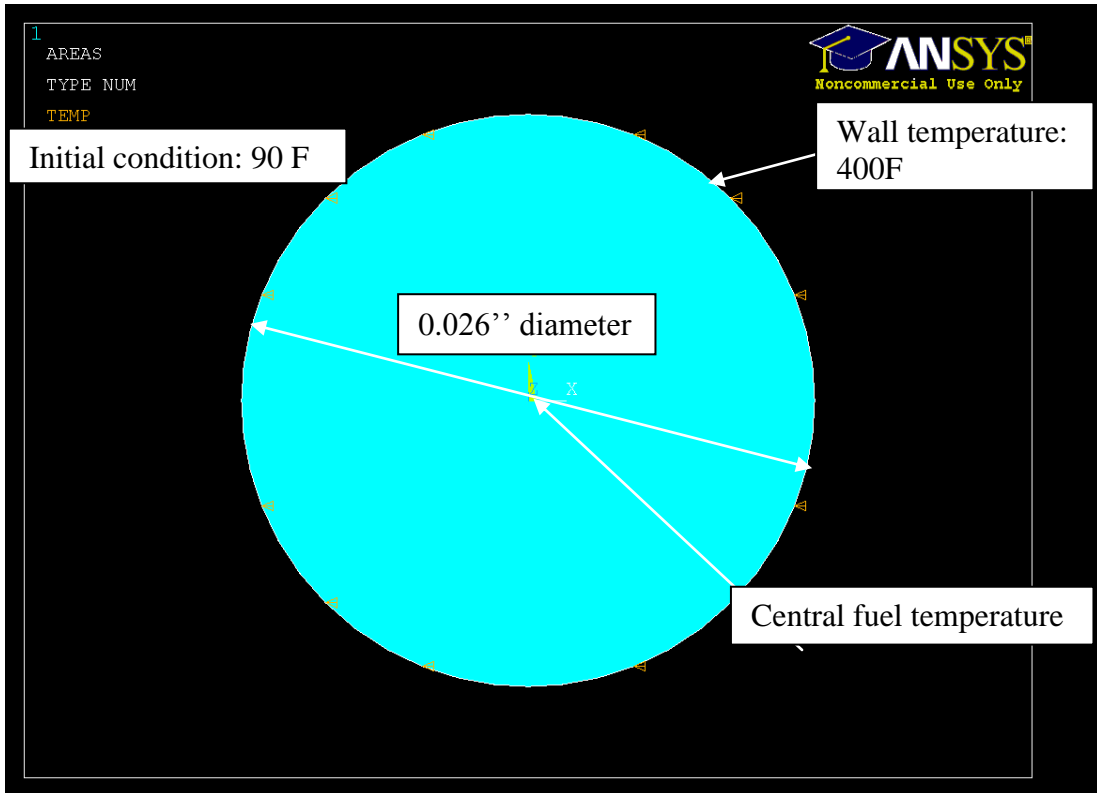


**Figure 86. FEM model of one tiny tube in a bundled tube heater**

From simulation results shown in Figure 87, the fuel can be heated up in less than 1 second. However, the problem with this design is that the length of the heater is quite long in order to meet volumetric flow rate requirement of fuel injector. 2.8'' length makes it difficult to maintain its mechanical strength at high temperature.



This thin tube idea has been tested by applying current to the tube with pulse power supply which can supply hundreds of amperes within micro-seconds ( $\mu\text{s}$ ). The concept takes advantage of the resistance of the tube. By applying voltage and high current through the tube, it certainly has gotten hot (the tube turned reddish color). However, the resultant outlet temperature of fluid is not high due to high flow rate and JP-8's low diffusivity. It was also quite a challenge to apply this much power to the thin tube which was pressurized under thousands of psi. The combined thermal and mechanical stress would make the system easy to break.

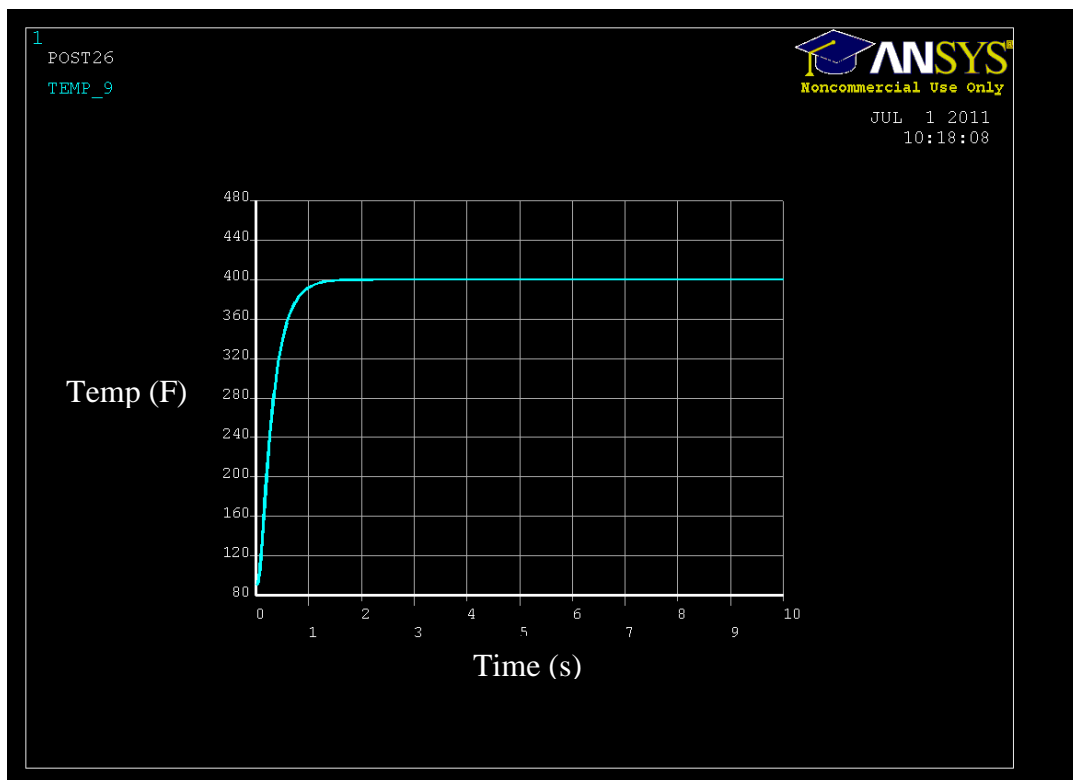


**Figure 87. Central fuel temperature transient with 26 mil tube and 400 F wall**

## 5. Small-hole Tube Preheater

Due to the concerns of bundled tube preheater, this following concept (as shown in Figure 88) was developed:

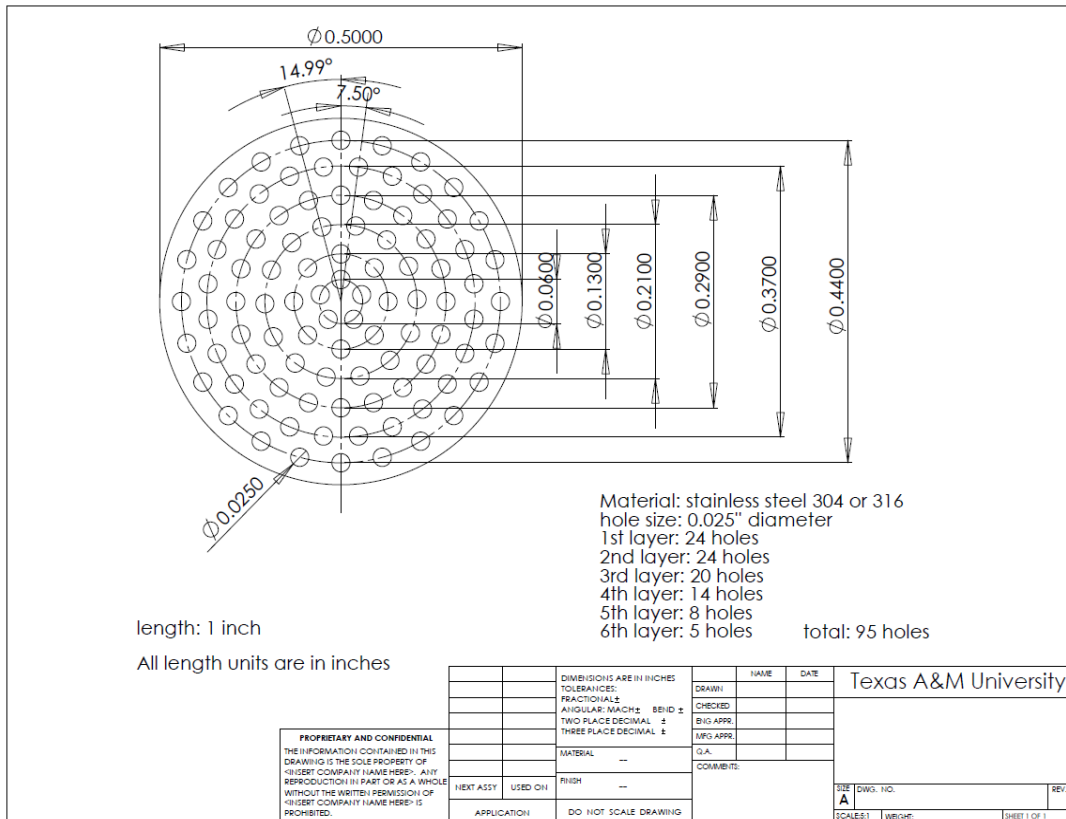


**Figure 88. Small-hole tube heater concept**

FEA solution from ANSYS is shown in Figure 89 assuming 500 F on the outer surface of the tube.

As shown in Figure 90, the response time of such heater is in the order of second. In addition, the cost of making such a heater is another prohibiting factor. The hole with 0.025" diameter requires plunge EDM.

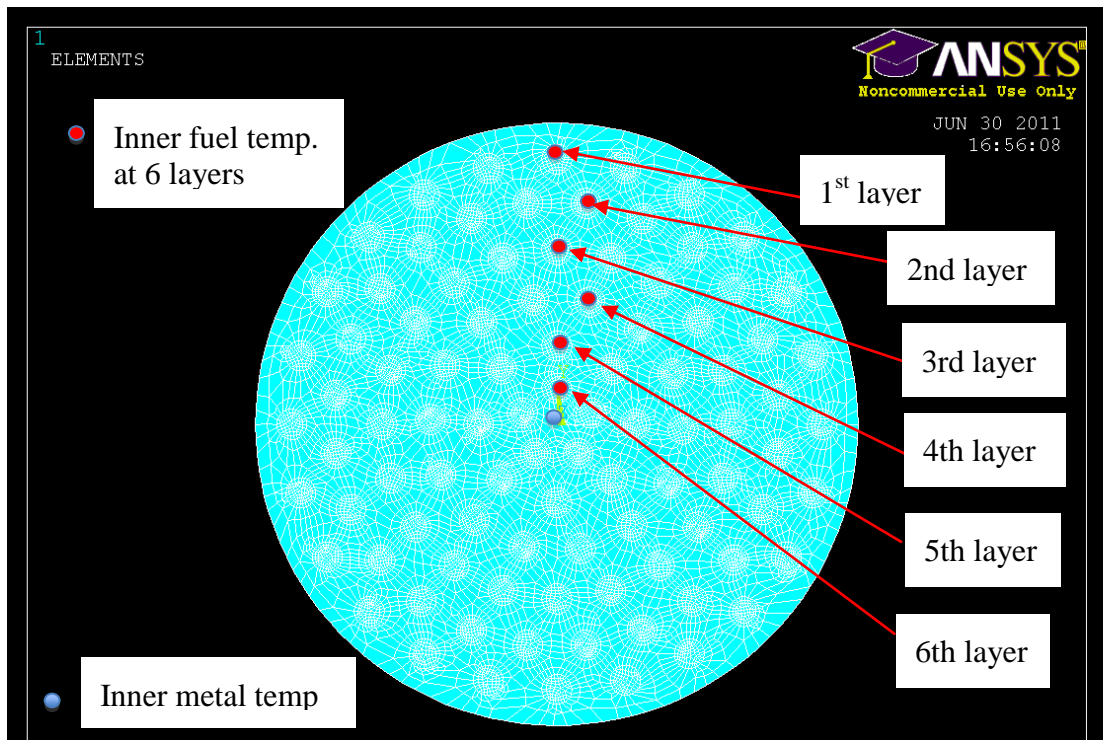


**Figure 89. Small-hole tube heater FEA model**

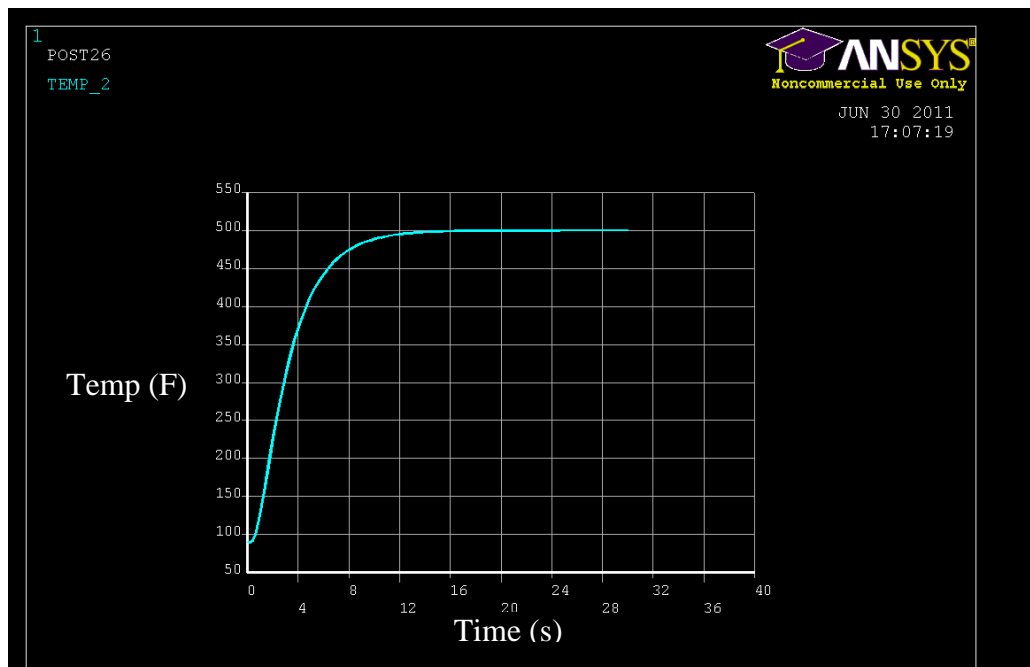


**Figure 90. Small-hole tube heater's inner metal temperature transient response**

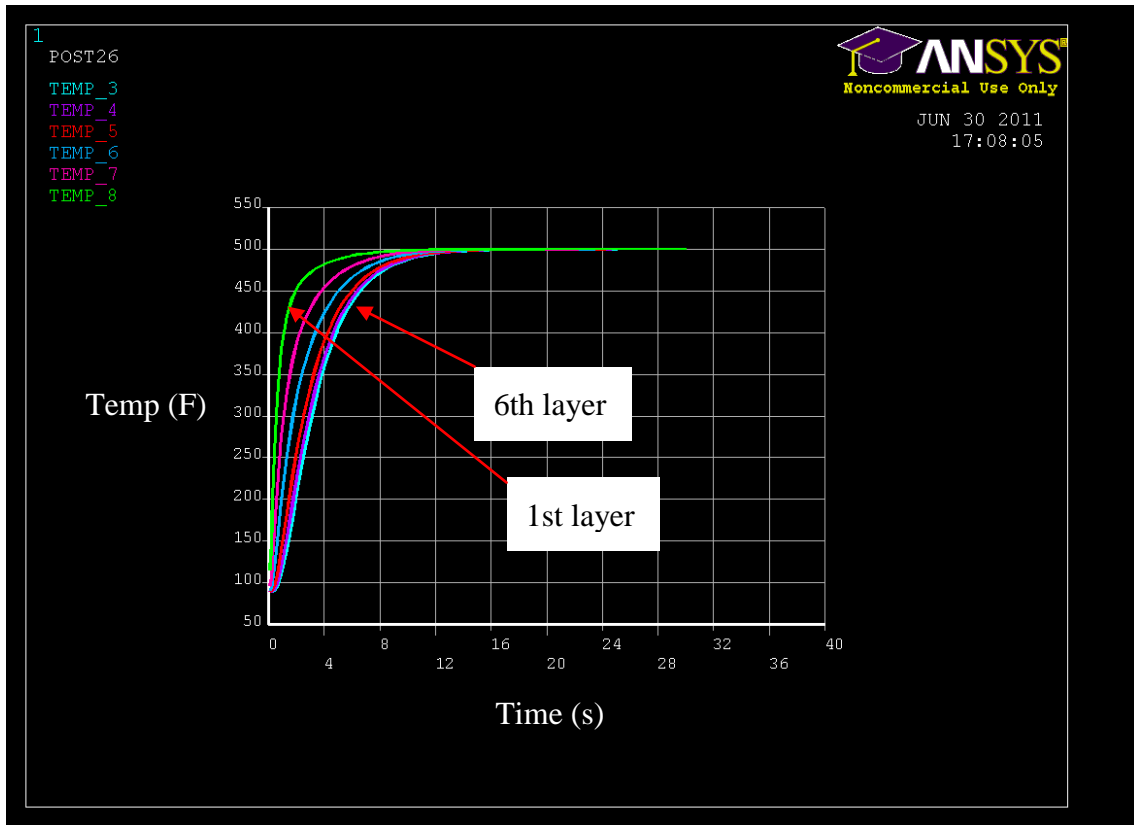


**Figure 91. Small-hole tube heater's fuel temperature transient response**

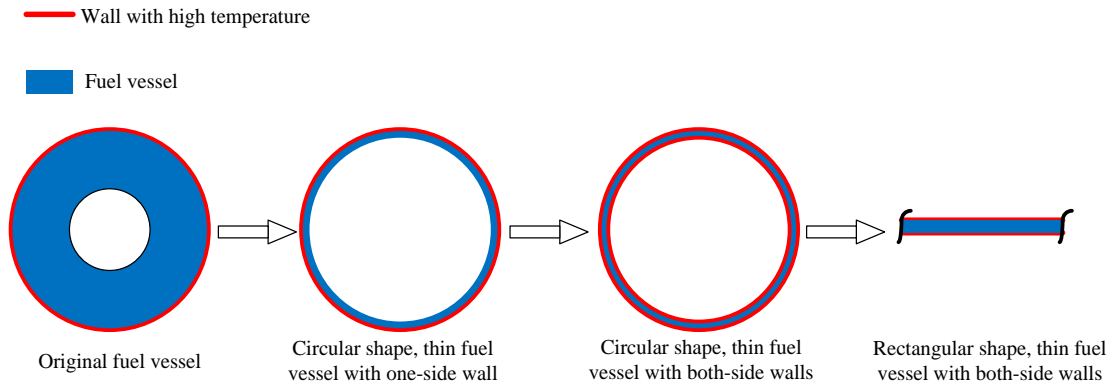
Figure 91 shows the inner fuel temperature transient response of six layers. The rise time varies from 2 to 6 s.

Up to now, we have learned (1) the thinner the passage, the quicker the response time will be; (2) manufacturing difficulty and its cost of making such thin circular passage should also be a concern. Exotic material or machining is not acceptable.

It is obvious that if both sides of the fuel vessel can be used to heat up the fuel, then the response time would be greatly improved. And if making the concentric circular

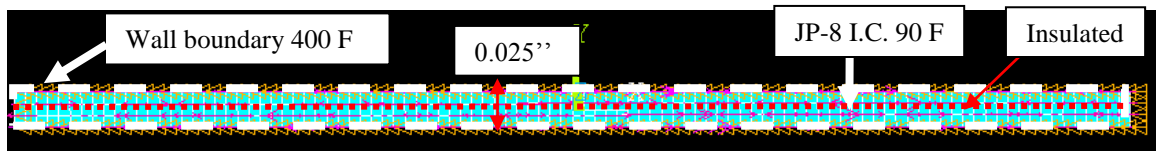
vessel is so difficult, why not consider making a rectangular fuel vessel, which provides larger contact area with fluid and can be created thin enough.

Figure 92 shows the evolution of heater ideas. It finally comes to the rectangular shape fuel vessel with both sides being heated.



**Figure 92. Evolution of heater ideas**

6. Rectangular Shape Fuel Vessel



**Figure 93. Rectangular shape fuel heating vessel**

As shown in Figure 93, only half of the rectangle is modeled due to the symmetry. The middle plane is insulated in this half model.

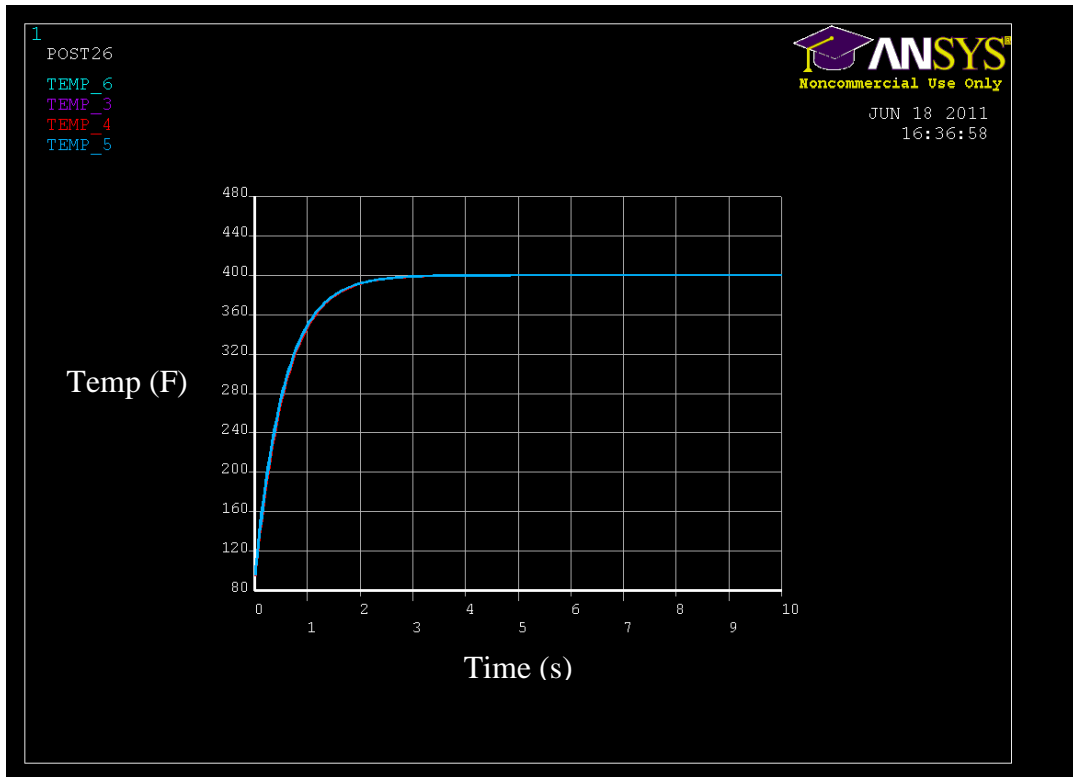


**Figure 94. Middle fuel temperature from a rectangular shape heater (shown in Figure 93)**

As shown in Figure 94, the rectangular shaped heater gives fastest temperature rise so far with 1 sec rise time. The flat channel preheater concept is shown in Figure 95. The complex lines in the bottom right corner are the wire heater wrapped around. Fuel vessel dimensions are: height: 0.025'', width: 1.5'', and length: 1.5''. Total volume inside the fuel vessel is:

$$V = a(\text{width}) \cdot b(\text{length}) \cdot h(\text{height}) = 0.0381m \cdot 0.0381m \cdot 0.000635m = 921 \times 10^{-9} m^3$$

With  $792 \times 10^{-9} \text{ m}^3 / \text{s}$  flow rate, the dwell time inside this flat channel heater is more than 1 sec, which means if wall temperature is maintained at 400 F, it could heat the JP-8 from 90 F to 360 F at the required flow rate.

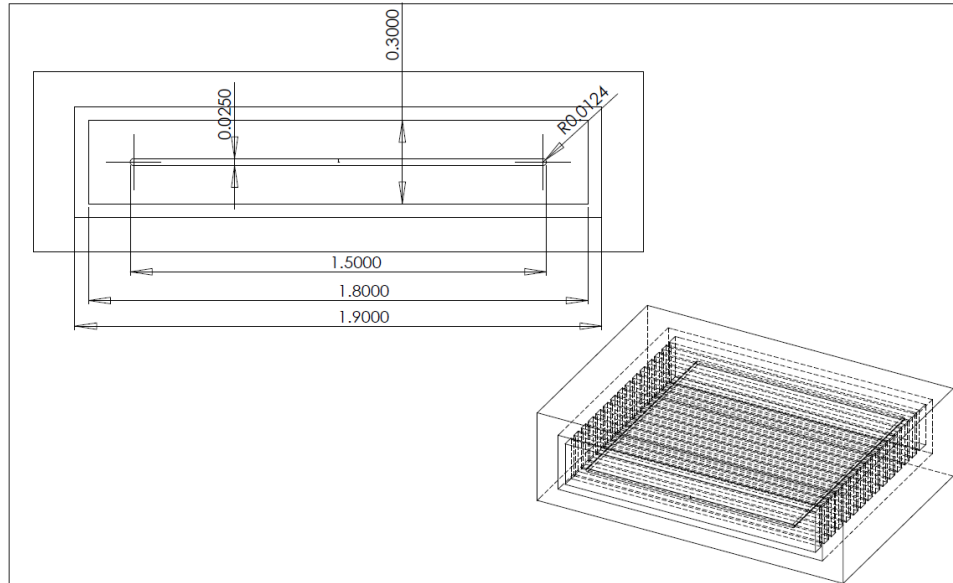


**Figure 95. Flat channel preheater**

The following shows analytical solutions to 1D heat transfer models.

### Analytical Solutions

From Analytical solution comparison between 1D flat model and 1D axisymmetric model as shown in Table 20, the axisymmetric model reaches higher temperature than its flat counterpart given the same radius or center-to-side distance. However, from fabrication point of view, it is easier to make rectangular slot than circular one. It is also more cost effective to make thinner rectangular slot compared with the same size circular one.

**Table 20. Analytical solution comparison between 1D flat model and 1D axisymmetric model**

	1D flat model	1D axisymmetric model
	<p>X = 0      X = L (L = 12.5 mil)</p>	<p>r = 0      r = R (R = 12.5 mil)</p>
D.E.	$\frac{\partial}{\partial x} \left( K \cdot \frac{\partial T}{\partial x} \right) = \rho \cdot C_p \frac{\partial T}{\partial t}$	$\frac{1}{r} \cdot \frac{\partial}{\partial r} \left( K \cdot r \frac{\partial T}{\partial r} \right) = \rho \cdot C_p \frac{\partial T}{\partial t}$
Non-dimensional D.E.	$\frac{\partial^2 \bar{T}}{\partial \bar{x}^2} = \frac{\partial \bar{T}}{\partial \bar{t}}$	$\frac{1}{r} \frac{\partial}{\partial r} \left( r \frac{\partial \bar{T}}{\partial r} \right) = \frac{\partial \bar{T}}{\partial \bar{t}}$
B.C.	$\left. \frac{\partial T}{\partial x} \right _{x=0} = 0, \quad T(x=L) = T_2 \text{ (400 F)}$	$\left. \frac{\partial T}{\partial r} \right _{r=0} = 0, \quad T(r=R) = T_2 \text{ (400 F)}$
Non-dimensional B.C.	$\left. \frac{\partial \bar{T}}{\partial \bar{x}} \right _{\bar{x}=0} = 0, \quad \bar{T}(\bar{x}=1) = 0$	$\left. \frac{\partial \bar{T}}{\partial \bar{r}} \right _{\bar{r}=0} = 0, \quad \bar{T}(\bar{r}=1) = 0$
I.C.	$T(x, t=0) = T_1 \text{ (90 F)}$	$T(r, t=0) = T_1 \text{ (90 F)}$
Non-dimensional I.C.	$\bar{T}(\bar{x}, \bar{t}=0) = 1$	$\bar{T}(\bar{r}, \bar{t}=0) = 1$
Close-form solution(non-dimensional)	$\bar{T}(\bar{x}, \bar{t}) = \sum_{n=1}^{\infty} \frac{4 \cdot (-1)^{n-1}}{(2n-1)\pi} \cdot e^{-\left(\frac{(2n-1)\pi}{2}\right)^2 \cdot \bar{t}} \cdot \cos\left(\frac{(2n-1)\pi}{2} \cdot \bar{x}\right)$	$\bar{T}(\bar{r}, \bar{t}) = 2 \sum_{n=1}^{\infty} \frac{J_0(\lambda_n \bar{r})}{\lambda_n J_1(\lambda_n)} \cdot e^{-\lambda_n^2 \bar{t}}$ where $J_0, J_1$ are 1 <sup>st</sup> kind of Bessel function n= 0, 1
Estimated temperature at 1 sec at x or r = 0 (real dimension)	Only use first 4 terms and convert it to real dimension: $T(x=0, t=1) = 349 \text{ F}$	Only use first 4 terms and convert it to real dimension: $T(r=0, t=1) = 396 \text{ F}$



## 7. Integrated Slot Heater with Thin Rectangular Fuel Passage (Proprietary Material)

Further development of the rectangular shaped heater requires the compactness and integratability with current fuel injector. This concept shown in Figure 96 uses thin rectangular fuel passage, while it can be easily integrated with existing fuel injector. In addition, the feature can be machined via standard wire EDM. Thus the cost is moderate.

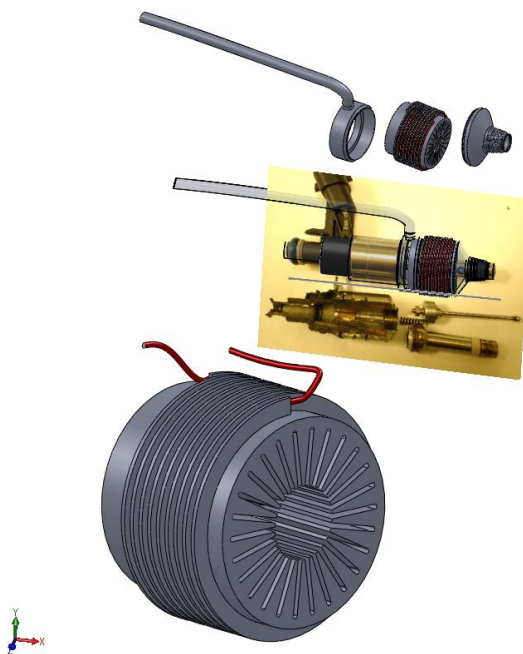


**Figure 96. Integrated slot heater with fuel injector concept (Proprietary. Texas A&M. Patent pending)**

This thin rectangular fuel passage is created by wire EDM. The .004'' wire would create .006'' slot. The manufacture process is straight-forward with this configuration as is shown in Figure 97 and Figure 98. The slot heater section is located below the injection solenoid. The whole assembly is shown in Figure 98. Fuel is

supplied from a side tube (not shown). The heated injector assembly uses laser weld to combine different stainless steel parts together.

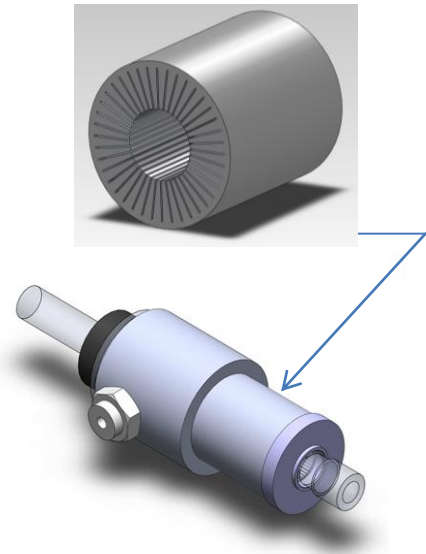


**Figure 97. Integrated slot heater with thin rectangular fuel passage (Proprietary. Texas A&M. Patent pending)**

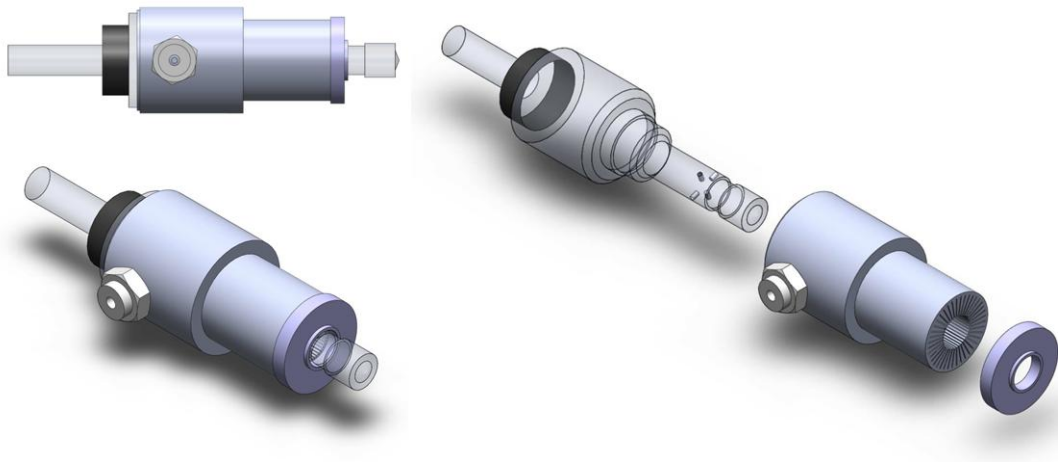


**Figure 98. Heated injector assembly (Proprietary. Texas A&M. Patent pending)**

In order to cool down fuel injector's solenoid coil, the heater section is extended towards the upper part of injector. The inlet fuel, therefore, first reaches solenoid section, in which there is no heat being applied. The fuel acts like coolant to cool down the injector coil. At the same time, the fuel is pre-heated by the injector body heat, which is a combined effect of solenoid heat and heat being transferred from heating section.

Fuel is warmed to certain temperature at the solenoid section before entering the heating section, where the fuel is divided to flow through very thin slots that is designed to heat up JP-8 quickly. After the heating section, the heated fuel flows into the original injector body through four holes drilled on the injector neck near nozzle and then be injected.

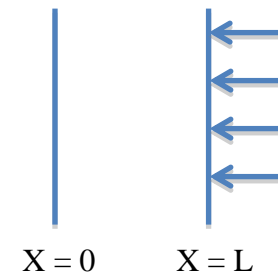
The design takes advantage of the flowing passage created externally to pre-heat the fuel by solenoid, which in turn cools down the solenoid coil, and an external thin passage heat exchanger for optimal heating efficiency.

The actual design of the cap after the heat exchanger is located away from nozzle. This is to prevent the damage of nozzle seal due to the overheating during the welding process.

The following discussion compares analytical and numerical solution of the static heating results with the thin slot heater assuming constant wall temperature. Table 21 is the closed form solution to the 1D flat heat transfer model. Results show very close match between analytical and numerical solutions. The static heating results show that the fuel can be heated up to 90% of its steady-state temperature within 0.1 second.

Analytical Solution

Table 21. Analytical solution to the slot heater

		1D flat model
	D.E.	$\frac{\partial}{\partial x} \left( K \cdot \frac{\partial T}{\partial x} \right) = \rho \cdot C_p \frac{\partial T}{\partial t}$
	Non-dimensional D.E.	$\frac{\partial^2 \bar{T}}{\partial \bar{x}^2} = \frac{\partial \bar{T}}{\partial \bar{t}}$
	B.C.	$\frac{\partial T}{\partial x} \Big _{x=0} = 0, \quad T(x=L) = T_2 \text{ (400 F)}$
	Non-dimensional B.C.	$\frac{\partial \bar{T}}{\partial \bar{x}} \Big _{\bar{x}=0} = 0, \quad \bar{T}(\bar{x}=1) = 0$
	I.C.	$T(x, t=0) = T_1 \text{ (90 F)}$
	Non-dimensional I.C.	$\bar{T}(\bar{x}, \bar{t}=0) = 1$
	Close-form solution (non-dimensional)	$\bar{T}(\bar{x}, \bar{t}) = \sum_{n=1}^{\infty} \frac{4 \cdot (-1)^{n-1}}{(2n-1)\pi} \cdot e^{-\left(\frac{(2n-1)\pi}{2}\right)^2 \bar{t}} \cdot \cos\left(\frac{(2n-1)\pi}{2} \cdot \bar{x}\right)$

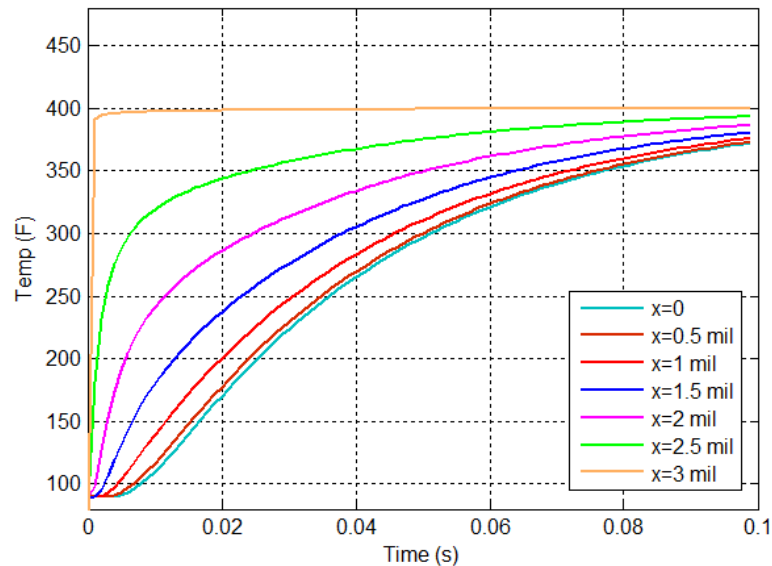
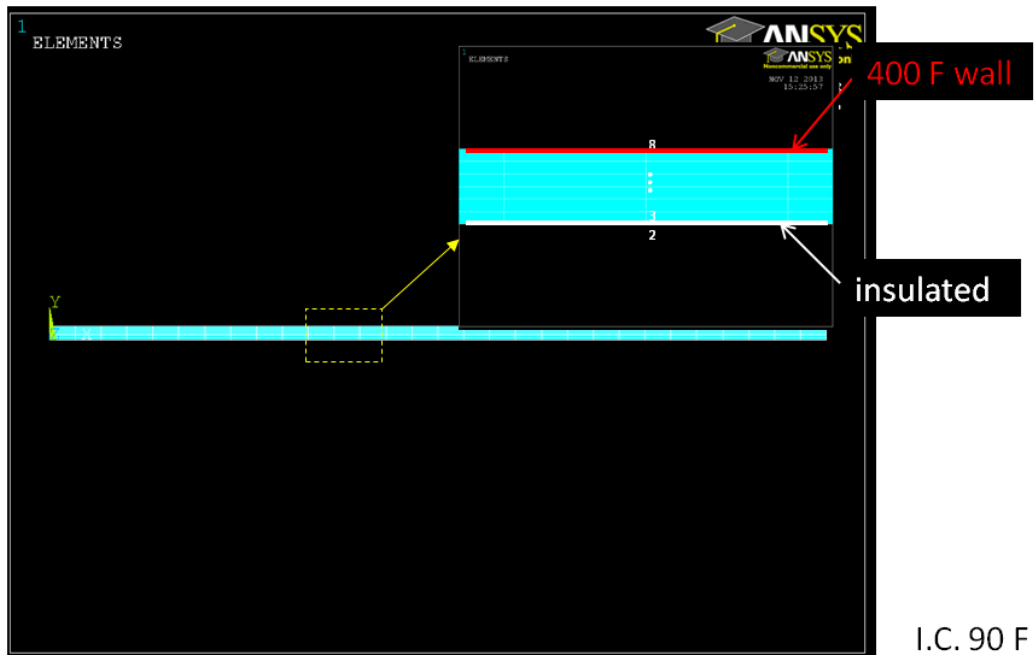
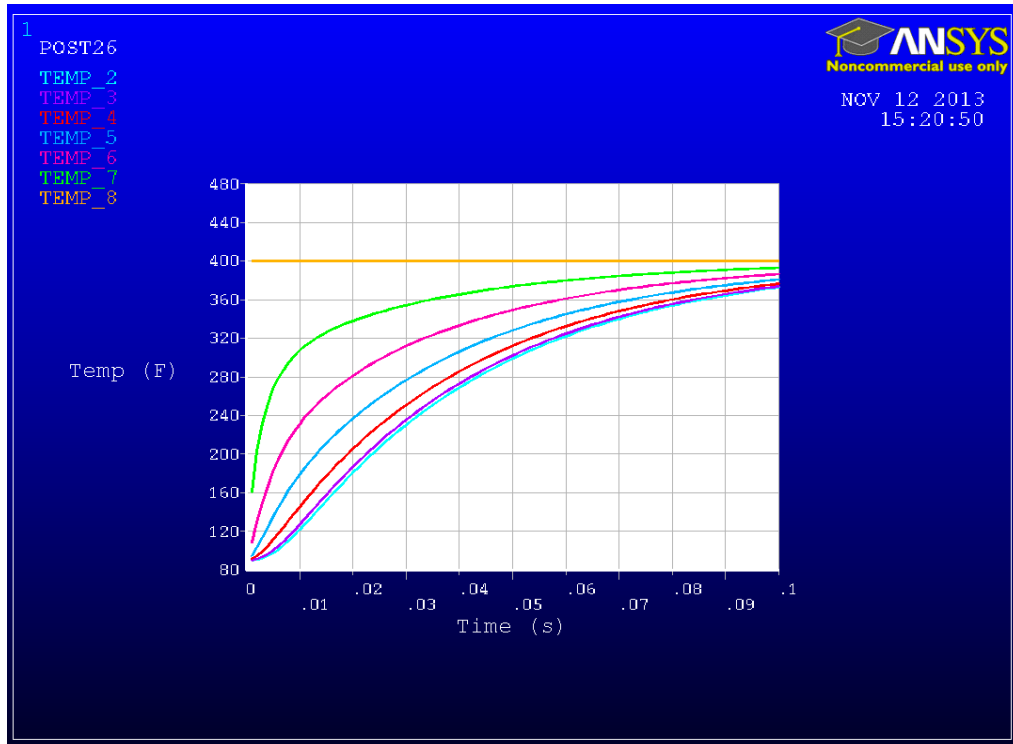


Figure 99. Analytical solution: fuel temp. vs. time at different locations (Thermal conductivity  $k = 0.1 \text{ W/m}^2 \text{ K}$  (at 300 F) Slot width .006'' (.003'' from center to side)  $x = 0$ : center;  $x = 3 \text{ mil}$ : wall )



**Figure 100. ANSYS heat transfer model for rectangular heater**

Figure 100 shows the ANSYS heat transfer model for rectangular heater and its boundary conditions. Results from analytical solution (Figure 99) and numerical solution (Figure 101) are identical. They all show the heater's ability to statically heat JP-8 from 90 F to above 300 F within less than 0.1 sec.



**Figure 101. Numerical solution with ANSYS: fuel temp. vs. time at different locations (Temp. 2 ~ temp. 8 correspond to nodes in the previous slide; Thermal conductivity  $k$  is dependent on temp. ( $k = 0.1 \text{ W/m}^2 \text{ K}$  at 300 F;  $k = 0.13 \text{ W/m}^2 \text{ K}$  at 90 F))**

### *Average Outlet Temperature Calculation*

This slot heater is proposed to solve low thermal diffusivity and coking problem during the heating of JP-8. As shown in previous pages, its thin rectangular slots facilitate the quick heating of JP-8. Since the heated JP-8 will only be in the heater for very short amount of time, the JP-8 particles will be flushed out from the heater before it can deposit onto the wall surface. The following calculation applies power balance method to estimate power requirement of the heater.

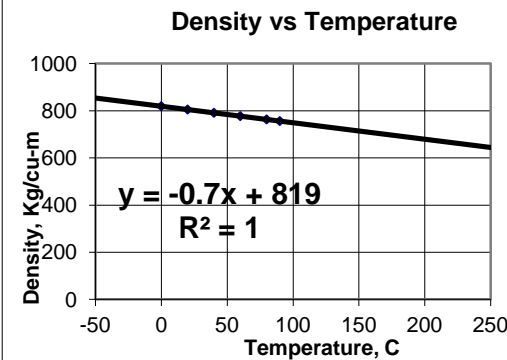
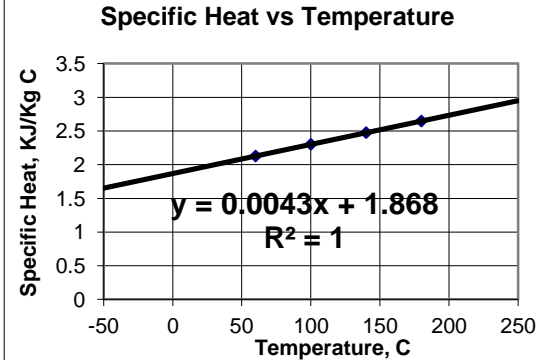
$$P_{in} = P_{out}$$

$$I^2 \cdot R \cdot \eta = \dot{m} \cdot C_p \cdot (T_{m,o} - T_{m,i})$$

Where, I is the current; R is the resistance;  $\eta$  is the efficiency;  $\dot{m}$  is the mass flow rate;  $C_p$  is the heat capacity;  $T_{m,o}$  is the mean outlet temperature;  $T_{m,i}$  is the mean inlet temperature.

Table 22 defines the fuel properties, i.e. density and specific heat capacity, as functions of temperature.

**Table 22. Temperature dependence of JP-8 density and specific heat [30]**

$\rho = a_1T + a_2$ $\rho = -0.6876T + 819.3$	$C_p = b_1T + b_2$ $C_p = 4.3T + 1868$
	
Where, $\rho$ - [Kg/m <sup>3</sup> ]; $C_p$ - [J/Kg-C]; T - [C]	

Substitute JP-8's temperature dependent properties into power balance equation, we get:

$$T_{m,o} = \frac{I^2 \cdot R \cdot \eta}{V(a_1T + a_2)(b_1T + b_2)} + T_{m,i}$$

Re-arrange the equation, it becomes a third order polynomial:

$$a_1 \cdot b_1 \cdot T_{m,o}^3 + (a_1 b_2 + a_2 b_1 - T_{m,i} \cdot a_1 \cdot b_1) \cdot T_{m,o}^2 + [a_2 b_2 - T_{m,i} \cdot (a_1 b_2 + a_2 b_1)] \cdot T_{m,o} - T_{m,i} \cdot a_2 \cdot b_2 - \frac{I^2 \cdot R \cdot \eta}{V} = 0$$

Solve  $T_{m,o}$  in the equation using ‘fsolve’ in MATLAB. The outlet temperature vs. volumetric flow rate at different power levels is shown in Figure 102. The volumetric flow rate can be calculated as volume per shot times injection frequency, which uses 100 Hz in the calculation. The total power input  $I^2 \cdot R$  is 245 watts (safe level for the heater).

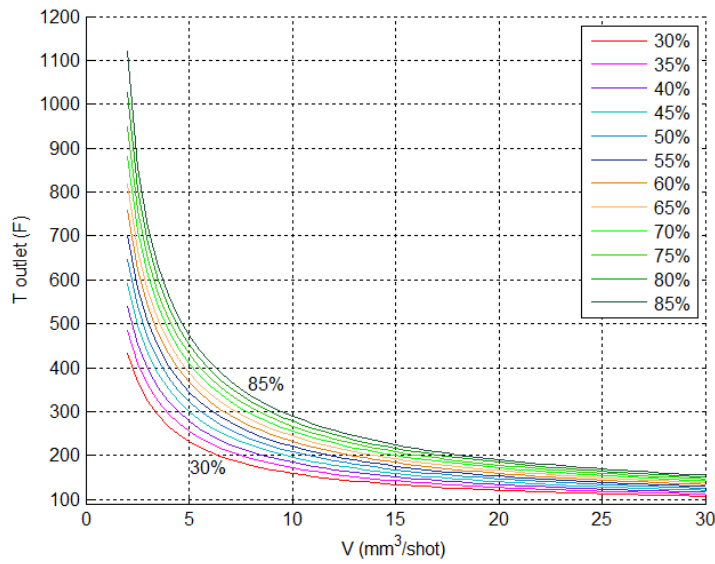


**Figure 102. Steady-state outlet fuel temperature vs. volumetric flow rate at different power levels (Proprietary. Texas A&M. Patent pending)**

To fully vaporize JP-8 at 100 Hz (>430 °F), the volume per shot needs to be reduced to 3.5 mm<sup>3</sup>/shot by assuming 50 % heater efficiency. However, to partially vaporize JP-8 at 100 Hz (>300 °F), the volume per shot increases to 6.5 mm<sup>3</sup>/shot. The



same temperature can be achieved at 10 mm<sup>3</sup>/shot if the total input power is increased to about 416 watts or heater efficiency increased to about 85%. With injection frequency at 50 Hz, 20 mm<sup>3</sup>/shot can be attained while maintaining the outlet fuel temperature at 300 F.

***Transient Heating Analysis (CFD) (Proprietary Material)***

***Basic Model***

A CFD model was built to simulate heat transfer with mass flow. The proposed physical model is shown in Figure 103. The geometry is not optimized at this point. The dimension is listed in Table 23.

***Table 23. Slot heater geometric parameters***

<b>Number of slots</b>	<b>Slot width</b>	<b>Outer radius</b>	<b>Inner radius</b>	<b>Slot radius</b>
40	0.006''	0.35''	0.15''	0.32''

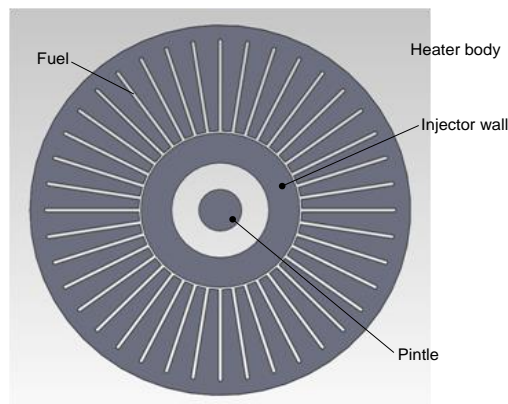


**Figure 103. Cross section view of the heat transfer model (Proprietary. Texas A&M. Patent pending)**

Since features in the full model are periodic, a pie shape model is used to represent the full model with periodic boundary condition on both sides of the wall as shown in Figure 104.

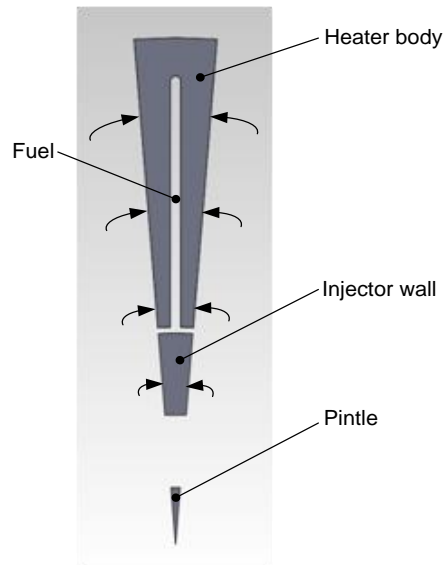


**Figure 104. Model with periodic boundaries (Proprietary. Texas A&M. Patent pending)**

After simplifying the periodic model by assuming constant heat flux from the upper surface and neglecting the heat transfer between the inner injector wall and pintle, the further simplified model is shown in Figure 105.

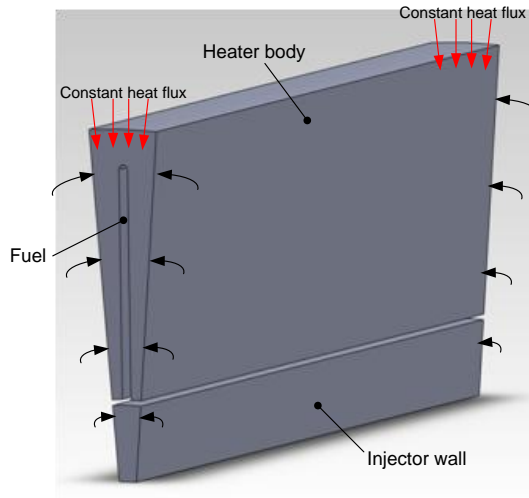


**Figure 105. Further simplified model for heat transfer analysis (Proprietary. Texas A&M. Patent pending)**

There are three equations defining this heat transfer with mass flow problem

[31]:

1. Continuity equation of fluid:

Assuming incompressibility of fuel, we have:  $\nabla \cdot u = 0$  ( $\frac{\partial u_x}{\partial x} + \frac{\partial u_y}{\partial y} + \frac{\partial u_z}{\partial z} = 0$  in

the Cartesian coordinate;  $\frac{\partial u_r}{\partial r} + \frac{1}{r}u_r + \frac{1}{r}\frac{\partial u_\theta}{\partial \theta} + \frac{\partial u_x}{\partial x} = 0$  in the cylindrical coordinate)

2. Momentum equation for a control volume (Navier-Stokes equation):

For an incompressible flow with constant kinematic viscosity  $\nu$ ,

$$\frac{Du}{Dt} = -\frac{1}{\rho}\nabla P + X_i + \nu\nabla^2 u$$

Where  $X_i$  is the external force terms (

$$\rho \left[ \frac{\partial u_x}{\partial t} + u_x \frac{\partial u_x}{\partial x} + u_y \frac{\partial u_x}{\partial y} + u_z \frac{\partial u_x}{\partial z} \right] = - \frac{\partial P}{\partial x} + X_i + \nu \left( \frac{\partial^2 u_x}{\partial x^2} + \frac{\partial^2 u_x}{\partial y^2} + \frac{\partial^2 u_x}{\partial z^2} \right) \text{ in partial}$$

differential form with  $u_x$  component in Cartesian coordinate)

Heat conduction in the metal and fluid, as well as the convection terms between metal and fluid utilizes the following energy equation.

3. Energy equation:

$$\frac{\partial}{\partial t} \left[ \rho \left( e + \frac{u^2}{2} \right) \right] + \frac{\partial}{\partial x_i} \left[ \rho \left( h + \frac{u^2}{2} \right) u_i \right] = \rho \dot{Q} - \frac{\partial q_i}{\partial x_i} + \rho X_i u_i + \frac{\partial}{\partial x_j} (\tau_{ij} u_i)$$

Where enthalpy  $h = e + \frac{P}{\rho}$  (the second term counts the work done by pressure

PdA)

$$\frac{\partial}{\partial t} \left[ \rho \left( e + \frac{u^2}{2} \right) \right] + \frac{\partial}{\partial x_i} \left[ \rho \left( h + \frac{u^2}{2} \right) u_i \right] = \underbrace{\rho \dot{Q}}_{\text{heat generation}} - \underbrace{\frac{\partial q_i}{\partial x_i}}_{\text{heat conduction}} + \underbrace{\rho X_i u_i}_{\text{work}} + \underbrace{\frac{\partial}{\partial x_j} (\tau_{ij} u_i)}_{\text{shear loss}}$$

$$\frac{D}{Dt} \left( e + \frac{u^2}{2} \right) = \dot{Q} + u_i X_i - \frac{1}{\rho} \frac{\partial}{\partial x_i} (P u_i) - \frac{1}{\rho} \frac{\partial q_i}{\partial x_i} + \frac{1}{\rho} \frac{\partial}{\partial x_j} (\tau_{ij} u_i)$$

$$\text{Or } \frac{D}{Dt} \left( h + \frac{u^2}{2} \right) = \dot{Q} + u_i X_i + \frac{1}{\rho} \frac{\partial P}{\partial t} - \frac{1}{\rho} \frac{\partial q_i}{\partial x_i} + \frac{1}{\rho} \frac{\partial}{\partial x_j} (\tau_{ij} u_i)$$

Assume no shear loss, it becomes:

$$\frac{D}{Dt} \left( h + \frac{u^2}{2} \right) = \dot{Q} + u_i X_i + \frac{1}{\rho} \frac{\partial P}{\partial t} - \underbrace{\frac{1}{\rho} \frac{\partial q_i}{\partial x_i}}_{\text{heat conduction}}$$

The last term in the energy equation is the heat conduction term in the fluid; if constant heat flux is enforced, stagnation enthalpy can be solved together with continuity and momentum equations.

Gibbs equation gives relationship between enthalpy and temperature:

$$dh = T \cdot ds + \frac{1}{\rho} \cdot \partial P$$

Splitting  $\frac{D}{Dt} \left( h + \frac{u^2}{2} \right) = \dot{Q} + u_i X_i + \frac{1}{\rho} \frac{\partial P}{\partial t} - \frac{1}{\rho} \frac{\partial q_i}{\partial x_i}$  into two and using Gibbs

heat conduction

equation:

$$T \frac{Ds}{Dt} = \dot{Q} - \frac{1}{\rho} \frac{\partial q_i}{\partial x_i} + \frac{1}{\rho} \tau_{ij} \frac{\partial u_i}{\partial x_j}$$

The entropy of a fluid particle can be changed by heat addition, either from heat sources or heat flux ( $q_i$ ), or by shear forces.

The internal energy  $e$  can be related to  $T$  by the following relationship if it is an ideal gas (constant specific heat):

$$e = c_v \cdot T, \text{ where } c_v \text{ is the specific heat at constant volume}$$

Now, for 3D incompressible flow (constant  $\rho$ ), we have 6 equations for 6 unknowns:  $u, v, w, P, e, T$ .

### Mesh Creation

All the domains (fluid and two solid domains) and all the surfaces need to be identified in ICEMCFD meshing software. Blocking strategy is used to construct hexahedron elements. There is a total of 65,917 ~ 380,000 hexahedral elements. Figure 106 shows the mesh.

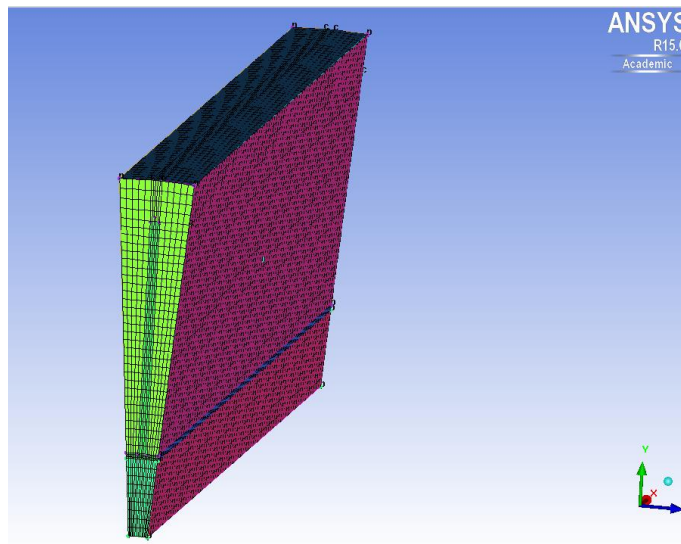


**Figure 106. Meshed domain in ICEMCFD**

### Grid Independence Study

Different mesh sizes have been used to check the grid independence. Figure 107 shows steady-state temperature with different element numbers. The higher element numbers represent finer mesh. However, finer mesh consumes more computational time. As can be seen from the graph, the outlet temperatures converge to final steady-state

temperature when element number increases beyond 160,000. Therefore, in the following study, the median mesh size 165,600 is used.

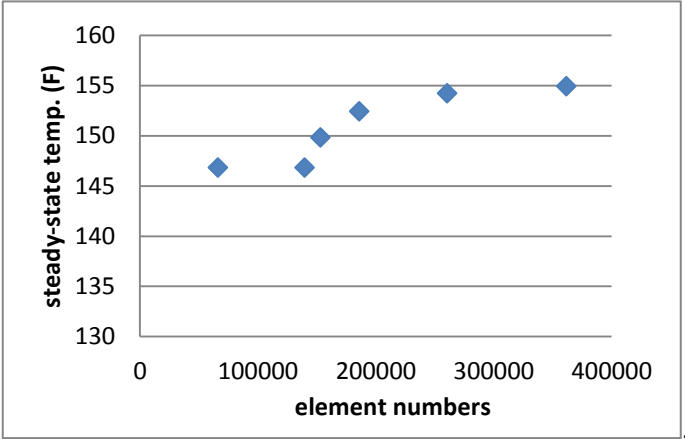


**Figure 107. Grid independence study**

Mesh Quality

Figure 108 shows two criteria of defining mesh quality. One is element angle. The other is determinant 2x2x2. For most CFD solvers, the mesh would be sufficient if it exceeds 0.1 for a determinant and 9 to 18 degrees for angle [32].

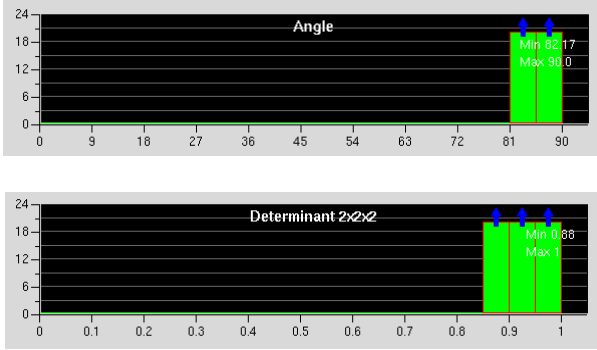


**Figure 108. Mesh quality: angle and determinant**

## CFX-Pre

Domain interface specification includes specifying fluid-solid interfacing surfaces, heat transfer method at the interface (conservative interface flux), as well as specifying different materials for different domains. Stainless steel 304 is specified constant properties, while JP-8 properties are treated as functions of temperature.

Table 25 and Table 26 show different material properties vs. temperature used in the simulation. Table 24 lists the initial and boundary conditions. Figure 109 illustrates the boundary conditions of the CFX model

***Table 24. Initial and boundary conditions for heat transfer with mass flow problem***

<b>Domain initialization (or initial condition):</b>	all temperatures are set to 90 F (305 K)
<b>Power input:</b>	245 watts, 50% efficiency, $Q = 245W \times 50\%$
<b>Heat flux to heater:</b>	$\dot{q} = \frac{Q}{A} = \frac{Q}{(\pi \cdot d) \cdot l} = 143914 [W / m^2]$
<b>Inlet fuel temperature:</b>	90 F
<b>Inlet fuel pressure:</b>	1,500 psi
<b>Outlet mass flow rate:</b>	0.8721 g/s (same as mass flow from test)

***Table 25. Stainless steel 304 properties vs. temperature***

<b>Density</b>	7,854 [kg/m <sup>3</sup> ]
<b>Specific heat capacity</b>	434 [J/kg-C]
<b>Thermal conductivity</b>	16.2 [W/m-C]



**Table 26. JP-8 (liquid form) properties vs. temperature**

<b>Density <math>\rho</math></b>	$\rho[\text{kg} / \text{m}^3] = -0.6876T[\text{C}] + 819.3$
<b>Specific heat capacity <math>C_p</math></b>	$C_p[\text{J} / \text{kg} - \text{C}] = 4.3T[\text{C}] + 1868$
<b>Kinematic viscosity <math>\nu</math></b>	$\nu[\text{m}^2 / \text{s}] = 0.009766.4 \cdot (T[\text{C}] + 80)^{-1.8339}$ Dynamic viscosity = $\frac{\text{kinematic viscosity}}{\text{density}}$
<b>Thermal conductivity <math>K</math></b>	$K[\text{W} / \text{m} - \text{C}] = 0.1283 - 0.0002T[\text{C}]$

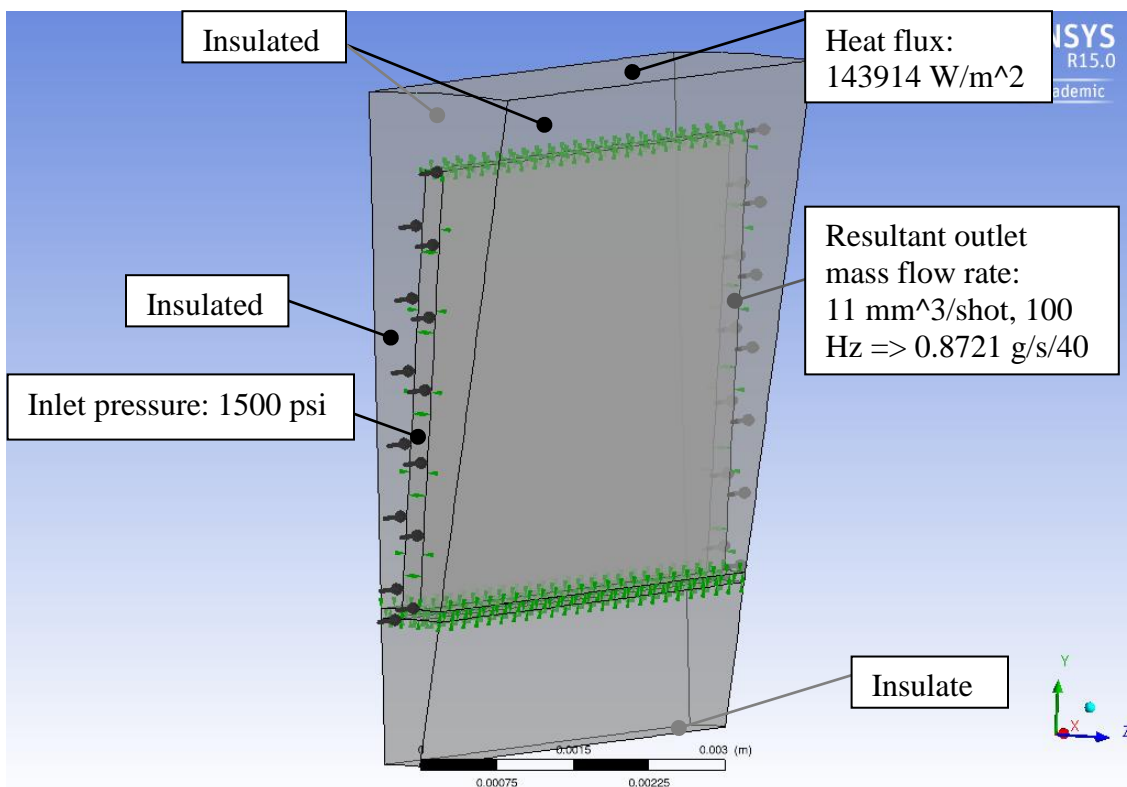


**Figure 109. Boundary conditions in the CFX-Pre**

## CFX-Solve

Transient simulation

Figure 110 shows the transient static heating (fuel not flowing) result. Total run time is 10 s with 0.1 s time step.

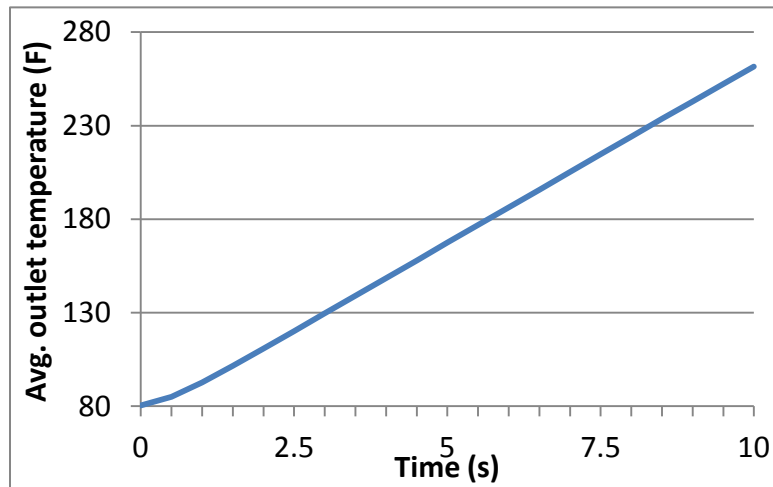


**Figure 110. Transient static heating: avg. outlet fuel temperature**

The purpose of simulating static heating is to find out the pre-heating time required to reach certain fuel temperature before the 1<sup>st</sup> injection. The pre-heating with fuel method is applied here. The result shows it takes 10 sec for outlet fuel temperature to rise from 80 °F to 260 °F once heat flux is applied to the heater initially at room temperature.

Due to the heat retention in the stainless steel body (act as both conduction path and heat sink), JP-8 temperature rise is much slower than static heating results.

However, once the body is heated up and the boundary temperature of previous static

heating cases is met, the fuel should be heated up to 90% of the boundary temperature in one tenth of a second if it is not flowing.

Figure 111 shows the transient heating results with fuel mass flow rate of 0.8721 g/s (correspond to 11 mm<sup>3</sup>/shot at 100 Hz with room temperature JP-8). Total run time is 10 s with 0.1 s time step. As shown in Figure 112, the outlet mean temperature is 363 K (194 °F) at the end of 10 sec.

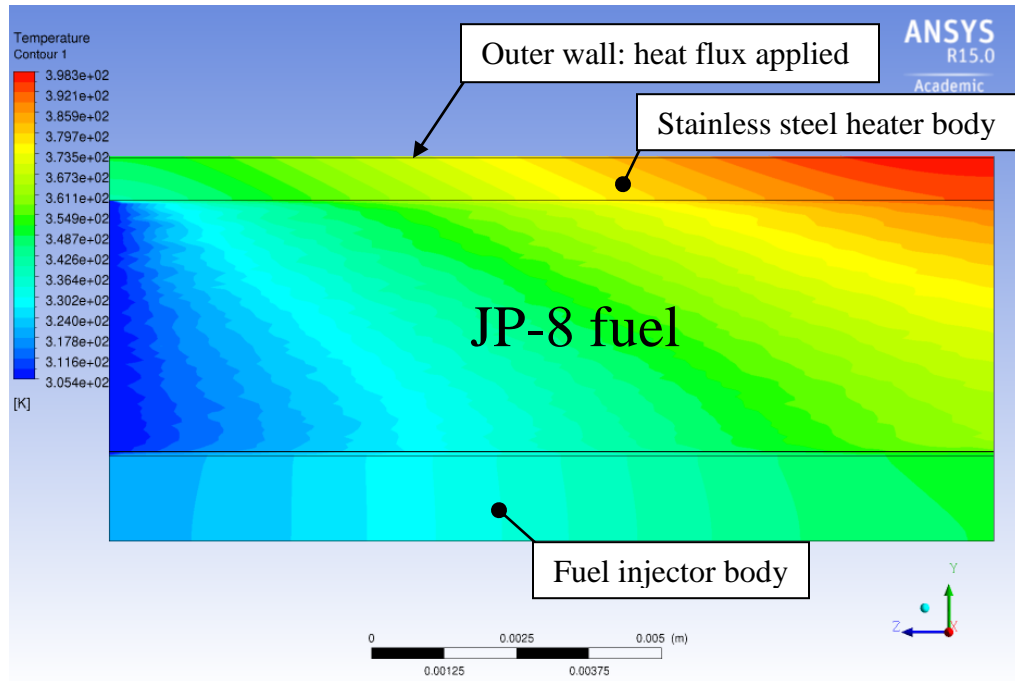


**Figure 111. Mid-plane temperature distribution at the end of 10 sec heating with fuel flow rate of 0.8721 g/s.**

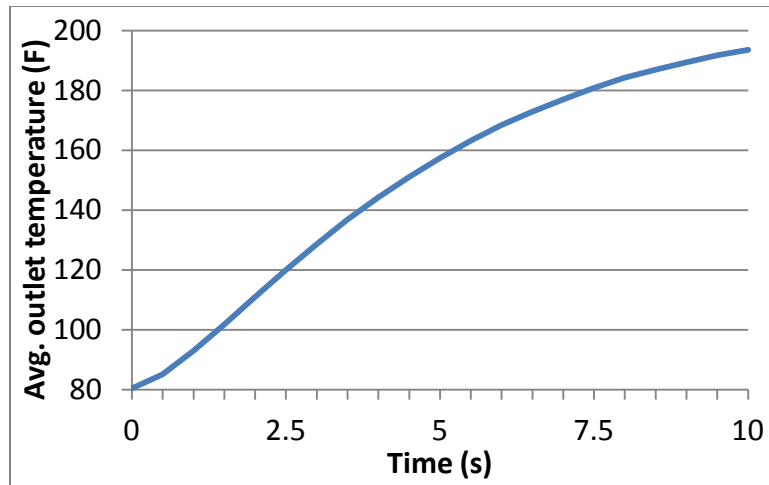


**Figure 112. Avg. fuel outlet temp. with 245 watts \* 50% (efficiency) heat flux, 0.8721 g/s mass flow rate**

Figure 113 compares effects of temperature dependent and independent JP-8 properties on transient response. As can be seen, if constant properties (at room temperature) were used, it would over-predict the outlet fuel temperature.

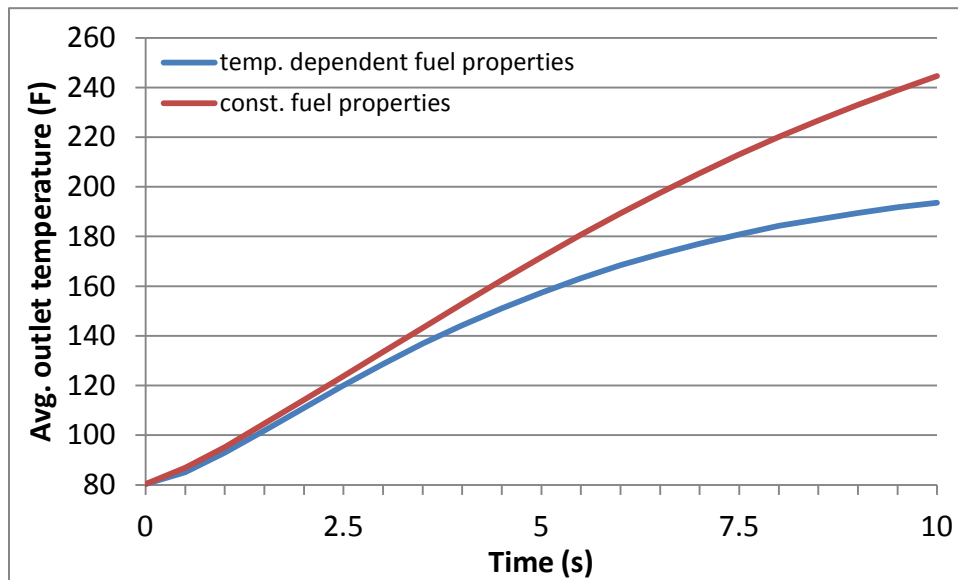


**Figure 113. Study of temperature dependent property effect**

At this point, we are able to determine the transient profile of outlet temperature rise given certain power input, flow rate and geometry of the heater. Among these three variables, the effects of power input and flow rate to outlet temperature can be easily predicted using power balance method: the higher the power input and the lower of the flow rate, the higher (or faster) outlet temperature rise can be expected.

However, the geometry effect to the outlet temperature rise is not so trivial. With the constraint of inner radius and length of the heater, there are 4 dimensions of the heater that can be designed differently: outer radius, slot radius, slot width, and number of slots. Figure 114 illustrates the design variables.

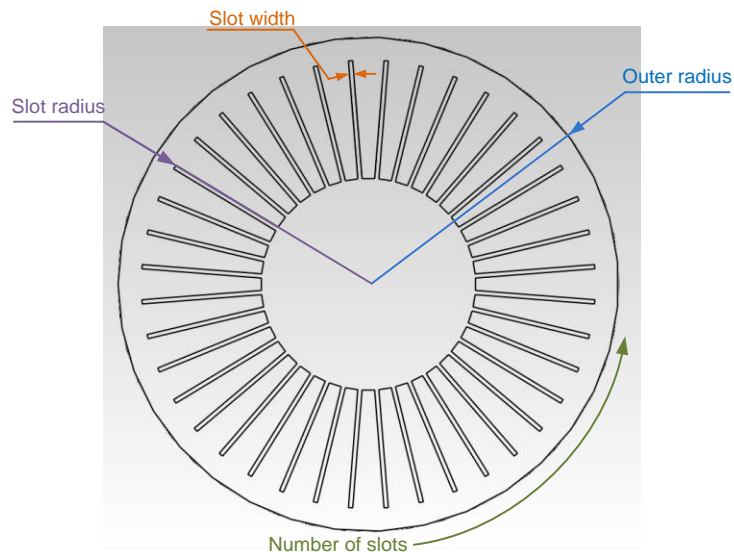


**Figure 114. Heater design variables (Proprietary. Texas A&M. Patent pending)**

The slot width needs to be as thin as possible from previous static heating analysis. However, the slot width is limited by the wire used in the wire electrical discharge machining (EDM). Due to the wear and tear, the ultra-thin wire needs to be replaced often, thus its cost is a lot higher than thicker wires. For reasonable machining price, .004'' wire is the thinnest wire that is available. The wire EDM usually has about .001'' burn on each side of the wire, thus giving a total of .006'' slot width.

The outer radius and slot radius can be integrated into one variable if the distance between the two can be determined. This distance needs to be minimized because the heat is conducting from outside to inside. The minimum distance means the shortest heat conducting path. On the other hand, if the wall thickness between the slot and outer radius is too thin, it might risk the failure of the part when the slot heater is pressurized up to 200 bar (20MPa).

The following finite element stress analysis using ANSYS shows the stress under 200 bar (20 MPa) at 0.03'' and 0.01'' wall thickness.

The stress is shown in Figure 115, where 3000 psi (20.7 MPa) is applied on the preference in contact with fuel with zero displacement on the outside circle. The resultant maximum von misses stress is .441e8 pa, while the yield strength of ss304 is 2.05e8 pa. This gives safety factor of 4.65. The zoomed-in view of the highest stress spot can be seen in Figure 116.

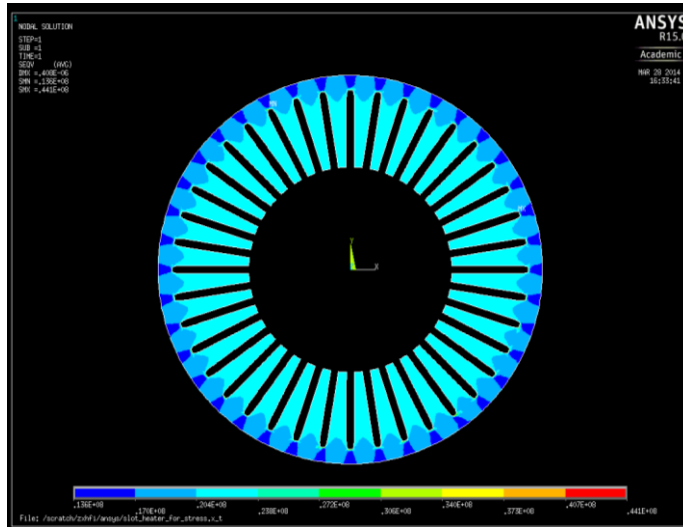


**Figure 115. Stress under 3000 psi with 0.03'' distance between the tip of the slot and outer wall**

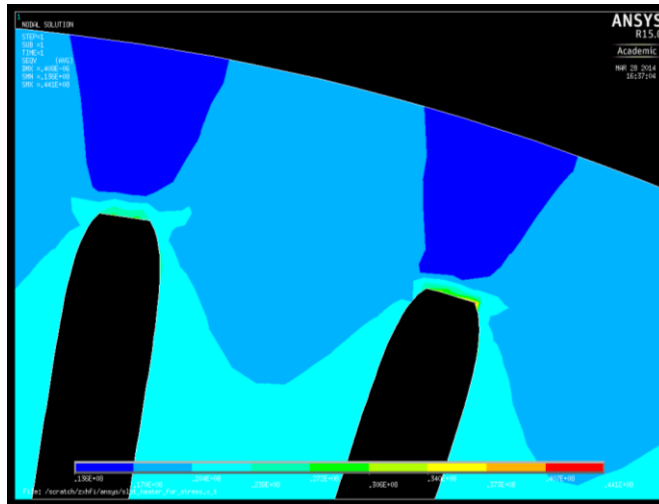


**Figure 116. Zoomed-in view of the stress under 3000 psi with 0.03'' wall thickness**

Figure 117 shows the case with 0.01'' wall thickness has maximum von mises stress .456e8 pa, which gives safety factor of 4.50.

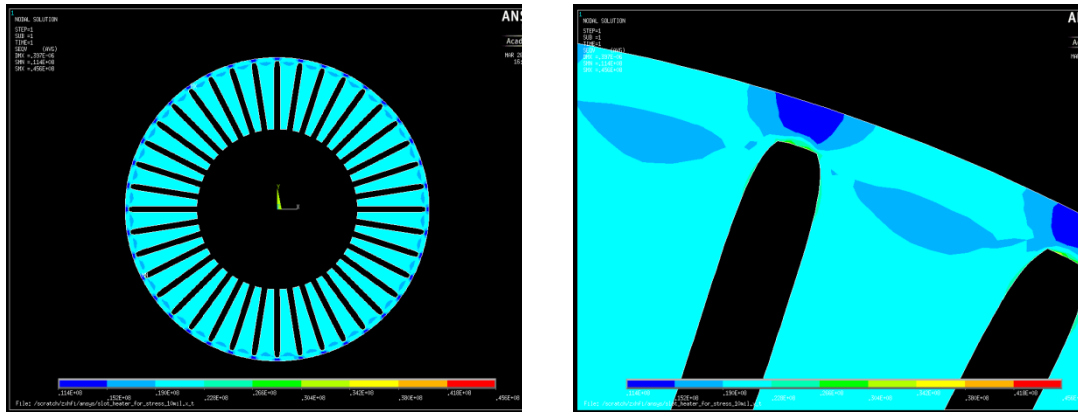


**Figure 117. Stress distribution of the .01'' wall thickness case under 3000 psi pressure**

Further reduction of wall thickness may risk the failure under high pressure and temperature. Even though the 0.01'' and 0.03'' wall thickness gave similar safety factor, 0.03'' is used in this study considering the combination of high pressure and temperature may risk the slot heater from premature failure.

### *Parametric Study*

#### Heater Geometry Optimization for Fast Transient Response (Average Outlet Fuel Temperature)

Intuition tells us that, the slower of the fluid (mass flow rate), the higher outlet temp it can achieve. The mass flow rate is dependent on the heater radius and number of slots given .006'' slot width and 0.6'' total length. The larger of the radius, the slower the mass flow rate will be. However, heat conduction path is longer with larger radius. Therefore, this is an optimization problem with two design parameters: radius of the heater (the minimum distance between the outer wall and furthest slot point is



determined to be 0.03’’ according to the stress analysis shown above) and number of slots.

A parametric Solidworks model was built with outer\_wall\_r and number\_of\_slots as two design parameters as illustrated in Table 28. The combination chart of different parameters is shown in Table 27. Only 1/n<sup>th</sup> of the heater is modeled due to its periodicity.

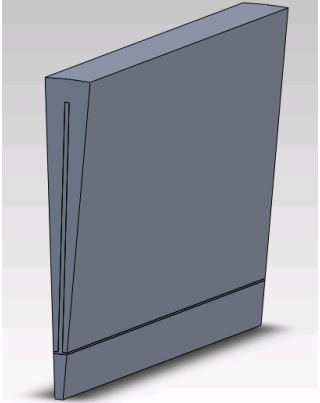
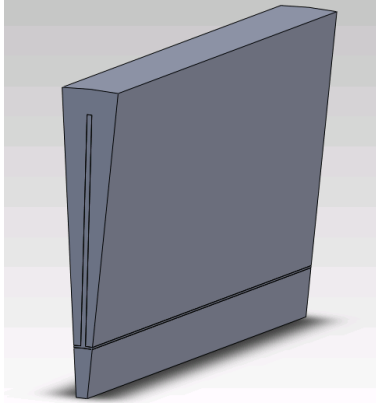
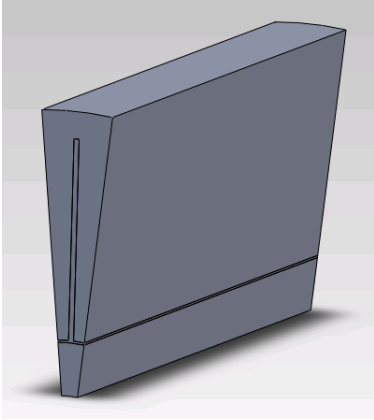
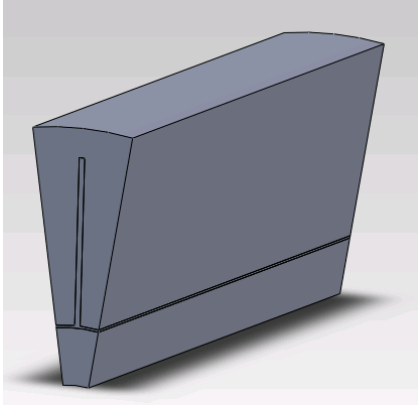
**Table 27. Design variables for heater optimization**

<b>No. of slots</b>	20	30	40	50
<b>Radius</b>				
0.35’’				
0.4’’				
0.45’’				
0.5’’				

Boundary Conditions

Constant heat flux on the outer wall: 200 watts (231294 W/m<sup>2</sup> on the outer surface of the heater), assume 100% efficiency; All initial conditions are set at 90 Ƴ. The same total mass flow rate (mass flow per channel times number of slots) was used. Notice these numbers are just for illustration purpose, the relative temperature rising speed under the same test condition is the key for this analysis. (Note: r – radius; n – number of slots)

**Table 28. Parametric models with different variables**

	
Radius: 0.5'' Number of slots: 50	Radius: 0.45'' Number of slots: 40
	
Radius: 0.4'' Number of slots: 30	Radius: 0.35'' Number of slots: 20

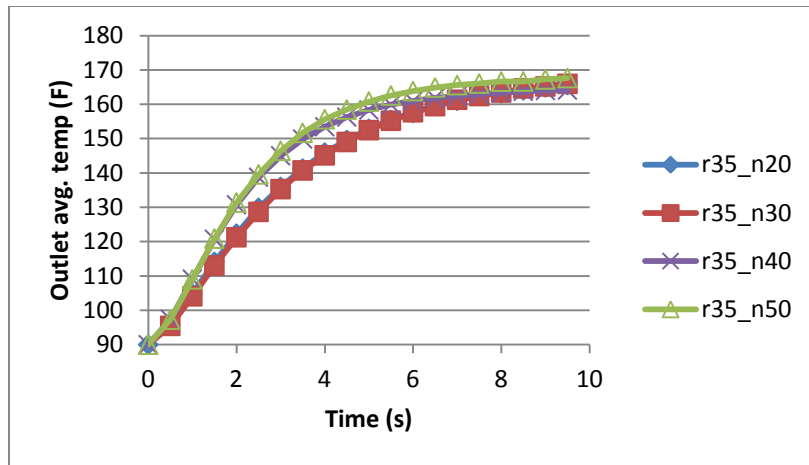


**Figure 118. Transient heating results of different No. of slots with 0.35'' radius**

As shown in Figure 118, the steady state temperatures with different number of slots are close. However, faster temperature rise is achieved with more number of slots. The difference between 40 and 50 slots are very little. From fabrication point of view, 40 slots is much easier to manufacture with wire EDM than 50 slot one. In addition, the remaining structure of 40 slots would be stronger than 50 slot one.

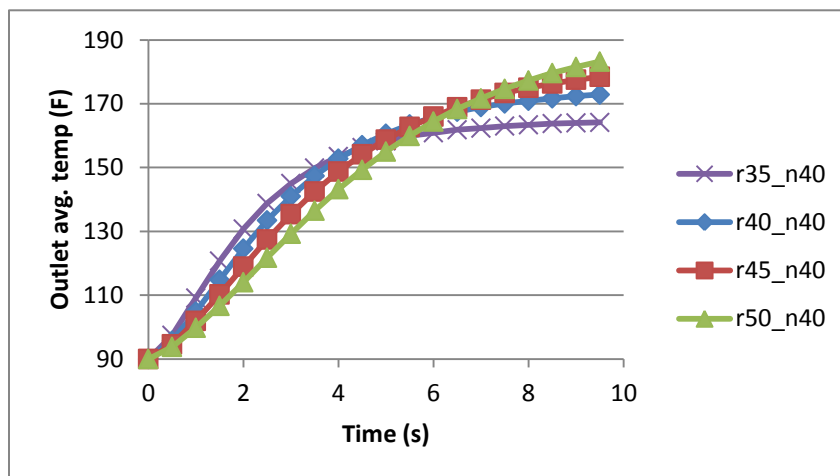


**Figure 119. Transient heating results of different radius with 40 slots**

If 40 slots were chosen, different radius would have very different outlet avg. temp profile as shown in Figure 119. Among the radii chosen, 0.35'' radius has fastest transient response. The reason why larger radius heater has higher steady-state temperature is because of its smaller thermal mass.

The cases with 50 slots, while radius varying from 0.35'' to 0.5'', have similar transient profiles as shown in Figure 120.

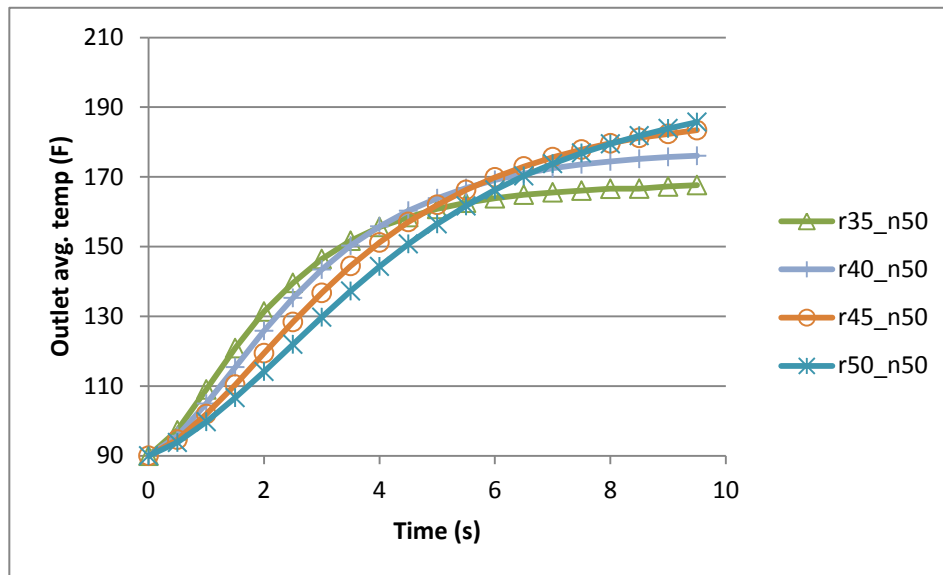


**Figure 120. Transient heating results of different radius with 50 slots**

### Preliminary Conclusion

Radius of 0.35'' (or even smaller) with 40 slots (or higher) results in faster transient response. The transient of the outlet fuel temperature is an indirect result from heating stainless steel heater. After the heater body temperature has risen to certain level, the model boundary conditions can be changed to constant temperature, which is the

case for static heating simulation. From that point on, the slower of the flow, the quicker it gets heated up.

Our heater has 0.35'' radius and 40 slots.

### **Fabrication**

There are 8 steps involved in fabricating flash vapor direct fuel injector.

1. Wire EDM the slug part of the heater
2. Machine the cap
3. Machine the tube fitting
4. Clean all the parts using ultrasound cleaner
5. Modify the original fuel injector
  - 5.1 Take off the ring
  - 5.2 Remove plastic mold at welding spot
  - 5.3 Drill four holes while pressurized with shop air pressure
6. Ship to be laser welded
7. Test laser welded injector at 3000 psi; Make sure there is no leakage

Figure 121 compares the original and modified heated fuel injector after laser-welding.



**Figure 121. Direct fuel injector before (left) and after (right) modified (Proprietary. Texas A&M. Patent pending)**

## 8. Make heater

8.1 Coat the body with high-temp insulation and attach a thermocouple on the heated section

8.2 Wind the 1<sup>st</sup> layer of nichrome wire heating element (about 20 turns) on the heated section. Gage 26 nichrome wire is chosen

8.3 Coat the 1<sup>st</sup> layer with high-temp insulation

8.4 Wind the 2<sup>nd</sup> layer. The total resistance of the heater is 20 ohm.

8.5 Coat the 2<sup>nd</sup> layer with high-temp insulation

8.6 Connect heating element with electric cable; attach the 2<sup>nd</sup> thermocouple

8.7 Mold the outer layer ceramic for thermal insulation

8.8 Unmold to complete.

The final heated fuel injector assembly is shown in Figure 122.



**Figure 122. Heated fuel injector assembly (Proprietary. Texas A&M. Patent pending)**

### **High Temperature Test Results**

The purpose of this section is to demonstrate the effectiveness of the heater and explore its temperature potential as well as its limitations. The test data will be correlated with analytical results to determine heater efficiency. The measured temperature should demonstrate partial vaporization of the injected JP-8 at elevated temperatures.

Because high temperature fuel was involved, safety was utmost concern when building the test rig. There are several safety features that are worth mentioning.

1. The injector fixture together with injection box was made of 0.5” thick steel plates. Different components and feedthrus for wires on the injection box were sealed. An o’ring was used to seal the injector as shown in Figure 124.

2. Nitrogen gas was continuously purging the injection box. CO<sub>2</sub> was continuously purging the cabinet, where injector fixture, condenser, and fuel bucket were located.

3. Two oxygen sensors were mounted on the test rig as shown in Figure 123. One was mounted on the injection box to continuously detect oxygen level inside the injection box. The other was mounted on the cabin to continuously detect oxygen level inside the cabinet, but outside the injection box.

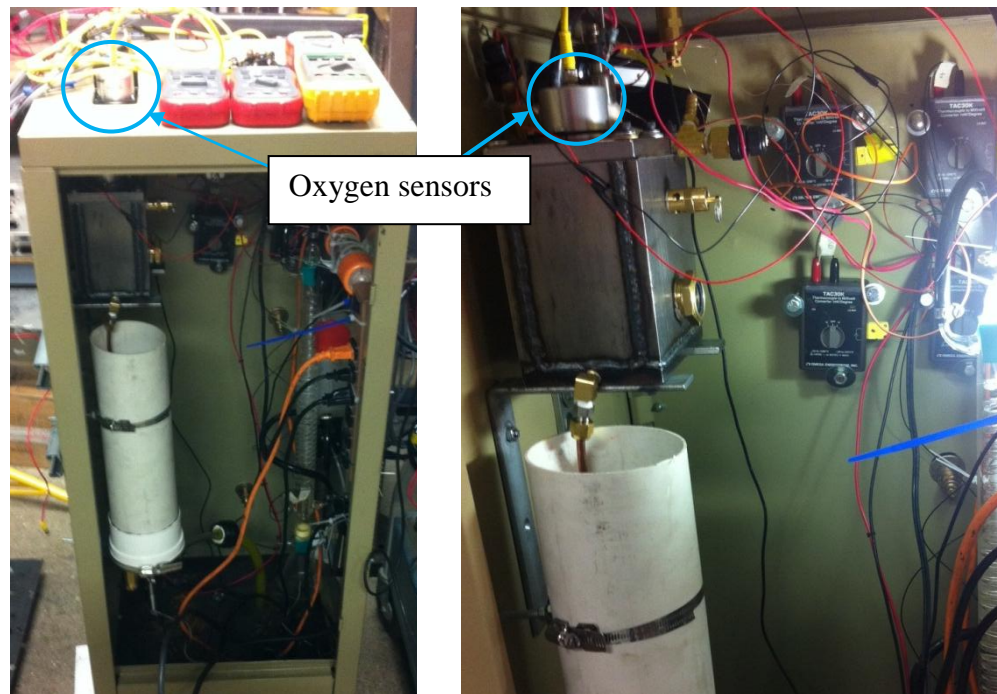


**Figure 123. Injector test cabinet**

4. Two webcams were placed inside the test cabin. One was pointing at the sight glass to watch fuel level. The other was pointing at heated fuel injector.

5. All valves required to operate during the heating test were remotely controlled valves, which can be operated 25 feet away from the test rig.

6. Two heavy duty steel doors were installed at the corner where injector heating cabinet was located. Doors were closed during the heating test.



7. Fuel rig was located 15 feet away from injector test cabinet. The fuel rig supplies fuel to the injector test cabinet. In case of emergency, an emergency shut-off valve can be operated to cut off the supply of high pressure fuel.

8. The test rigs are mobile. All fuel related tests were done in an open area outside the lab.

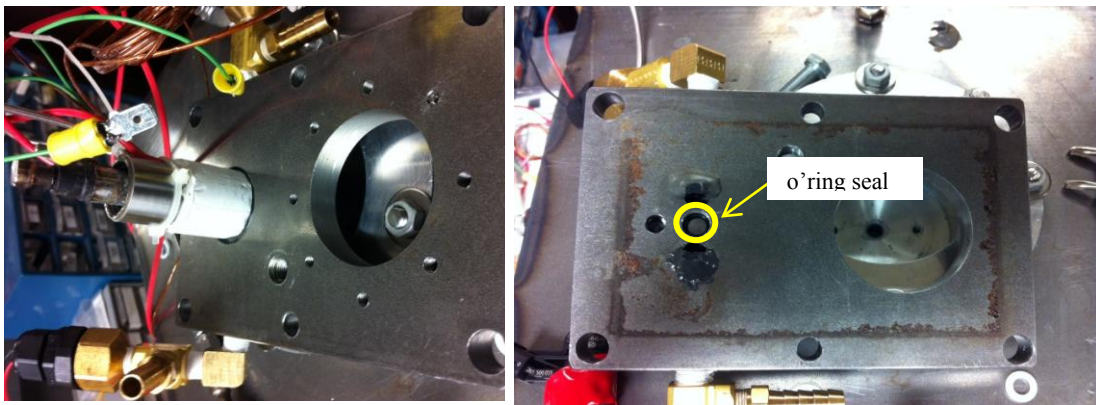


**Figure 124. Top plate of injector test fixture with o’ring seal**

### ***Test Procedure***

The test procedure was followed during each heating test.

1. Set up the rig. This step places every rig in place. Cables, fuel lines, etc. are connected. Make sure fuel line fittings are tightened.
2. Pressurize the fuel line at 300 psi and check for leaks.
3. Check electronics. Make sure fuel injector, heater, oxygen sensors, thermocouples, load cell, and remote valves are operational.
4. Calibration load cell with known weight.
5. Start with room temperature test and slowly increase the heater.

6. Heater's AC power supply has 140 V voltage and 10 A current at its maximum power. Adjust the voltage percentage from 0% to higher percentage as needed. The heater has 20 ohm total resistance and its maximum safe temperature was tested at 3.5 A. The voltage percentage of AC power supply should not exceed 70%. Otherwise, it would risk the melting of nichrome wire heating element.

Important safety notice during heating test:

1. Always check both oxygen sensors and make sure the oxygen levels are well below ignitable percent, which is about 10%;
2. Watch webcams for any abnormality;
3. Use one webcam to watch fuel level inside the injector box and make sure it is low; Open drain valve as needed to maintain this low fuel level;
4. Always wear fire suits and safety goggles during tests;

Figure 125 is a screen shot of high temperature fuel heating test Labview program. In addition to the injector function block, there are oxygen level monitors, temperature monitors and load cell reader. Two webcams are located inside the injection cabinet. One oversees the fuel level through a glass window. The other oversees the heated fuel injector.

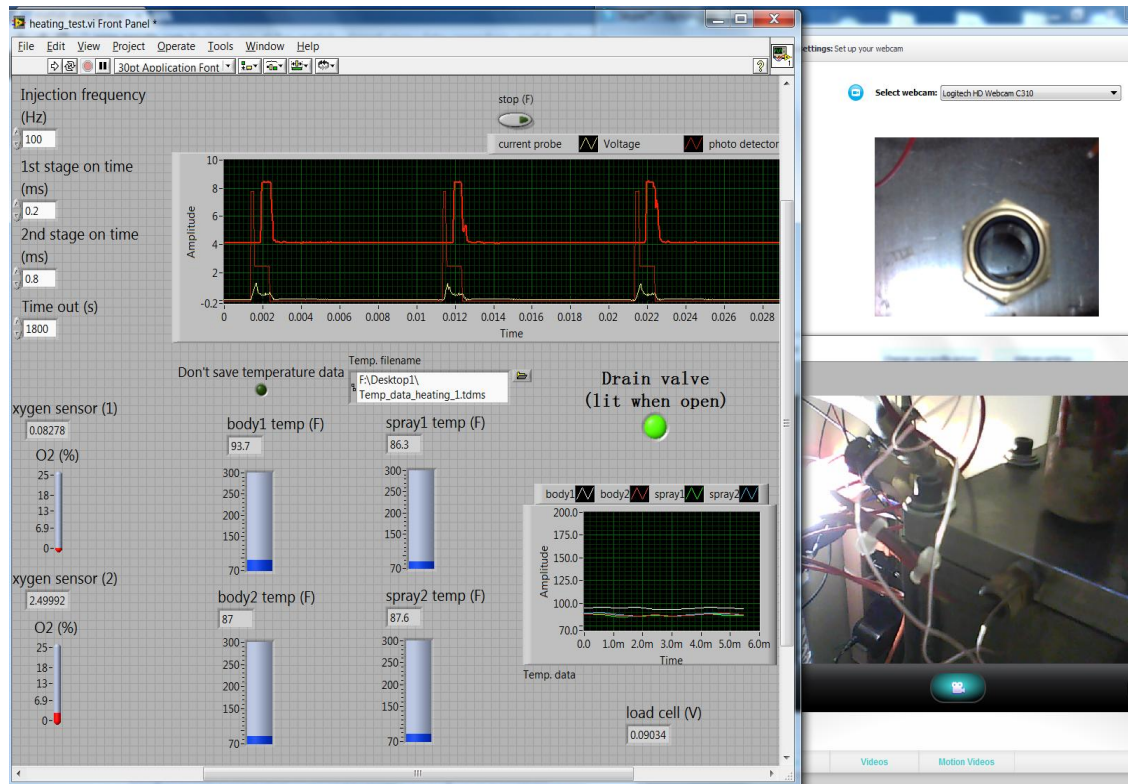


**Figure 125. Labview user interface for heating test**

### ***Test Results***

Test matrices are shown from Table 29 to Table 31.

***Table 29. Test matrix for heating test 1***

---

April 22, 2014: Flow rate test and comparison with unmodified injector

---

case	pressure (psi)	freq. (Hz)	1 <sup>st</sup> stage (ms)	2 <sup>nd</sup> stage (ms)	total inj. 1 min	(mg/shot)	(mm <sup>3</sup> /shot)
1	1500	100	0.2	0			
2	1500	150	0.2	0			
3	1500	100	0.2	0.05			
4	1500	150	0.2	0.05			
5	1500	100	0.2	0.1			
6	1500	150	0.2	0.1			

**Table 29, Continued**

case	pressure (psi)	freq. (Hz)	1 <sup>st</sup> stage (ms)	2 <sup>nd</sup> stage (ms)	total inj. 1 min	(mg/shot)	(mm <sup>3</sup> /shot)
7	1500	100	0.2	0.15			
8	1500	150	0.2	0.15			

April 22, 2014: Heating

case	AC power %	freq. (Hz)	1 <sup>st</sup> stage (ms)	2 <sup>nd</sup> stage (ms)	RMS Amp	pressure	nozzle steady-state temp. (F)	spoon steady-state temp. (F)
9	50%	100	0.2	0.15	2.5A	1500 psi	185	203
10	60%	100	0.2	0.15	3A	1500 psi	219	245
11	70%	100	0.2	0.15	3.5A	1500 psi	257	284
12	50%	100	0.2	0.1	2.5A	1500 psi	206	234
13	60%	100	0.2	0.1	3A	1500 psi	255	271
14	70%	100	0.2	0.1	3.5A	1500 psi	295	304
17	70%	100	0.2	0.05	3.5A	1500 psi	355	348
20	70%	100	0.2	0	3.5A	1500 psi	395	310

**Table 30. Test matrix for heating test 2**

April 26 -2014: Flow rate test and comparison with unmodified injector

case	pressure (psi)	freq. (Hz)	1 <sup>st</sup> stage (ms)	2 <sup>nd</sup> stage (ms)	total inj. 1 min	mg/shot)	(mm <sup>3</sup> /shot)
1	1500	100	0.2	0.15			
2	1500	150	0.2	0.15			
3	1500	100	0.2	0.1			
4	1500	150	0.2	0.1			
5	1500	100	0.2	0.05			
6	1500	150	0.2	0.05			
7	1500	100	0.2	0			
8	1500	150	0.2	0			

April 26 -2014: Heating

case	AC voltage %	freq. (Hz)	1 <sup>st</sup> stage (ms)	2 <sup>nd</sup> stage (ms)	RMS Amp	pressure	Nozzle steady-state temp (F)	Spoon steady-state temp (F)
9	50%	100	0.2	0.15	2.5A	1500 psi	165	175

**Table 30, Continued**

case	AC voltage %	freq. (Hz)	1 <sup>st</sup> stage (ms)	2 <sup>nd</sup> stage (ms)	RMS Amp	pressure	Nozzle steady-state temp (F)	Spoon steady-state temp (F)
10	60%	100	0.2	0.15	3A	1500 psi	215	250
11	70%	100	0.2	0.15	3.5A	1500 psi	270	298
12	70%	100	0.2	0.1	3.5A	1500 psi	300	302
13	70%	100	0.2	0.05	3.5A	1500 psi	370	325
14	70%	100	0.2	0	3.5A	1500 psi	395	300
15	70%	100	0.2	0.15	3.5A	1500 psi		
16	70%	100	0.2	0.1	3.5A	1500 psi		
17	70%	100	0.2	0.05	3.5A	1500 psi		
18	70%	100	0.2	0	3.5A	1500 psi		
19	70%	100	0.2	0	3.5A	1500 psi		
20	70%	100	0.2	0.05	3.5A	1500 psi		
21	70%	100	0.2	0.1	3.5A	1500 psi		
22	70%	100	0.2	0.15	3.5A	1500 psi		

**Table 31. Test matrix for heating test 3**

May 17 -2014: Flow rate test and comparison with unmodified injector							
case	pressure (psi)	freq. (Hz)	1st stage (ms)	2nd stage (ms)	total inj. 1 min	ref. (mg/shot)	ref. (mm <sup>3</sup> /shot)
1	1500	100	0.2	0.15			
2	1500	100	0.2	0.15			
3	1500	100	0.2	0.1			
4	1500	100	0.2	0.1			
5	1500	100	0.2	0.05			
6	1500	100	0.2	0.05			
7	1500	100	0.2	0			
8	1500	100	0.2	0			

May 17 -2014: Heating						
case	AC power %	freq. (Hz)	1st stage (ms)	2nd stage (ms)	RMS Amp	pressure
9	50%	100	0.2	0.15	2.5A	1500 psi
10	60%	100	0.2	0.15	3A	1500 psi
11	70%	100	0.2	0.15	3.5A	1500 psi
12	70%	100	0.2	0.1	3.5A	1500 psi
13	70%	100	0.2	0.05	3.5A	1500 psi

**Table 31, Continued**

case	AC power %	freq. (Hz)	1st stage (ms)	2nd stage (ms)	RMS Amp	pressure
14	70%	100	0.2	0	3.5A	1500 psi
15	70%	100	0.2	0.15	3.5A	1500 psi
16	70%	100	0.2	0.1	3.5A	1500 psi
17	70%	100	0.2	0.05	3.5A	1500 psi
18	70%	100	0.2	0	3.5A	1500 psi
19	70%	100	0.2	0	3.5A	1500 psi
20	70%	100	0.2	0.05	3.5A	1500 psi
21	70%	100	0.2	0.1	3.5A	1500 psi
22	70%	100	0.2	0.15	3.5A	1500 psi
23	26%	100	0.2	0.15	1.3A	1500 psi
24	32%	100	0.2	0.15	1.6A	1500 psi
25	32%	100	0.2	0.15	1.6A	1500 psi
26	from 32% to 70%	100	0.2	0.15	from 1.6A to 3.5A	1500 psi

The room temperature test gives baseline flow rate data. 70% of the AC power supply voltage gives about 245 watts power input to the heater.

From May 17 tests (Table 31), each room temperature test lasts 1 min 10 sec. The purpose is to obtain flow rate data at room temperature. Each heating test lasts at least 2 min (including cooling time after turning off the heater). Test 23, 24 and 25 are preheating tests to determine the temperature of the initial injections after preheating the heater at 400 °F. The following are the descriptions of each test:

Test 23: preheat heater without fuel (during preheating, use emergency valve in the upstream to stop the fuel from going into fuel injector);

Test 24, 25: preheat heater with fuel (during preheating, there is no injection).

Test 26: preheat heater with fuel. Heater power increased to 70% when injection starts.

Load cell calibration:

As a means to measure the mass flow rate, a load cell (Interface model: MB-5) was attached to the weighing system to measure the mass of accumulator. The mass of accumulator indicates the fuel mass change during injections.

The calibration of load cell uses known weights on the accumulator and measures the milli-volts output from load cell. The curve-fit equation is used to calculate the average mass flow rate.

A typical load cell calibration curve is shown in Figure 126. The “up” and “down” curves indicate the adding and subtracting of the known weights. The discrepancy between adding and subtracting curve is due to hysteresis of the hoses attached to the accumulator. Because of the position change of hoses and change of balance weight or distance, the load cell needs to be calibrated every time before the injection test. Each time the curve might be slightly different.

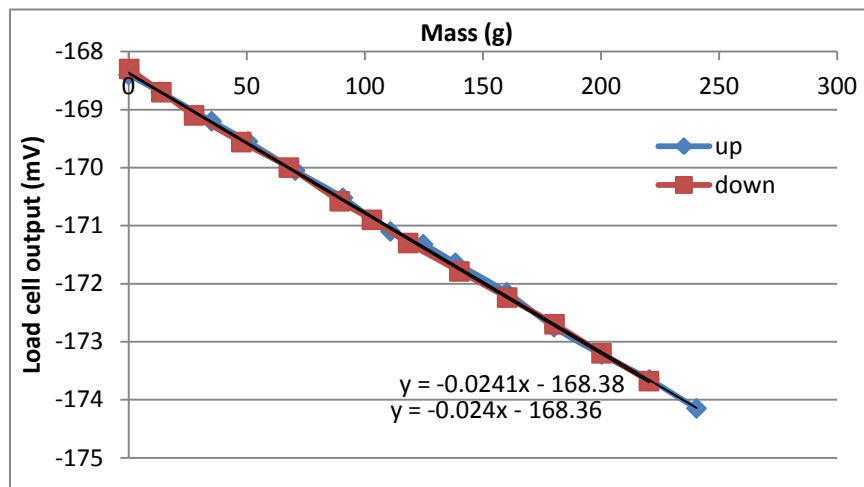
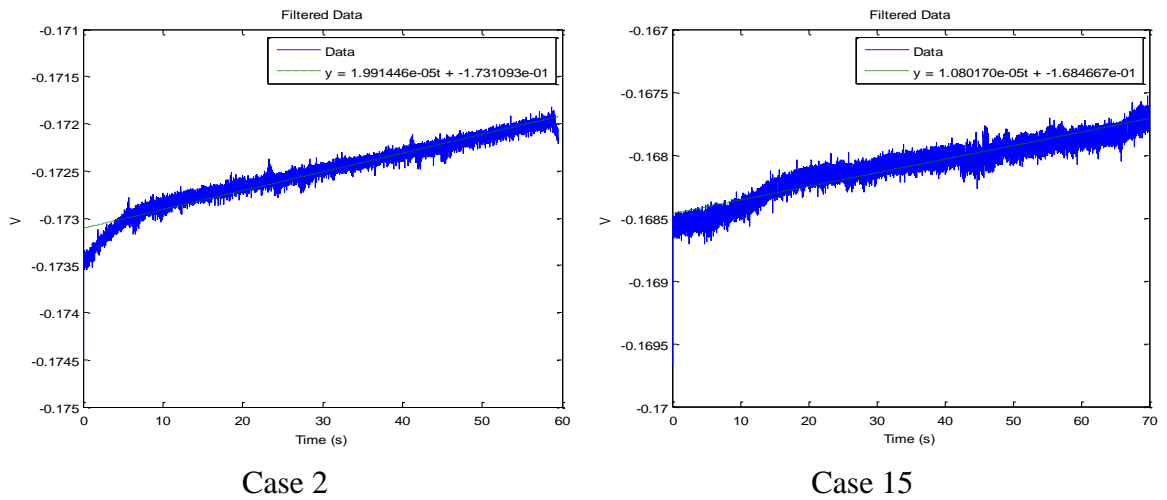


Figure 126. Load cell calibration curve

Load cell output during test:

The load cell output was recorded during the injection test. A low pass filter was used to eliminate noise from 30 kHz data. During post-processing of flow rate data, a low pass filter was used in the Matlab code: `fir1(20,0.0002)`, which applied a 20 orders, 3 Hz filter. Two typical filtered flow rate data (from April 26 test in Table 30) are plotted in Figure 127.



**Figure 127. Load cell output during two injection tests**

The mass flow rate is then calculated using the first order coefficients of the curve-fits from the test and calibration. The formulas are given as follows:

$$\text{Mass flow rate} = \frac{V / s}{V / g} = g / s$$

$$\text{Volumetric flow rate} = \frac{\text{mass flow rate}}{\rho(T)}$$



Using the above formulas, the average mass flow rate can be calculated. Figure 128 shows flow rates at different injection control on-times. Temperature effect on fuel density was considered when converting mass to volume.

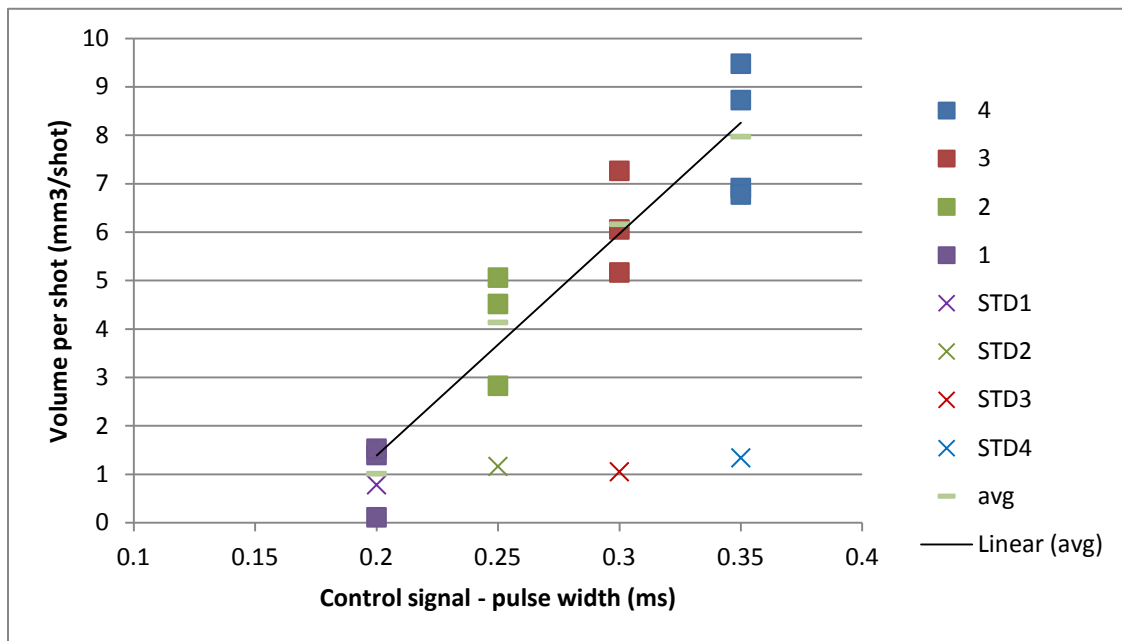


**Figure 128. Volume per shot vs. pulse width using weighing system**

The standard deviation (STD) is less than 1.5 mm<sup>3</sup>/shot for each pulse width data set. Each pulse width data set includes at least three tests.

The temperature of the spray is measured through two fine-gage thermocouples (.005” diameter, response time in the moving air: 0.08 sec [33]). One thermocouple is mounted right near the nozzle where fuel exits. The other one is measuring the bottom surface temperature near nozzle. Notice that the thermocouple is bare wired. In other words, it is not insulated. Direct contact with the injector metal body would create

ground loop that messes up with its output. Thus, JB-weld (electric insulation material) is first applied onto the bottom surface near nozzle. The thermocouple actually measures the temperature of the JB-weld, instead of the true temperature of the injector bottom surface. To protect both thermocouples from breaking, stainless steel tubings are used to guide them. The positions of the thermocouples are adjustable in vertical and horizontal directions. The thermocouple structure is shown in Figure 129.

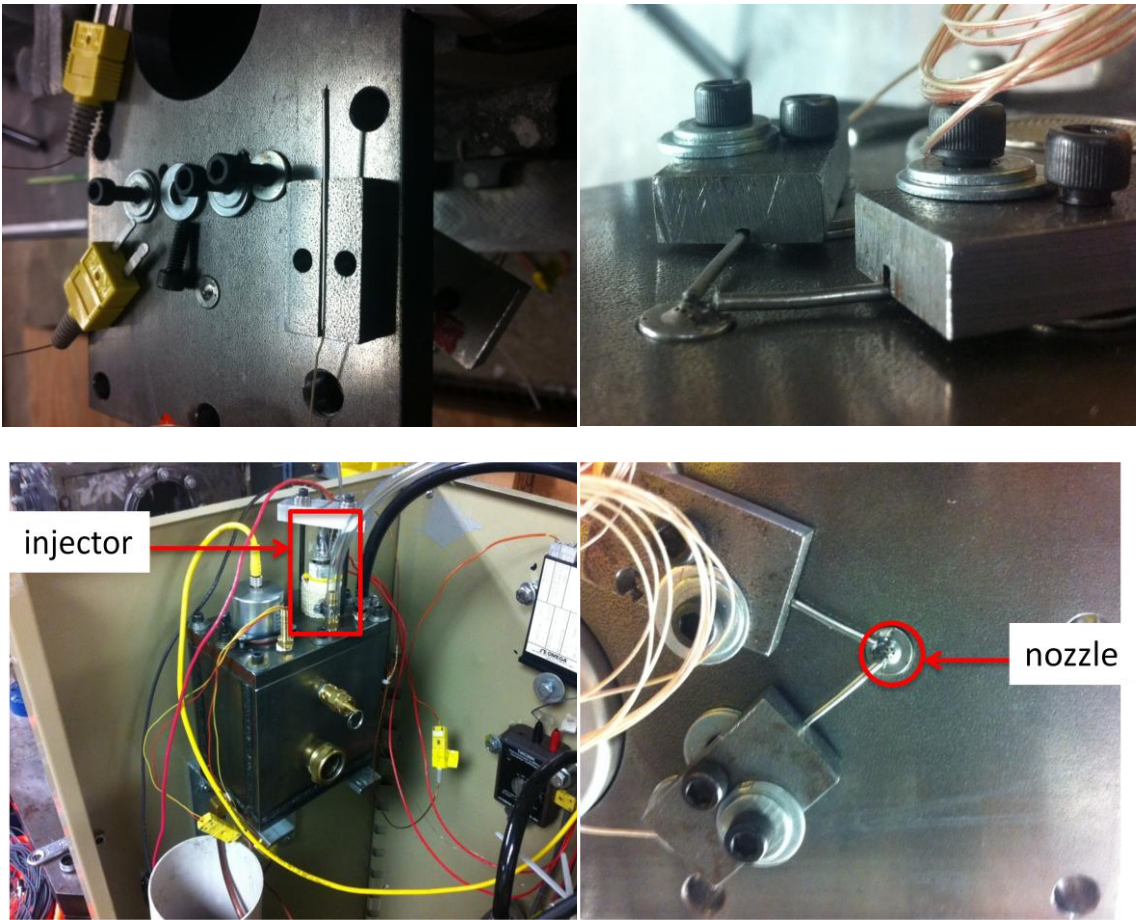


**Figure 129. Thermocouples to measure spray temperature**

Because of the error (or disturbance) in the weighing system (due to vibration or even wind), the temperature effects on the mass flow rate cannot be discerned from measured flow rate data. The flow rate data from May 17's test is shown in Figure 130.

The raw data taken at pulse width less than 0.35 ms has lots of noise. These small flow rates suffer more from disturbances. The injection inconsistency under these short pulse widths could be another factor that contributes to the noisy flow data. It is recommended that the injector be tested at pulse width equal or greater than 0.35 ms for better injection consistency.

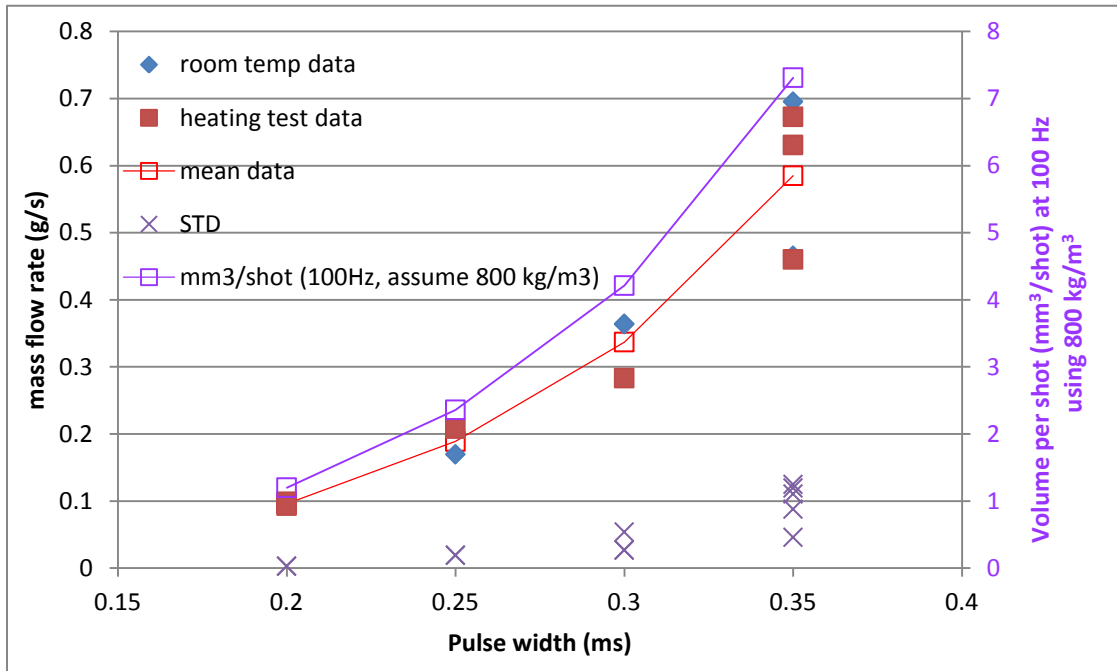


**Figure 130. Flow rate data from May 17 test (Proprietary. Texas A&M. Patent pending)**

The temperature data from Figure 131 shows the rise of spray temperature as flow rate decreases. Spray temperature is consistently higher than nozzle temperature. The measured spray temperature at 0.35 ms injection control pulse width (or 7 mm<sup>3</sup>/shot, 100 Hz with room temperature JP-8) gives about 300 °F. While the measured spray temperature is close to 400 °F at 0.25 ms pulse width (or 3 mm<sup>3</sup>/shot, 100 Hz with room temperature JP-8). Notice the body temperature is measured from the embedded thermocouple inside the ceramic layer. It is not the true body temperature of the stainless steel body. The nozzle temperature is the JB-weld temperature attached to injector bottom surface. Spray temperature is the exit fuel temperature near nozzle.

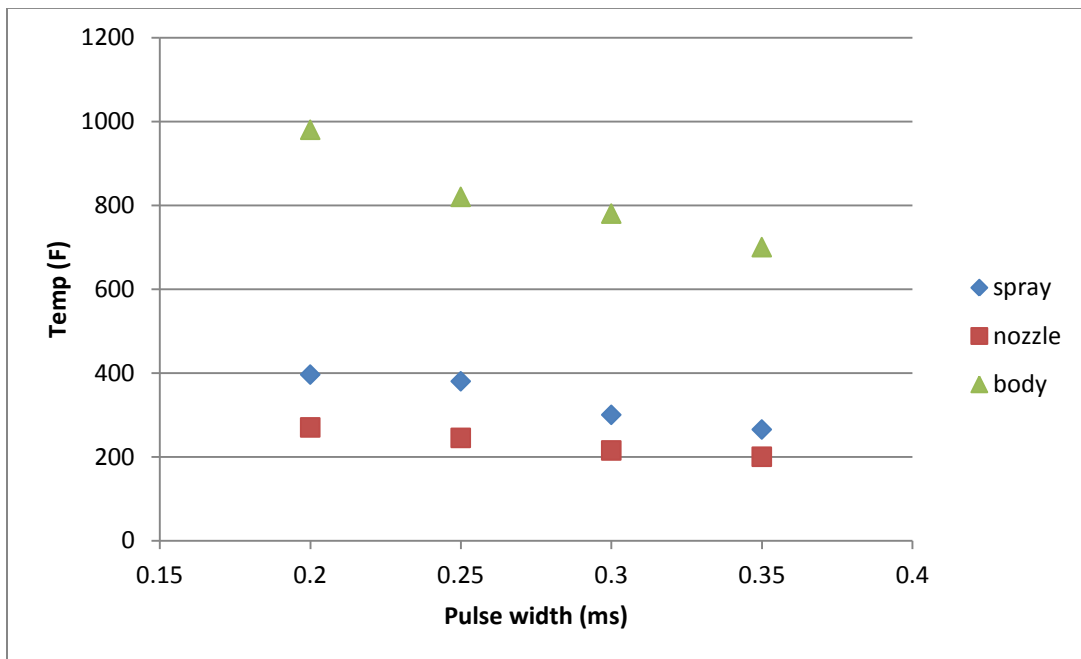


**Figure 131. Temperature data from May 17 heating test (Proprietary. Texas A&M. Patent pending)**

**Table 32. JP-8 transient-heating test**

Date	Case	Pre-heat AC power	Freq. (Hz)	1st stage (ms)	2nd stage (ms)	Pre-heat temp. (F)	Pre-heat time (s) after reaching pre-heat temp.	Pre-heat condition
May 31st	1	30%	100	0.2	0.15	400 F	20 sec	Pre-heat w.o. fuel
May 31st	2	36%	100	0.2	0.15	450 F	20 sec	Pre-heat w.o. fuel
June 5th	2-1	36%	100	0.2	0.15	450 F	60 sec	Pre-heat w.o. fuel
June 5th	3	40%	100	0.2	0.15	500 F	60 sec	Pre-heat w.o. fuel
May 31st	4	32%	100	0.2	0.15	400 F	20 sec	Pre-heat w. fuel
May 31st	5	36%	100	0.2	0.15	450 F	20 sec	Pre-heat w. fuel
June 5th	5-1	36%	100	0.2	0.15	450 F	60 sec	Pre-heat w. fuel
June 5th	6	40%	100	0.2	0.15	500 F	60 sec	Pre-heat w. fuel

The purpose of the transient-heating tests is to find out the temperature transient response of the initial fuel after pre-heating it to certain temperature before injection.

Test conditions are shown in Table 32.

Transient heating tests were done in two ways. One is to pre-heat the heater with fuel. The other one is to pre-heat the heater without fuel. For both methods, the heater temperature was maintained at 500 °F before starting the injection. Once the heater body reaches designated temperature, the pre-heating time does not have influence on the outlet fuel temperature rise. Figure 132 and Figure 133 show the temperature transient at the first few seconds measured at the nozzle exit with the two preheating methods. The heater power was increased as the injection started in order to maintain the exit fuel temperature at a constant level. The heater power started from 32% for pre-heating and 70% for transient heating. The temperature profile was obtained as soon as the injection started. The thermocouple used to measure this spray temperature is a K-type 36 gage bare wire thermocouple. The time constant, which is defined as the time required to reach 63.2% of an instantaneous temperature change, is 0.08 second. The temperature data acquisition rate is 20 kHz. [23]

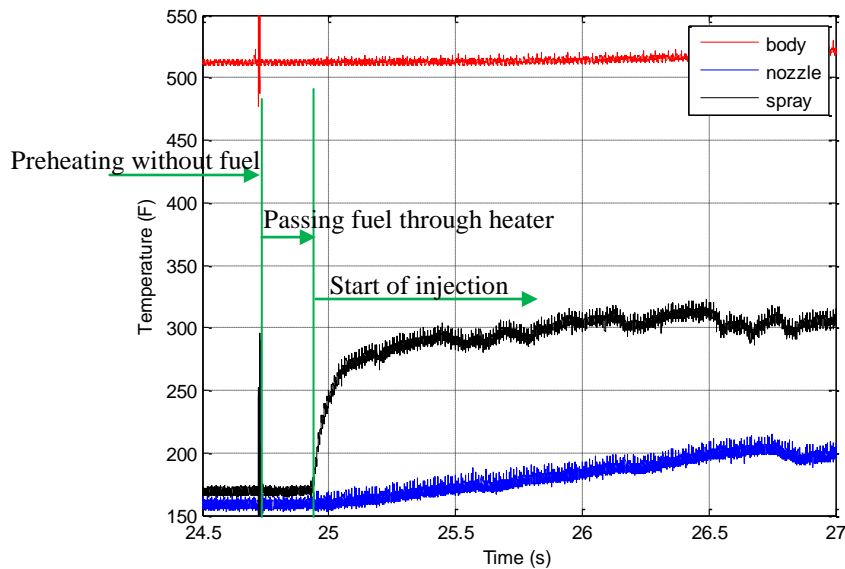


**Figure 132. Transient temperature response at the start of injection measured at the nozzle exit using 500 F pre-heating temperature without fuel (Proprietary. Texas A&M. Patent pending)**

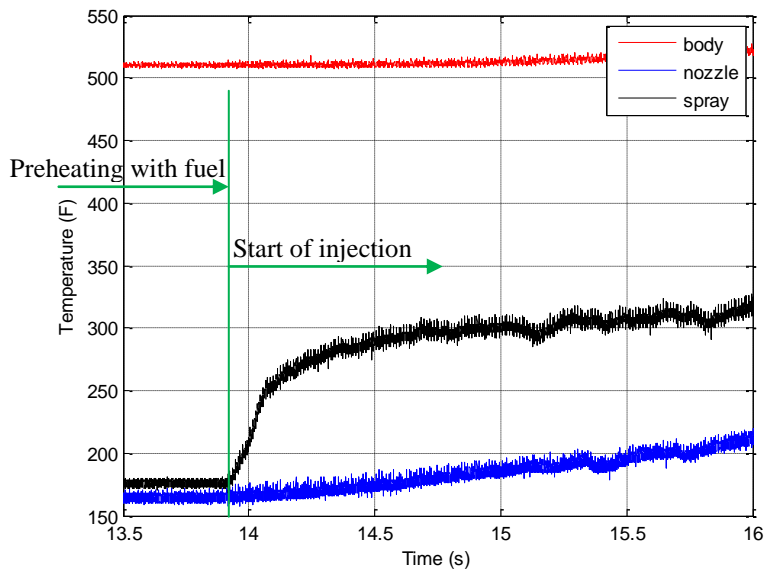


**Figure 133. Transient temperature response at the start of injection measured at the nozzle exit using 500 F pre-heating temperature with fuel (Proprietary. Texas A&M. Patent pending)**

As can be seen, preheat without fuel gives faster temperature rise at initial injections. This means the fuel can be heated up to higher temperature when passing through the heater rather than sitting in the injector and relies on thermal conduction to heat up the fuel near the nozzle. This pre-heating strategy should be practiced when the initial injections need to be at high temperatures.

To illustrate how fast the temperature rises at initial injections, a time constant is defined in the following equation.  $\tau$  dictates how long it takes for temperature to rise from baseline temperature to final temperature.

$$T = T_o + (1 - e^{-t/\tau}) \cdot \Delta T$$

Where,  $T_o$  is the baseline temperature, which is 150 F in our cases (the ambient temperature near the nozzle);  $t$  is the time elapsed;  $\Delta T$  is the temperature difference between the baseline and final temperature. Since the final (steady-state) temperature is 300 F,  $\Delta T$  is 150 F.

Figure 134 shows the overlapping of 0.1 sec time constant with the temperature profile. This indicates the time constant of the temperature rise is 0.1 sec. When 0.08 sec time constant is considered for the thermocouple's mass, the actual rise time is 0.02 sec for the injected fuel. Or we can conclude that, it takes only 0.02 sec for the heater to heat up the fuel from room temperature to 300 F.



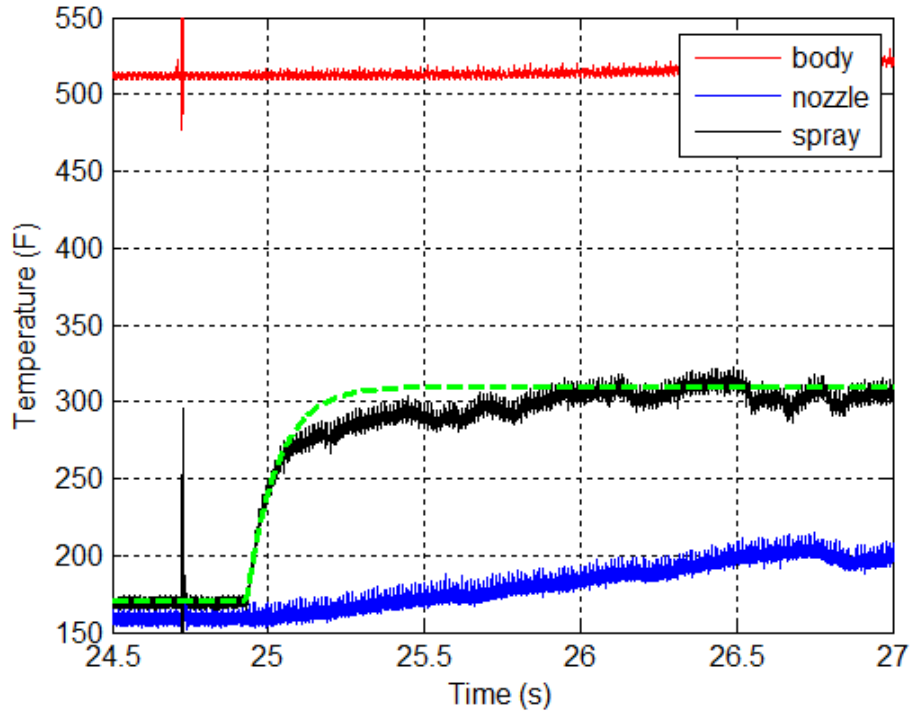


**Figure 134. Overlapping 0.1 second time constant curve with transient temperature profile in the case of preheating without fuel at 500 F (Proprietary. Texas A&M. Patent pending)**

**Table 33. Long duration heating test (Proprietary. Texas A&M. Patent pending)**

Case	AC power	Freq. (Hz)	1 <sup>st</sup> stage (ms)	2 <sup>nd</sup> stage (ms)	Total heating time (min)	Measured steady-state temp. (F)	Theoretical vapor fraction	Steady-state flow rate (g/s)
7	70%	100	0.2	0.15	10 min	310 F (713 kg/m <sup>3</sup> )	>0%	0.460 g/s (6.45 mm <sup>3</sup> /shot, 100 Hz)
8	70%	100	0.2	0.1	10 min	360 F (694 kg/m <sup>3</sup> )	20%	0.368 g/s (5.30 mm <sup>3</sup> /shot, 100 Hz)
9	70%	100	0.2	0.05	10 min	410 F (675 kg/m <sup>3</sup> )	60%	0.253 g/s (3.75 mm <sup>3</sup> /shot, 100 Hz)

\* Corresponding JP-8 densities at different measured temperatures

The purpose of long duration heating test is to check the mass flow rate over longer period of time, which is another way of checking for coking. If coking happens in the heater, the flow rate would be reduced. Case 7-9 from Table 33 are transient heating tests to test the long duration heating. Each case lasted more than 10 min. No flow rate change was observed. Vapor fraction is extrapolated from JP-8 distillation curve in Figure 135.

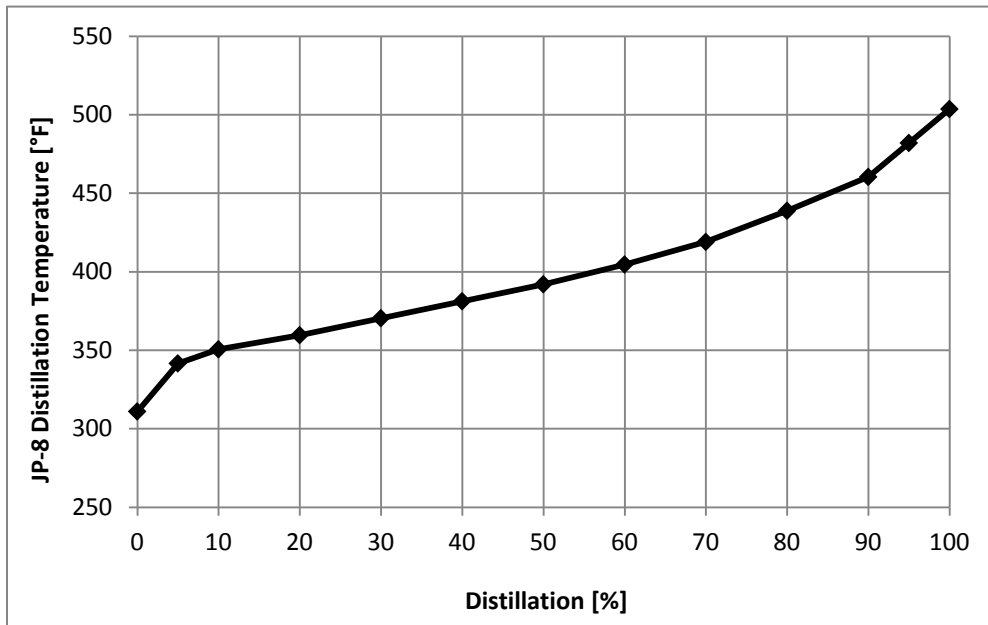


**Figure 135. JP-8 distillation curve (reproduced from [2])**

The heating target is above 300 °F for JP-8, at which temperature it starts vaporizing. Higher temperature may not be necessary due to the heat released from ignition could help vaporize more fuel.

The designed heater is tested to be capable of providing 300 °F JP-8 from the initial injections. The pre-heating without fuel method ensures the initial injections are above its vaporization temperature. As the injection starts, the heater power should be raised to maintain the outlet fuel temperature at 300 °F level. Long duration heating tests demonstrate the durability and consistency of the developed flash vapor fuel injector.

### ***Determining Heater Efficiency***

According to the heating test results, it is possible to match the outlet fuel temperature and flow rate data with theoretical results generated using power balance method.

Figure 136 shows the outlet temperature vs. flow rate data (volume per shot at 100 Hz) correlation. The red curves are the calculated outlet temperature vs. flow rate results by assuming 245 watts, 50% and 55% efficiency heater.

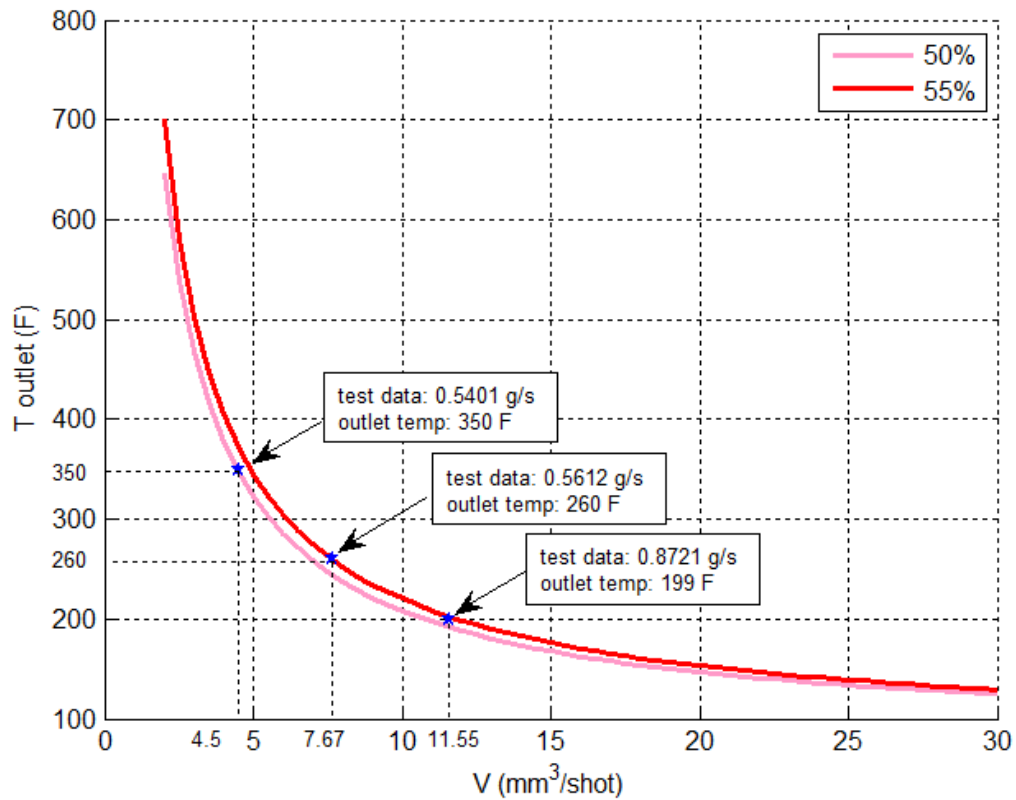


**Figure 136. Heater efficiency determination (Proprietary. Texas A&M. Patent pending)**

The heating test results consistently fall into the region between 50% and 55% efficiency lines. Therefore, we conclude that the heater we designed has about 55% efficiency. Note that this efficiency can be improved by adding more insulation on the outer layer of the heater.

### Conclusion

A flash heater integrated with direct fuel injector was developed to enable low compression ratio Wankel rotary engines to run on low vapor pressure fuel – JP-8. This

flash heater prepares better fuel air mixture by heating JP-8 to its vaporization temperature. However, if JP-8 stays at high temperature long enough, it risks “coking”, which happens when JP-8 reacts with dissolved oxygen and forms carbonized fuel deposit on the heater wall. Coking lowers heat transfer ability and would eventually clog up the fuel pipeline. Therefore, the majority of design effort was put into developing a “flash” heater that could heat up JP-8 extremely fast. By heating the fuel fast, there is little time for heated JP-8 to react with dissolved oxygen. In the event of carbon particle already formed, it ensures that there is no time for it to deposit on metal surface.

The conductive heater was designed to have fastest fuel heating capability. Finite Element Analysis (FEA) code ANSYS was applied to study static heating cases, while Computational Fluid Dynamics (CFD) code ANSYS CFX was applied to study transient heating cases. Heater geometry was optimized for fastest heating ability. The final design contains ultra-thin fuel passages that allow fuel to be heated up quickly as it passes through the heater. The designed heater was then manufactured and integrated with direct fuel injector. Finally, the test results showed with volumetric flow rate less than  $8 \text{ mm}^3/\text{shot}$  at 100 Hz, the measured spray temperature achieved 300 °F. The flow rate requirement ( $20\text{-}30 \text{ mm}^3/\text{shot}$  at 100 Hz) can be realized by using two injectors to supply fuel. The heated fuel injector provides the initial shot for ignition, while the second injector provides room temperature fuel for the continued combustion [23].

There is no flow rate change observed after an hour long heating test at heater temperature above 1000 °F. Note that the fuel is always flowing during the high temperature heating test. The continuous flow ensures the dwell time of fuel inside the

heater is short, which is the key to keep coking from happening. Longer duration heating test is needed to validate the method is indeed effective in preventing coking.

Ignition test is the next important step to validate the performance of combustion with the flash vapor fuel injector.

## CHAPTER V

### IGNITION TEST

#### **Overview**

Since the goal of the developed flash vapor fuel injector is to run Wankel rotary engines with JP-8, the ignition behavior of the proposed heated JP-8 needs to be studied and compared with the original fuel - AVGAS used in the UAVs. This ignition test is the last test to validate the idea of flash heating and the practicality of using the developed flash vapor fuel injector in the Wankel engine.

AVGAS is a high vapor pressure fuel. The high vapor pressure allows AVGAS to easily form ignitable fuel air mixture. For JP-8, however, the low vapor pressure means it would be difficult to vaporize and form ignitable mixture. Because of this, the ignition delay time for AVGAS is much shorter than JP-8's even though JP-8 has lower Octane Number (ON) (which is a measure of the tendency of pre-ignition). What's worse, because of its low vapor pressure, JP-8 might not have enough vapor to create ignition at all if the surrounding air temperature is too low. This is the case when cold-start becomes an issue for JP-8 powered engines.

To overcome the low vapor pressure of JP-8, we proposed in chapter I and II to heat JP-8 to its partial vaporization temperature ( $> 300$  °F). In chapter IV, the developed flash vapor fuel injector has demonstrated its ability to heat JP-8 to its vaporization temperature under one tenth of a second.

In this chapter, as the last step to verify the idea of flash heating, an ignition test rig is designed and built to compare ignition characteristics of AVGAS, unheated JP-8

and heated JP-8. The heated JP-8 is supplied by the developed flash vapor fuel injector. Ignition delay time and pressure rise are measured for AVGAS and JP-8 under various conditions. Ignition results show the benefit of flash heating and demonstrate the superiority of the heated JP-8.

### **Ignition of JP-8**

The ignition of heavy fuel injections has been under investigation for decades. The majority of the work is to understand the ignition process and to study factors that affect the ignition process in the gas turbine engines. Due to the complexity of combustion kinetics, these studies are all experimental based.

Regardless of the application (gas turbine or IC engines), a full understanding of detailed ignition process is still not available. Early research includes a study of ignition of kerosene fuel sprays in a flowing air stream by Subba Rao and Lefebvre [34]. They found droplet size, injection velocity and igniter position were all contributing factors to the minimum ignition energy. In addition, fuel atomization could be improved by local reduction of air velocity in the ignition zone. In a work done by Char et al. [35], ignition and combustion of JP-8 fuel in a supersonic flowfield was studied using a shock tube. They controlled test parameters such as gas temperature, fuel droplet size, initial fuel temperature, and oxygen concentration, and found the influence of these parameters on ignition delay, ignition limitation, and detonation. The most important finding is the initial fuel temperature plays an important role in determining the ignition characteristics. A more recent study compared the shock tube experiment and surrogate model predictions on jet fuel ignition delay times [36]. This study was the first report of



shock tube ignition delay time data for JP-8 and it had broader range of conditions than previous Jet-A data. The Jet-A experimental results were consistent with previous studies. They found that although there was slight difference in JP-8 and Jet-A composition, their ignition delay times were very similar.

The aforementioned ignition delay time measurements were all done using shock tubes. The conditions for these shock tube experiments are more applicable to gas turbine engines, where high temperature stagnant mixture forms in a steady-state condition. For IC engines, these data are not of much use due to the totally different ignition conditions in these highly dynamic machines.

Besides shock tubes, Rapid Compression Machines (RCMs) can also be used to measure ignition delay times. As mentioned in the previous paragraph, shock tube is more often used to study chemical kinetics from stagnant homogeneous mixture, while RCM is better suited when mixing motion is counted. While shock tube normally provides ignition data above 1000 K range temperature, RCM provides ignition data at lower temperature range: 600 ~ 1000 K [37]. Given the nature of the IC engine application, RCM design is preferred in our ignition test setup.

Most RCMs are used to study compression ignitions. As its name suggests, RCM provides a means to compress the air or air fuel mixture rapidly similar to the compression stroke in the CI engine. The fuel is either injected into air or pre-mixed with air. Ignition delay time is measured to be the time interval between the start of compression stroke to the onset of pressure spike caused by auto-ignition. The majority of previous literature of characterizing this ignition delay time uses temperature

controllable heater to raise the air temperature, whereas fuel is being prepared in another chamber. The two chambers then open to create test charge in a high-pressure mixing vessel, where auto-ignition takes place. As one can imagine, the temperature required to actually cause auto-ignition is quite high given the heat transfer between the heated air and cool fuel. From previous research, JP-8 and Jet A fuel exhibits similar auto-ignition characteristics. The fuel air mixing temperature requires above 650 K under 7 bar pressure to bring about auto-ignition. Ignition delay time is in the order of 10 milliseconds. The exact delay time depends on equivalence ratio, with longer ignition delay on lower fuel air equivalence ratio [38, 39].

Using RCM to study spark ignition is very rare due to SI engines' low compression ratio. Park and Keck developed a RCM to measure ignition delays for primary reference fuels using spark-ignition [40]. Matekunas did a visualization study on flame propagation. In this work, he uses a RCM to simulate the spark ignition engines [41]. Muroki et al. developed rotary recess shaped piston in a RCM to study the pilot flame ignition system [42]. The work done by spark-ignition RCM all uses high vapor pressure fuels.

Characterizing JP-8 using spark-ignition RCM has not been done before. This is because SI engines are not designed to run on heavy fuel and room temperature JP-8 would have hard time to ignite in typical SI engines.

However, as an important step to compare ignition behaviors for different fuels, RCM provides the similarity to Wankel rotary engines and controllability over testing

conditions. The test results would provide fundamental guidance on the Wankel rotary engine retrofit.

It is worth mentioning that, the ignition delay times are defined differently depending on the ignition and fuel induction configurations. For example, in the Compression Ignition (CI) Direct Injection (DI) case, the ignition delay time is defined as the time interval between the injection and ignition. In the CI carbureted fuel induction (or pre-mixing) case, it is defined as the time from maximum compression to ignition. In the spark ignition (SI) pre-mixing case, the ignition delay is defined as the time interval between the spark and ignition. While for SI DI case, which is our case, the ignition delay is defined as the time interval between injection and ignition. Different configurations plus different conditions, i.e. equivalence ratio, ambient temperature and pressure, turbulence, fuel droplet size, oxygen concentration, fuel temperature, etc. make the ignition delay time a most challenging parameter to accurately measure.

## **Ignition Test Rig Design**

### ***General Configuration***

The ignition test rig is similar to Rapid Compression Machine (RCM). The ignition test rig was designed and built from ground up. The ideal ignition test rig should replicate Wankel rotary engine's parameters, i.e. compression ratio, maximum and minimum volumes.

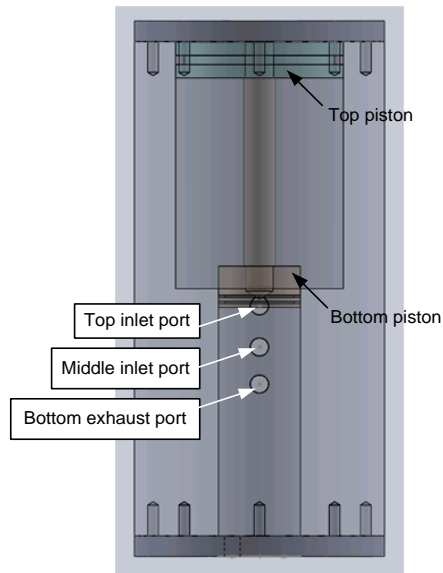
Since the ignition test rig is only for ignition test, simplicity is the key. We do not want to over design it or make another engine! The ignition test rig does not require continuous running cycle like the one in the engine. Therefore, the intake, exhaust valves

and its timing chain can all be eliminated. The single piston provides the compression stroke and expansion for ignition. No connecting rod mechanism is required to harvest the combustion energy. Since the rig is designed for single ignition test (long time interval in between ignitions), its component temperature rating, i.e. o'ring, gasket, can be relaxed due to significant cooling effect after each ignition.

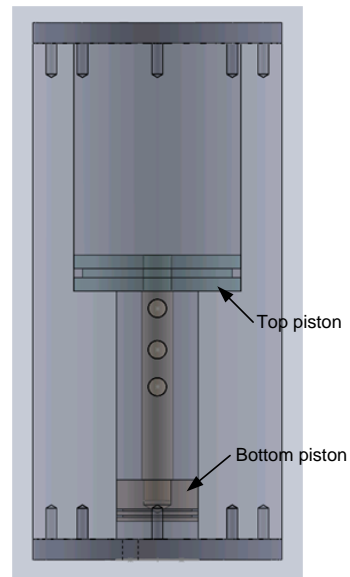
The core of the test rig is a piston assembly. The cylinder outer dimension is 6'' (diameter) by 12'' (length). In order to achieve high compression on the combustion chamber, the piston is designed in a way that the area of lower pressure end is four times of the higher pressure end. Given the 4:1 area ratio, the amplification of the pressure is four times. In other words, in order to achieve compression pressure of 260 psi, it only requires the source pressure of 65 psi. A Porter-Cable C2002 air compressor (Part No. N087062) is used to provide source pressure for compression stroke, as well as fresh air intake for combustion.

Figure 137 shows the piston assembly at two maximum positions with three ports on the side. At the top position, bottom piston is at its highest position, inlet port is exposed. At the bottom position, bottom piston is at its lowest position, maximum compression is achieved. The compression ratio can be varied. For example, the top inlet port gives 12.7:1 compression ratio when the other two ports are closed, while the bottom exhaust port gives 8:1 compression ratio when the other two ports are closed.

Figure 138 shows the piston assembly with top and bottom pistons and connecting shaft. Figure 139 shows the cylinder assembly.



Top position



Bottom position (maximum compression)

**Figure 137. Piston assembly in the ignition test rig**

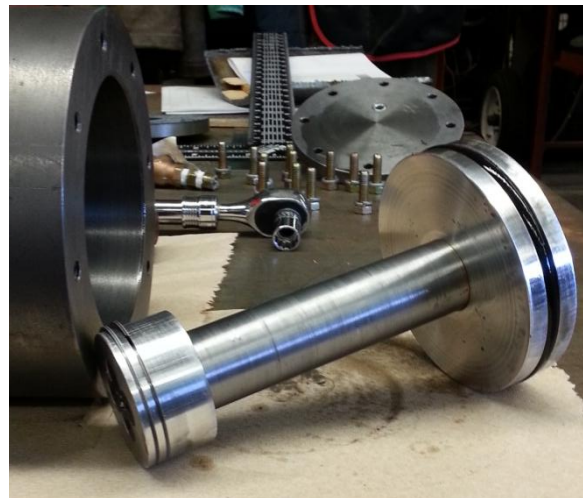
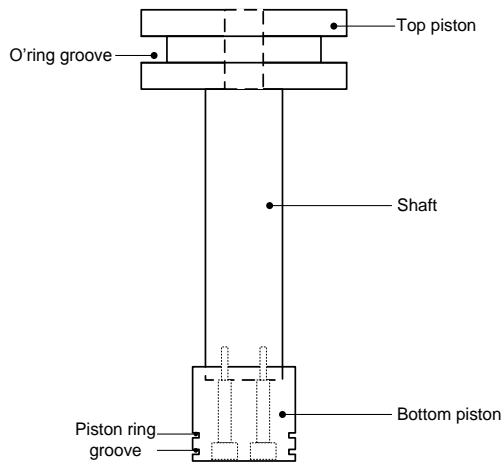
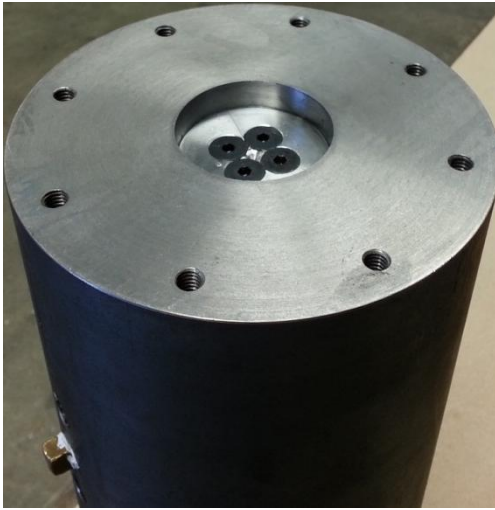


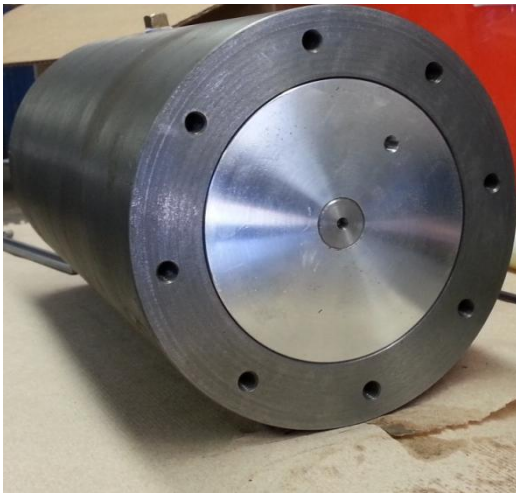
**Figure 138. Piston assembly**



Maximum compression position (bottom piston) with 2'' diameter by 0.4'' depth combustion chamber



Maximum compression position (top piston)



Top position (top piston)



Three ports

**Figure 139. Cylinder assembly**

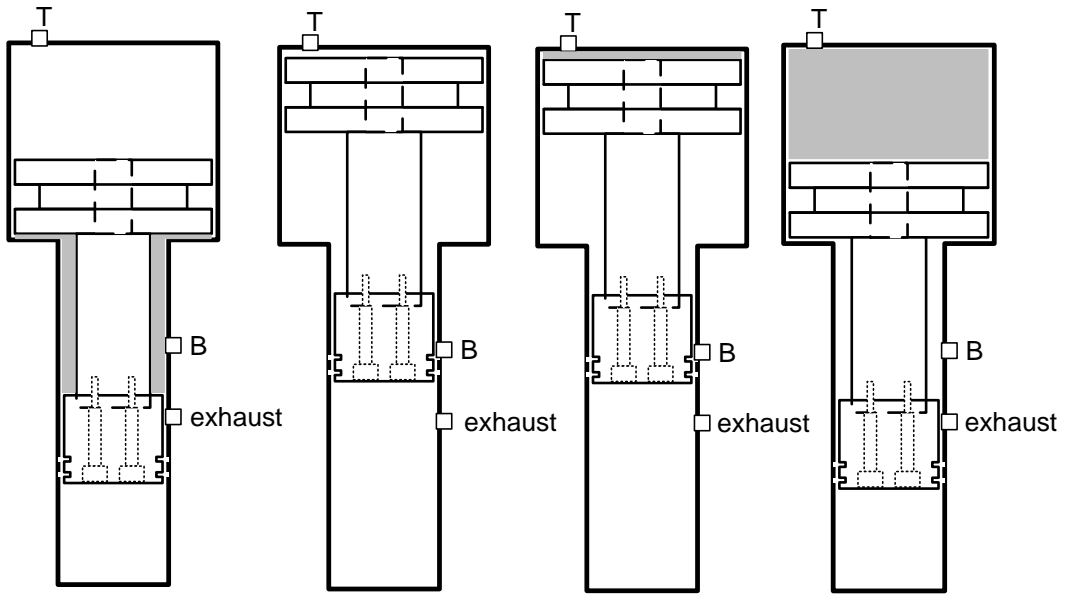
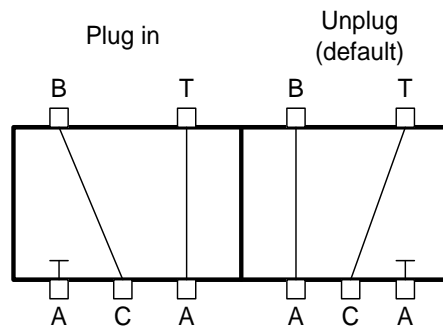


**Figure 140. Operating procedure of the piston assembly**

Figure 140 shows the schematic of the operating procedure for the piston. T represents top port. B is the inlet port (either top inlet port or middle inlet port). Exhaust port is the bottom port. A four way solenoid air control valve switches between the top (T) and bottom (B) ports. Its internal pathways are shown in Figure 141.



C is connected to air source (up to 125 psi)

**Figure 141. Air valve position illustration**

Procedure to compress the air:

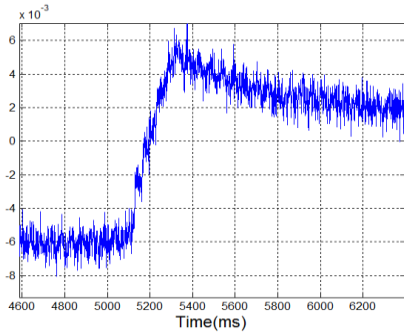
1) Close exhaust, switch air valve position (plug in), connect air source to push piston toward its top position; 2) open the exhaust, purge combustion chamber using the air; 3) close exhaust after finishing purging, pre-charge the chamber with air source pressure; 4) keep exhaust valve closed, switch air valve position (unplug, default) so that the piston is pushed downward to its maximum compression.

It is worth mentioning that because of its dynamic seal nature, the piston ring cannot hold pressure for long period of time after reaching maximum compression. An o'ring groove was added after piston rings as static seal (not shown in the pictures). It prolongs the holding time of maximum pressure, allowing sufficient time for injection and ignition.

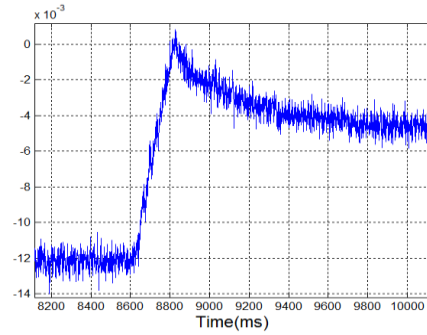
The pressure profiles using different operating modes are shown in Figure 142 (The y-axis is the voltage signal (V) from charge amplifier. The absolute pressure value is not calibrated. The relative pressure can be calculated using 1 mV/10 psi relationship).

For all these cases, there is no pre-charge in the combustion chamber before the compression. As can be seen, the pressure does not get really high even with 12.7 compression ratio. The leakage from piston ring and o'ring is shown to be too great.

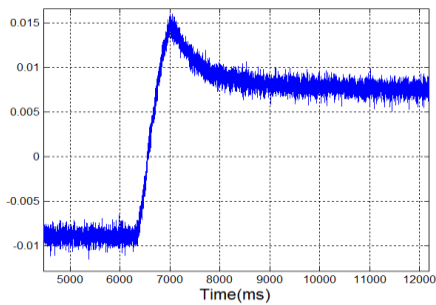




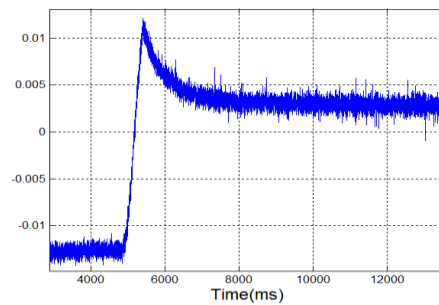
90 psi source, 8:1, Pmax: 110 psi



125 psi source, 8:1, Pmax: 120 psi



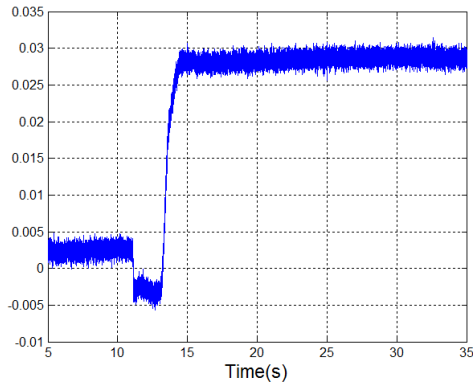
90 psi source, 12.7:1, Pmax: 240 psi



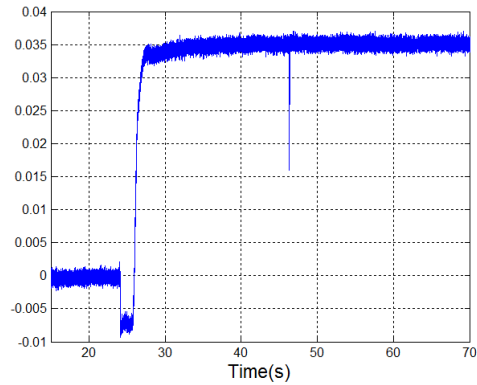
125 psi source, 12.7:1, Pmax: 250 psi

**Figure 142. Pressure profiles using different operating modes**

Another mode that can be operated is pre-charge mode as mentioned in the operating procedure 3). The combustion chamber is pre-charged with air source after purging is finished. Depending on the pre-charge pressure, the maximum pressure can reach as high as 470 psi with 90 psi air source. Two pre-charge cases are shown in Figure 143.



90 psi source, pre-charged, 12.7:1,  
Pmax: 310 psi



125 psi source, pre-charged, 12.7:1,  
Pmax: 470 psi

**Figure 143. Pressure profiles using pre-charge modes**

The pre-charge pressure can be seen as the first stage in the pressure profile in Figure 143. As soon as the air valve switches (from pre-charge chamber to top piston chamber), the pressure drops a little due to the time lags between switching valve and when the bottom piston covers the inlet port. Pre-charge pressure leaks to atmosphere in between this switching time, which causes a dip in the pressure profile. However, because of this slight pre-charge, the maximum compression pressure rises much higher than the one with atmospheric pre-charge. By varying the pre-charge pressure, any feasible pressure in the engine compression cycle can be achieved. It also helps conduct parametric study of the pressure impact on the ignition delay time if necessary.

Theoretical pressure at the maximum compression rises much higher than its experimental counterpart mainly due to the leakage during the compression process. Another factor is the adiabatic boundary condition used in the theoretical derivation, which assumes no heat exchange between the gas and wall.

Apply ideal-gas equation of state:

$$P = \rho RT$$

Where, P is pressure,  $\rho$  is density, R is gas constant, T is temperature.

In an isentropic process, the entropy is constant, for ideal gas:

$$PV^\gamma = \text{constant}$$

$$P_1 V_1^\gamma = P_2 V_2^\gamma \Rightarrow (P_2/P_1) = (V_1/V_2)^\gamma \Rightarrow (P_2/P_1) = CR^\gamma$$

For  $CR = 8.06$ ,  $\gamma = 1.4$ ,  $P_1 = 1 \text{ atm (14.7 psi)}$ ,

$$P_2 = 273 \text{ psi}$$

Assume  $P_1 = 2 \text{ atm (29.4 psi)}$ ,  $P_2 = 546 \text{ psi}$ . In other words, the theoretical maximum compression pressure would rise proportionally given the rise of intake pressure, i.e. if the intake pressure doubles, the maximum compression pressure would double as well. Because of the unavoidable leakage from dynamic seals, i.e. piston rings and o'ring in this case,  $P_2$  can never reach its theoretical value. Depending on the speed, the piston ring or Wankel rotor apex seal may hold the pressure quite high in a fraction of a second. The ignition and combustion then happens and the gas expands to do work. This dynamic nature of the seal works only when the piston or rotor moves continuously, in which case the maximum pressure is not required to hold for prolonged time period. On the other hand, the leakage sometimes may be desired so that the engine oil can be splashed to cool down and lubricate the parts in direct contact with combustion gas. All these contribute to the reason why the measured maximum compression pressure is much lower than its theoretical counterpart.

Another point that is worth mentioning is the actual pressure measurement in the rotating engine. Our Wankel rotary engine has a running speed range of 4,000 ~ 9,000 rpm. It is a challenge to turn the shaft at this high speed using electric motor because most medium to heavy duty electric motors do not operate at this high speed. As mentioned before, the holding time at maximum compression has large impact on the sealed pressure in the compression chamber. Typically, there is a speed range that the dynamic seal works best. According to experienced autoworkers, the typical maximum compression pressure is 150 ~ 200 psi for gasoline engines. Given Wankel's similar compression ratio and higher speed (less dwell time at maximum compression), our rotary engine may fall into slightly higher range: 200 ~ 250 psi.

In order to create similar pressure before ignition takes place, the pre-charge method is applied. It was found that, at 65 psi pre-charge pressure, the resultant maximum compression pressure is 200 psi. Depending on pre-charge pressure, the pressure at maximum compression can be varied. This becomes a merit of this test rig. Without changing the compression ratio, maximum compression pressure can be varied almost continuously. For the actual ignition test, 60 psi pre-charge pressure is used.

The ignition test rig includes ignition rig and other components. Their schematic is shown in Figure 144.

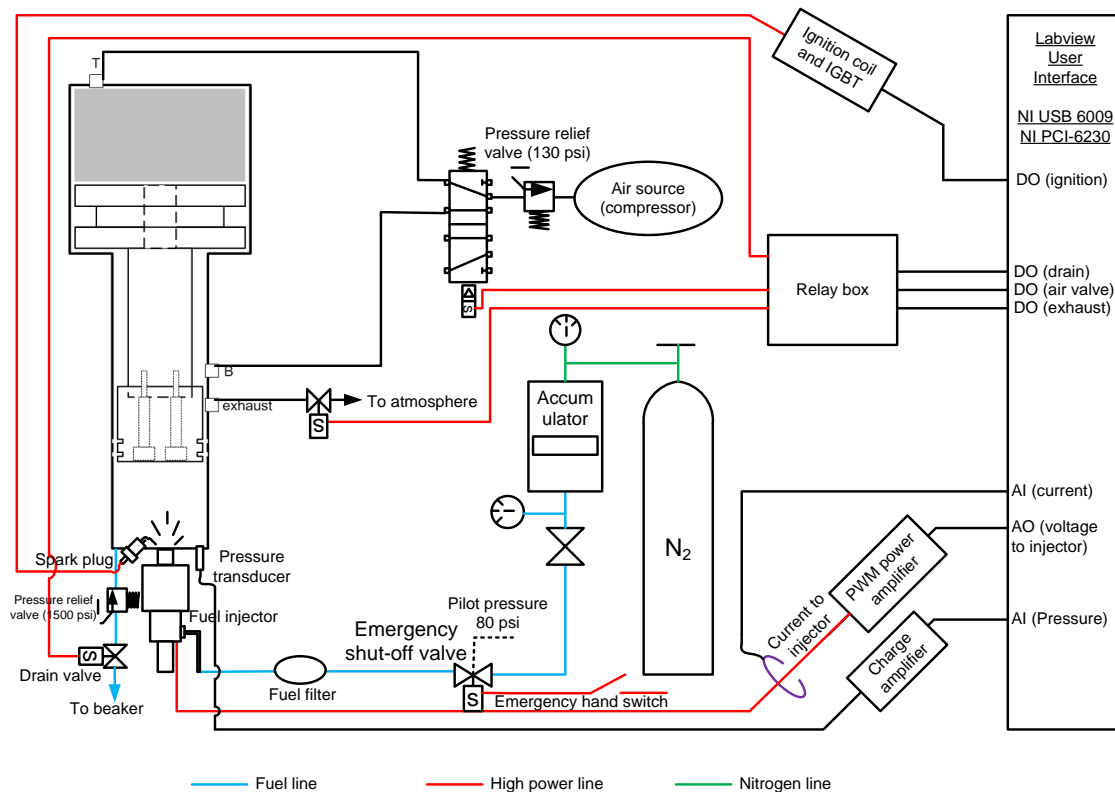


**Figure 144. Test rig schematic**

The test rig is built with safety and automation functions in mind. Pre-cautions need to be practiced when heating of fuel above its auto-ignition temperature is involved. Inert environment in the heating compartment needs to be created while fresh air intake should not be interfered. To do so, the rig is enclosed in an external structure (1/4" thick steel) with purging carbon dioxide while the intake and exhaust ports are routed through the external structure. An oxygen sensor is equipped to ensure oxygen level is low in the enclosure during heating test. The whole ignition test rig concept is shown in Figure 145. The actual rig pictures are shown from Figure 146 to Figure 150.

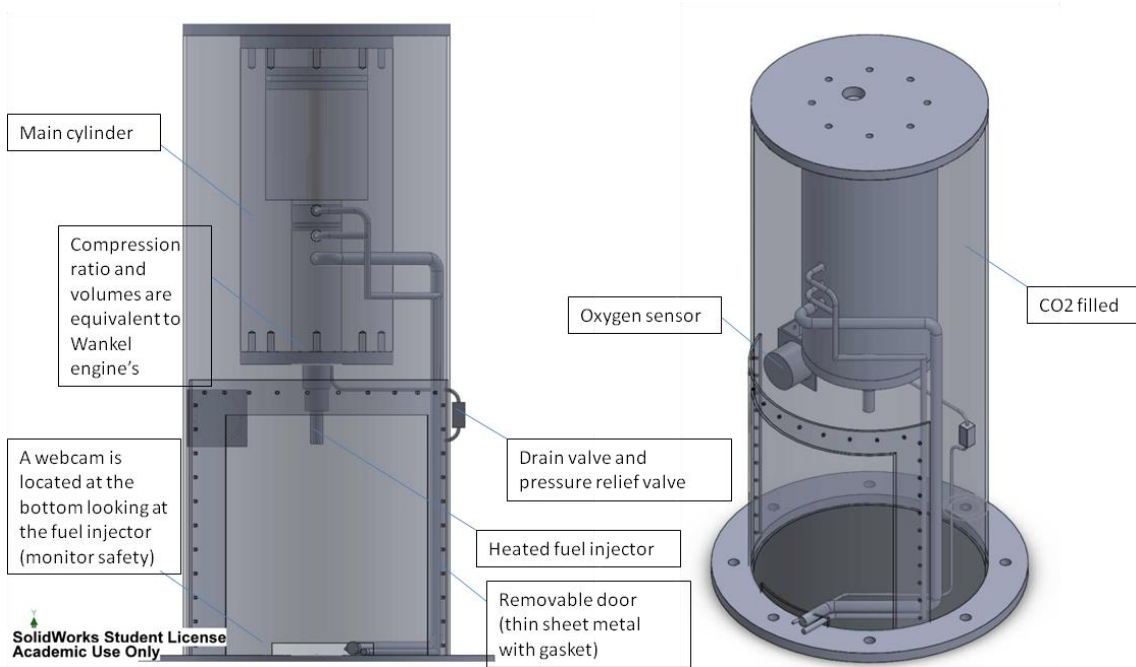


**Figure 145. Ignition test rig concept**



**Figure 146. Top half of the ignition test rig**

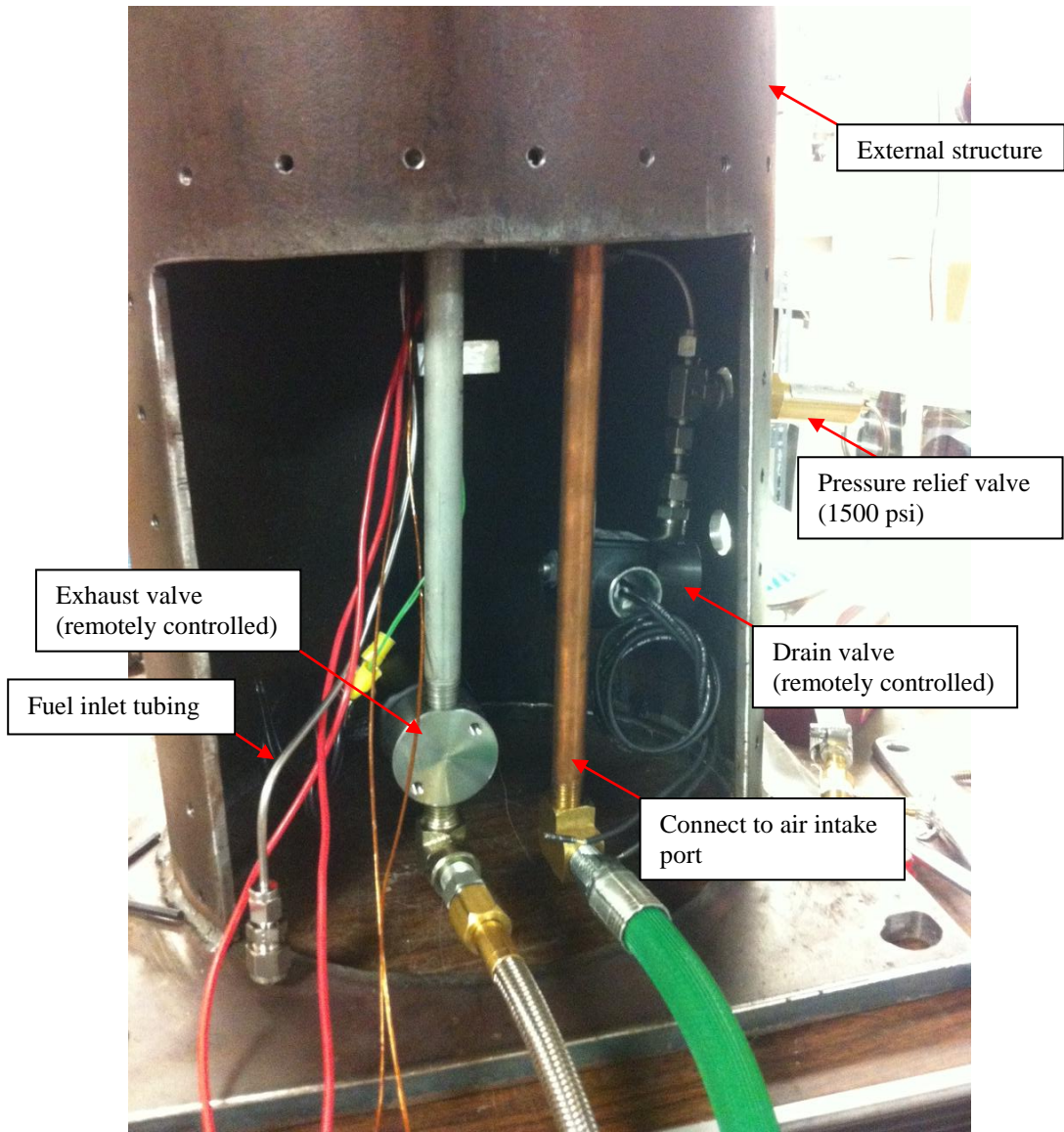


**Figure 147. Bottom half of the ignition test rig**



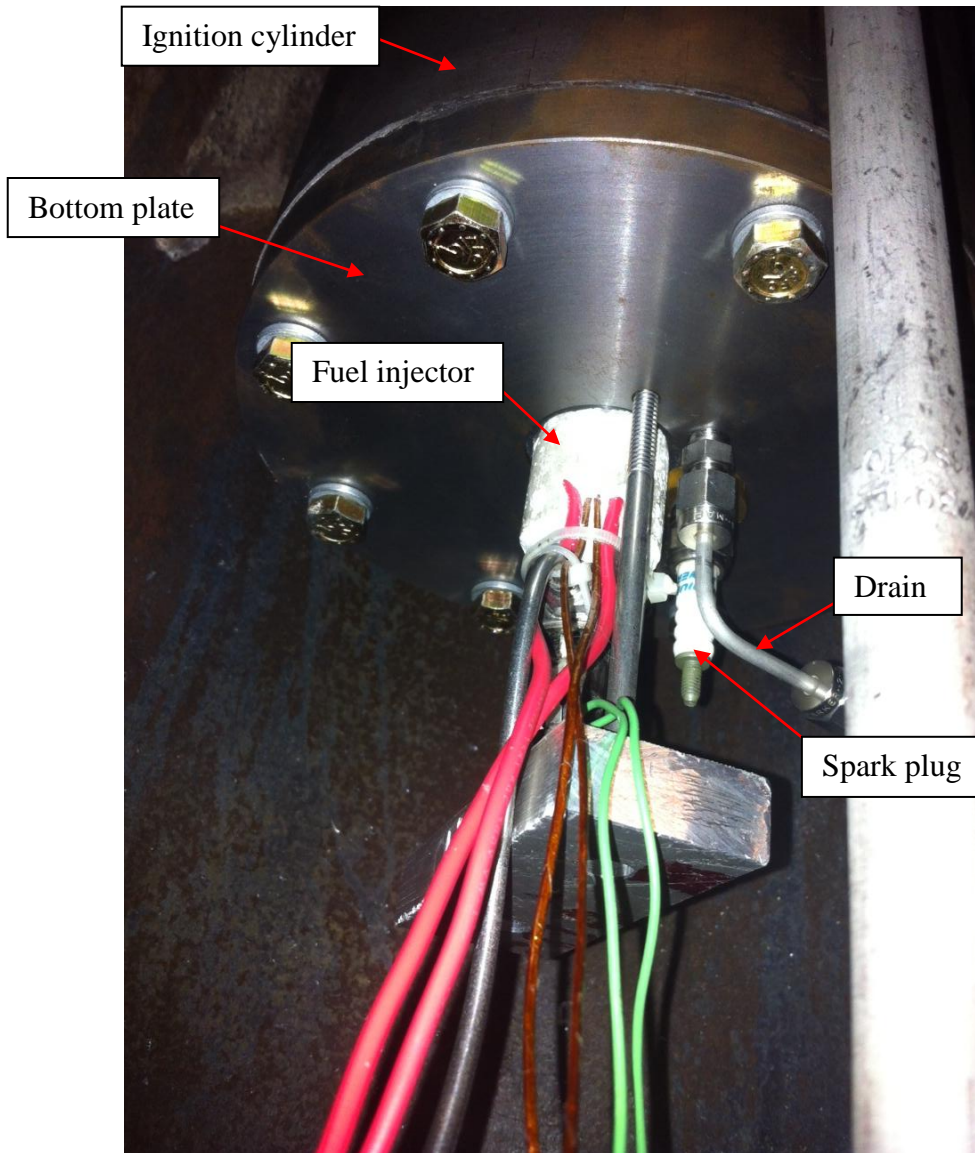


**Figure 148. Components on the bottom plate of the ignition cylinder**



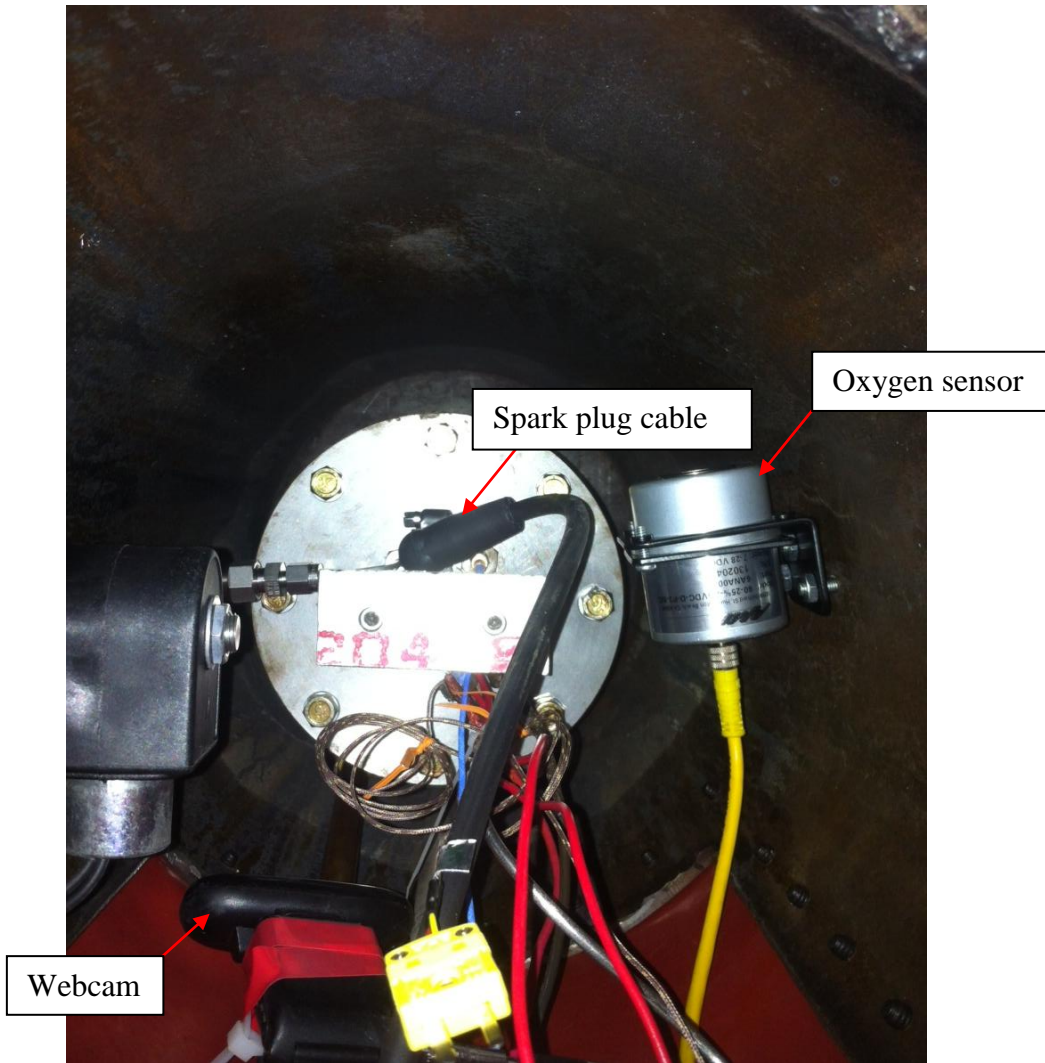


**Figure 149. Bottom view inside the ignition test rig (looking at bottom plate)**



**Figure 150. The whole ignition test rig**

The test rig is designed to operate remotely. As shown in Figure 144, the valves that require operation (on and off) are all controlled by NI data acquisition cards through computer. The Labview user interface is shown in Figure 151.

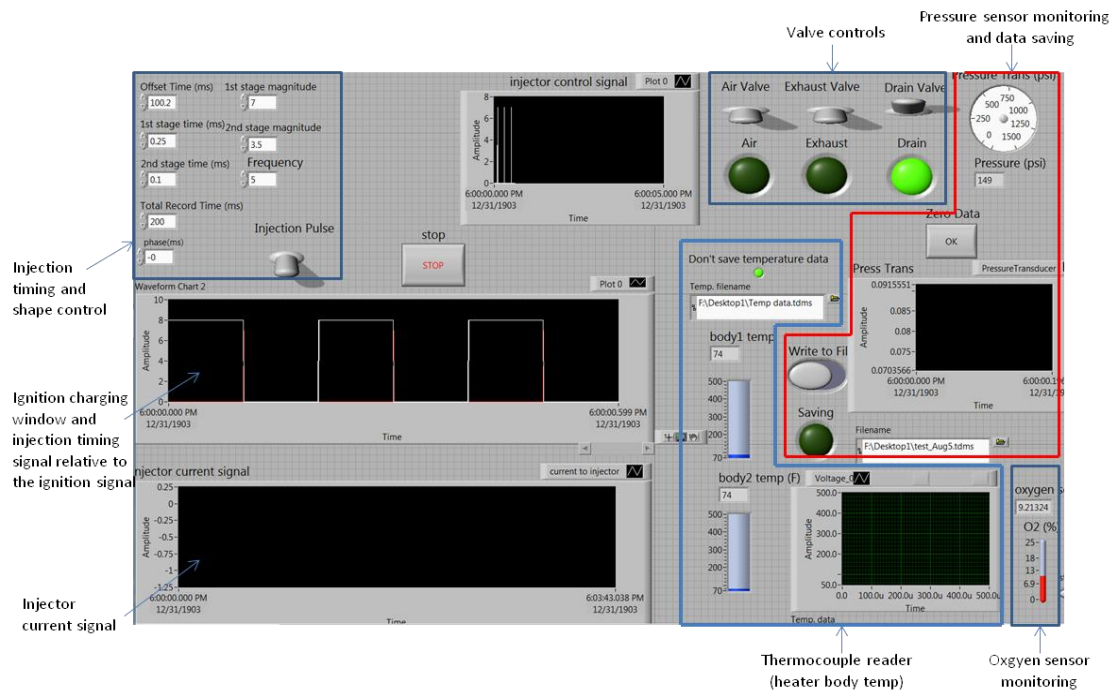


**Figure 151. Labview user interface for ignition test**

Key hardware includes fuel injector, spark plug, remotely controlled valves, pressure transducer, and accumulator. Their functionalities are discussed in the following:

(1) Fuel injector. The fuel injector is controlled by control signal from Labview, which is amplified through pulse width modulation (PWM) power amplifier. The Labview program is capable of varying injection timing, two stage control signal's magnitudes and time durations. Details of power electronics that drive the fuel injector and its current shapes have been discussed in chapter III. The current to fuel injector is measured using an eddy-type current probe. The fuel quantity delivered by fuel injector

is directly related to the time duration of the two-stage control signal. From previous experiment, it was found that 0.35 milli-second control on-time delivers about  $10 \text{ mm}^3$  of JP-8 at 200 atm fuel pressure. The volume drops to  $8 \text{ mm}^3$  at 100 atm. Please refer to chapter III for more details about flow rate calibration of fuel injector.

(2) Spark plug. The ignition circuit in this test rig uses ignition coil instead of capacitive discharge ignition (CDI) method used in the actual engine. Even though CDI is the ignition module in the Wankel rotary engine, the intention of this test rig is for low-speed ignition, not for high-speed continuous firing. Thus the simple inductance ignition method is used for our ignition test rig. The schematic of this ignition circuit is shown in Figure 152. The working principle of ignition circuit is fairly simple. As NI USB 6009 digital output port sends a 5 V logic high signal to insulated-gate bipolar transistor (IGBT), the gate closes a solenoid relay, which controls the primary ignition circuit. Kepco power supply (40V, 15A) supplies current to go through the primary coil. This primary current induces shared magnetic field of both primary and secondary coils. Spark happens when the NI USB 6009's digital output port is low (0 V), which opens the relay and interrupts the primary circuit. The current in the primary circuit is decreased because of the open circuitry. However, the magnetic field is strengthened to prevent the primary circuit current from decreasing. This sudden strengthening of magnetic field creates high voltage potential at the secondary coil. This voltage potential is dictated by the spark plug gap. The larger the gap, the higher voltage potential it could reach. The gap determines when the air breaks down and when the free ions in the air get to accelerate to the point where a large amount of particles collide and make spark.

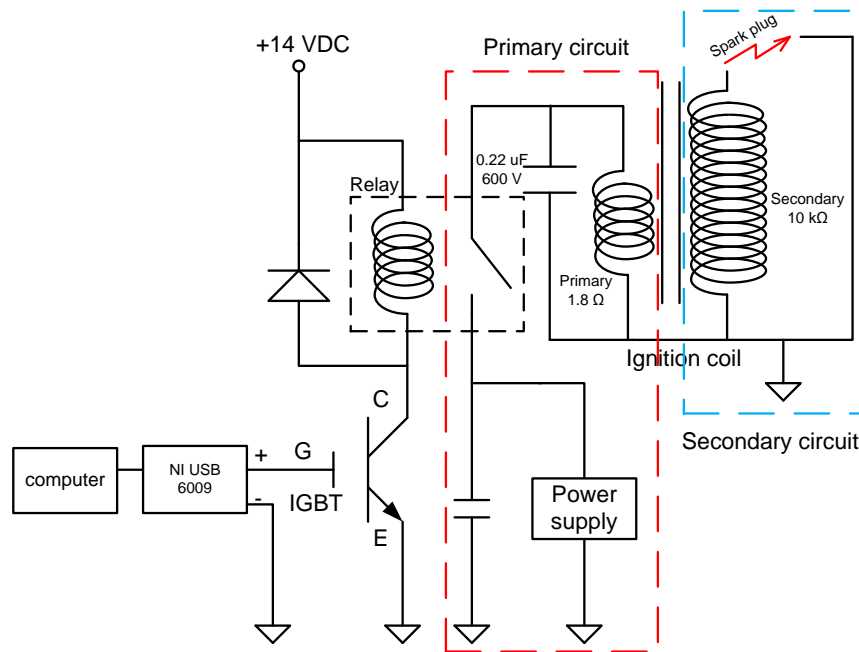


**Figure 152. Ignition circuit diagram**

The charging signal to the primary circuit is controlled automatically by the Labview program, where 100 milli-second charging time is needed before it cuts off the signal to open the IGBT circuit. Then the relay opens the primary circuit and causes a surge of magnetic field of secondary coil which creates high voltage on the secondary circuit. This high voltage breaks down the air in between the spark plug electrodes and makes spark. The initial strike of the spark has a consistent 1.25 milli-second delay after the falling edge of the charging circuit due to the switching delay from relay. The injection control signal is adjustable according to the falling edge of the charging circuit.

(3) Remotely controlled valves. There are three computer controlled valves and one emergency switch remotely controlled by operator. Among these three computer controlled valves, one is air valve (discussed in previous section), two others are

solenoid valves for drain and exhaust. The drain valve is rated at 1500 psi with PTFE (Polytetrafluoroethylene) seal which has maximum operating temperature at 500 °F. The exhaust valve is rated at 400 psi with fluoroelastomer seal which has temperature range from -20 °F to 400 °F. All valves are operated through relays which are controlled by NI data acquisition card.

(4) Pressure transducer. Kistler 601B1 pressure sensor together with 5004 charge amplifier are used to measure the pressure inside the ignition chamber. The pressure profile is saved together with current profile to fuel injector. The time elapse between the start of injection and the onset of pressure rise is defined as the ignition delay. The data acquisition rate for the pressure sensor and current probe is 20 kHz.

(5) Accumulator. The accumulator provides high pressure fuel to fuel injector. The injector test rig uses high-pressure inert gas as pressure source. The accumulator transfers pressure from high-pressure nitrogen side to fuel side through a piston. On the nitrogen side, a 6,000 psi compressed nitrogen cylinder is regulated to the outlet pressure from 0 to 3,000 psi.

In addition to the main functional parts discussed above, CO<sub>2</sub> is purged within the external structure in the event of high-temperature fuel test. In this occasion, heated fuel injector will be monitored through a webcam located at the bottom of the external structure to watch for any leakage or smoke (sign of burning). Heater temperatures and oxygen level inside the external structure will be closely monitored through the Labview program. The purpose of these safety measures is to prevent ignition outside of the

ignition chamber but inside the external structure in case of any leakage of high-temperature fuel getting into contact with oxygen and high-temperature heater.

### ***Bottom Plate Configuration***

The key to this ignition rig is the fuel injector – spark plug configuration. As mentioned in other literature, pilot injection is the key in the heavy fueled SI engines. Some literature even found that rotary engines can be run and cold-started with heavy fuel using pilot injection configuration [9, 12]. The pilot injection configuration does not rely on the global fuel air ratio in the combustion chamber. Instead, it acts like a blow-torch type flame jet [10].

Many experiments have been done to figure out the correct injector-spark plug position. Figure 153 shows the original design where injector (at the center of the plate) and spark plug are far apart. Tests show there won't be any ignition unless large fuel quantity is injected and the overall fuel vapor and air ratio falls into the ignition range.

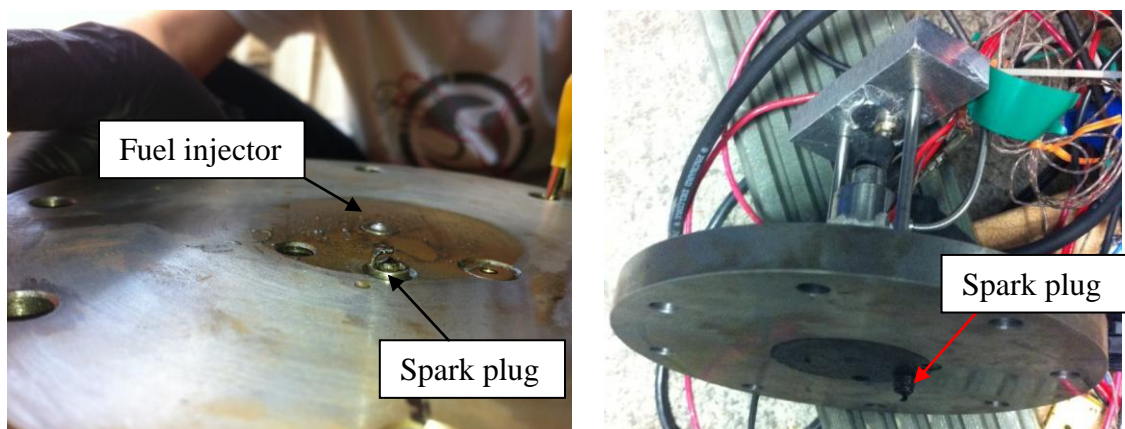


**Figure 153. Original injector-spark plug configuration on the bottom plate**



The problem with this configuration is the fuel air ratio around spark plug can hardly be correct without the mixing motion inside the combustion chamber as in the real engine. The wall-wetting of the direct injected fuel makes it even worse for ignition to happen.

The failure of the first attempt leads to the following pilot injection configuration as shown in Figure 154. The bottom plate is modified to include an angled long spark plug (NGK 31909-MEN-A31 SILMAR9A9S) in the vicinity of the fuel injector. A copper seal is machined to seal the spark plug and control its intrusion depth so that the electrode is located on the periphery of spray path. A close view of the pilot injection configuration is shown in Figure 155.

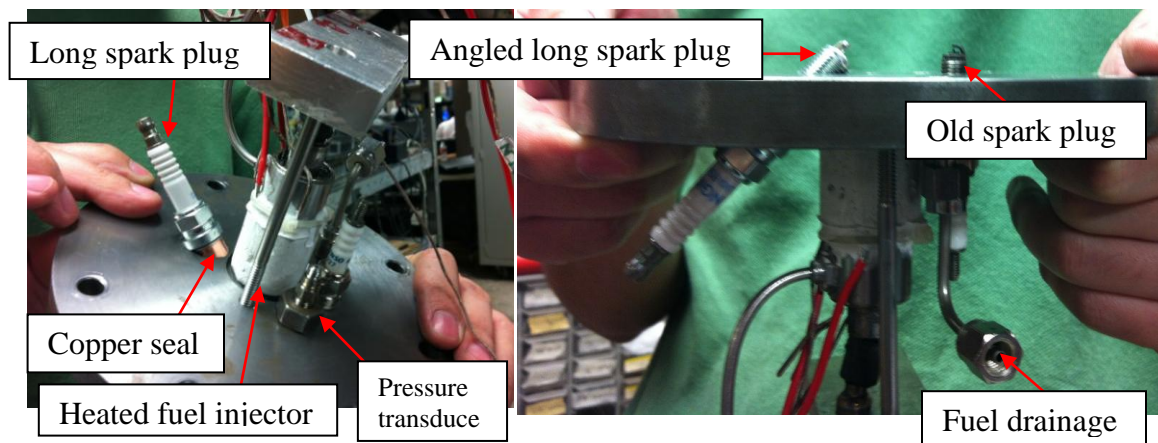


**Figure 154. Pilot injection configuration**



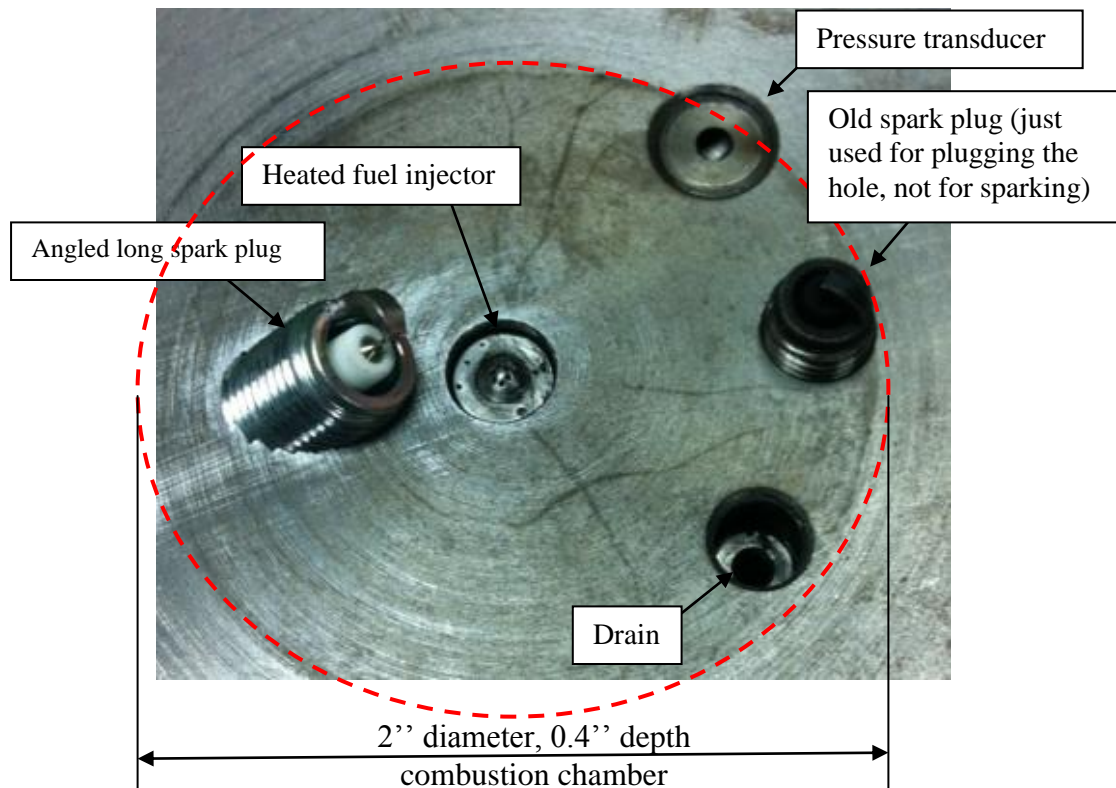


**Figure 155. Close view of pilot injection configuration**

There is one more additional note on this injector-spark plug configuration. The spray pattern was found to be not symmetric to the injector axis. This six-hole direct fuel injector has a spray region more towards one half of a full circle than the other half. The angled spark plug is positioned in this spray region to catch the spray.

***Calculation on Chamber Condition before Ignition***

The purpose of the ignition test is to study the fuel property effect on the ignition behavior in a comparative manner. By comparing ignition behavior among AVGAS, unheated JP-8 and heated JP-8 under the same conditions, insights can be drawn on the

benefits of heating JP-8 and its operability on the Wankel rotary engine. This section discusses the calculation of fuel quantity requirement to form fuel air mixture in the range of combustion limit in both Wankel and ignition test rig.

*Calculation on Pressure and Temperature at the Maximum Compression*

The engine geometry is scanned using 3D scanner as shown in Figure 156 and Figure 157. The maximum and minimum volume of the rotating chamber can then be calculated as shown in Figure 158 and Figure 159.



**Figure 156. Scanned Wankel engine housing**

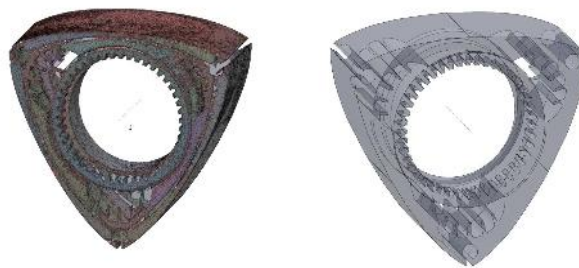


**Figure 157. Scanned Wankel engine rotor**

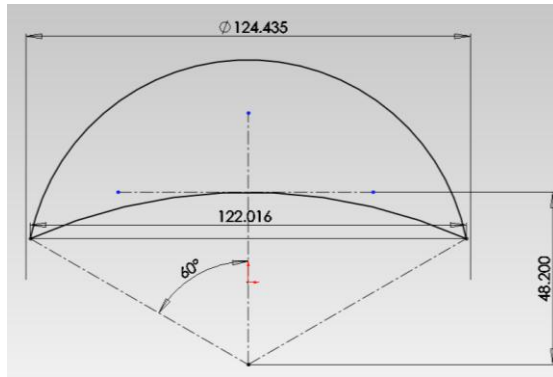


**Figure 158. Maximum volume without pocket**

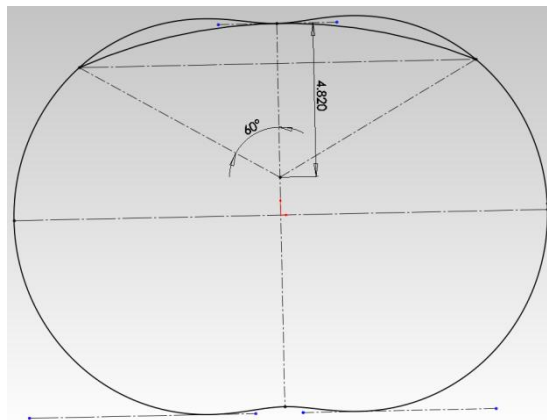


**Figure 159. Minimum volume without pocket**

The volume of the recess (pocket) on the rotor is calculated using Solidworks software. It is subtracted from the total volumes to get maximum and minimum volumes. The pocket model is shown in Figure 160.

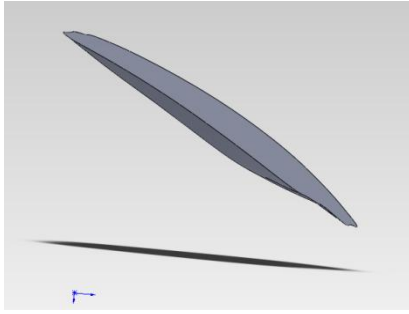


**Figure 160. Pocket volume**

Volume of one pocket: 4357.7 mm<sup>3</sup>

Height of the rotor (shorter than housing): 47.93 mm

Maximum volume in one pocket: 47.93 mm \* 3506.16 mm<sup>2</sup> + V<sub>pocket</sub> =  
172407.9 mm<sup>3</sup>

Minimum volume in one pocket: 47.93 mm \* 177.55 mm<sup>2</sup> \* 2 + V<sub>pocket</sub> =  
21377.6 mm<sup>3</sup>

$$CR = \text{Max.} / \text{Min.} = 8.06$$

In an isentropic process, the entropy is constant, for ideal gas:

$$PV^\gamma = \text{constant}$$

$$P_1 V_1^\gamma = P_2 V_2^\gamma \Rightarrow (P_2/P_1) = (V_1/V_2)^\gamma \Rightarrow (P_2/P_1) = CR^\gamma$$

For CR = 8.06,  $\gamma = 1.4$ ,  $P_1 = 1 \text{ atm (14.7 psi)}$ ,

$$P_2 = 273 \text{ psi}$$

Estimate temperature at  $P_2$  from equation of state, for ideal gas:  $PV = nRT$ ,

The change of entropy is:

$$ds = \frac{du}{T} + \frac{PdV}{T}$$

$$\Rightarrow s_2 - s_1 = \int_1^2 \frac{du}{T} + \int_1^2 \frac{P \cdot dV}{T}$$

Because enthalpy  $h = u(\text{internal energy}) + P V$  (work)

$$dh = du + P \cdot dV + V \cdot dP$$

$$\Rightarrow s_2 - s_1 = \int_1^2 \frac{dh - V \cdot dP}{T}$$

Because for unit mass ideal gas,  $PV = RT$

$$\frac{V}{T} \cdot dP = \frac{R}{P} \cdot dP$$

$$\Rightarrow s_2 - s_1 = \int_1^2 \frac{dh}{T} - \int_1^2 \frac{R}{P} \cdot dP$$

Because  $dh = C_p \cdot dT$

$$\Rightarrow s_2 - s_1 = C_p \cdot \ln\left(\frac{T_2}{T_1}\right) - R \cdot \ln\left(\frac{P_2}{P_1}\right)$$

For isentropic process, entropy change = 0

$$\Rightarrow s_2 - s_1 = C_p \cdot \ln\left(\frac{T_2}{T_1}\right) - R \cdot \ln\left(\frac{P_2}{P_1}\right) = 0$$

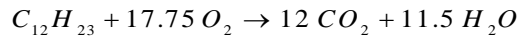
Assume  $T_1 = 25 \text{ C} = 298 \text{ K}$

$$T_2 = T_1 \cdot \left(\frac{P_2}{P_1}\right)^{\frac{R}{C_p}} = T_1 \cdot \left(\frac{P_2}{P_1}\right)^{\frac{\gamma-1}{\gamma}} = (298 \text{ K}) \cdot \left(\frac{273 \text{ psi}}{14.7 \text{ psi}}\right)^{\frac{1.4-1}{1.4}} = 686.7 \text{ K} = 413.7 \text{ C}$$

Since the piston assembly is built using the same maximum and minimum volumes, the calculation is also applicable to the ignition test rig.

#### *Calculation on Fuel Quantity Requirement*

Assuming complete combustion, the chemical equation for JP-8 combustion is:



$C_{12}H_{23}$  is the surrogate of JP-8 in the calculation. Note that the real JP-8 has more than a hundred components and additives.

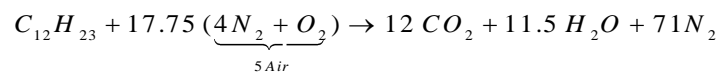
Stoichiometric ratio for mass of fuel to mass of oxygen:

$$\text{Mass of fuel} = \text{number of moles } C_{12}H_{23} * \text{mass per mole } C_{12}H_{23}$$

$$\text{Mass of Oxygen} = \text{number of moles } O_2 * \text{mass per mole } O_2$$

Stoichiometric ratio for mass of fuel to mass of oxygen = 0.294

The chemical equation in terms of air is:



Stoichiometric ratio  $\lambda$  for mass of fuel to mass of air = 0.065

Equivalence ratio:

$$\Phi = \frac{\text{fuel / air}}{(\text{fuel / air})_{st}} = \frac{\left(\frac{\text{mass of fuel}}{\text{mass of air}}\right)}{\left(\frac{\text{mass of fuel}}{\text{mass of air}}\right)_{st}}$$

Notice this is the global equivalence ratio given total fuel and air quantity and assume they are homogeneously mixed. For local equivalence ratio near spark electrode, the equivalence ratio can be very different from this homogeneous charge.

Maximum volume in one pocket of wankel rotary engine is  $172,407.9 \text{ mm}^3$ . The air mass can be calculated at 1 atm, where air density is  $1.2922 \text{ [kg/m}^3\text{]}$ .

$$m_{air} = \rho \cdot V = 1.2922[\text{kg} / \text{m}^3] * 0.1724 E - 3[\text{m}^3] = 0.000222785[\text{kg}]$$

For stoichiometric combustion, it requires JP-8 mass:

$$m_{fuel} = \Phi_{st} \cdot m_{air} = 0.065 * 0.000222785 [kg] = 0.01448[g] = 14.48[mg]$$

This 14.48 mg JP-8 equals to 18 mm<sup>3</sup> at room temperature. Test result showed injection quantity of 12 mg for 1 milli-second injection on-time at 1500 psi fuel pressure at room temperature. The same calculation can be carried out using 100 octane AVGAS (C<sub>8</sub>H<sub>18</sub>). The fuel quantity is 19.5 mm<sup>3</sup> for stoichiometric ratio.

Since there would be leakage from either rotary engine's apex seal or ignition rig's piston ring, the actual air mass at maximum compression would be lower than the ideal number in the above calculation. This lowers the requirement of fuel quantity for stoichiometric ratio.

As mentioned previously, pilot injection configuration works more like a blow-torch type flame jet. The local fuel air ratio around spark plug electrode, rather than the global fuel air ratio, is the key to the ignition. The calculation above is just to give an idea of how much fuel might be required for each ignition test. The actual fuel quantity that causes ignition might be much lower than the calculated value. This fuel quantity will be determined from experiment.

## **Test Results**

Because our goal is to compare different fuels' ignition characteristics under the same conditions, it is important to have parameters consistent for all ignition tests. One of the most important parameters is the fuel quantity and local fuel air ratio. In order to achieve repeatable local fuel air ratio between tests, only one injection should be allowed. Multiple injections would wet the wall and create local fuel air uncertainty between tests. The consistency of ignition conditions requires the 1<sup>st</sup> shot ignition. This

ensures the fuel quantity, local fuel air ratio, and other test conditions are repeatable from test to test. Efforts are directed to make this 1<sup>st</sup> shot ignition happen and happen repeatedly.

The key to the success of first shot ignition is the timing between the injection and spark. The timing diagram includes charging circuit (falling edge as the trigger signal), injection control signal and spark voltage is shown in Figure 161. The spark voltage spikes at the moment when the relay opens the primary circuit. There is a constant 1.25 ms delay from the falling edge of the charging circuit to the spark spike due to the delay of relay. The injection control signal timing can be varied with a minimum increment of 0.1 ms.

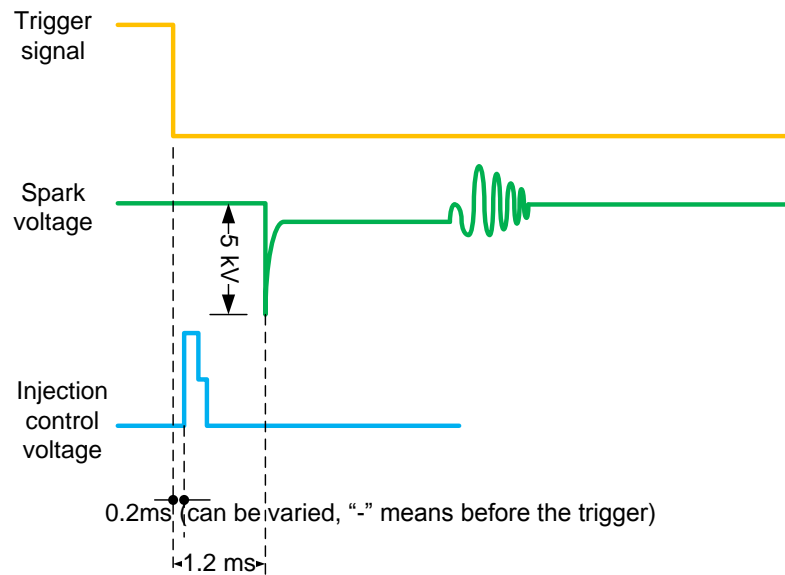


**Figure 161. Timing diagram for ignition test**



The spark signal has been optimized to have the highest initial voltage strike and longest spark duration without breaking down the insulation. A screen shot of the actual signals is shown in Figure 162. As can be seen, the initial strike voltage is 6 kV and the spark duration is 2.5 ms. This spark voltage is measured by a x1000 high voltage probe.

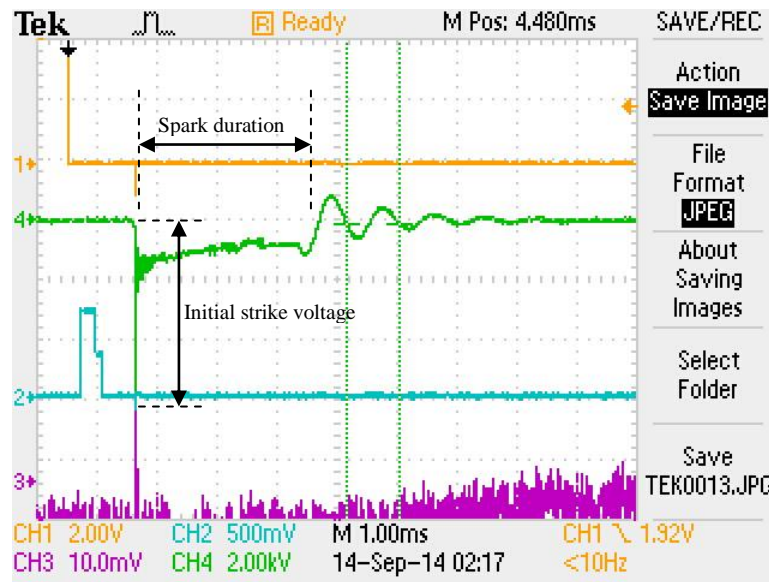


**Figure 162. Actual signals during ignition test**

***With AVGAS***

Table 34 lists the test conditions for AVGAS. The general test procedure is as follows:

- Pre-charge the chamber with 60 psi air;
- Purge the chamber by opening exhaust and drain;

- Close drain, switch air valve to compress the air in the bottom chamber (combustion chamber);
- Click injection pulse in the Labview program. Before running the program, the parameters are pre-defined either by the program or by the user. Ignition circuit charging time is set to be 100 ms. Spark timing is determined by the relay. Injection timing and shape are defined by the user input in the Labview program.
- Click data save. The computer saves pressure and current (to injector solenoid) data at 20 kHz.

Data post-processing mainly include three parameters: (1) first shot ignition success rate; (2) ignition delay time; (3) ignition pressure rise. These three parameters form comparison criteria for different fuels under different conditions.

**Table 34. Test condition with AVGAS**

<b>Pre-charge air pressure (psi)</b>	60
<b>Spark timing</b>	1.25 ms delay relative to trigger signal
<b>Ignition circuit charging voltage</b>	9 V
<b>Injection control on-time (ms)</b>	0.35 / 0.45 / 0.55 / 0.65
<b>Injection timing relative to trigger signal (ms)</b>	0 / 0.1 / 0.2 / 0.3 / 0.4 / 0.5 / 0.6 / 0.7 / 0.8 / 0.9 / 1.0 / 1.1 / 1.2
<b>Fuel rail pressure (psi)</b>	1500 / 3000
<b>Fuel temperature</b>	Not heated (room temperature: 80 F)
<b>Pressure transducer sensitivity</b>	1 mV / 10 psi

Ignitions were obtained after the sequence of events from test procedure. The data were saved to study the ignition characteristics. The pressure and current data is shown in Figure 163. Note that the absolute pressure value is not calibrated due to drifting. However, the pressure difference at short time span is still valid. In this case, the pressure rises from 65 psi to 250 psi. The absolute values are not accurate. However, the pressure difference, or pressure rise in this case, is accurate. From this 1<sup>st</sup> shot ignition, it has a pressure rise of 185 psi.

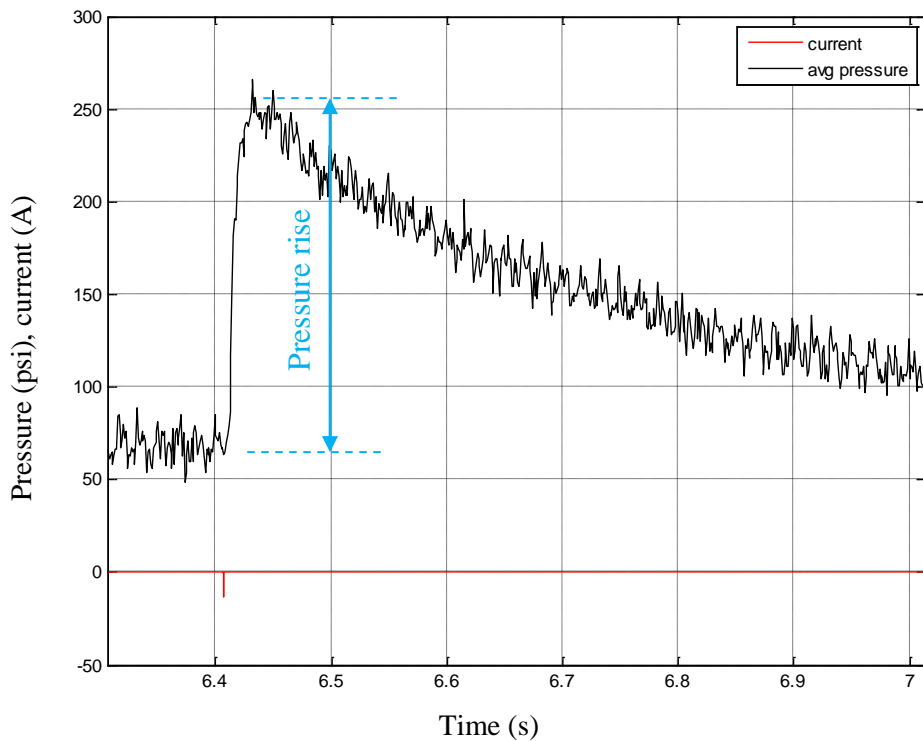


**Figure 163. Injection timing: 0.5 ms, injection control on-time: 0.45 ms, fuel rail pressure: 3000 psi, 1<sup>st</sup> shot ignition**

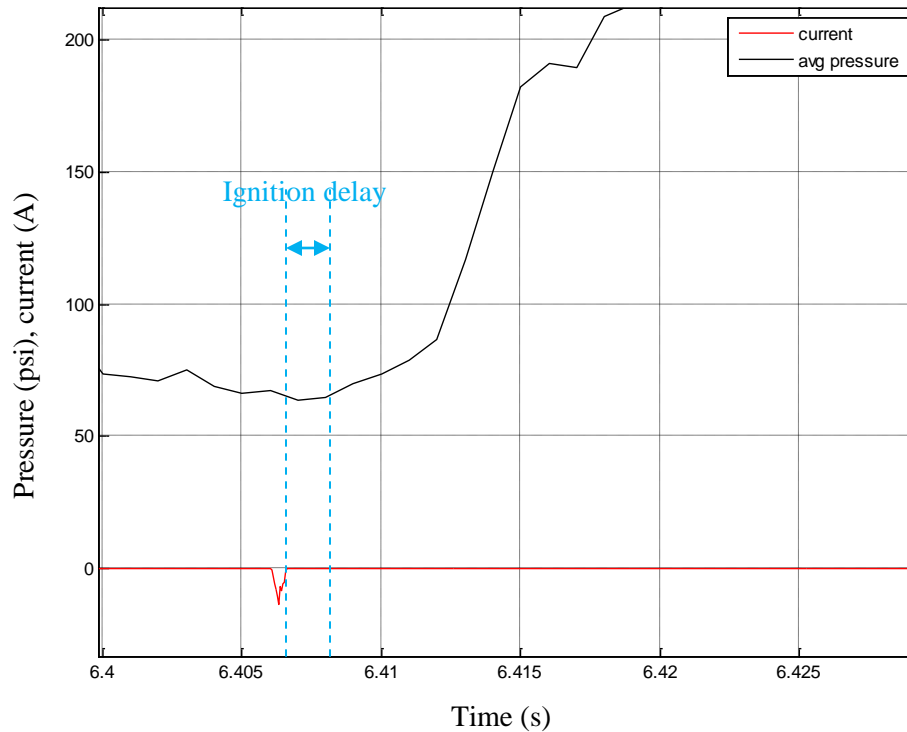


**Figure 164. Zoomed-in view of Figure 163**

Figure 164 is the zoomed-in view of Figure 163 case. Ignition delay is measured from the start of injection to the onset of pressure rise. Note that the red signal is the current of the injector. The actual injection happens about 0.1 ms after the peak of the current profile (refer to Chapter III for details). Therefore, the ignition delay is measured to be the time interval shown in Figure 164.

The DAQ rate is 20 kHz. The pressure data were averaged using 20 data points to mitigate oscillation due to noise. The measured ignition delay times may include +/- 1 ms error due to this averaging process. Note that there is a difference between ignition and pressure rise. The ignition happens when flame kernel forms. The pressure rise is

measured by the pressure sensor as the pressure wave caused by the flame front reaches the sensor. In this study, the actual ignition (flame kernel) cannot be measured. Thus, ignition delay time should refer to the time interval between the start of actual injection and the start of pressure rise.

The following study discusses different factors that might affect ignition characteristics.

### *Injection Pressure Effect*

Figure 165 and Figure 166 show the average ignition pressure rise and ignition delay time under different fuel rail pressures. Fuel rail pressure is raised from 1500 psi to 3000 psi. The ignition pressure rise increases from an average of 80 psi to 105 psi, while the ignition delay times are all around 3.5 ms. There are 2 tests for each rail pressure. All tests are 1<sup>st</sup> shot ignitions. STD stands for standard deviation.

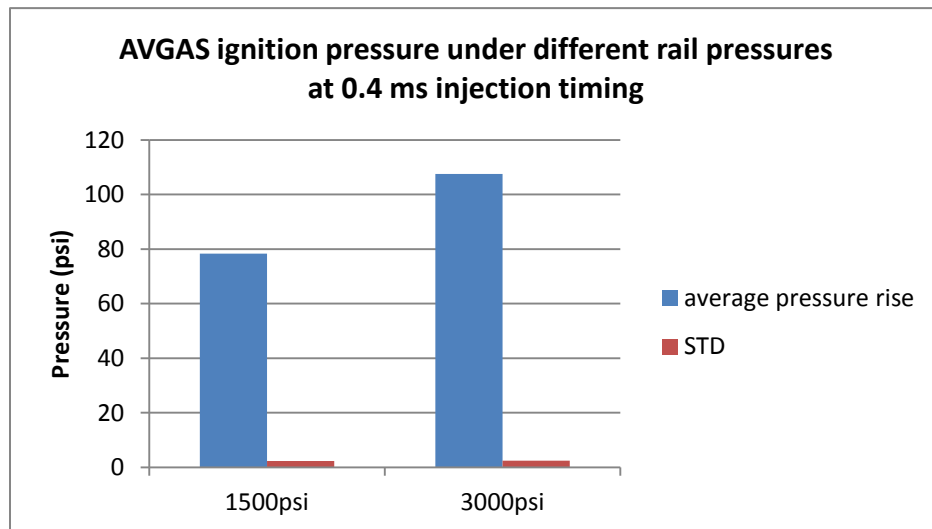


**Figure 165. AVGAS ignition pressure rise under different rail pressures at 0.4 ms injection timing and 0.35 ms injection control on-time**

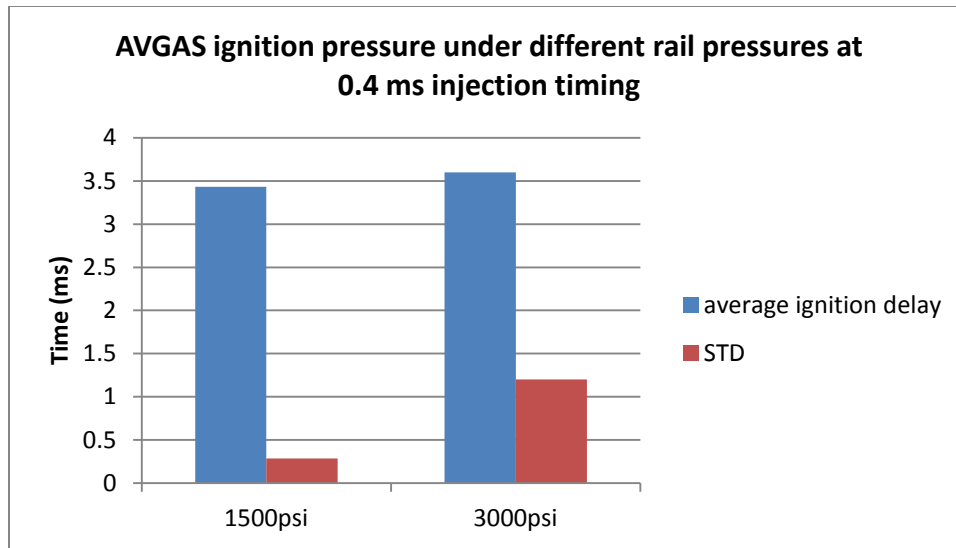


**Figure 166. AVGAS ignition delay time under different rail pressures at 0.4 ms injection timing and 0.35 ms injection control on-time**

The high pressure rise with higher rail pressure should be expected for two reasons. On one hand, higher rail pressure allows larger quantity of fuel injection given the same injector opening time. This larger quantity results higher total energy which explains the higher pressure rise. On the other hand, higher pressure injection results in better atomization. The better atomization creates more complete combustion which could also contribute to higher pressure rise.

*Injection Quantity Effect*

Figure 167 and Figure 168 are cases with different injection quantities. The injection control on-time is increased from 0.35 ms to 0.45 ms at 3000 rail pressure. There is about 10 psi more pressure rise with 0.1 ms more injection quantity (about 2 mm<sup>3</sup> volume) and less than 0.5 ms change on ignition delay time.

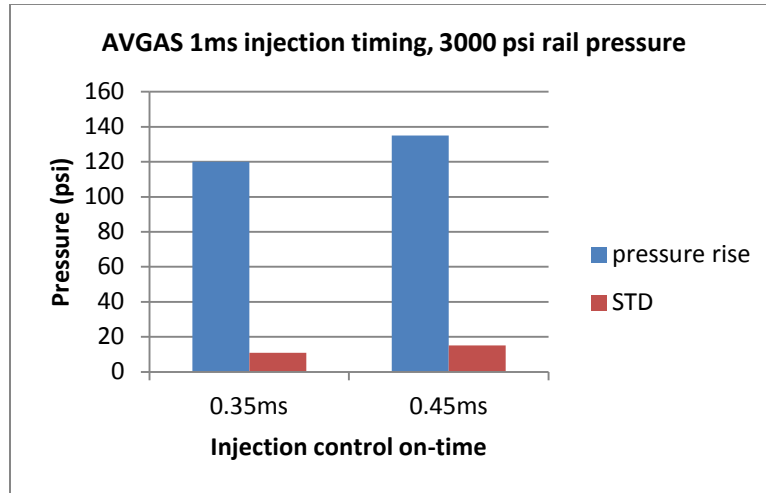


**Figure 167. AVGAS ignition pressure rise at different injection control on-times with 1 ms injection timing and 3000 psi rail pressure**

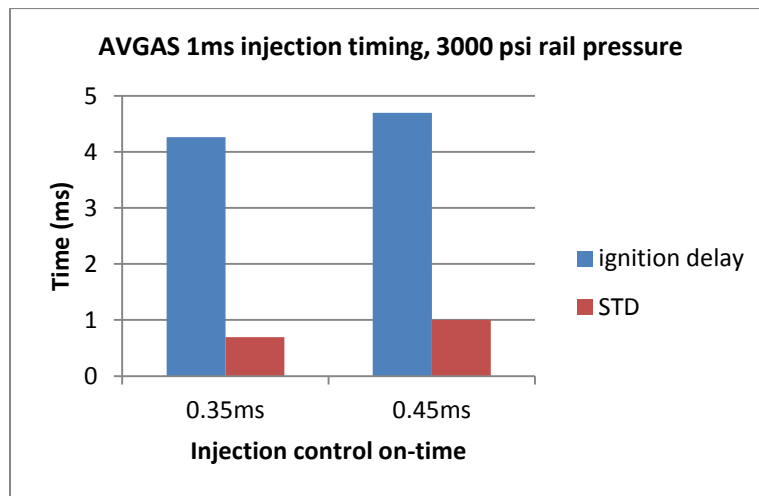


**Figure 168. AVGAS ignition delay time at different injection control on-times with 1 ms injection timing and 3000 psi rail pressure**

*Injection Timing Effect*

The injection timing is varied to determine the timing effect on ignition. Figure 169 shows the injection timing effect on the 1<sup>st</sup> shot ignition success rate with 0.2 ~ 0.6

ms being the best timing in terms of 1<sup>st</sup> shot ignition success rate. However, the 0 ms injection timing gives the highest pressure rise as shown in Figure 170. 0.2 ms injection timing gives the shortest ignition delay of 3.5 ms as shown in Figure 171.

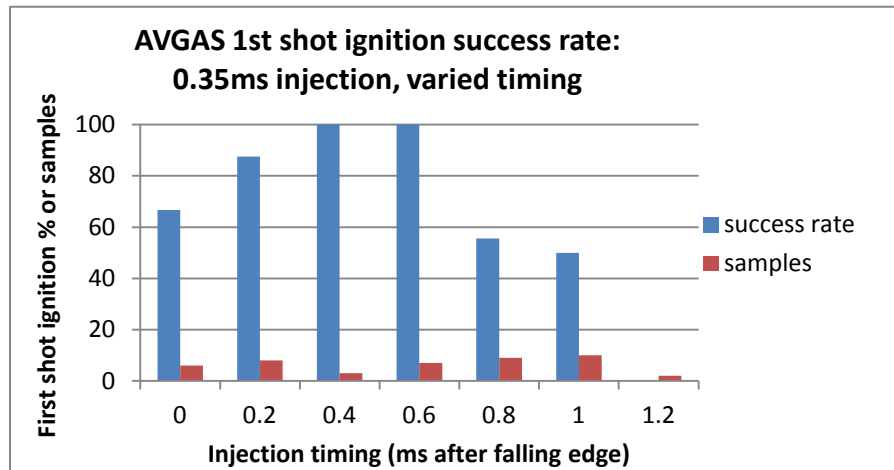


**Figure 169. AVGAS 1<sup>st</sup> shot ignition success rate at different injection timing under 1500 psi rail pressure**

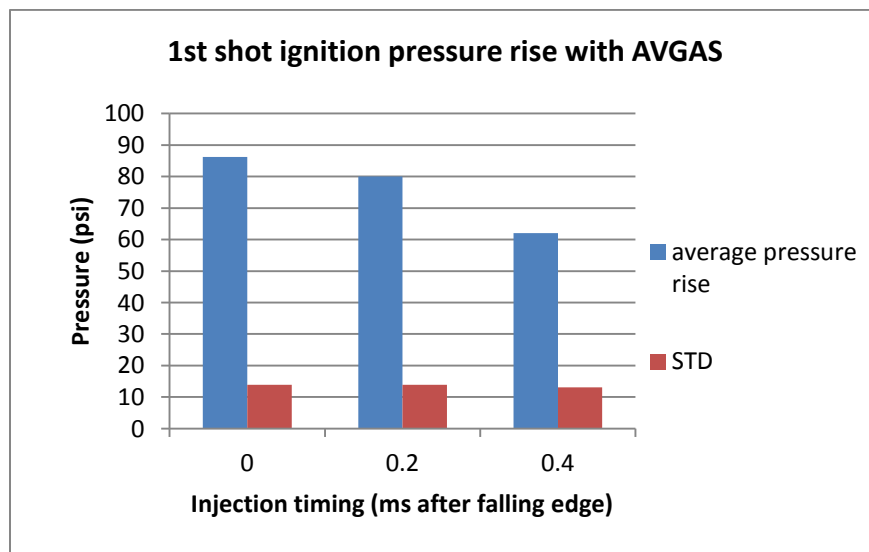


**Figure 170. AVGAS 1<sup>st</sup> shot ignition pressure rise at different injection timing under 1500 psi rail pressure**



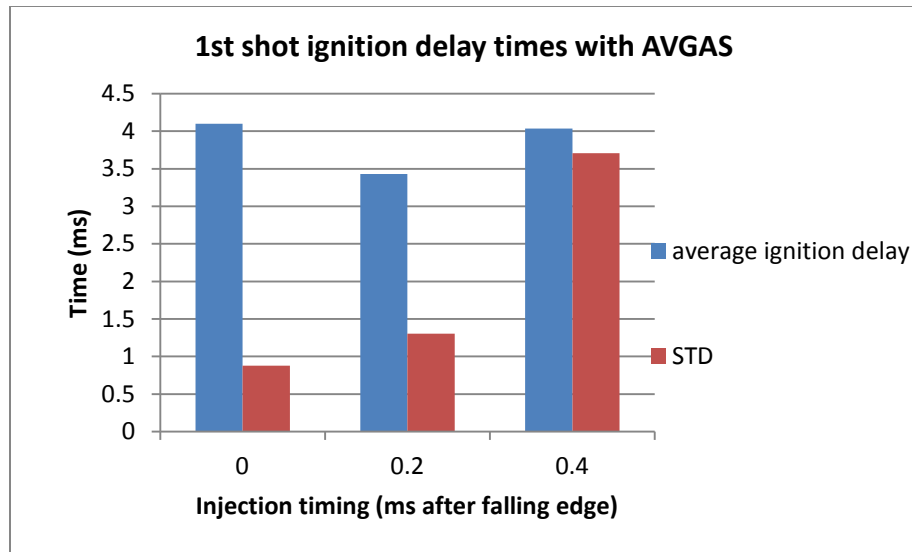


**Figure 171. AVGAS 1<sup>st</sup> shot ignition delay times at different injection timing under 1500 psi**

**With JP-8**

JP-8 ignition test condition is listed in Table 35.

**Table 35. Test condition with JP-8**

<b>Pre-charge air pressure (psi)</b>	60
<b>Spark timing</b>	1.25 ms delay relative to trigger signal
<b>Ignition circuit charging voltage</b>	9 V
<b>Injection control on-time (ms)</b>	0.35 // 0.55 / 0.75
<b>Injection timing relative to trigger signal (ms)</b>	-4.0 / -2.5 / -2.0 / -1.6 / -1.2 / -0.8 / -0.6 / -0.4 / -0.2 / 0 / 0.2
<b>Fuel rail pressure (psi)</b>	1500
<b>Fuel temperature</b>	From room temperature 80 F to heater body temperature 550 F
<b>Pressure transducer sensitivity</b>	1 mV / 10 psi

Heating test procedure:

Besides the procedure that is used to carry out AVGAS test, JP-8 test involves the following additional procedure due to the heating:

- Purge injector with air;
- Pre-heat injector without fuel; (ensures the first several shots are at high temperature)
- After reaching designated temp. (500 °F in this case), turn on valve to let fuel flow into injector;
- Adjust variable power supply for steady-heating at designated temperature.

Acquired signal:

JP-8 temperature used in the charts from this page on is not true fuel temperature. This temperature is the heater ceramic temperature measured by embedded thermocouple.

The following data were taken using 0.35 ms injection control on-time (equivalent to 8 mm<sup>3</sup> at room temperature), and 1500 psi fuel rail pressure. Injection timing is 0.2 ms after the trigger signal. Figure 172 and Figure 173 show the 1<sup>st</sup> shot ignition with 120 psi pressure rise and 3 ms ignition delay with 550 °F preheating temperature.

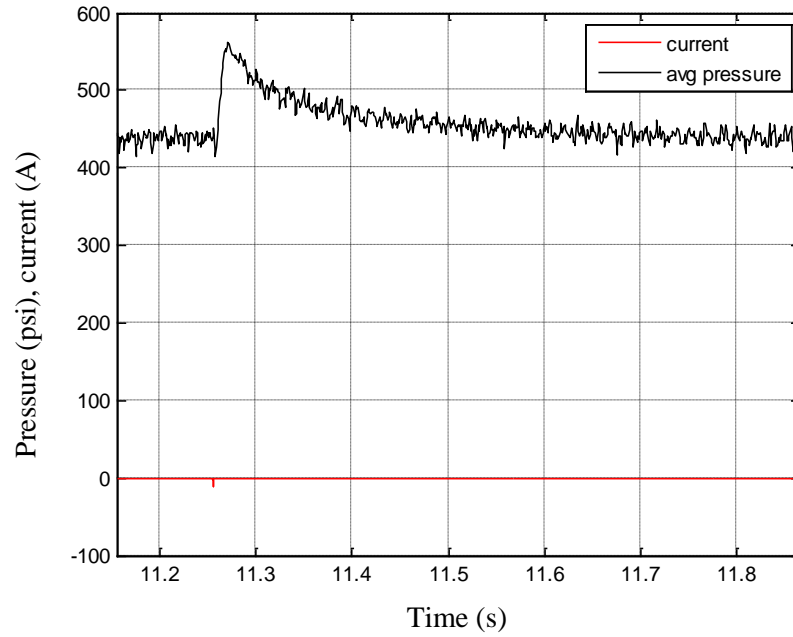


**Figure 172. Preheated JP-8, injection timing: 0.2 ms, injection control on-time: 0.35 ms, fuel rail pressure: 1500 psi, 1st shot ignition**

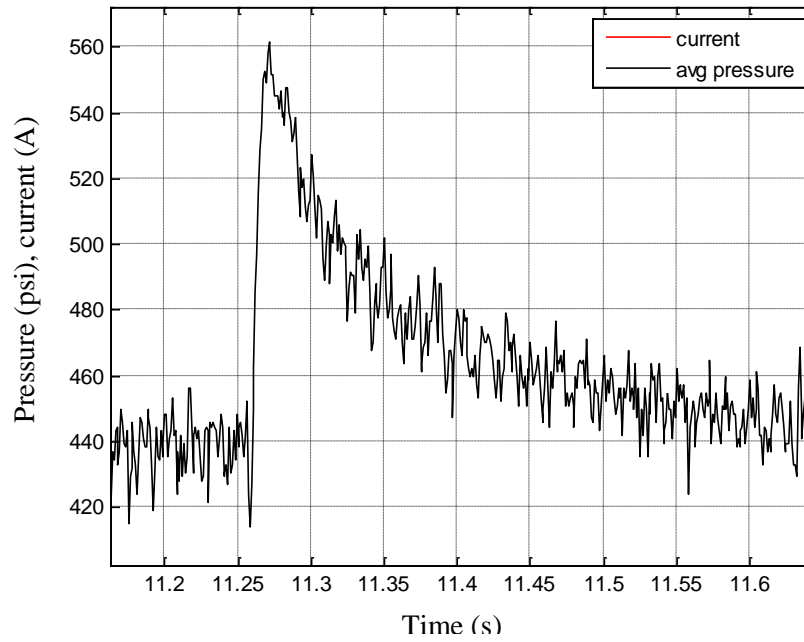


**Figure 173. Zoom-in view of Figure 172**

*Temperature Effect*

JP-8 temperature was varied by changing the heater temperature from 550 °F to 140 °F. The test results are shown in Figure 174 and Figure 175.

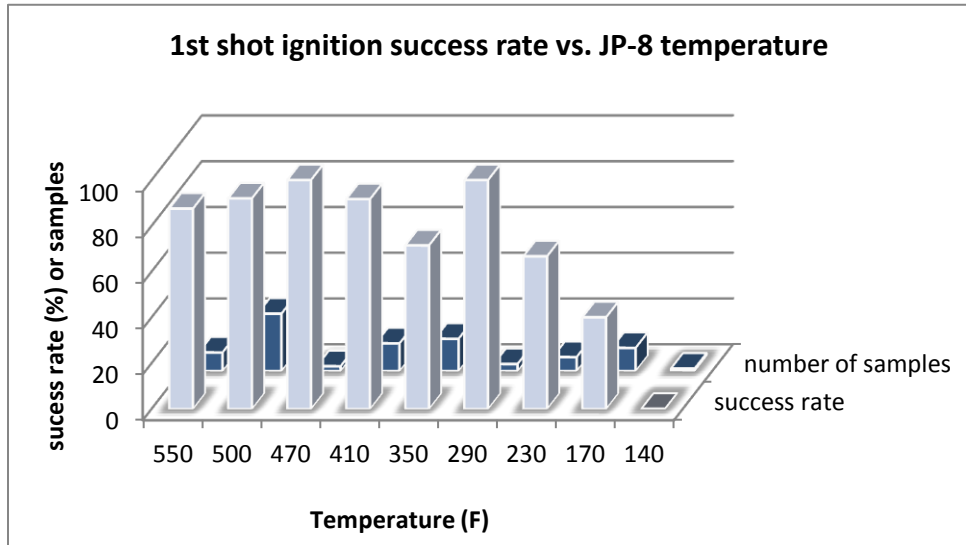


**Figure 174. 1<sup>st</sup> shot ignition success rate vs. JP-8 pre-heating body temperature**

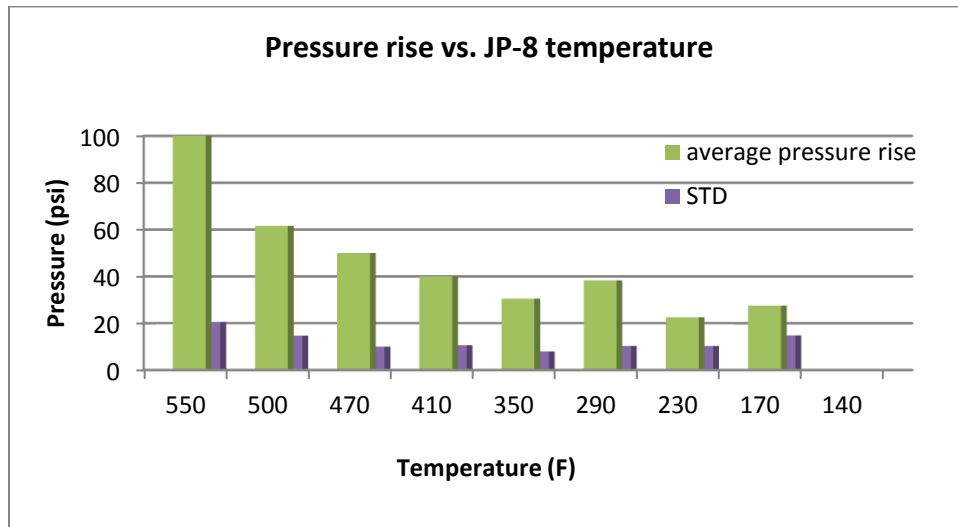


**Figure 175. 1<sup>st</sup> shot ignition pressure rise vs. JP-8 pre-heating body temperature**

As can be seen from Figure 174 and Figure 175, 1<sup>st</sup> shot ignition success rate and pressure rise all increase with the increase of JP-8 temperature in general. The pre-heating temperature of 500 °F corresponds to the outlet JP-8 temperature of 300 °F (refer to Chapter IV high temperature test section). The improvement of 1<sup>st</sup> shot ignition as JP-8 temperature increases demonstrates the benefit of the proposed pre-heating JP-8 idea.

### *Injection Quantity Effect*

Figure 176 and Figure 177 show the pressure rise and 1<sup>st</sup> shot ignition success rate at different injection control on-times (0.35ms, 0.55ms, and 0.75ms) at pre-heating temperature of 500 °F.

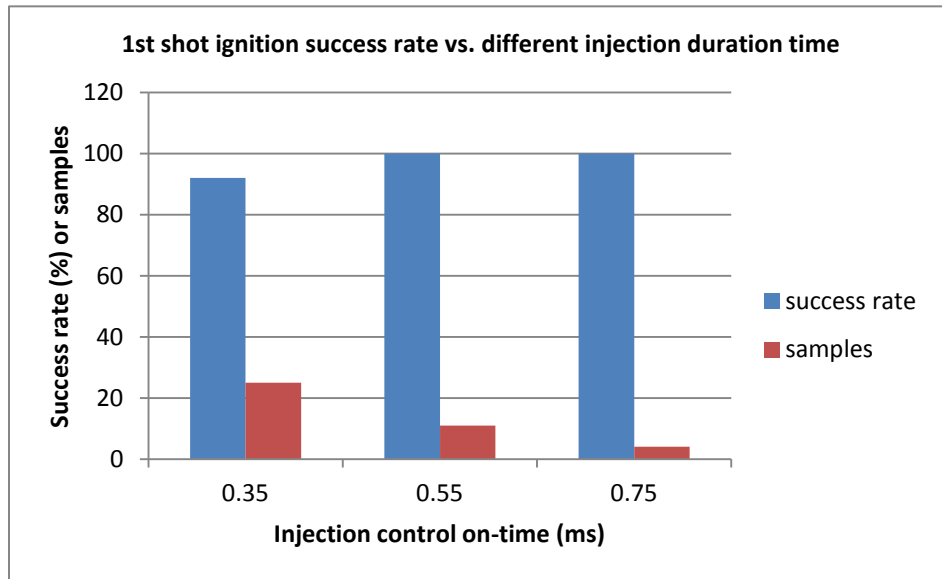


**Figure 176. 500 F preheated JP-8's 1<sup>st</sup> shot ignition success rate at different injection control on-times**

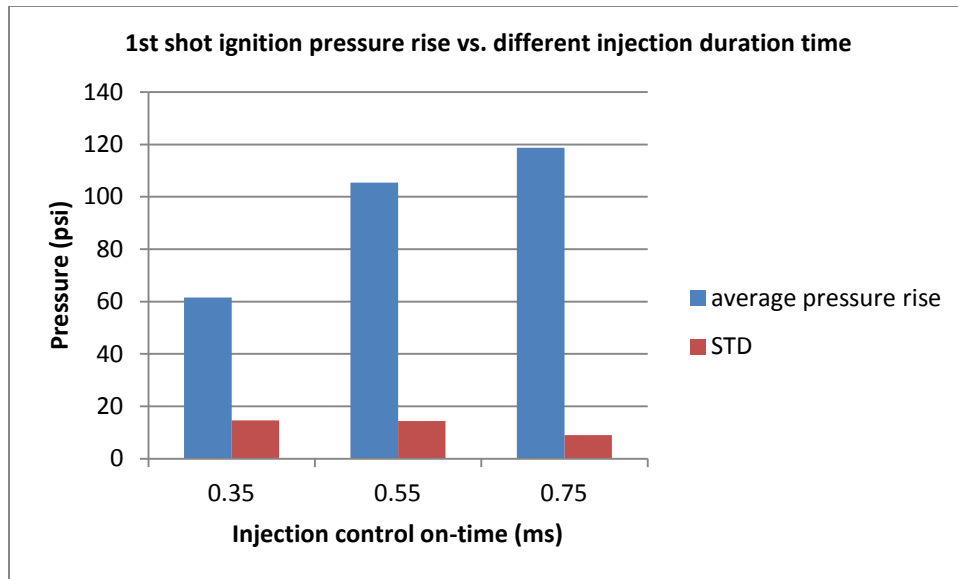


**Figure 177. 500 F preheated JP-8's 1<sup>st</sup> shot ignition pressure rise at different injection control on-times**

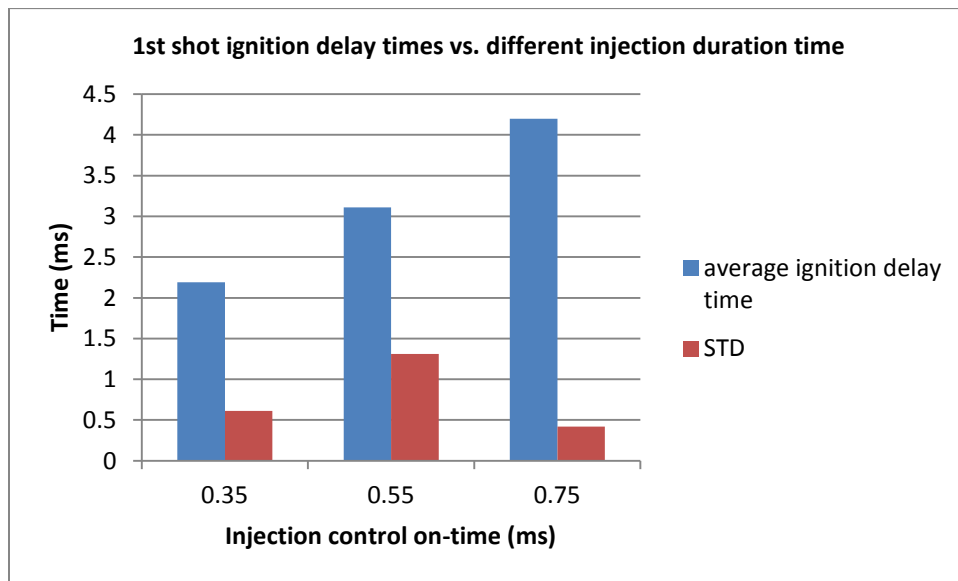


**Figure 178. 500 F preheated JP-8's 1<sup>st</sup> shot ignition delay times at different injection control on-times**

As shown from Figure 176 to Figure 178, the larger quantity injection has higher 1<sup>st</sup> shot ignition success rate. Not surprisingly, the pressure rise is much higher with higher injection quantity. More injection quantity also tends to prolong the ignition delay time.

The fuel quantity for 0.35ms, 0.55ms, and 0.75ms injection control on-time under 1500 psi at room temperature correspond to 8mm<sup>3</sup>, 11mm<sup>3</sup>, and 15mm<sup>3</sup>, respectively. These volumes would be slightly lower for high temperature JP-8.

*Injection Timing Effect*

Injection timing effect was studied by varying it further advanced to sparking. All cases use 0.35ms injection control on-time and 1500 psi rail pressure.

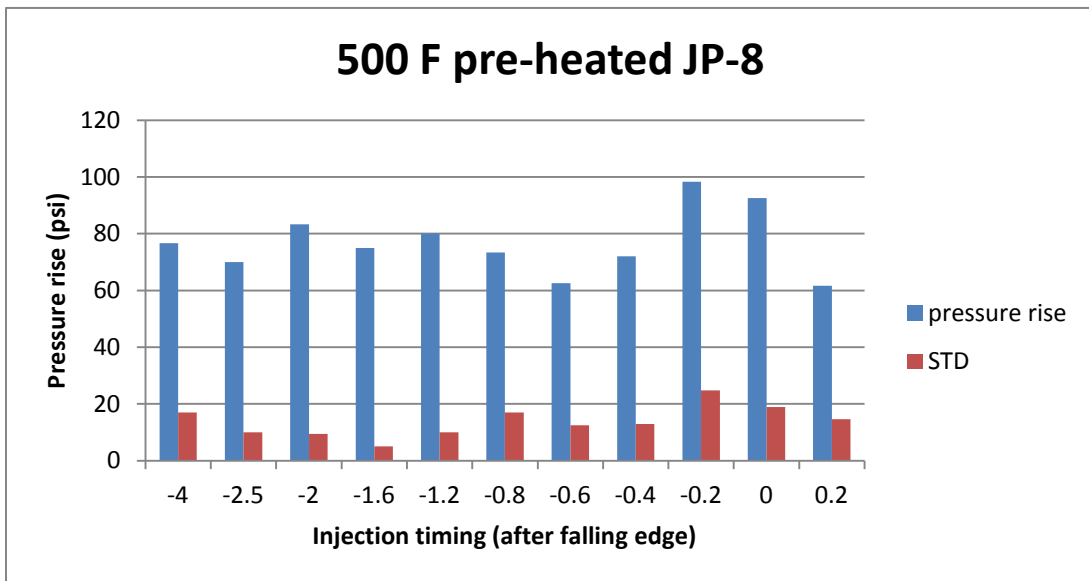


**Figure 179. 500F preheated JP-8's pressure rise at different injection timings**

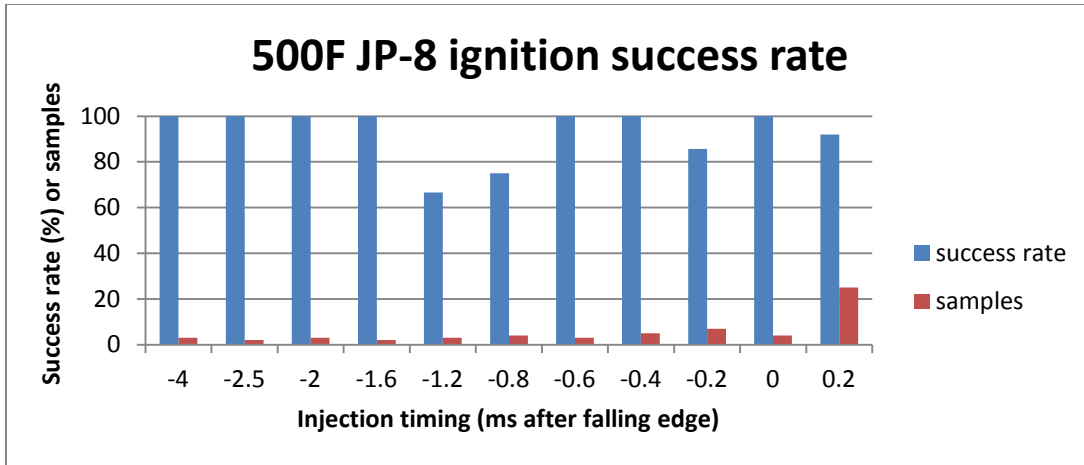


**Figure 180. 500F preheated JP-8's ignition success rate at different injection timings**

As can be seen from Figure 179, the highest pressure rise happens at -0.2 to 0 ms injection timing, while the overall ignition success rate is very high regardless of the injection timing (as shown in Figure 180).

Case comparison among two singled out injection timing -0.4 ms and 0.2 ms cases is shown in Figure 181. For 0.35ms injection control on-time case, -0.4 ms injection timing is where injection stops before the spark takes place and 0.2 ms injection timing is where the spark takes place right at the end of the injection. For 0.75ms injection control on-time case, -0.4 ms injection timing is where the spark takes place right at the end of the injection and 0.2 ms injection timing is where the spark takes place in the middle of the injection.



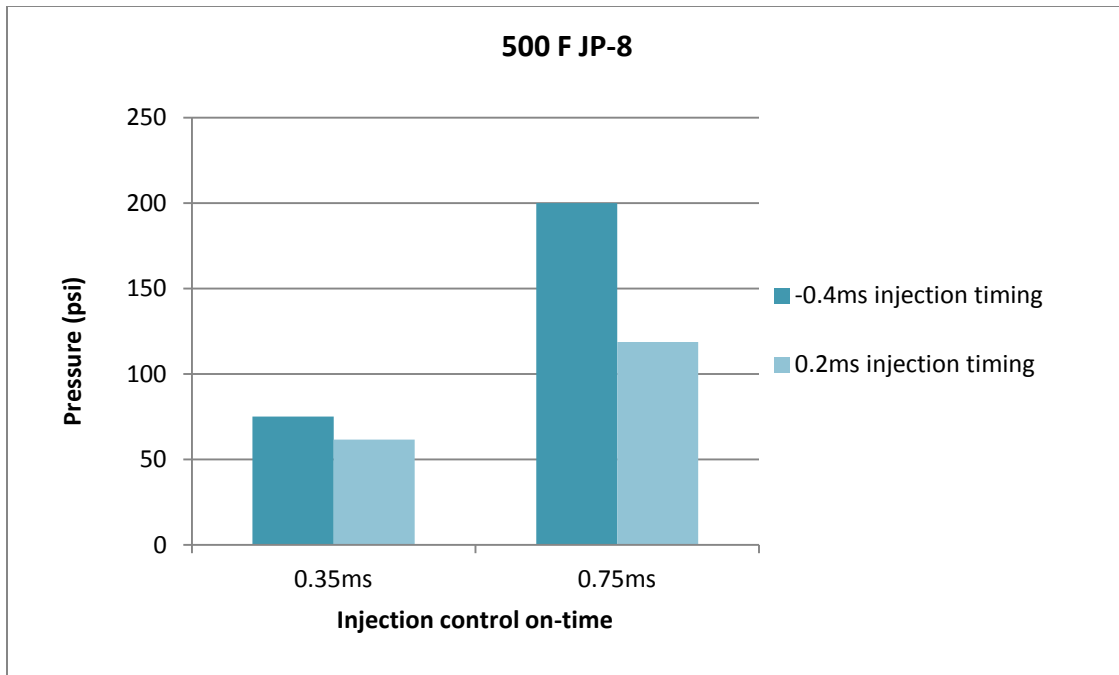


**Figure 181. Preheated JP-8 at different injection timings**

***AVGAS and Heated JP-8 Comparison***

Test condition for the comparison of ignition characteristics between AVGAS and heated JP-8 is listed in Table 36.

***Table 36. AVGAS and heated JP-8 test condition***

<b>Injection timing</b>	0.2 ms
<b>Injection control on-time</b>	0.35 ms
<b>Fuel rail pressure</b>	1500 psi

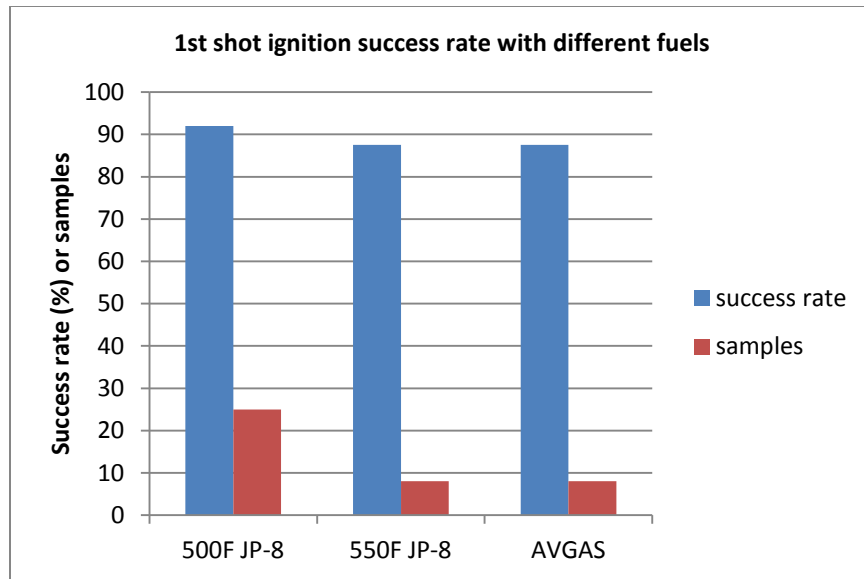


**Figure 182. 1st shot ignition success rate with different fuels**

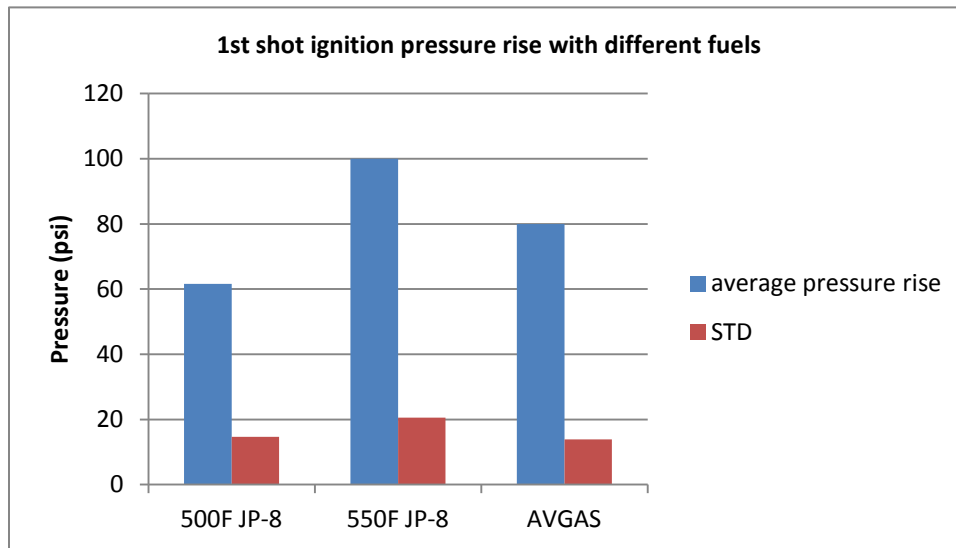


**Figure 183. 1<sup>st</sup> shot ignition pressure rise with different fuels**

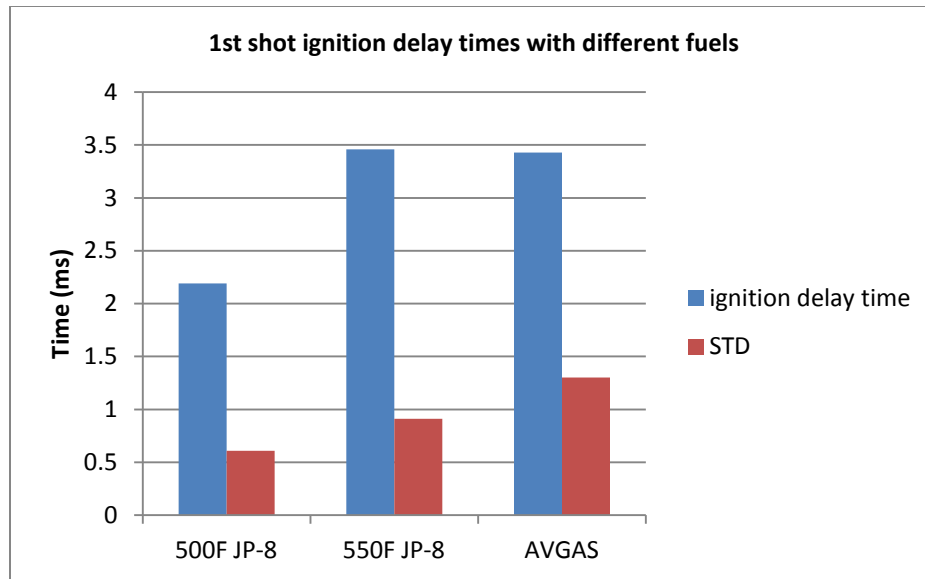


**Figure 184. 1<sup>st</sup> shot ignition delay time with different fuels**

As can be seen from Figure 182 and Figure 184, the 550 °F preheated JP-8 and non-heated AVGAS have similar 1<sup>st</sup> shot ignition success rate and ignition delay time under this test condition. From Figure 183, the 550 °F preheated JP-8 has even higher pressure rise than AVGAS. The superiority of the ignition behavior with 550 °F preheated JP-8 over AVGAS demonstrates the idea of flash heating and the practicality of using the developed flash vapor fuel injector in the Wankel engine.

### ***Conclusion***

(1) Heated JP-8 at its optimal timing and temperature is superior than AVGAS in terms of pressure rise and ignition delay time.

- 1500 psi , 550 °F pre-heated JP-8 at 0.2ms injection timing has equivalent pressure rise and ignition delay time to 3000 psi AVGAS at 0.4ms injection timing. Both have 100 psi pressure rise and 3.5 ms ignition delay.

- 1500 psi, 550 °F pre-heated JP-8 has 20 psi greater pressure rise than 3000 psi AVGAS at the same 0.2ms injection timing. Both have 3.5ms ignition delay time.

(2) The JP-8 temperature plays a dominant role in dictating ignition quality and ignitability. The higher the JP-8 temperature, the better ignition it would create. It also demonstrated the JP-8 would not ignite without pre-heating.

(3) It should be noted that, “JP-8 temperature” is measured from the heater ceramic. It is not the true temperature of fuel at the nozzle. From previous heated JP-8 measurement, the first several shots are measured to be 300 °F when preheating temperature is 500 °F. This measurement, too, may not be the true temperature due to JP-8’s partial vaporization at the temperature greater than 310 °F.

### **Advantages of the Heated JP-8**

The advantages of pre-heated JP-8 from ignition point of view are listed as follows:

- 1) Equivalent ignition delay times (550 °F pre-heated JP-8) to AVGAS.
- 2) Higher ignition pressure rise compared to AVGAS under the same conditions (which means more energy is released with 550 °F pre-heated JP-8).
- 3) Higher ignition pressure rise with higher pre-heated JP-8 temperature.
- 4) Because of the heating, large quantity of fuel can be injected without wetting the spark plug.

Heated JP-8 has higher pressure rise with larger injection quantity, while AVGAS would wet spark plug with relative small quantity. The AVGAS hardly worked

beyond 0.65 ms injection control on-time, while 550 °F pre-heated JP-8 worked at 0.75 ms injection control on-time with much higher ignition pressure rise.

5) Better atomization than room temperature AVGAS.

Under the same rail pressure, 550 °F pre-heated JP-8 has higher pressure rise than room temperature AVGAS. 550 °F pre-heated JP-8 at 1500 psi injection pressure has equivalent ignition pressure rise as room temperature AVGAS at 3000 psi injection pressure. Notice that AVGAS injects more fuel at 3000 psi than 1500 psi JP-8, while the ignition pressure rise favors JP-8. Part of the reason why with smaller quantity heated JP-8 created high ignition pressure rise is that, JP-8 has higher heat release of enthalpy (MJ/Kg) compared to AVGAS. Another reason is that, the heated JP-8 has better atomization (or vaporization) characteristics than room temperature AVGAS under the same injection pressure. From the ignition pressure rise comparison, the heated JP-8 at 1500 psi injection may have similar atomization (or vaporization) characteristics compared to 3000 psi AVGAS injection.

6) Lower pressure fuel rail is required for heated JP-8.

From test results, 1500 psi 550 °F pre-heated JP-8 behaves similarly to 3000 psi AVGAS. The benefit of lower fuel pressure requirement is the lower pumping power used to maintain the fuel injection pressure. This saves engine power and reduces pumping loss.

## CHAPTER VI

### CONCLUSION

Following U.S. army's single fuel initiative, a flash vapor fuel injector was designed, tested and validated to enable Wankel rotary engines on UAVs to run on JP-8.

The challenges of running Wankel with JP-8 originates from JP-8's low vapor pressure and rotary engines' low compression ratio. If no other measures are taken, the rotary engine cannot run or cold start with JP-8. Heating the fuel was proposed to solve this problem. Through a preliminary experiment by running a small piston engine with heated JP-8, the following two important conclusions were made: (1) Heating the fuel helps the engine run and cold start with JP-8. (2) Coking is an issue which must be addressed if high temperature JP-8 heating is needed.

A flash vapor fuel injector concept was developed. The idea was to locally heat JP-8 in a very short amount of time by super-fast heating and releasing it through injection. The short dwell time of high temperature JP-8 was proposed to solve the coking problem. By flash heating, the high temperature JP-8 would have little time to react with dissolved oxygen or if oxidized particle does exist, it would prevent it from further depositing on the wall.

A COTS direct fuel injector made by BOSCH was evaluated as a first-step study of the direct fuel injector characteristics. Because of the application in the Wankel, which operates at 4000 ~ 9000 rpm, the direct fuel injector needs to be run at high frequency and short pulse width. At the same time, it must keep up with the volumetric flow rate for the power requirement.

Injection temporal characteristics were measured by a photo detector. Detailed multiphysics model of a coupled electrical, electromagnetic, fluid, and rigid body dynamic system was studied. The power drive was optimized for the shortest injection opening delay, repeatability and low power consumption. Room temperature fuel injection temporal characteristics and flow rates were calibrated under various conditions.

A flash heater integrated with this direct fuel injector, aiming at heating JP-8 from room temperature to its vaporization temperature within milli-seconds, was designed, built, and tested. High temperature injection tests verified its flash heating capability. No significant coking sign was found after high temperature testing.

As the last step to verify the effectiveness of flash heating, an ignition test rig was designed and built to compare ignition characteristics of AVGAS, unheated JP-8 and heated JP-8. The 550 °F preheated JP-8 demonstrated even higher pressure rise than AVGAS under the same testing conditions. The superiority of the ignition behavior with 550 °F preheated JP-8 over AVGAS proved the effectiveness of flash heating and the practicality of using the developed flash vapor fuel injector in the Wankel rotary engines.

Future work includes: (1) 4 hour long heating test to fully demonstrate mitigated coking with flash heating. (2) Study the location of fuel injector in the Wankel engine to guide the retrofit work. (3) Retrofit the engine with the developed flash vapor fuel injector. Compare engine performance with AVGAS.

## REFERENCES

1. Kalghatgi, G., "Auto-ignition Quality of Practical Fuels and Implications for Fuel Requirements of Future SI and HCCI Engines," SAE Technical Paper 2005-01-0239, 2005.
2. Kweon, C.M., "Small Engine Flash Vapor JP-8 Fuel Injector Testing, Simulation and Development," ARL Internal Report, U.S. Army Research Laboratory, November 4, 2013.
3. Tucker, K.C., P.I. King, R.P. Bradley and F.R. Schauer, "The Use of a Flash Vaporization System With Liquid Hydrocarbon Fuels in a Pulse Detonation Engine," 42nd AIAA Aerospace Sciences Meeting and Exhibit, Reno, NV, 2004.
4. Kubota, M., K. Yoshida, H. Shoji and H. Tanaka, "A Study of the Influence of Fuel Temperature on Emission Characteristics and Engine Performance of Compression Ignition Engine," SAE Technical Paper 2002-32-1777, 2002.
5. Hsu, B., Practical Diesel-Engine Combustion Analysis. Illustrated ed.: Society of Automotive Engineers Inc, 2002.
6. She, J., "Experimental Study on Improvement of Diesel Combustion and Emissions Using Flash Boiling Injection," SAE Technical Paper 2010-01-0341, 2010.
7. Jones, C., "A Survey of Curtiss-Wright's 1958-1971 Rotating Combustion Engine Technological Developments," SAE Technical Paper 720468, 1972.
8. Mount, R.E. and W.L. Greiner, "High Performance, Stratified Charge Rotary Engines for General Aviation," AIAA/ASME/SAE/ASEE 22nd Joint Propulsion Conference, Huntsville, Alabama, 1986.
9. Gavrun, M.T. and R.E. Mount, "Stratified charge rotary engine with dual fuel injection," U.S. Patent 3894518, July 15, 1975.
10. Jones, C., "Advanced Development of Rotary Stratified Charge 750 and 1500 HP Military Multi - Fuel Engines at Curtiss - Wright," SAE Technical Paper 840460, 1984. Doi: 10.4271/840460.
11. Jones, C., J. Mack and M. Griffith, "Advanced Rotary Engine Developments for Naval Applications," SAE Technical Paper 851243, 1985. Doi: 10.4271/851243.
12. Mount, R. and G. LaBouff, "Advanced Stratified Charge Rotary Engine Design," SAE Technical Paper 890324, 1989. Doi: 10.4271/890324.



13. Jones, C. and R.E. Mount, "Design of a High Performance Rotary Stratified Charge Aircraft Engine," AIAA Paper 84-1395, 1984.
14. Mount, R.E. and G. Guarda, "Stratified Charge Rotary Engines for Aircraft," The American Society of Mechanical Engineers, Amsterdam, The Netherlands, 1988.
15. Badgley, P.R., C.E. Irion and D.M. Myers, "Stratified charge rotary aircraft engine technology enablement program," January 31, 1985, 1985.
16. Eiermann, D., R. Nuber and J. Breuer, "An Experimental Approach for the Development of a Small Spark Assisted Diesel Fueled Rotary Engine," SAE Technical Paper 930683, 1993.
17. Groenewegen, J.-R., C. Wilson, P. Litke, J. Hoke and S. Sidhu. "The performance and emissions effects of utilizing heavy fuels and biodiesel in a small spark ignition internal combustion engine," in Aerospace Sciences Meeting. 2011. Orlando, FL: AIAA, 2011.
18. Wilson, C., F.R. Schauer, P. Litke and J. Hoke, "Petroleum-Based and Bio-Derived Jet Fuel Efficiency Optimization Using Fuel Injection in a 34cc 4-Stroke Spark-Ignition Engine," SAE Technical Paper 2011-32-0601, 2011.
19. Suhy, P., L. Evers, E. Morgan and J. Wank, "The Feasibility of a Kerosene Fueled Spark Ignited Two-Stroke Engine," SAE Technical Paper 911846, 1991. Doi: 10.4271/911846.
20. Heavy Fuel Engine Technology. 2007; Available from: <http://www.hirth-motoren.de/UAV/PDF/Heavy%20Fuel%20Presentation.pdf>.
21. Zhang, X., A. Palazzolo, C. Kweon, E. Thomas, R. Tucker and A. Kascak, "Direct Fuel Injector Temporal Measurements," SAE Technical Paper 2014-01-1444, 2014.
22. Zhang, X., A. Palazzolo, C. Kweon, E. Thomas, R. Tucker and A. Kascak, "Direct Fuel Injector Power Drive System Optimization," SAE Int. J. Engines, 7(3), 2014. Doi: 10.4271/2014-01-1442.
23. Palazzolo, A., R. Tucker, X. Zhang, A. Kascak, C. Kweon and E. Thomas, "Flash Vapor Fuel Injector," U.S. Patent (Provisional patent in process), Applied on September 16th, 2014.
24. Tucker, K., "A Flash Vaporization System for Detonation of Hydrocarbon Fuels in a Pulse Detonation Engine," Department of the Air Force Air University, Ph.D. dissertation, Air Force Institute of Technology, 2005.

25. BOSCH HDEV 5.2 data sheet. Available from: <http://www.bosch-motorsport.de/content/language2/html/3444.htm>.
26. Photodarlington optical interrupter switch user's manual, Fairchild Semiconductor Corporation, 2002.
27. Eser, S., R. Venkataraman and O. Altin, "Deposition of Carbonaceous solids on different substrates from thermal stressing of JP-8 and jet a fuels," *Industrial & Engineering Chemistry Research*, 45(26): 8946-8955, 2006. Doi 10.1021/Ie060968p.
28. Altin, O. and S. Eser, "Analysis of solid deposits from thermal stressing of a JP-8 fuel on different tube surfaces in a flow reactor," *Industrial & Engineering Chemistry Research*, 40(2): 596-603, 2001. Doi: 10.1021/Ie0004491.
29. Huong, T., E. Hiroshi, K. Motoki and S. Takaaki, "Effect of Fuel Temperature on Spray Properties Using Local-Contact Microwave-Heating Injector," FISITA2010-SC-0-16, 2010.
30. Handbook of Aviation Fuel Properties, Society of Automotive Engineers, 1988.
31. Greitzer, E.M., C.S. Tan and M.B. Graf, *Internal Flow: Concepts and Applications*. 1st ed. Cambridge Engine Technology Series. 2007.
32. "ANSYS ICEM CFD 13.9 Tutorial Manual," 85.
33. Omega data sheet. Available from: [http://www.omega.com/pptst/IRCO\\_CHAL\\_P13R\\_P10R.html](http://www.omega.com/pptst/IRCO_CHAL_P13R_P10R.html).
34. Subba Rao, H.N. and A.H. Lefebvre, "Ignition of Kerosine Fuel Sprays in a Flowing Air Stream," *Combustion Science and Technology*, 8(1-2): 95-100, 1973. Doi 10.1080/00102207308946633.
35. Char, J.M., W.J. Liou, J.H. Yeh and C.L. Chiu, "Ignition and combustion study of JP-8 fuel in a supersonic flowfield," *Shock Waves*, 6(5): 259-266, 1996. Doi: 10.1007/Bf02535739.
36. Vasu, S.S., D.E. Davidson and R.K. Hanson, "Jet fuel ignition delay times: Shock tube experiments over wide conditions and surrogate model predictions," *Combustion and Flame*, 152(1-2): 125-143, 2008. Doi: 10.1016/j.combustflame.2007.06.019.
37. Kumar, K. and C.J. Sung, "An experimental study of the autoignition characteristics of conventional jet fuel/oxidizer mixtures: Jet-A and JP-8,"

- Combustion and Flame, 157(4): 676-685, 2010. Doi: 10.1016/j.combustflame.2010.01.001.
38. Allen, C., E. Toulson, T. Edwards and T. Lee, "Application of a novel charge preparation approach to testing the autoignition characteristics of JP-8 and camelina hydroprocessed renewable jet fuel in a rapid compression machine," Combustion and Flame, 159(9): 2780-2788, 2012. Doi: 10.1016/j.combustflame.2012.03.019.
  39. Allen, C., D. Valco, E. Toulson, T. Edwards and T. Lee, "Ignition behavior and surrogate modeling of JP-8 and of camelina and tallow hydrotreated renewable jet fuels at low temperatures," Combustion and Flame, 160(2): 232-239, 2013. Doi: 10.1016/j.combustflame.2012.10.008.
  40. Park, P. and J. Keck, "Rapid Compression Machine Measurements of Ignition Delays for Primary Reference Fuels," SAE Technical Paper 900027, 1990. Doi: 10.4271/900027.
  41. Matekunas, F.A., "A schlieren study of combustion in a rapid compression machine simulating the spark ignition engine," Symposium (International) on Combustion, 17(1): 1283-1294, 1979. Doi: 10.1016/s0082-0784(79)80121-6.
  42. Muroki, T., Y. Moriyoshi, M. Takagi, K. Suzuki and M. Imai, "Research and development of a direct injection stratified charge rotary engine with a pilot flame ignition system," SAE Technical Paper 2001-01-1844/4263, 2001.